WAVELET ANALYSIS OF AUTONOMIC AND CARDIOVASCULAR SIGNALS

By

Robert James Brychta

Dissertation
Submitted to the Faculty of the
Graduate School of Vanderbilt University
in partial fulfillment of the requirements
for the degree of
DOCTOR OF PHILOSOPHY
in
Biomedical Engineering

August, 2006
Nashville, Tennessee

Approved:
Professor Richard Shiavi
Professor André Diedrich
Professor Robert Galloway
Professor Alfred B. Bonds
Professor Mitch Wilkes

ACKNOWLEDGEMENTS

First and foremost, I would like to thank the various institutions and grants that have sponsored this research, including the National Institute of Health (NIH) funded Vanderbilt Vascular Biology Training Grant which has provided my stipend and tuition over the last three years, the Discovery Grant sponsored by the Vanderbilt University Medical Center Intramural Grants Program that supplied much needed aid, and NIH grants RR00095 and 1PO1 HL56693, which funded the bulk of this research. Without the help of these organizations, this experience would not have been possible.

I would also like to acknowledge the faculty members of the Vanderbilt Department of Biomedical Engineering and the members of the Vanderbilt Autonomic Dysfunction Center (ADC) for providing me with a thorough background in the fields of biomedical engineering and clinical autonomic research. The members of the Vanderbilt ADC deserve my special thanks for the technical and financial support they have supplied over the last several years.

I also thank my dissertation committee for their time, support, and expert advice on the various projects found in this dissertation. I must give special thanks to my primary advisors, Drs. Richard Shiavi and André Diedrich, for supporting my work and so clearly imparting to me the detailed information of their respective fields. I deeply respect both of these individuals and I have truly enjoyed working with them.

Finally, I give my deepest thanks to my family and friends for their support, encouragement, and companionship. I would especially like to thank my mother and my new wife Felice for all of the little things and the big things they have done for me over the last few years. Without them, I may never have made it to this point.

TABLE OF CONTENTS

Page

LIST OF TABLES

LIST OF FIGURES

CHAPTER I

INTRODUCTION

Motivation

The autonomic nervous system is a regulatory structure primarily responsible for the physiologic response to environmental change. Pathologic disorders affecting this system disrupt the body's natural coping mechanisms, leading to a significantly reduced quality of life. Since primary autonomic disorders, such as orthostatic intolerance [1], neurally-mediated syncope [2], and pure autonomic failure [3] are generally regarded as non-life threatening, they garner less attention than other, more severe medical conditions. However, more common diseases including hypertension [4-7], obesity [8;9], diabetes [10], and congestive heart failure [11] have all been shown to have underlying autonomic components. Therefore, the study and understanding of both the normal and abnormal characteristics of the autonomic nervous system is of great importance to the medical community.

The Vanderbilt Autonomic Dysfunction Center (ADC) is a rare environment consisting of physicians, clinicians, and research scientists devoted to the care, treatment, and study of autonomic disorders. This institution places an emphasis on research investigating the underlying etiologies of these autonomic impairments in order to develop improved treatments for its patients. One of the most important and informative tools used to examine the autonomic origins of these diseases is a technique introduced in the mid-1960's by Hagbarth and Vallbo known as microneurography [12]. It consists of directly recording the sympathetic nerve activity from large extremity nerves using a minimally invasive electrode [13]. Using this technique, scientists have been able to investigate the properties of many autonomic disorders as well as establish links between sympathetic activity and hypertension [4-7], congestive heart failure [11], and other diseases.

Since its inception, the human muscle sympathetic nerve activity, a signal recorded using microneurography, has been analyzed using the same general integrated processing scheme. While this signal-conditioning technique was advantageous when confronting the limitations posed by early data-acquisition devices, it also discarded large amounts of potentially useful data which can easily be recorded with modern computers. Although, an alternative method has

recently been presented [14], its performance was not thoroughly assessed under the many dynamic conditions observed to occur in the sympathetic nerve activity during physiological, pharmacological, or pathological situations. Improvements in its basic mathematical premise have also been suggested. In response to these needs, we have developed and tested an improved quantification scheme for human sympathetic nerve activity.

Along these same lines, there is currently a need to develop a similar analysis technique for murine sympathetic nerve activity. The rapidly emerging field of murine transgenic research has grown to include mouse models of various autonomic dysfunctions [15-17]. However, current quantification strategies of the murine sympathetic activity are limited to simple hardware-based amplitude discriminators whose parameters lack standardization. We have thus employed similar methods to those used for the human sympathetic nerve activity in the hopes of extending the sympathetic nerve quantification options in the mouse.

Although microneurography is a useful research tool, the technique is time consuming, difficult to master, and requires specialized processing and recording devices [13]. Consequently, it is not practical for clinical monitoring and diagnosis of sympathetic abnormalities. At the Vanderbilt ADC and many other institutions worldwide clinicians are in need of diagnostic tools which can be administered with little effort and minimal technical training but are still capable of accurately and consistently assessing autonomic health. In the late 1970's, Akselrod and others were able to partially achieve this goal by applying the Fourier transform and other frequency domain methods to the heart rate variability [18]. These innovative techniques were able to indirectly estimate sympathetic and parasympathetic control of the heart and have been used to study a wide variety of pathologies. Many scientists have continued in this same vein and are extending these non-invasive tools to include indirect analysis methods suitable for all forms of autonomic and cardiovascular interactions.

A trait common in many biomedical signals in general and autonomic/cardiovascular signals specifically is a non-stationary and, for the most part, unpredictable nature. In the past, however, analysis of signals such as the heart rate and blood pressure variability has been generally limited to mathematical techniques whose basic principals include an assumption of stationarity. Over the past decade, wavelet transforms with compact support have been applied to a number of biomedical signals for the purpose of data compression, noise-reduction, and non-stationary signal analysis amongst others [19]. Wavelets are now beginning to gain popularity in

the analysis of cardiovascular and autonomic signals [20-23], and could be used to fill gaps left by previous methods in both the direct and indirect assessment of autonomic function.

The motivation for this work is two-fold. First, we would like to improve upon the current technology used to directly assess autonomic sympathetic nerve function in humans and mice for the purpose of researching the neural basis of autonomic disorders. Secondly, we plan to augment the existing tools used to rapidly and consistently provide indirect estimates of autonomic function for use in clinical diagnoses of autonomic disorders. Given the flexibility of the wavelet transform and the non-stationary nature of these autonomic signals, we believe the wavelet analysis can be used to achieve both of these goals.

Overview

The research discussed in this thesis was performed to achieve two main objectives: (1) To improve the quantification of the sympathetic nerve activity to allow for more complete characterization of human and murine sympathetic function and (2) To extend indirect estimates of sympathetic and parasympathetic influence on cardiovascular function ostensibly for use in clinical diagnosis. As discussed above, due to the non-stationary nature of this data we believe that wavelet-based analysis is well-suited to handle these problems. Included below is a brief summary of the sub-objectives achieved during each stage of this work.

Chapter II provides a general background on the anatomy and physiology of the autonomic nervous system and describes the methodology and limitations of various autonomic function tests and quantification strategies. Brief qualitative descriptions of each problem are also discussed. Also presented are the important differences between Fourier- and wavelet-based analysis, the discrete and stationary wavelet transforms, and human and mouse sympathetic nerve activity. The objective of this chapter is to provide the reader with a background necessary to fully grasp the work and outcomes presented in each of the chapters that follows. A more mathematical description of the techniques used in this work, however, is presented in Appendix A.

Chapter III discusses improvements made in the quantification of human muscle sympathetic nerve activity. This work focuses on an action potential detection strategy that takes advantage of both the burst-like temporal discharge patterns of the human sympathetic activity and the properties of stationary wavelet transform de-noising. Kurtosis, a higher-order statistical

property, is used to distinguish bursts of sympathetic activity from noise within the stationary wavelet transform coefficients and, ultimately, individual sympathetic spikes are identified through wavelet de-noising. This chapter concludes with an evaluation of the detection performance of this new algorithm using simulated signals and compares the spike detection to commonly used integrated burst information in recordings made during a graded head-up tilt protocol.

Chapter IV describes an action potential detector designed specifically for the mouse renal sympathetic nerve activity. Although wavelet spike detection is again used in the mouse, a different strategy is employed to account for disparities between the temporal discharge patterns observed in human and mouse sympathetic activity. Additionally, a comparison is made between the detection performance of the discrete and stationary wavelet transforms. This comparison was also repeated for the human sympathetic activity, the results of which are presented in Appendix B. Each mouse method is evaluated using both simulated data and signals recorded during infusion of the pharmacological vaso-pressor agent phenylephrine. The outcome of this chapter was then used to demonstrate differences between the sympathetic activity recorded in normal mice and several transgenic mouse models of dysautonomias, the results of which are summarized in Appendix C.

The primary objective of Chapter V was to establish a temporal link between the low frequency fluctuations in blood pressure and those found in the sympathetic nerve activity. Once this relationship has been established, the blood pressure fluctuations can be used as an indirect estimate of sympathetic function in situations where the recording of sympathetic nerve activity is impractical or impossible. For completeness, the relationship between the high frequency fluctuations and those found in the respiration were also examined. A model of the complete blood pressure fluctuations with sympathetic and respiratory inputs was evaluated in healthy subjects at rest and during a graded head-up tilt experiment.

Chapter VI uses the result of Chapter V along with other wavelet-based analyses to study the mechanisms involved in different types of neurally-mediated syncope. In this chapter, the power of the inherently non-stationary fluctuations in the blood pressure and heart rate are quantified using a modified continuous wavelet transform, the details of which are discussed in Appendix D. The differences between normal subjects who experience neurally-mediated syncope alone and those who experience neurally-mediated syncope with asystole, a rare

stoppage of the heart, are highlighted. This information may be helpful for clinicians to indirectly assess the autonomic origins of patients with recurrent neurally-mediated syncope.

Chapter VII summarizes this work and follows with a set of global conclusions and future directions.

References

[1] R. Furlan, G. Jacob, M. Snell, D. Robertson, A. Porta, P. Harris, and R. Mosqueda-Garcia, "Chronic orthostatic intolerance: a disorder with discordant cardiac and vascular sympathetic control," *Circulation*, vol. 98, no. 20, pp. 2154-2159, Nov.1998.

[2] R. Mosqueda-Garcia, R. Furlan, J. Tank, and R. Fernandez-Violante, "The elusive pathophysiology of neurally mediated syncope," *Circulation*, vol. 102, no. 23, pp. 2898-2906, Dec.2000.

[3] "The definition of orthostatic hypotension, pure autonomic failure, and multiple system atrophy," *J Auton Nerv Syst*, vol. 58, no. 1-2, pp. 123-124, Apr.1996.

[4] G. Mancia, G. Grassi, G. Parati, and A. Daffonchio, "Evaluating sympathetic activity in human hypertension," *J Hypertens. Suppl*, vol. 11 Suppl 5, p. S13-S19, Dec.1993.

[5] B. G. Wallin, W. Delius, and K. E. Hagbarth, "Sympathetic activity in peripheral nerves of normo-and hypertensive subjects," *Clin. Sci. Mol. Med. Suppl*, vol. 45 Suppl 1, pp. 127s-30, Aug.1973.

[6] B. G. Wallin, W. Delius, and K. E. Hagbarth, "Comparison of sympathetic nerve activity in normotensive and hypertensive subjects," *Circ. Res.*, vol. 33, no. 1, pp. 9-21, July1973.

[7] B. G. Wallin and G. Sundlof, "A quantitative study of muscle nerve sympathetic activity in resting normotensive and hypertensive subjects," *Hypertension*, vol. 1, no. 2, pp. 67-77, Mar.1979.

[8] G. Grassi, G. Seravalle, B. M. Cattaneo, G. B. Bolla, A. Lanfranchi, M. Colombo, C. Giannattasio, A. Brunani, F. Cavagnini, and G. Mancia, "Sympathetic activation in obese normotensive subjects," *Hypertension*, vol. 25, no. 4 Pt 1, pp. 560-563, Apr.1995.

[9] G. Grassi, B. M. Cattaneo, G. Seravalle, M. Colombo, F. Cavagnini, and G. Mancia, "Obesity and the sympathetic nervous system," *Blood Press Suppl*, vol. 1, pp. 43-46, 1996.

[10] R. J. Huggett, E. M. Scott, S. G. Gilbey, J. Bannister, A. F. Mackintosh, and D. A. Mary, "Disparity of autonomic control in type 2 diabetes mellitus," *Diabetologia*, vol. 48, no. 1, pp. 172-179, Jan.2005.

[11] A. Malliani and M. Pagani, "The role of the sympathetic nervous system in congestive heart failure," *Eur. Heart J*, vol. 4 Suppl A, pp. 49-54, Jan.1983.

[12] K. E. Hagbarth and A. B. Vallbo, "Pulse and respiratory grouping of sympathetic impulses in human muscle- nerves," *Acta Physiol Scand.*, vol. 74, no. 1, pp. 96-108, Sept.1968.

[13] B. G. Wallin, "Sympathetic Microneurography," in *Primer on the Autonomic Nervous System*, 2 ed. D. Robertson, Ed. Oxford, UK: Elsevier, 2004, pp. 224-227.

[14] A. Diedrich, W. Charoensuk, R. J. Brychta, A. C. Ertl, and R. Shiavi, "Analysis of raw microneurographic recordings based on wavelet de-noising technique and classification algorithm: wavelet analysis in microneurography," *IEEE Trans. Biomed. Eng*, vol. 50, no. 1, pp. 41-50, Jan.2003.

[15] N. R. Keller, A. Diedrich, M. Appalsamy, S. Tuntrakool, S. Lonce, C. Finney, M. G. Caron, and D. Robertson, "Norepinephrine transporter-deficient mice exhibit excessive tachycardia and elevated blood pressure with wakefulness and activity," *Circulation*, vol. 110, no. 10, pp. 1191-1196, Sept.2004.

[16] N. R. Keller, A. Diedrich, M. Appalsamy, L. C. Miller, M. G. Caron, M. P. McDonald, R. C. Shelton, R. D. Blakely, and D. Robertson, "Norepinephrine transporter-deficient mice respond to anxiety producing and fearful environments with bradycardia and hypotension," *Neuroscience*, Mar.2006.

[17] P. C. Usera, S. Vincent, and D. Robertson, "Human phenotypes and animal knockout models of genetic autonomic disorders," *J Biomed. Sci.*, vol. 11, no. 1, pp. 4-10, Jan.2004.

[18] S. Akselrod, D. Gordon, F. A. Ubel, D. C. Shannon, A. C. Berger, and R. J. Cohen, "Power spectrum analysis of heart rate fluctuation: a quantitative probe of beat-to-beat cardiovascular control," *Science*, vol. 213, no. 4504, pp. 220-222, July1981.

[19] M. Akay, "Wavelets in biomedical engineering," *Ann. Biomed. Eng*, vol. 23, no. 5, pp. 531-542, Sept.1995.

[20] V. Pichot, S. Buffiere, J. M. Gaspoz, F. Costes, S. Molliex, D. Duverney, F. Roche, and J. C. Barthelemy, "Wavelet transform of heart rate variability to assess autonomic nervous

system activity does not predict arousal from general anesthesia," *Can. J. Anaesth.*, vol. 48, no. 9, pp. 859-863, Oct.2001.

[21] V. Pichot, J. M. Gaspoz, S. Molliex, A. Antoniadis, T. Busso, F. Roche, F. Costes, L. Quintin, J. R. Lacour, and J. C. Barthelemy, "Wavelet transform to quantify heart rate variability and to assess its instantaneous changes," *J. Appl. Physiol*, vol. 86, no. 3, pp. 1081-1091, Mar.1999.

[22] K. Tanaka and A. R. Hargens, "Wavelet packet transform for R-R interval variability," *Med. Eng Phys.*, vol. 26, no. 4, pp. 313-319, May2004.

[23] E. Toledo, O. Gurevitz, H. Hod, M. Eldar, and S. Akselrod, "Wavelet analysis of instantaneous heart rate: a study of autonomic control during thrombolysis," *Am. J. Physiol Regul. Integr. Comp Physiol*, vol. 284, no. 4, p. R1079-R1091, Apr.2003.

CHAPTER II

QUANTITATIVE ASSESSMENT OF AUTONOMIC FUNCTION

Anatomy and Physiology of the Autonomic Nervous System

Sympathetic and parasympathetic nerves serve as the antagonistic neural pathways between neurons of the central nervous systems (CNS) and visceral target (or affector) organs. In both systems, the pathway from the CNS to the target organ consists of two neurons. The cell body of the first neuron is housed within the CNS while its axon projects into the periphery and synapses with a second neuron whose cell body can be found in a peripheral ganglion. For this reason, the first and second neurons in the pathway are referred to as the pre- and post-ganglionic fibers, respectively [1]. The postganglionic fibers of the two autonomic divisions differ chemically in that the parasympathetic fibers almost exclusively release acetyl-choline (ACh), while most sympathetic terminals secrete norepinephrine (NE). These neurotransmitters are bound by different receptors on the target organ and, in this way, the two divisions can elicit antagonistic responses [2].

One of the primary roles of the ANS is to buffer against changes in blood pressure caused by environmental and internal stimuli [1]. The autonomic pathway for blood pressure control, known as the baroreflex, typically responds to short-term oscillations in blood pressure (Fig. 1). This reflex begins with stretch sensitive cells, termed baroreceptors, which are embedded in the walls of the carotid artery, aorta, heart, and lungs. These receptors modulate their firing rate in response to both prolonged and transient changes in local arterial blood pressure [3;4]. Generally speaking, an increase in the local pressure causes an increase in arterial stretch which results in an increased firing rate from the baroreceptor.

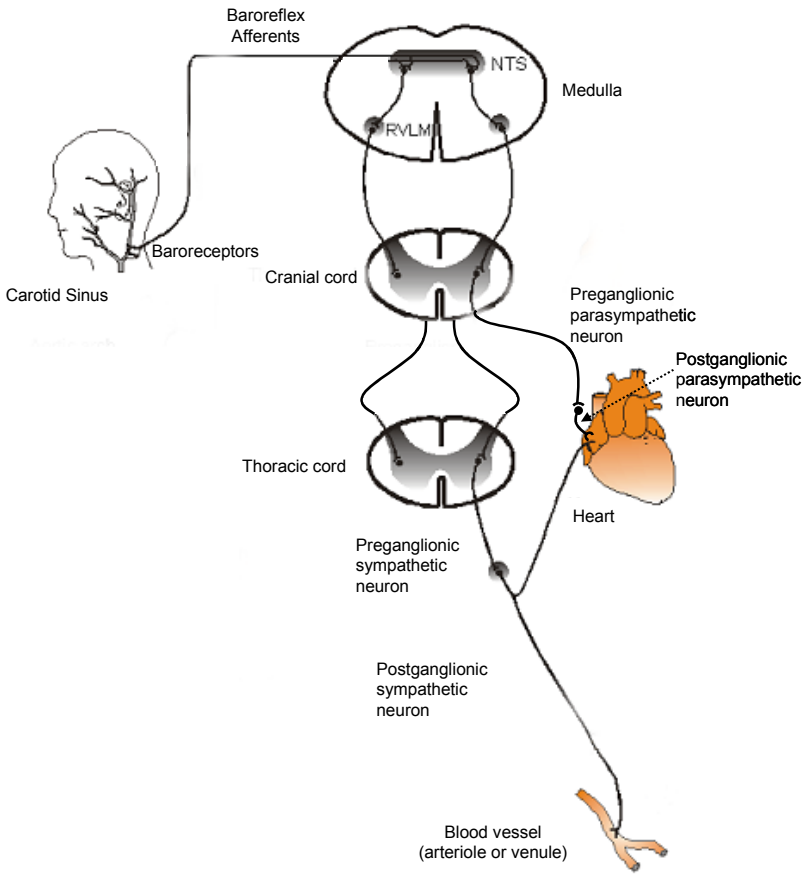

Figure 1. The anatomy of the baroreceptor reflex.

The higher firing rate is sensed by afferent sympathetic fibers that carry the message to the brainstem, ultimately reaching the nucleus of the tractus solitarius (NTS) in the medulla oblongata [1]. At this point, inhibitory messages are sent to the efferent sympathetic branch of the ANS while the output of parasympathetic neurons is amplified. The result of the sympathetic inhibition results primarily in a dilation of many arteries especially those in the skeletal muscle [2]. A secondary consequence of this inhibition is a reduction in heart rate and cardiac contractility. The parasympathetic excitation mainly works to further reduce the heart rate until blood pressure returns to a normal level [2]. The decrease in the cardiac output and peripheral resistance causes a reduction in the blood pressure. If a drop in blood pressure occurs, the opposite chain of events takes place and the sympathetic division is activated to increase heart rate and contractility and constrict peripheral arteries until blood pressure is sufficiently increased [1].

Situations that trigger the baroreceptor response commonly occur under normal physiological circumstances. For instance, the force of gravity experienced upon standing causes blood to pool in the veins and interstitium of the lower extremities, creating an offsetting drop in mean arterial blood pressure that is sensed by the carotid baroreceptors. This scenario elicits increased sympathetic activity to tighten arteries and increase cardiac output in an attempt to force blood through the cardiovascular system to return the blood pressure to normal levels [2]. Although this example demonstrates the ability of modern science to explain normal physiology, many current explanations fall short of elucidating the pathological states of these systems.

General Methods to Assess Autonomic Function

Direct Measures of Autonomic Function

Progress in the field of clinical research has helped physicians identify several abnormal conditions with underlying autonomic pathologies, including orthostatic intolerance [5], pure autonomic failure [6], multiple system atrophy [6], hypertension [7-10], and congestive heart failure [11]. However, the underlying etiologies of these diseases are largely unknown, motivating clinicians and scientists to develop quantitative assays of sympathetic activity. The two most prominent tools to assess sympathetic activity are determination of plasma catecholamine concentration (NE-spillover) and direct electrical recordings from the sympathetic nerve itself.

Norepinephrine Spillover NE-spillover, involves the measurement of plasma NE concentrations [12]. The NE-spillover is thought to represent an excess portion of the NE that is neither bound by target organ receptors or recycled by postganglionic sympathetic neurons and is thought to mirror human sympathetic tone [12]. Nevertheless, blood draws for NE spillover are invasive, require lengthy intervals between samples (5-10 minutes), and produce inconsistent results. Further, this method may only reveal a partial picture of the sympathetic activity [12].

Integrated Sympathetic Nerve Activity Microneurography, a technique introduced by Hagbarth and Vallbo in the late 1960s, represents a more direct and less invasive assessment of sympathetic nerve activity [13]. During this procedure, a signal known as a neurogram is formed using a microelectrode to record the current created by the ion flux across neuronal membranes. Neurograms formed specifically from bundles of postganglionic sympathetic axons projecting to

a skeletal muscle vascular bed are termed the muscle sympathetic nerve activity (MSNA) and neurograms recorded from sympathetic neurons in the renal nerve are known as the renal sympathetic nerve activity (RSNA).

Figure 2. Tungsten microelectrode (2μm, uninsulated tip, 2MΩ impedance) used to record MSNA.

Neurograms of the MSNA are typically formed by inserting a tungsten microelectrode, such as that shown in Figure 2, into the peroneal nerve near the fibular head. The sympathetic fibers that are measured for the recording are found together with afferent C fibers inside Schwann cells which are distributed amongst various myelinated axons within a muscle fascicle (FigureA) [14]. The electrical activity from a collection of these fibers is generally recorded simultaneously, creating a *multiunit sympathetic nerve recording*.

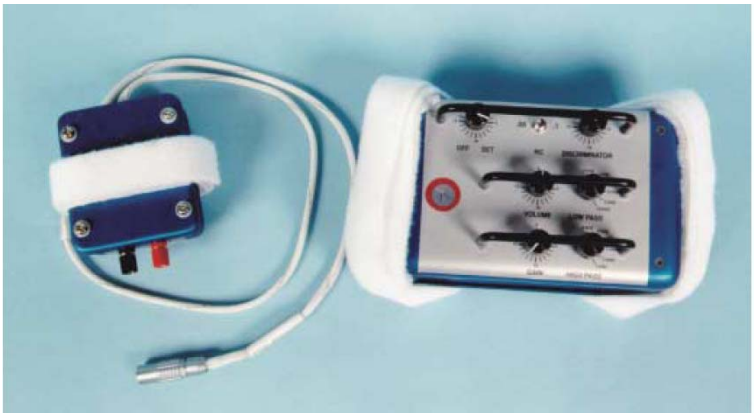

Figure 3. Nerve traffic analysis system used during the NASA Neurolab experiments [15].

The initial recording of the MSNA, known as the raw neurogram (Fig. 4B), has characteristically small spike amplitudes, on the order of a single microvolt, and is significantly corrupted by environmental noise due to the monopolar recording arrangement. Therefore, a nerve traffic analysis unit, as shown in Figure 3, is normally used to amplify, filter, rectify, and integrate the raw neurogram to display a more visually appealing signal. The output of the nerve traffic analyzer has been specifically termed the integrated neurogram for the processing step that defines its appearance (Fig. 4B).

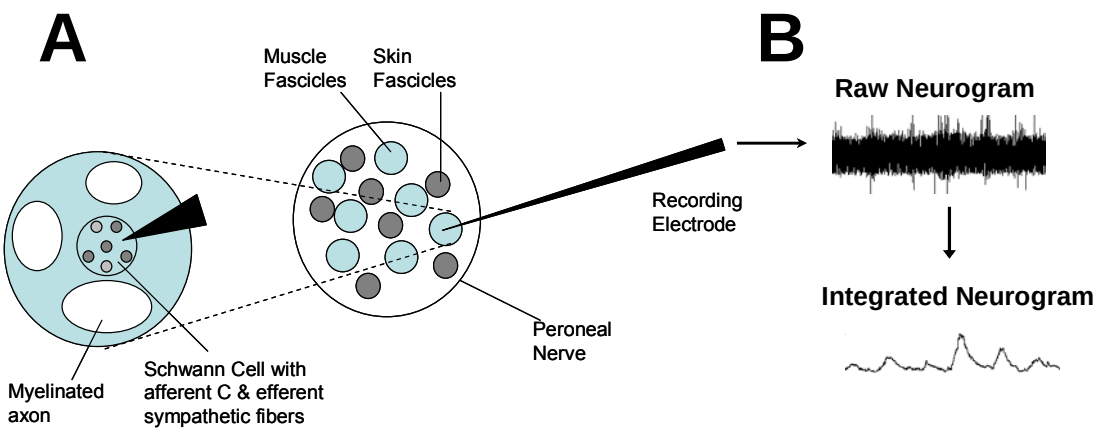

Figure 4. (A) Electrode position for sympathetic nerve recordings. Sympathetic efferent fibers are contained within fascicles that innervate either skin or muscle. They are found along with afferent C-fibers within Schwann cells that are distributed amongst myelinated fibers. Modified from [14]. **(B)** Representative example of the multiunit raw and integrated neurograms.

Single-Unit Sympathetic Nerve Activity The traditional method of recording sympathetic activity integrates the electrical activity of multiple sympathetic neurons using a single electrode. Recently, however, several groups have developed techniques to isolate and record single-unit sympathetic activity [16-22]. Single-sympathetic nerve fibers can be isolated for recordings by repeated minute adjustments of the electrode in the vicinity of a high-quality multiunit recording site [14]. Groups that have successfully accomplished this procedure have reported interesting relationships between single-unit sympathetic firing patterns and several autonomic parameters in subjects with normal [17;20;21] and abnormal or pathological [16;18;19;22] autonomic physiologies. Several studies suggest the existence of several populations of muscle sympathetic neurons with distinctive behavior during basal and activated states [16;18;19;22]. In fact, the single-unit MSNA recordings were found to exhibit behavior different from that of the multi-unit burst activity and have provided additional information about several pathologies including essential hypertension [22] and congestive heart failure [16;19;22].

Indirect Assessment of Autonomic Function

Due to the technical difficulty associated with directly measuring nerve activity and the inconsistency and temporal constraints of NE spillover, interest has grown in developing indirect assessments of autonomic activity. For instance, consistent, non-invasive techniques have been developed to record the electrocardiogram (ECG) and blood pressure waveforms which are used

to monitor the electrical and mechanical properties of the affector organs of the autonomic nervous system. The variability found in these sequences is related to the sympathetic and parasympathetic control of these organs which can provide an indirect assessment of autonomic health [23;24].

Measurement of Heart Rate and Blood Pressure Standard surface ECG lead II is used to record the electrical activity of the heart during all experiments. The recorded ECG waveform can then be used to assess instantaneous heart rate and R-peak to R-peak interval (RRI) length.

The Finapres (FINger Arterial PRESsure) is an instrument which allows for continuous, non-invasive measurement of arterial blood pressure in the finger using a finger cuff. This piece of equipment uses the volume clamp method described by Peñaz [25]. This method clamps the volume in the finger and determines a "set-point" or the pressure found in the arteries at an unstressed diameter, i.e. zero transmural pressure [26]. Once the set-point is established, a servo-controller driven by the output of a photo-plethysmograph is used to dynamically change the finger cuff pressure to match the arterial pressure in the finger [26]. Using this method, a continuous blood pressure output is derived from the instantaneous pressure required to clamp the volume of the arteries [25]. An example of the continuous blood pressure output of the Finapres is displayed in Figure 5.

Oscillations in Heart Rate and Blood Pressure Rhythmic oscillations in specific frequency ranges are common to all cardiovascular and autonomic signals [23;27]. For instance, oscillations with a 10-second period are noticeable in the heart rate and arterial blood pressure, particularly during interventions known to increase sympathetic activity (Fig. 5). When a normal subject is administered an infusion of the pharmacological agent nitroprusside (NTP), the subject will experience a mean blood pressure drop followed by a baroreflex mediated increase in sympathetic activity and heart rate. During this time, both the diastolic and systolic values are shown to change in a near sinusoidal fashion with roughly the same 10-second periods. Similar changes are noticed in the length of time between heart beats. These rhythmic oscillations are typically quantified using some form of spectral analysis to indirectly estimate the level of sympathetic activation.

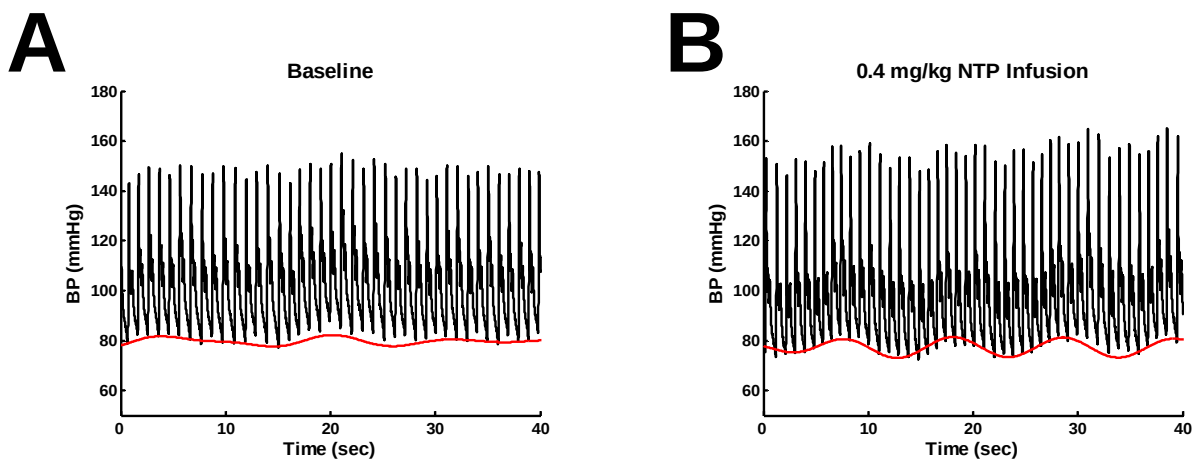

Figure 5. Regular oscillations in diastolic (red) arterial blood pressure. During baseline **(A)**, the cyclic trend is modest, but it appears to become more pronounced during pharmacological enhancement of sympathetic activity with nitroprusside (NTP) **(B)**.

Stimulation of Autonomic Function

Valsalva Maneuver The Valsalva maneuver is conducted by having a subject expire against a closed glottis. This can be monitored by having the subject exhale into a manometer while the blood pressure and ECG are recorded. The cardiovascular changes that occur during this process in healthy individuals are predictable and have been described in four phases (Fig. 6) [28]. During Phase I, blood is squeezed out of the aorta due to the increase in intrathoracic pressure, causing a transient increase in stroke volume and blood pressure and brief reduction in sympathetic activity. In Phase 2 the strained expiration is continued and intrathoracic pressure remains high, limiting the venous return to the heart. This results in a drop in the cardiac output and blood pressure, which in turn causes an increase in heart rate (response tachycardia) and sympathetic activity. A release of the Valsalva maneuver (Phase III) causes blood pressure to drop further for a brief period while sympathetic activity remains high. Phase IV occurs about 5 seconds later and is characterized by an increase in arterial blood pressure, beyond baseline levels (overshoot) that causes a dramatic reduction in the sympathetic nerve activity and heart rate (reflex bradycardia).

The physiological response to the Valsalva maneuver can be altered by pharmacology and diseases. For instance, response tachycardia is absent or blunted in patients with dysfunction of the sympathetic nervous system [28] and patients with congestive heart failure do not experience a drop in blood pressure during Phases II and III [29].

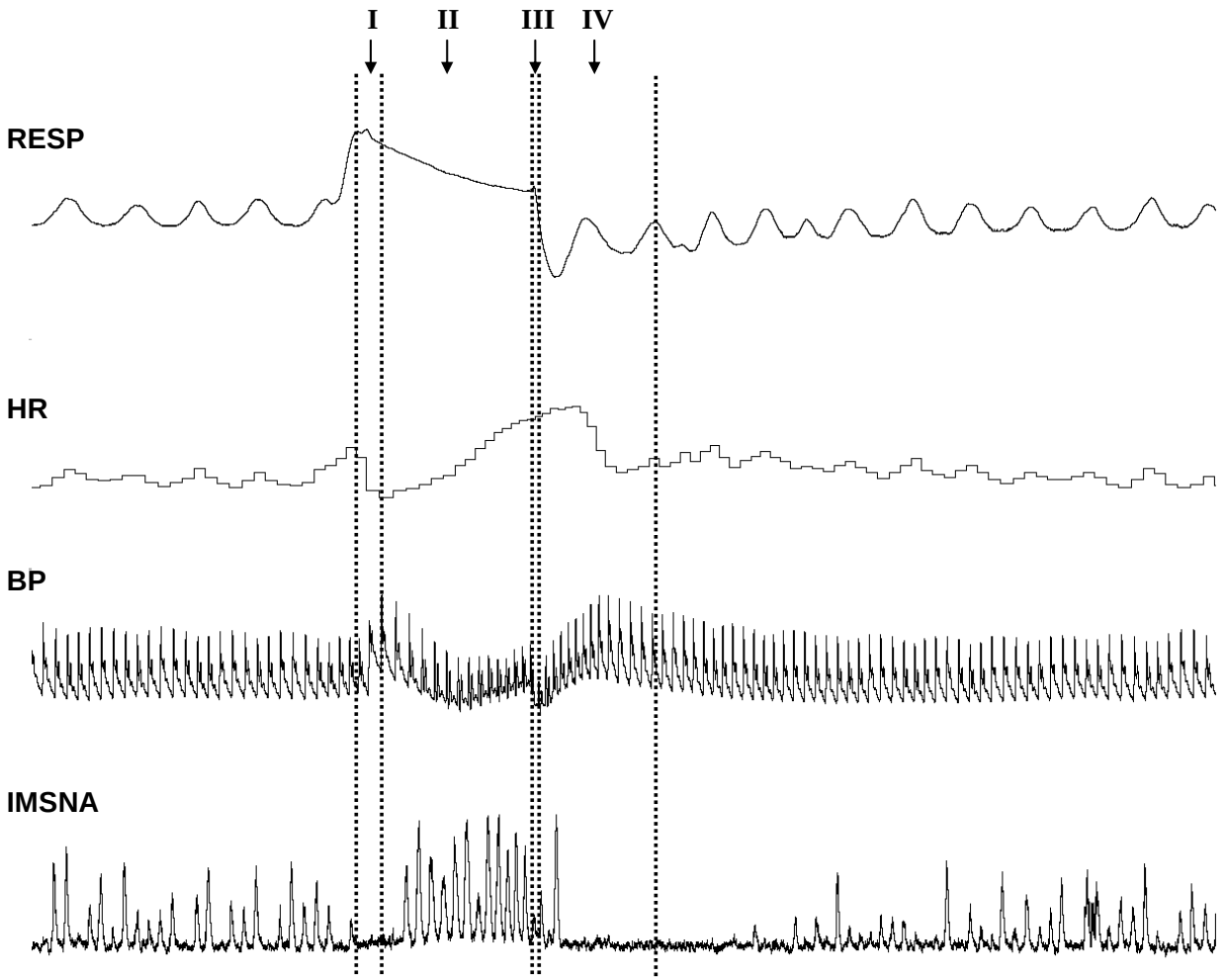

Figure 6. Illustration of the changes in respiration (RESP), heart rate (HR), blood pressure (BP), and integrated muscle sympathetic nerve activity (IMSNA) during the four phases of the Valsalva maneuver (I-IV).

Tilt Test A tilt test can be accomplished using one of two general strategies. Both protocols begin with the subject in a supine position for baseline measures of autonomic and cardiovascular activity for 10 to 20 minutes. During an *upright tilt protocol*, the subject is immediately tilted to an upright position (60^o or 70^o), which is maintained for a period of 30 to 60 minutes [28]. Alternatively, during a *graded tilt protocol*, the tilt angle is incrementally increased by 15^o until a tilt angle of 75^o is reached. At each tilt angle, the autonomic activity is monitored and recorded for a period of 3 to 10 minutes. The upright position is typically maintained for a period of 10 to 20 minutes [28]. After both protocols, a recovery period is recorded for 10 to 20 minutes in the supine position. The normal physiological response to

upright tilt is similar to that described for moving from a supine to standing position and the graded tilt protocol typically results in graded increases in heart rate, blood pressure, and sympathetic nerve activity.

The tilt test can be used to identify patient with various autonomic impairments who typically faint during the test. However, the tilt test has been noted to produce a significant number of false positives [28]. An estimated 20% of healthy young adults will have syncope during an upright tilt test [30]. This may be due to the absence or limited use of the calf and postural muscles during this procedure. These muscles are normally used to force blood pooled in the venous system of the legs back toward the heart.

Pharmacology Various pharmacological agents are used to elicit autonomic responses. One such agent is phenylephrine (PHE), an α_1-adrenoreceptor agonist, which evokes vasoconstriction and a subsequent increase in blood pressure [31]. Alternatively, sodium nitroprusside (NTP) has the opposite effect of vasodilatation followed by an increase in sympathetic activity. These pharmacological agents can be administered either in a bolus or in stepwise infusion. Stepwise infusion of PHE and NTP can be used to produce graded changes in blood pressure, which can be used to generate a baroreflex response curve that plots sympathetic nerve activity against changes in blood pressure. This curve is typically used to assess the function of the baroreflex [32].

Reboxetine is an agent that inhibits the function of the norepinephrine transporter (NET), which functions in the reuptake of unused norepinephrine. Human studies involving blockade of NET with reboxetine have demonstrated a paradoxical tachycardia and elevated blood pressure with a drop in the sympathetic nerve activity [33;34].

Trimethaphan is a substance which is capable of inhibiting sympathetic activity through ganglionic blockade [35]. When this substance is infused, the low frequency oscillations in blood pressure are abolished, but the high frequency oscillations in the range of the breathing frequency are unaffected [35].

Neck Suction Negative neck suction pressure applied over the region of the carotid baroreceptors can also be used to stimulate autonomic function. The neck suction device includes two deformable cuffs and a vacuum pump used to create negative pressure (Fig. 7). During neck suction, the negative pressure in the cuffs is transmitted to transmural pressure of the vessels housing the carotid baroreceptors, causing the vessels to stretch (similar to the affects of elevated

local blood pressure) and ultimately leading to an elevated baroreceptor firing rate. The increased baroreceptor firing rate results in a decrease in sympathetic nerve activity, heart rate, and mean blood pressure. The neck suction process attempts to emulate the baroreflex response to locally elevated blood pressure [3].

The negative neck suction pressure can be applied in either a static or dynamic manner. Sinusoidal neck suction has been demonstrated to induce rhythmic modulation of sympathetic activity, blood pressure, and the RRI [36].

Figure 7. Device used for neck suction of the carotid baroreceptors.

Lower Body Negative Pressure Lower body negative pressure (LBNP) is used to redistribute fluid from the thorax and upper extremity to the lower extremity. This fluid redistribution leaves the upper body hypovolemic resulting in a lower local blood pressure in the aorta and carotid sinuses which is sensed by the aortic and carotid baroreceptors. In response, sympathetic activity and heart rate are increased through the baroreflex.

The device used to create LBNP is shown in Figure 8. LBNP is typically increased in a graded fashion while sympathetic activity, heart rate, and blood pressure are recorded. Sympathetic activity has been shown to increase linearly with LBNP load [37].

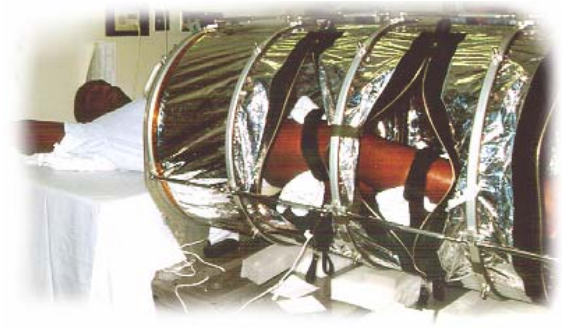

Figure 8. Device used to create lower body negative pressure.

Murine Models to Assess Autonomic Disorders.

Due to the many recent insights into the murine genome, several transgenic and gene targeted mouse models have been developed to aid in the study of cardiovascular [38;39] and autonomic [40-42] diseases. One example of a mouse model of autonomic dysfunction is the norepinephrine transporter (NET) deficient mouse. NET impairment has been implicated in human disorders such as essential hypertension and orthostatic intolerance [33]. Human studies involving blockade of NET using drugs such as reboxetine [33;34] and desipramine [43] have demonstrated a paradoxical tachycardia and elevated blood pressure with a drop in the baseline sympathetic nerve activity. Previous studies with the NET knockout mice have shown similarly high heart rate and blood pressure values, but sympathetic nerve activity was not previously analyzed in these animals [40].

Assessment of autonomic sympathetic function by directly recording sympathetic nerve activity from the renal nerve (RSNA) has recently been introduced in mice [44-47] and there is some debate as to how it should be objectively quantified. The low amplitude, multiunit sympathetic action potentials (AP) recorded from the renal nerve are significantly corrupted by high levels of bioelectric, mechanical, and environmental noise. Contamination from biological noise sources is particularly common in mice because many of the electrically active organs are in close proximity to the recording electrode due to the small frame of the animal.

Signal Processing of ECG, Blood Pressure, and Sympathetic Nerve Activity

Processing of Sympathetic Nerve Activity

Integrated Muscle Sympathetic Nerve Signal Early observations of the human MSNA time series revealed a burst-like nature in the firing patterns of the sympathetic nerves that appeared to correspond to rhythmic changes in the cardiac and respiratory cycles [13]. However, due to characteristically small spike amplitudes (less than 10 μV) and a monopolar recording arrangement that allows for significant corruption from environmental and bioelectric noise, quantification of the MSNA is not straightforward. Consequently, the signal must undergo several stages of preprocessing prior to being analyzed (Fig. 9).

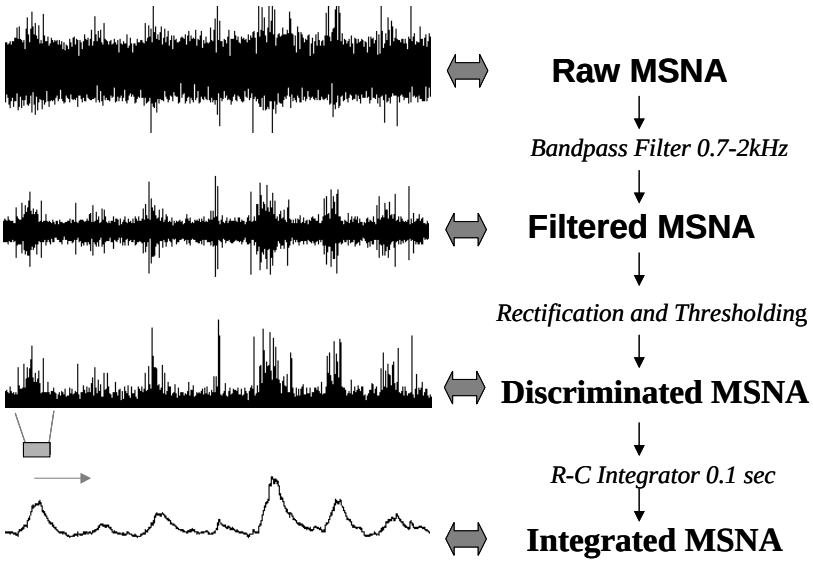

Figure 9. Common signal preprocessing steps to create an integrated neurogram. The recorded raw neurogram is amplified, bandpass-filtered, and full-wave rectified. Threshold discrimination is applied to reduce noise. The final step is to create a linear envelope with an integration network using a time constant of 0.1 seconds.

The traditional MSNA processing scheme takes advantage of the burst-like and band-limited nature of the signal. Typically, the analog recorded signal, termed here the raw neurogram, is amplified with a gain between 1,000 and 99,000, band-pass filtered from 700 to 2,000 Hz, and full-wave rectified. At this point, threshold discrimination is often performed to reduce baseline noise. Finally, the rectified waveform is passed through an RC-integrating network with a time constant of 0.1 seconds to create a linear envelope of the neural activity. For the sake of clarity, the output of this procedure will be referred to as the integrated neurogram or the integrated MSNA (IMSNA).

The integrated preprocessing scheme led to several disputes about data interpretation, including different hypotheses concerning the physical interpretation of the integrated burst amplitude. For instance, burst amplitude variation between subjects may reflect the proximity of the recording electrode to the sympathetic axons or differences in the packing density of the sympathetic fibers [21]. Similarly, it is unclear as to whether an intra-subject increase in burst amplitude represents the recruitment of more neurons to encode different information or simply a change in the firing rate in response to cardiovascular stimulation.

To account for these different theories, various integrated burst parameters have been developed to quantify the sympathetic activity from the integrated neurogram. However, at this time, there is no universally accepted method to measure the integrated bursts. Common conventions of burst quantification include burst frequency (bursts/min) and burst incidence (bursts/100 heart beats) which can both be used to analyze differences in the speed at which

bursts occur in the integrated neurogram [48]. While these parameters are comparable between subjects, neither takes into account the integrated burst amplitude variability which may hold information about the number and firing frequency of neurons contributing to each burst. Another popular quantification strategy involves averaging the burst area over a finite duration, as in burst area/min [49]. This method fails to account for the variability in inter-subject electrode position and the different levels of pass-band noise integrated into each burst [50]. Furthermore, each of these methods is inadequate in evaluating the relationship between the MSNA and other common cardiovascular signals, such as the ECG and the arterial blood pressure [51], and is limited in the study of basal MSNA activity, where burst activity is reduced and many isolated sympathetic action potentials are averaged out of the integrated display [50].

Spike Detection in Murine Renal Sympathetic Nerve Activity Currently, the murine RSNA is quantified using two general strategies: (1) integrating the nerve signal over short periods of 5 to 10 seconds [44] or (2) using a hardware amplitude discriminator to detect APs [45-47]. The integration method suffers from the same limitations discussed in the previous section for the human MSNA. The second approach using amplitude discrimination involves manually adjusting a voltage threshold trigger until the threshold exceeds the level of the noise. All signal amplitudes that exceed the threshold are detected as spikes [52]. The level of the murine RSNA threshold is typically established as the voltage at which no spikes are detected following a bolus injection of a pharmacological agent known to increase blood pressure and suppress the heart rate and RSNA via the baroreceptor-reflex, such as phenylephrine (PHE), [45;46] (Fig. 10). Similarly, investigators studying the rat RSNA have used the highest voltage in the postmortem recording as a threshold for a subsequent off-line amplitude discrimination procedure [53] (Fig. 10). Postmortem activity has also been used to correct total activity recorded during the experiment to obtain an estimate of the true neural activity in mice [47].

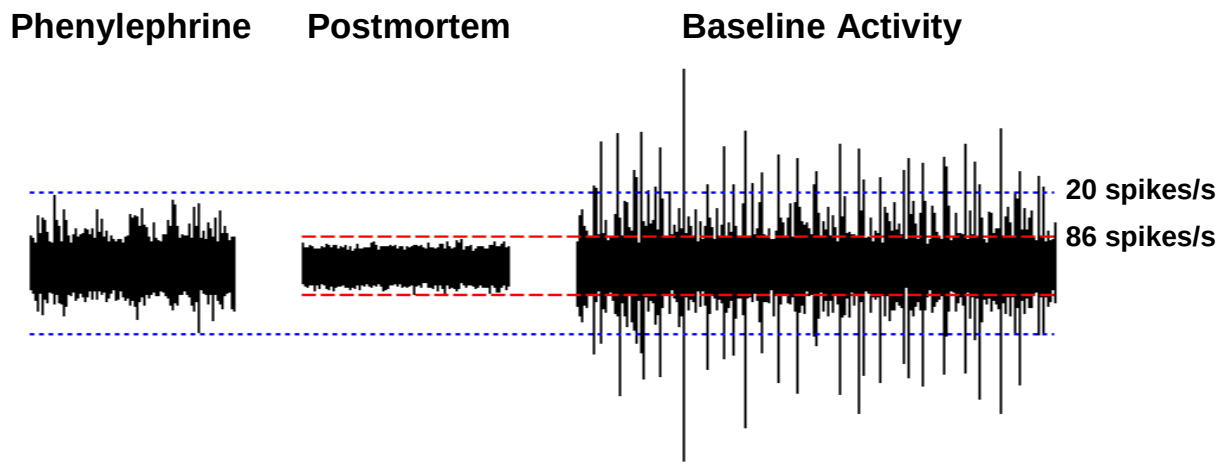

Figure 10. Noise threshold estimates using recordings during baroreflex mediated suppression of RSNA using phenylephrine (PHE) bolus injection (left) and postmortem recordings (middle) in the same mouse produce different spike rates.

Both amplitude discrimination methods currently used in the processing of small animal RSNA signals have specific limitations. Selecting a threshold based on the maximum voltage level during baroreflex mediated decrease of sympathetic nerve activity necessitates having to perform pharmacological tests during each experimental protocol and it does not account for incomplete RSNA suppression due to the presence of baroreflex independent nerve activity. Further, this procedure can not be applied in mouse models that exhibit baroreflex dysfunction. A threshold procedure that uses the maximum voltage of the postmortem nerve recording can only be used for off-line analysis, may not be accurate due to changes in needle position throughout the recording, and does not take into account bioelectric noise present during the living state. The postmortem noise level is usually lower than the living state noise level due additional physiological activities and biological noise in the living animal. Threshold estimation following PHE bolus in the living mouse or after death can produce substantially different spike detection results, as illustrated in Figure 10.

Hardware amplitude discriminators also have several obvious general drawbacks. To begin, they require manual threshold selection which can be both tedious and subjective. Additionally, they only take into account the amplitude and duration of the waveform and disregard other potentially useful attributes such as shape and frequency content. Over the past several decades, a number of spike detection algorithms have taken advantage of these properties and improved upon the classic amplitude discriminator approach, as discussed in several comprehensive reviews [54;55].

Discrete Wavelet Transform Processing of the Sympathetic Nerve Signal Recently, several wavelet-based methods have been used for unsupervised de-noising and detection of single channel, multiunit data with low signal-to-noise ratio [50;56-58]. In particular, spike detection with the discrete wavelet transform (DWT) has been proposed as an alternative to the integrated processing scheme and amplitude discriminators in the quantification of human sympathetic activity [50].

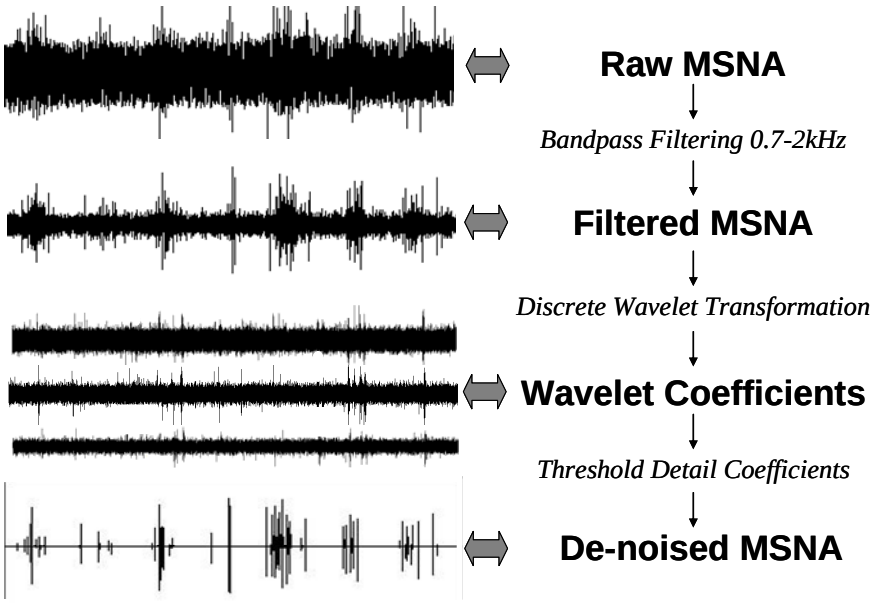

Figure 11. DWT MSNA De-noising algorithm. The recorded raw neurogram is digitally filtered and decomposed into wavelet coefficients using the DWT. The detail coefficients are thresholded and the noise-free signal is reconstructed from the modified wavelet coefficients.

The scheme used to detect the sympathetic spikes, termed here the DWT MSNA de-noising algorithm, consists of an ideal band pass filter, a wavelet de-noising procedure, and an AP detector (Fig. 11**Figure 11.**). The specifications of these components were established based on physiological evidence of the MSNA signal characteristics. For instance, the limits for the band-pass filter were established to enhance the frequency range in which the MSNA is thought to be concentrated while eliminating frequencies significantly corrupted by noise [50]. Evidence of the MSNA band limits can be seen in Figure 12. When given even small amounts of a pharmacological agent known to reduce sympathetic nerve traffic, such as 1 mg/kg trimethaphan (TMT), the power in the 700-2000 Hz frequency range is visually diminished.

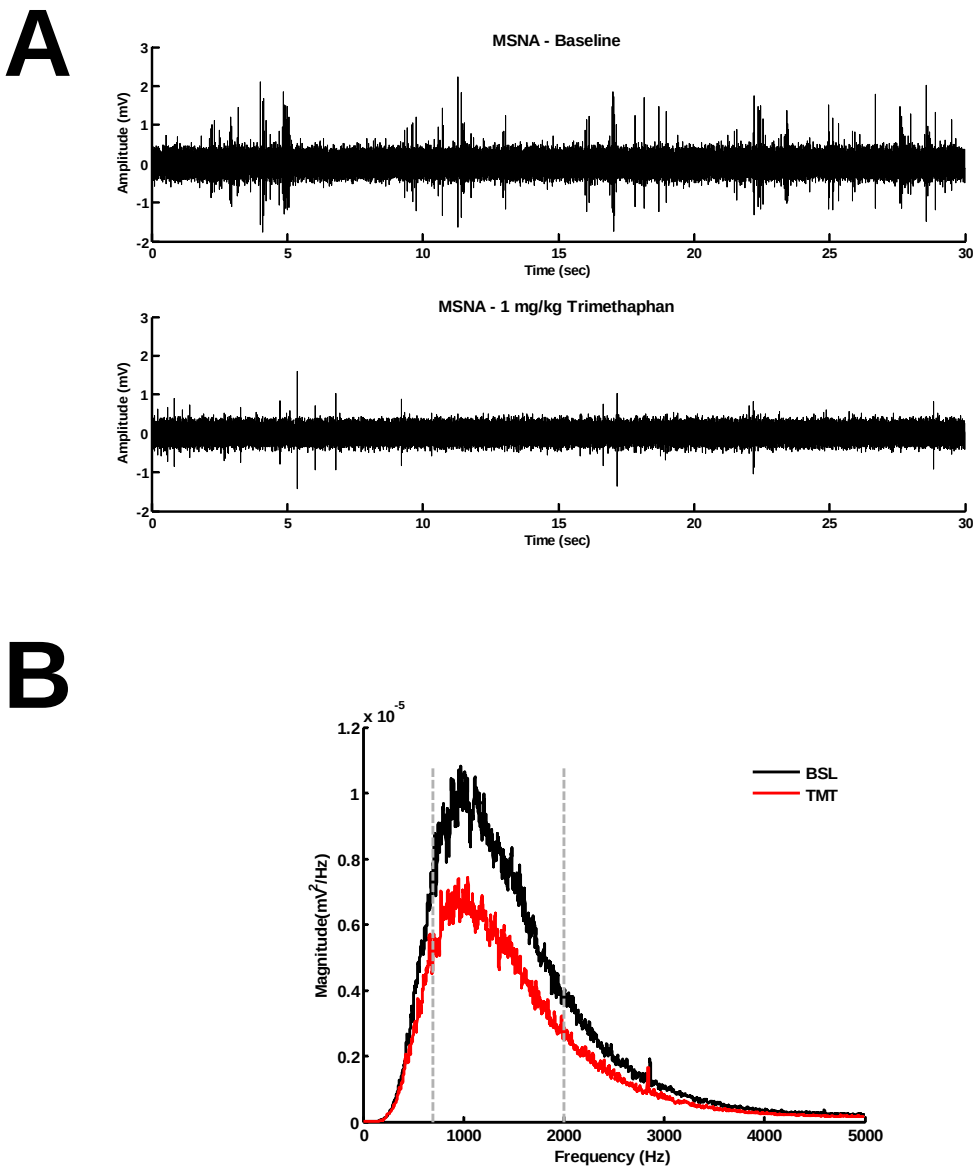

Figure 12. (A) Raw MSNA time series during baseline (top) and 1mg/kg trimethaphan (TMT) infusion (bottom). TMT significantly reduces sympathetic nerve traffic. **(B)** PSD of the MSNA during baseline (black) and 1 mg/kg TMT infusion (red). Broken gray lines indicate the bounds of the 700 – 2000Hz bandwidth. The MSNA power is diminished in this frequency range during TMT infusion.

After band-pass filtering the MSNA signal, DWT de-noising was used to reduce any noise within the 700 – 2000 Hz pass band. A brief description of the discrete wavelet transform and wavelet de-noising is given below; however Appendix A contains a more comprehensive review of these subjects.

The discrete wavelet transform (DWT) methods use a *mother wavelet*, Ψ, which can be translated and dilated according to the following equation (Matlab notation):

$$\psi_{j,k}(t) = 2^{j/2}\Psi\left(2^j t - k\right) \quad j,k \in Z \tag{1}$$

where $\psi_{j,k}$ corresponds to the *wavelet function* at wavelet level *j* and temporal translation *k*. An increase in the wavelet *level* from *j* to *j*+1 results in a more dilated wavelet function, $\psi_{j+1,k}$, with a center frequency and bandwidth that is roughly half that of $\psi_{j,k}$. Symmlet 7 was chosen as the mother wavelet for the DWT MSNA de-noising algorithm due to its morphological similarity to a MSNA action potential (Fig. 13).

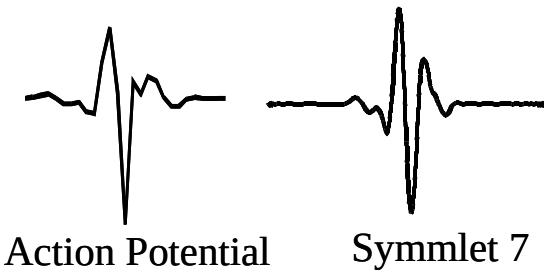

Figure 13. Morphological similarity between a MSNA action potential and the Symlet 7 wavelet.

The fast DWT algorithm proposed by Mallat (1989) decomposes a signal, *f*, using a set of quadrature mirror *decomposition filters*, g_0 and h_0, that have respective band-pass and low-pass properties specific to each mother wavelet [59]. Equations (2) and (3) describe the DWT decomposition process. The broad scale, or *approximation*, coefficients a_j^{DWT} are convolved separately with g_0 and h_0 and the result is down-sampled by two. This process splits the a_j^{DWT} frequency information roughly in half, partitioning it into a set of fine scale, or *detail* coefficients d_{j+1}^{DWT} and a coarser set of approximation coefficients a_{j+1}^{DWT}. This procedure can be iteratively continued until the desired level of decomposition, *j*=*J*, is obtained. Note that the algorithm is initiated by setting $a_0^{DWT} = f$.

$$a_{j+1}^{DWT}(k) = \sum_n h_0(n-2k)a_j^{DWT}(k) \tag{2}$$

$$d_{j+1}^{DWT}(k) = \sum_n g_0(n-2k)a_j^{DWT}(k) \tag{3}$$

The a_j^{DWT} coefficients can be reconstructed from a_{j+1}^{DWT} and d_{j+1}^{DWT} by placing a zero between each consecutive value found in a_{j+1}^{DWT} and d_{j+1}^{DWT} (e.g. up-sampling by two), convolving

the results with the respective reconstruction filter, $h_0(-n)$ or $g_0(-n)$, and summing. This process can be iteratively continued until the original signal, *f*, is recovered.

$$a_j^{DWT}(k) = \sum_n h_0(k-2n) a_{j+1}^{DWT}(n) + \sum_n g_0(k-2n) d_{j+1}^{DWT}(n) \quad \textbf{(4)}$$

Down-sampling the DWT coefficients between each level acts to halve their effective sample frequency and halve the effective corner frequencies of the h_0 and g_0 filters for the next level of processing. Therefore, identical filters can be used for each step of the DWT procedure. The DWT has two main advantages: 1) Each step of the DWT requires half as many computations as the previous step, and 2) The total number of DWT coefficients never exceeds *N*, the length of the original signal. A number of AP detection and classification algorithms currently use this decomposition technique [50;57;60;61].

Most wavelet based spike detection algorithms include some modified form of a process known as *wavelet de-noising* [62]. In this process, a nerve signal with additive noise, *f*, is decomposed using the DWT and a threshold is applied to each of the detail coefficient levels. All coefficients with an absolute value greater than the threshold are thought to be part of an action potential and those below the threshold are presumably derived from noise. The noise coefficients can be set to zero and a noise-free signal can then be reconstructed and used for AP detection [50].

In the DWT MSNA de-noising algorithm, the probability distribution of the wavelet detail coefficients provided the motivation for a modified version of a standard mathematically derived threshold (see APPENDIX A for details). After filtering of the MSNA, the remaining noise is assumed to be correlated, but normally distributed and additive. Action potential peaks are assumed to have large amplitudes, causing the tails of the MSNA distribution to become heavier as more action potentials are added. These properties are carried over to the detail coefficients once the DWT decomposition is performed. Evidence for this affect can be seen in the Quantile-Quantile plot (QQ-plot) of the level 3 detail coefficients (Fig. 14) for the baseline and trimethaphan data shown previously. A QQ-plot is constructed in such a way that plotting the quantiles of a data set against those of a test distribution, in this case the standard normal distribution, should result in a straight line if the two distributions are the same, irrespective of their parameters [63]. If a straight line is present, the slope of the line is the standard deviation of the data and the y-intercept is its mean. In Figure 14B, the central portion of the QQ-plot is linear

and conforms to the normal distribution, while curvature is introduced in the non-normal tails. The noise characteristics of the recordings made during baseline and trimethaphan infusion, a common ganglionic blocker, are assumed to be the same, since both were recorded during the same experiment. The slope of the QQ-plot line between the first and third quartiles of the detail coefficients at level j was used to estimate of the standard deviation of the noise-related detail coefficients, σ_j.

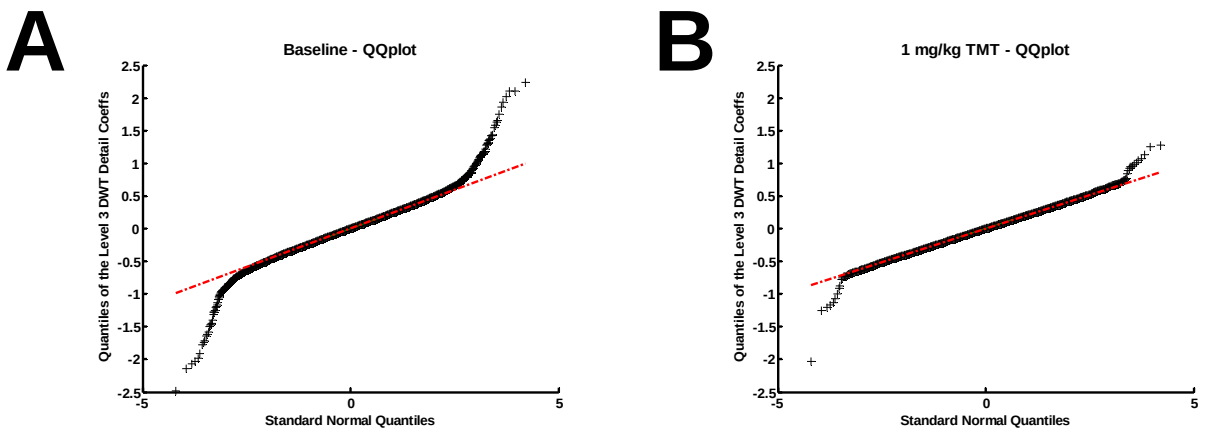

Figure 14. QQ-plots of the level 3 DWT detail coefficients during baseline (A) and 1mg/kg TMT (B). Broken red lines indicate the QQ-plot of the model distribution.

The modified thresholding rule, T_j^M, is stated in Eq. (5. In Eq. (5, k is a correction factor that was found to be 0.8 through simulation, and N is the number of points in the signal [50]. This threshold was modified from a standard colored-noise threshold, T_j^S, found in Appendix A, which does not include k and estimates σ_j as the median absolute deviation of the detail coefficients from zero divided by 0.6745, the 75th percentile of the standard normal distribution.

$$T_j^M = k\sigma_j\sqrt{2\log_e(N)} \quad \textbf{(5)}$$

The optimal sampling rate, 10,000 Hz, and number of wavelet decomposition levels used to de-noise the MSNA signal, 5, were also determined from analysis of simulated signals [50]. This optimized MSNA DWT de-noising method was shown to perform better than common amplitude discrimination procedures in the detection of action potentials in simulated signals [50]. Several other neural de-noising schemes involving the DWT have been shown to exhibit similar performance advantages over other, non-wavelet methods of spike detection [56;57].

Spectral Analysis of Heart Rate and Blood Pressure

In order to analyze the quasi-periodic fluctuations in heart rate and blood pressure, a beat-to-beat variability series is formed using the R-R intervals (RRI), systolic, or diastolic values (Figure 15) [64;65]. The R-wave peaks in the electrocardiogram (ECG) are an established and easily detectable landmark from which the position of a subsequent diastolic and systolic blood-pressure event can be identified. The beat-to-beat series is then resampled at regular intervals and spectral analysis can be performed on the resultant tachogram (series of RRI), systogram (series of SBP), or diastogram (series of DBP) using fast Fourier transform (FFT) [66-68], or autoregressive (AR) [51;64;69-72] based methods.

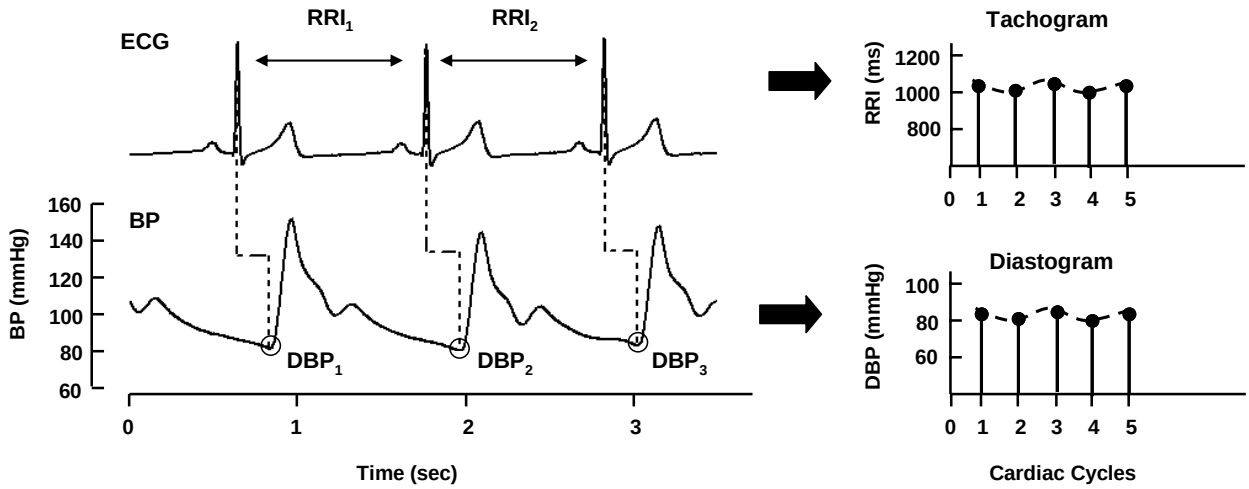

Figure 15. Formation of the tachogram and diastogram from the ECG and continuous blood pressure records. Each diastolic event can be detected with knowledge of the R-wave peak of the ECG signal. The R-R intervals (RRI) and diastolic values are inserted consecutively into variability sequences which can then be evenly resampled using linear interpolation.

Once the power spectral density (PSD) of the variability series is computed, it has become standard practice to analyze the power in established frequency ranges of the spectrum (Figure 16) [23;27;51;64;66-72]. Three specific regions of the frequency domain are typically considered important: the very low frequency (VLF; 0.004-0.04 Hz), the low frequency (LF; 0.04 – 0.15 Hz), and the high frequency (HF; 0.15 – 0.40 Hz) [27]. The power in each of these regions is thought to represent changes in heart rate or blood pressure values brought about by different physiological systems. For instance, the relative control of systems that typically require long periods of time to exert an affect on the blood pressure, such as the hormonal action

of various glands in the endocrine system, is typically quantified using the VLF power [23]. Similarly, as demonstrated in Figure 5, the influence of the sympathetic nervous system on the vasomotor tone of the arterial blood pressure, reflected in a 10-second wave, known as a Mayer wave, whose power is found in the LF range [64;70]. In fact, spectral analysis of long time segments (>5 minutes) has demonstrated that the LF components of blood pressure undergo changes correlated to the sympathetic nerve activity during pharmacological interventions, such as nitroprusside and phenylephrine infusion [72], and physiological autonomic stresses, such as head-up tilting [70]. The LF component of the RRI series has been proposed as an index of sympathetic modulation on the heart rate; however, it may also be affected by the parasympathetic system. The HF range is thought to represent vagal modulation of the sinoatrial node and parasympathetic control of the arterial blood pressure. The most common peak in this range is typically found at the normal breathing rate (0.25 – 0.30 Hz) and is brought about by parasympathetic respiratory input [73].

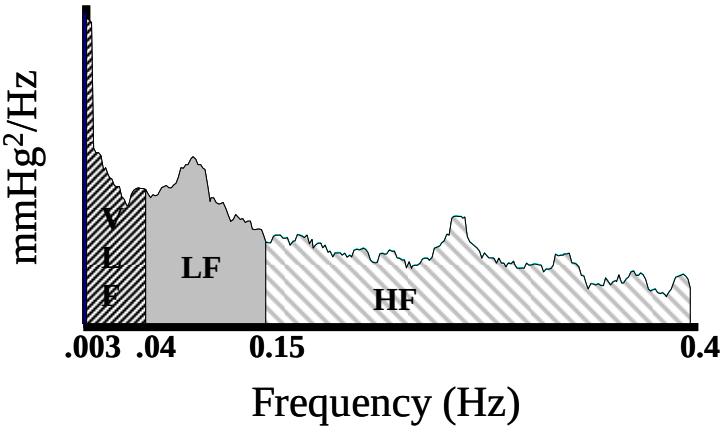

Figure 16. PSD and defined frequency regions of the blood pressure variability. The regions defined by the Task Force of the European Society of Cardiology and the North American Society of Pacing and Electrophysiology are very low frequency (VLF; 0.003 – 0.04 Hz), low frequency (LF; 0.04 – 0.15 Hz), and high frequency (HF; 0.15 – 0.40 Hz) (Camm et al., 1996). The power in each region is thought to represent the influence of different factors on blood pressure variability.

Limitations of the Discrete Wavelet Transform in Neural Signal Processing

The DWT MSNA de-noising algorithm uses the discrete wavelet transform to decompose sympathetic nerve signals prior to de-noising and AP detection. One complication that arises from the level-to-level decimation of the DWT coefficients, however, is a lack of *translation invariance* in the DWT representation of the signal [74-79]. Dyadically down-sampling the approximation and detail coefficients from *f*(*n*) leads to a completely different set of DWT coefficients than down-sampling the coefficients from its shifted version, *f*(*n+1*). Similarly, choosing to retain the odd wavelet coefficients during the dyadic down-sampling will result in a different outcome than retaining the even wavelet coefficients (Figure 17) [74-79].

As a result of the shift variability of the DWT, several authors have used translation invariant decomposition techniques, such as the continuous wavelet transform or stationary wavelet transform (SWT), for the purpose of detecting action potentials [56;58] (Appendix A). In contrast to the DWT, the SWT up-samples the decomposition filters by inserting zeros between every other filter coefficient and, consequently, avoids the translational variance problem caused by decimation [80]. Therefore, the SWT uses a set of *level dependent decomposition filters*, h_j and g_j, which are the h_0 and g_0 filters with 2^j-1 zeros between each discrete filter coefficient. The SWT approximation and detail coefficients can then be computed using Eq. 7 and 8.

$$a_{j+1}^{SWT}(k) = \sum_n h_j(n-k) a_j^{SWT}(k) \quad \textbf{(6)}$$

$$d_{j+1}^{SWT}(k) = \sum_n g_j(n-k) a_j^{SWT}(k) \quad \textbf{(7)}$$

The SWT reconstruction process is similar to that of the DWT, although the reconstruction filters are level dependent an include 2^j-1 zeros between each filter coefficients. This reconstruction process is described in Eq. 9.

$$a_{j+1}^{SWT}(k) = \sum_n h_j(k-n) a_j^{SWT}(n) + \sum_n g_j(k-n) d_j^{SWT}(n) \quad \textbf{(8)}$$

Inserting zeros between the filter coefficients allows the SWT to analyze every possible shift of the signal while the effective sample rate at each wavelet level remains unchanged. In the frequency domain, up-sampling acts to halve the corner frequency of both the low-pass and high-

pass decomposition filters, resulting in the same bandwidth decomposition as is found in the DWT. The result is a redundant, or over-complete, set of detail and approximation coefficients [75]. The drawbacks of the SWT algorithm include its increased computational complexity and the increased number of wavelet coefficients it generates. The differences between the DWT and SWT are depicted in Figure 17 for one level of processing. A more detailed description of SWT decomposition can be found in Appendix A.

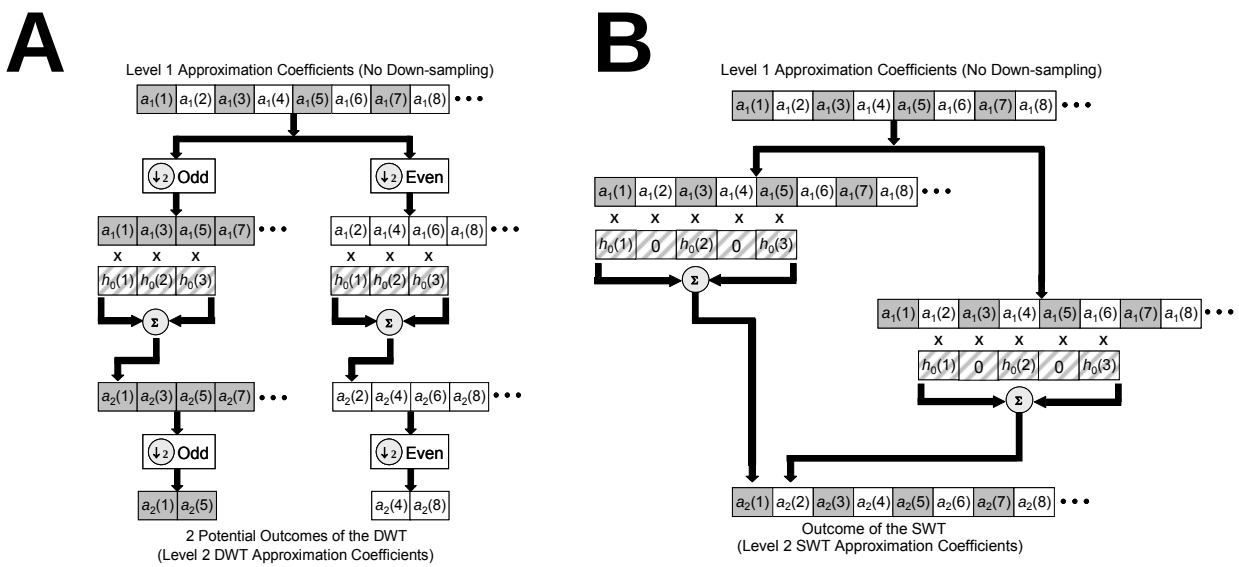

Figure 17. Relationship between the DWT (A) and the SWT (B) in the wavelet domain. The DWT keeps either the odd (grey) or even (white) approximation coefficients at level 1, whereas the SWT retains all of the coefficients. At level 2, the problem is amplified, as the DWT only computes every 4th approximation coefficient, while the SWT computes all possible approximation coefficients by up-sampling the decomposition filters.

The differences between DWT- and SWT-based spike detection in sympathetic nerve recordings will be explored in Chapters III and IV of this thesis.

Differences in Human and Murine Sympathetic Nerve Activity

The murine RSNA has slightly different signal and noise characteristics than the human MSNA. First, the physiologically important frequency of the RSNA appears to be different from that of the human MSNA signal (Fig. 18). The power spectral density (PSD) of human MSNA during a graded head-up tilt protocol is shown in Figure 18A and the PSD of the renal nerve activity in mice during periods of baseline (BSL), nitroprusside (NTP) bolus injection, phenylephrine (PHE) bolus injection, and postmortem is depicted below in Figure 18B. The

human range of 700 to approximately 2500 Hz is activated in a graded fashion as the tilt angle is increased and sympathetic activity is further activated. In the mouse RSNA, however, power in the range of 100 Hz to 1000 Hz was dominant during all interventions in the living animal but was significantly abolished postmortem. NTP is a pharmacological agent that causes blood pressure decrease and a baroreflex mediated increase in sympathetic activity. Consequently, an increase of power in the 100 Hz to 1000 Hz frequency range is observed during NTP bolus injection. PHE has the opposite affect on blood pressure and sympathetic activity, and resulted in a reduction of this power.

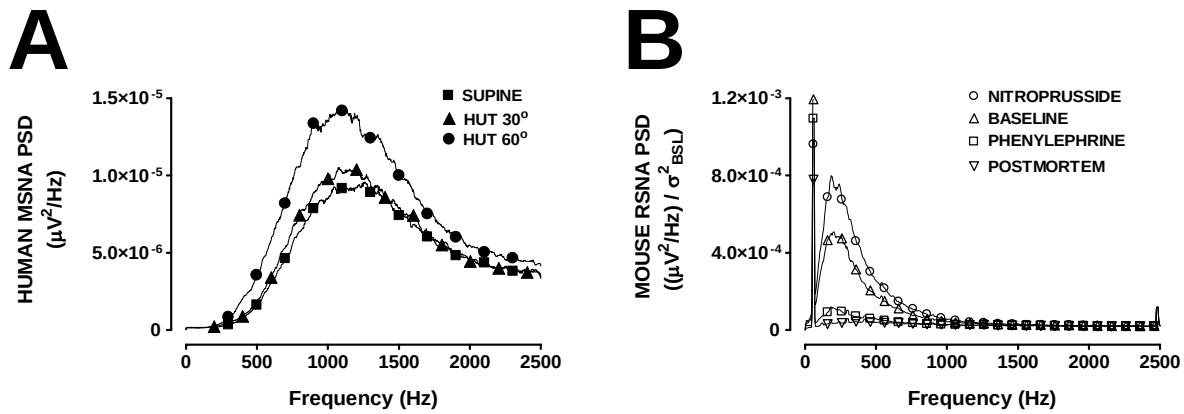

Figure 18. (A) Power spectral density (PSD) of human muscle sympathetic nerve activity (MSNA) during a graded head-up tilt (HUT) protocol. As the tilt angle increases from supine (HUT 0^o) to HUT 30^o and HUT 60^o, sympathetic activity is further activated, and power in the range of 700-2500 Hz increases. **(B)** Average normalized PSD of murine renal sympathetic nerve activity (RSNA) recordings during nitroprusside (Δ), baseline (□), phenylephrine (O), and postmortem (∇) periods. The power in the range of 100-1000 Hz is increased by vasodilator nitroprusside and reduced during vasopressor phenylephrine infusion and postmortem. The PSD calculated for each period of the mouse RSNA was normalized to the respective baseline variance to demonstrate relative changes for 9 mice.

The difference in the frequency characteristics of the human and mouse sympathetic nerve signals is also reflected in the shape of a typical action potential from each species (Figure 19). The murine AP has a much longer period than the human AP, which may be a result of different conduction velocities in the murine and human sympathetic neurons.

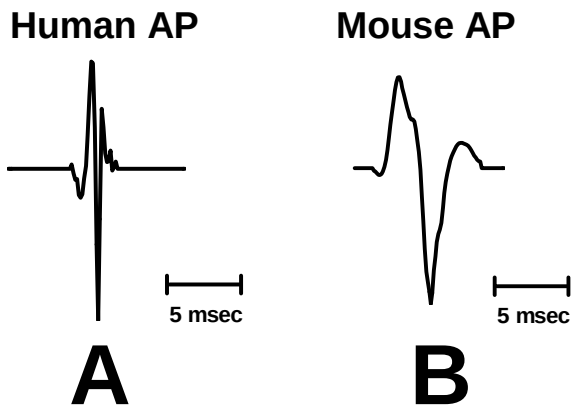

Figure 19. Typical action potentials recorded from human muscle sympathetic nerve fibers **(A)** and murine renal sympathetic nerve fibers **(B)**.

Lastly, the general appearance and overall temporal characteristics of the sympathetic signals from each species differs substantially. As described previously, the human muscle sympathetic discharge is organized into burst synchronized to the heart beat and respiration [81] (Fig. 20A). The mouse RSNA, on the other hand, consists of individual spikes which appear to lack group synchrony (Fig. 20B).

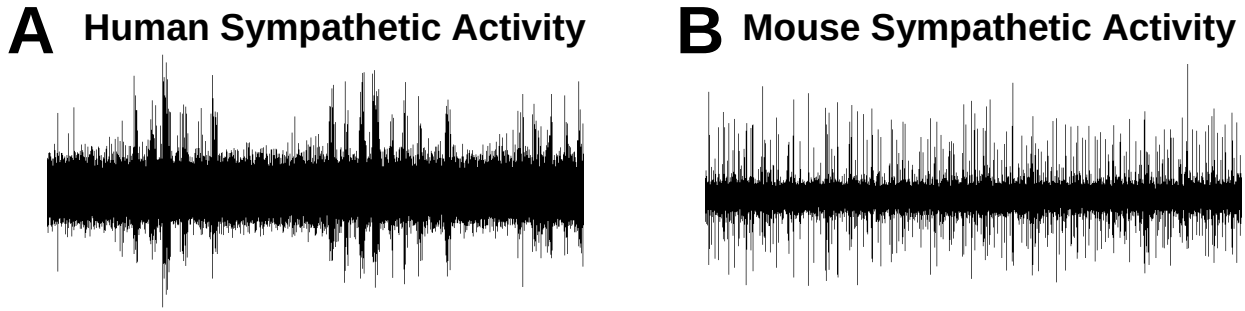

Figure 20. Comparison of the discharge properties of human and mouse basal sympathetic nerve activity. **(A)** Human muscle sympathetic nerve activity (MSNA) is composed of synchronized discharges from a group of sympathetic neurons. **(B)** Murine renal sympathetic nerve activity is composed of non-synchronous discharge from a group of sympathetic neurons.

Although simple hardware discriminators with manual noise level estimates have been applied to the murine RSNA signal, no automated spike detection schemes have been described. Due to the increasing popularity of transgenic and gene targeted mouse models in the study of autonomic and cardiovascular diseases, there is a growing need for such an unsupervised spike detection algorithm. However, due to the differences in the frequency content, action potential

shape, and temporal discharge characteristics the murine RSNA will require parameters and, conceivably, an entire detection strategy that is distinct from that of the human MSNA. In Chapter IV, an automated detection algorithm is parameterized specifically for the murine RSNA and this system is later utilized to examine differences in sympathetic activity between normal and transgenic mouse populations.

Limitations in Fourier Based Spectral Analysis of Heart Rate and Blood Pressure

The traditional methods of obtaining time-varying spectral information, such as the short-time Fourier Transform (STFT) and moving autoregressive (AR) models, typically divide the signal into an arbitrary number of consecutive or overlapping segments of equal length and compute spectral estimates over the entire frequency bandwidth for each of these segments. The frequency resolution of the time-varying spectra is governed by the length of each of the segments. Longer segments yield higher frequency resolution and more accurate information about broader trends in the signal. However, longer segments also lead to reduced time resolution and inaccurate spectro-temporal information about abrupt changes in the signal. Therefore, this type of time-frequency analysis may be inappropriate during dynamic physiological interventions that cause signals to become non-stationary (Figure 21) [82-85].

Wavelet analysis offers a more flexible solution to the problem of time-frequency analysis by using scalable, finite duration basis functions. Rather than analyzing the entire bandwidth of a signal using a fixed time window, the continuous wavelet transform (CWT) uses broad, dilated wavelets to analyze long-term trends and short, compact wavelets to detect high frequency oscillations. In this way, the CWT is able to use an adjustable time window to analyze different frequency bands (Figure 21).

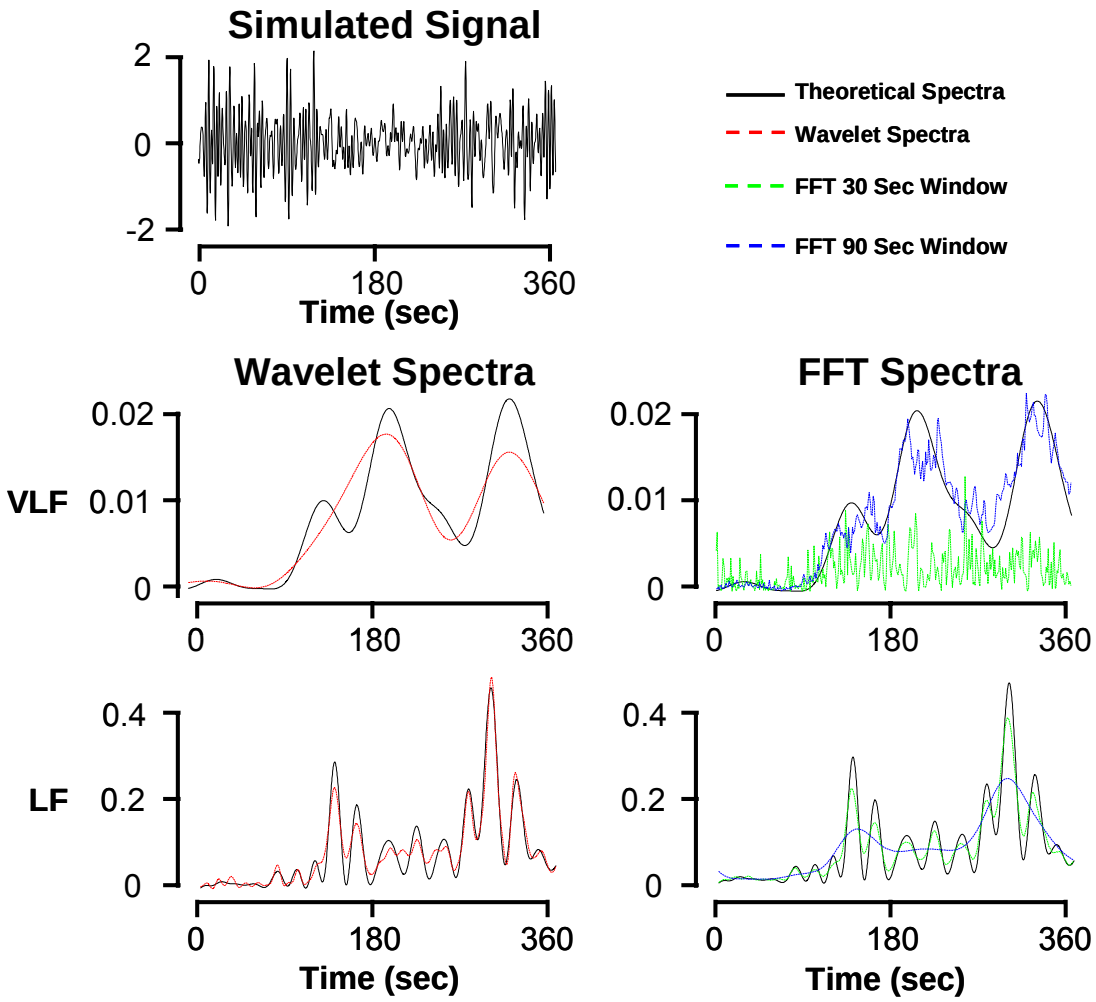

Figure 21. Performance of wavelet-based spectral analysis (left) and FFT-based spectral analysis (right) on a simulated signal (top). The FFT-based method with a 30 sec window length is not able to accurately estimate the very low frequency component (VLF) of the simulated signal but can accurately detect changes in the low frequency component (LF). The FFT-based method with the 90 sec window length accurately estimates VLF power, but smoothes out changes in the LF. The wavelet based method uses a broad wavelet to analyze VLF and a more compact wavelet to analyze the LF, and, consequently, is able to estimate the spectral power in both frequency ranges wit good accuracy.

Several authors have successfully demonstrated the utility of the continuous and discrete wavelet transform in time-varying spectral analysis of heart-rate variability during dynamic cardiovascular stimulation [82-85]. A modified form of these methods will be used to analyze non-stationary syncope data from healthy subjects during orthostatic stress. The differences between normal individuals with syncope alone and syncope with asystole, a rare stoppage of the heart for greater than 3 seconds, will be examined.

References

[1] R. M. Berne and M. N. Levy, *Physiology*. St. Louis, MO: Mosby, 1998.

[2] D. U. Silverthorn, W. C. Ober, C. W. Garrison, and A. C. Silverthorn, *Human Physiology: An Integrated Approach*. Upper Saddle River, NJ: Prentice Hall, 1998.

[3] D. L. Eckberg, "High-Pressure and Low-Pressure Baroreflexes," in *Primer on the Autonomic Nervous System*, 2 ed. D. Robertson, Ed. Oxford, UK: Elsevier, 2004, pp. 147-151.

[4] H. R. Kirchheim, "Systemic arterial baroreceptor reflexes," *Physiol Rev*, vol. 56, no. 1, pp. 100-177, Jan.1976.

[5] R. Furlan, G. Jacob, M. Snell, D. Robertson, A. Porta, P. Harris, and R. Mosqueda-Garcia, "Chronic orthostatic intolerance: a disorder with discordant cardiac and vascular sympathetic control," *Circulation*, vol. 98, no. 20, pp. 2154-2159, Nov.1998.

[6] "The definition of orthostatic hypotension, pure autonomic failure, and multiple system atrophy," *J Auton Nerv Syst*, vol. 58, no. 1-2, pp. 123-124, Apr.1996.

[7] G. Mancia, G. Grassi, G. Parati, and A. Daffonchio, "Evaluating sympathetic activity in human hypertension," *J Hypertens. Suppl*, vol. 11 Suppl 5, p. S13-S19, Dec.1993.

[8] B. G. Wallin, W. Delius, and K. E. Hagbarth, "Sympathetic activity in peripheral nerves of normo-and hypertensive subjects," *Clin. Sci. Mol. Med. Suppl*, vol. 45 Suppl 1, pp. 127s-30, Aug.1973.

[9] B. G. Wallin, W. Delius, and K. E. Hagbarth, "Comparison of sympathetic nerve activity in normotensive and hypertensive subjects," *Circ. Res.*, vol. 33, no. 1, pp. 9-21, July1973.

[10] B. G. Wallin and G. Sundlof, "A quantitative study of muscle nerve sympathetic activity in resting normotensive and hypertensive subjects," *Hypertension*, vol. 1, no. 2, pp. 67-77, Mar.1979.

[11] A. Malliani and M. Pagani, "The role of the sympathetic nervous system in congestive heart failure," *Eur. Heart J*, vol. 4 Suppl A, pp. 49-54, Jan.1983.

[12] G. Grassi and M. Esler, "How to assess sympathetic activity in humans," *J Hypertens.*, vol. 17, no. 6, pp. 719-734, June1999.

[13] K. E. Hagbarth and A. B. Vallbo, "Pulse and respiratory grouping of sympathetic impulses in human muscle- nerves," *Acta Physiol Scand.*, vol. 74, no. 1, pp. 96-108, Sept.1968.

[14] B. G. Wallin, "Sympathetic Microneurography," in *Primer on the Autonomic Nervous System*, 2 ed. D. Robertson, Ed. Oxford, UK: Elsevier, 2004, pp. 224-227.

[15] A. C. Ertl, A. Diedrich, I. Biaggioni, B. D. Levine, R. M. Robertson, J. F. Cox, J. H. Zuckerman, J. A. Pawelczyk, C. A. Ray, J. C. Buckey, Jr., L. D. Lane, R. Shiavi, F. A. Gaffney, F. Costa, C. Holt, C. G. Blomqvist, D. L. Eckberg, F. J. Baisch, and D. Robertson, "Human muscle sympathetic nerve activity and plasma noradrenaline kinetics in space," *J. Physiol*, vol. 538, no. Pt 1, pp. 321-329, Jan.2002.

[16] M. Elam and V. Macefield, "Multiple firing of single muscle vasoconstrictor neurons during cardiac dysrhythmias in human heart failure," *J Appl. Physiol*, vol. 91, no. 2, pp. 717-724, Aug.2001.

[17] V. G. Macefield and B. G. Wallin, "The discharge behaviour of single sympathetic neurones supplying human sweat glands," *J Auton. Nerv. Syst.*, vol. 61, no. 3, pp. 277-286, Dec.1996.

[18] V. G. Macefield and B. G. Wallin, "Firing properties of single vasoconstrictor neurones in human subjects with high levels of muscle sympathetic activity," *J Physiol (Lond)*, vol. 516 (Pt 1), pp. 293-301, Apr.1999.

[19] V. G. Macefield, B. Rundqvist, Y. B. Sverrisdottir, B. G. Wallin, and M. Elam, "Firing properties of single muscle vasoconstrictor neurons in the sympathoexcitation associated with congestive heart failure," *Circulation*, vol. 100, no. 16, pp. 1708-1713, Oct.1999.

[20] V. G. Macefield and B. G. Wallin, "Respiratory and cardiac modulation of single sympathetic vasoconstrictor and sudomotor neurones to human skin," *J Physiol (Lond)*, vol. 516 (Pt 1), pp. 303-314, Apr.1999.

[21] V. G. Macefield, M. Elam, and B. G. Wallin, "Firing properties of single postganglionic sympathetic neurones recorded in awake human subjects," *Auton. Neurosci.*, vol. 95, no. 1-2, pp. 146-159, Jan.2002.

[22] D. A. Mary and J. B. Stoker, "The activity of single vasoconstrictor nerve units in hypertension," *Acta Physiol Scand.*, vol. 177, no. 3, pp. 367-376, Mar.2003.

[23] S. Akselrod, D. Gordon, F. A. Ubel, D. C. Shannon, A. C. Berger, and R. J. Cohen, "Power spectrum analysis of heart rate fluctuation: a quantitative probe of beat-to-beat cardiovascular control," *Science*, vol. 213, no. 4504, pp. 220-222, July1981.

[24] S. Guzzetti, E. Piccaluga, R. Casati, S. Cerutti, F. Lombardi, M. Pagani, and A. Malliani, "Sympathetic predominance in essential hypertension: a study employing spectral analysis of heart rate variability," *J Hypertens.*, vol. 6, no. 9, pp. 711-717, Sept.1988.

[25] J. Penaz, "Photoelectric measurement of blood pressure, volume and flow in the finger," *Digest of the 10th international conference on medical and biological engineering - Dresden.*, p. 104, 1973.

[26] K. Wesseling, "A century of noninvasive arterial-pressure measurement - from Marey to Penaz and FINAPRES," *HOMEOSTASIS HLTH DIS HOMEOSTASIS HLTH DIS*, vol. 36, no. 2-3, pp. 50-65, 1995.

[27] Task Force, "Heart rate variability: standards of measurement, physiological interpretation and clinical use. Task Force of the European Society of Cardiology and the North American Society of Pacing and Electrophysiology," *Circulation*, vol. 93, no. 5, pp. 1043-1065, Mar.1996.

[28] R. Mosqueda-Garcia, "Evaluation of autonomic failure," in *The Autonomic Nervous System*. G. Burnstock, Ed. Luxembourg: Harwood Academic Press, 1995, pp. 25-59.

[29] D. L. Eckberg, "Parasympathetic cardiovascular control in human disease: a critical review of methods and results," *Am. J Physiol*, vol. 239, no. 5, p. H581-H593, Nov.1980.

[30] R. B. Hickler, R. G. Hoskins, and J. T. Hamlin, III, "The clinical evaluation of faulty orthostatic mechanisms," *Med Clin North Am*, vol. 44, pp. 1237-1250, Sept.1960.

[31] V. J. Parks, A. G. Sandison, S. L. Skinner, and R. F. Whelan, "Sympathomimetic drugs in orthostatic hypotension," *Lancet*, vol. 1, no. 7187, pp. 1133-1136, 1961.

[32] J. Tank, A. Diedrich, E. Szczech, F. C. Luft, and J. Jordan, "Baroreflex Regulation of Heart Rate and Sympathetic Vasomotor Tone in Women and Men," *Hypertension*, vol. 25, no. 6, pp. 1159-1164, May2005.

[33] C. Schroeder, J. Tank, M. Boschmann, A. Diedrich, A. M. Sharma, I. Biaggioni, F. C. Luft, and J. Jordan, "Selective norepinephrine reuptake inhibition as a human model of orthostatic intolerance," *Circulation*, vol. 105, no. 3, pp. 347-353, Jan.2002.

[34] J. Tank, C. Schroeder, A. Diedrich, E. Szczech, S. Haertter, A. M. Sharma, F. C. Luft, and J. Jordan, "Selective impairment in sympathetic vasomotor control with norepinephrine transporter inhibition," *Circulation*, vol. 107, no. 23, pp. 2949-2954, June2003.

[35] A. Diedrich, J. Jordan, J. Tank, J. R. Shannon, R. Robertson, F. C. Luft, D. Robertson, and I. Biaggioni, "The sympathetic nervous system in hypertension: assessment by blood pressure variability and ganglionic blockade," *J. Hypertens.*, vol. 21, no. 9, pp. 1677-1686, Sept.2003.

[36] E. Bath, L. E. Lindblad, and B. G. Wallin, "Effects of dynamic and static neck suction on muscle nerve sympathetic activity, heart rate and blood pressure in man," *J Physiol (Lond)*, vol. 311, pp. 551-564, Feb.1981.

[37] W. H. Cooke and V. A. Convertino, "Association between vasovagal hypotension and low sympathetic neural activity during presyncope," *Clin Auton Res*, vol. 12, no. 6, pp. 483-486, Dec.2002.

[38] M. Bader, "Mouse knockout models of hypertension," *Methods Mol. Med*, vol. 108, pp. 17-32, 2004.

[39] E. Popova, M. Bader, and A. Krivokharchenko, "Production of transgenic models in hypertension," *Methods Mol. Med*, vol. 108, pp. 33-50, 2004.

[40] N. R. Keller, A. Diedrich, M. Appalsamy, S. Tuntrakool, S. Lonce, C. Finney, M. G. Caron, and D. Robertson, "Norepinephrine transporter-deficient mice exhibit excessive tachycardia and elevated blood pressure with wakefulness and activity," *Circulation*, vol. 110, no. 10, pp. 1191-1196, Sept.2004.

[41] N. R. Keller, A. Diedrich, M. Appalsamy, L. C. Miller, M. G. Caron, M. P. McDonald, R. C. Shelton, R. D. Blakely, and D. Robertson, "Norepinephrine transporter-deficient mice respond to anxiety producing and fearful environments with bradycardia and hypotension," *Neuroscience*, Mar.2006.

[42] P. C. Usera, S. Vincent, and D. Robertson, "Human phenotypes and animal knockout models of genetic autonomic disorders," *J Biomed. Sci.*, vol. 11, no. 1, pp. 4-10, Jan.2004.

[43] M. D. Esler, G. Wallin, P. K. Dorward, G. Eisenhofer, R. Westerman, I. Meredith, G. Lambert, H. S. Cox, and G. Jennings, "Effects of desipramine on sympathetic nerve firing and norepinephrine spillover to plasma in humans," *Am J Physiol*, vol. 260, no. 4 Pt 2, p. R817-R823, Apr.1991.

[44] G. Y. Ling, W. H. Cao, M. Onodera, K. H. Ju, H. Kurihara, Y. Kurihara, Y. Yazaki, M. Kumada, Y. Fukuda, and T. Kuwaki, "Renal sympathetic nerve activity in mice: comparison between mice and rats and between normal and endothelin-1 deficient mice," *Brain Res*, vol. 808, no. 2, pp. 238-249, Oct.1998.

[45] X. Ma, F. M. Abboud, and M. W. Chapleau, "A novel effect of angiotensin on renal sympathetic nerve activity in mice," *J Hypertens.*, vol. 19, no. 3 Pt 2, pp. 609-618, Mar.2001.

[46] X. Ma, M. W. Chapleau, C. A. Whiteis, F. M. Abboud, and K. Bielefeldt, "Angiotensin selectively activates a subpopulation of postganglionic sympathetic neurons in mice," *Circ. Res*, vol. 88, no. 8, pp. 787-793, Apr.2001.

[47] W. Zhang, J. L. Li, M. Hosaka, R. Janz, J. M. Shelton, G. M. Albright, J. A. Richardson, T. C. Sudhof, and R. G. Victor, "Cyclosporine A-induced hypertension involves synapsin in renal sensory nerve endings," *Proc. Natl. Acad. Sci. U. S. A*, vol. 97, no. 17, pp. 9765-9770, Aug.2000.

[48] J. Fagius, B. G. Wallin, G. Sundlof, C. Nerhed, and S. Englesson, "Sympathetic outflow in man after anaesthesia of the glossopharyngeal and vagus nerves," *Brain*, vol. 108 (Pt 2), pp. 423-438, June1985.

[49] Y. Sugiyama, T. Matsukawa, H. Suzuki, S. Iwase, A. S. Shamsuzzaman, and T. Mano, "A new method of quantifying human muscle sympathetic nerve activity for frequency domain analysis," *Electroencephalogr. Clin Neurophysiol.*, vol. 101, no. 2, pp. 121-128, Apr.1996.

[50] A. Diedrich, W. Charoensuk, R. J. Brychta, A. C. Ertl, and R. Shiavi, "Analysis of raw microneurographic recordings based on wavelet de-noising technique and classification algorithm: wavelet analysis in microneurography," *IEEE Trans. Biomed. Eng*, vol. 50, no. 1, pp. 41-50, Jan.2003.

[51] A. Nakata, S. Takata, T. Yuasa, A. Shimakura, M. Maruyama, H. Nagai, S. Sakagami, and K. Kobayashi, "Spectral analysis of heart rate, arterial pressure, and muscle sympathetic nerve activity in normal humans," *Am. J. Physiol*, vol. 274, no. 4 Pt 2, p. H1211-H1217, Apr.1998.

[52] M. J. Bak and E. M. Schmidt, "An improved time-amplitude window discriminator," *IEEE Trans. Biomed. Eng*, vol. 24, no. 5, pp. 486-489, Sept.1977.

[53] W. G. Haynes, D. A. Morgan, S. A. Walsh, A. L. Mark, and W. I. Sivitz, "Receptor-mediated regional sympathetic nerve activation by leptin," *J Clin Invest*, vol. 100, no. 2, pp. 270-278, July1997.

[54] E. N. Brown, R. E. Kass, and P. P. Mitra, "Multiple neural spike train data analysis: state-of-the-art and future challenges," *Nat Neurosci*, vol. 7, no. 5, pp. 456-461, 2004.

[55] M. S. Lewicki, "A review of methods for spike sorting: the detection and classification of neural action potentials," *Network.*, vol. 9, no. 4, p. R53-R78, Nov.1998.

[56] K. H. Kim and S. J. Kim, "A wavelet-based method for action potential detection from extracellular neural signal recording with low signal-to-noise ratio," *IEEE Trans. Biomed. Eng*, vol. 50, no. 8, pp. 999-1011, Aug.2003.

[57] H. Nakatani, T. Watanabe, and N. Hoshimiya, "Detection of nerve action potentials under low signal-to-noise ratio condition," *IEEE Trans. Biomed. Eng*, vol. 48, no. 8, pp. 845-849, Aug.2001.

[58] Z. Nenadic and J. W. Burdick, "Spike detection using the continuous wavelet transform," *IEEE Trans. Biomed. Eng*, vol. 52, no. 1, pp. 74-87, Jan.2005.

[59] S. G. Mallat, "A Theory for Multiresolution Signal Decomposition - the Wavelet Representation," *Ieee T Pattern Anal*, vol. 11, no. 7, pp. 674-693, 1989.

[60] J. C. Letelier and P. P. Weber, "Spike sorting based on discrete wavelet transform coefficients," *J Neurosci Methods*, vol. 101, no. 2, pp. 93-106, Sept.2000.

[61] K. G. Oweiss and D. J. Anderson, "Spike sorting: a novel shift and amplitude invariant technique," *NEUROCOMPUTING NEUROCOMPUTING*, vol. 44-46, pp. 1133-1139, June2002.

[62] D. L. Donoho, "De-Noising by Soft-Thresholding," *Ieee T Inform Theory*, vol. 41, no. 3, pp. 613-624, 1995.

[63] R. A. Johnson, *Applied Multivariate Statistical Analysis*, 3 ed Prentice-Hall, Inc., 1992.

[64] G. Baselli, S. Cerutti, S. Civardi, D. Liberati, F. Lombardi, A. Malliani, and M. Pagani, "Spectral and cross-spectral analysis of heart rate and arterial blood pressure variability signals," *Comput. Biomed. Res.*, vol. 19, no. 6, pp. 520-534, Dec.1986.

[65] R. W. de Boer, J. M. Karemaker, and J. Strackee, "Relationships between short-term blood-pressure fluctuations and heart-rate variability in resting subjects. I: A spectral analysis approach," *Med. Biol. Eng Comput.*, vol. 23, no. 4, pp. 359-364, July1985.

[66] D. L. Eckberg, C. Nerhed, and B. G. Wallin, "Respiratory modulation of muscle sympathetic and vagal cardiac outflow in man," *J. Physiol*, vol. 365, pp. 181-196, Aug.1985.

[67] B. A. Kingwell, J. M. Thompson, D. M. Kaye, G. A. McPherson, G. L. Jennings, and M. D. Esler, "Heart rate spectral analysis, cardiac norepinephrine spillover, and muscle sympathetic nerve activity during human sympathetic nervous activation and failure," *Circulation*, vol. 90, no. 1, pp. 234-240, July1994.

[68] J. P. Saul, R. F. Rea, D. L. Eckberg, R. D. Berger, and R. J. Cohen, "Heart rate and muscle sympathetic nerve variability during reflex changes of autonomic activity," *Am. J Physiol*, vol. 258, no. 3 Pt 2, p. H713-H721, Mar.1990.

[69] G. Baselli, D. Bolis, S. Cerutti, and C. Freschi, "Autoregressive modeling and power spectral estimate of R-R interval time series in arrhythmic patients," *Comput. Biomed. Res.*, vol. 18, no. 6, pp. 510-530, Dec.1985.

[70] R. Furlan, A. Porta, F. Costa, J. Tank, L. Baker, R. Schiavi, D. Robertson, A. Malliani, and R. Mosqueda-Garcia, "Oscillatory patterns in sympathetic neural discharge and cardiovascular variables during orthostatic stimulus," *Circulation*, vol. 101, no. 8, pp. 886-892, Feb.2000.

[71] M. Pagani and A. Malliani, "Interpreting oscillations of muscle sympathetic nerve activity and heart rate variability," *J Hypertens.*, vol. 18, no. 12, pp. 1709-1719, Dec.2000.

[72] M. Pagani, N. Montano, A. Porta, A. Malliani, F. M. Abboud, C. Birkett, and V. K. Somers, "Relationship between spectral components of cardiovascular variabilities and direct measures of muscle sympathetic nerve activity in humans," *Circulation*, vol. 95, no. 6, pp. 1441-1448, Mar.1997.

[73] R. Furlan and A. Malliani, "Assessment of the Autonomic Control of the Cardiovascular System by Frequency Domain Approach," in *Primer on the Autonomic Nervous System*, 2 ed. D. Robertson, Ed. Oxford, UK: Elsevier, 2004, pp. 228-230.

[74] R. R. Coifman and D. L. Donoho, "Translation-Invariant De-Noising," *Lecture Notes on Statistics*, vol. 103, pp. 125-150, 1995.

[75] M. Lang, H. Guo, J. Odegard, C. Burrus, and R. Wells, "Noise reduction using an undecimated discrete wavelet transform," *IEEE SIGNAL PROC LET*, vol. 3, no. 1, pp. 10-12, 1996.

[76] J. Liang and T. W. Parks, "A translation-invariant wavelet representation algorithm with applications," *Ieee T Signal Proces*, vol. 44, no. 2, pp. 225-232, 1996.

[77] J. Pesquet, H. Krim, and H. Carfantan, "Time-invariant orthonormal wavelet representations," *Ieee T Signal Proces*, vol. 44, no. 8, pp. 1964-1970, 1996.

[78] B. Silverman, "Wavelets in statistics: beyond the standard assumptions," *PHILOS T ROY SOC A*, vol. 357, no. 1760\, pp. 2459-2473, 1999.

[79] E. P. Simoncelli, W. T. Freeman, E. H. Adelson, and D. J. Heeger, "Shiftable Multiscale Transforms," *Ieee T Inform Theory*, vol. 38, no. 2, pp. 587-607, 1992.

[80] S. Mallat, "Zero-Crossings of a Wavelet Transform," *Ieee T Inform Theory*, vol. 37, no. 4, pp. 1019-1033, 1991.

[81] B. G. Wallin and J. Fagius, "Peripheral sympathetic neural activity in conscious humans," *Annu. Rev. Physiol*, vol. 50, pp. 565-576, 1988.

[82] V. Pichot, S. Buffiere, J. M. Gaspoz, F. Costes, S. Molliex, D. Duverney, F. Roche, and J. C. Barthelemy, "Wavelet transform of heart rate variability to assess autonomic nervous system activity does not predict arousal from general anesthesia," *Can. J. Anaesth.*, vol. 48, no. 9, pp. 859-863, Oct.2001.

[83] V. Pichot, J. M. Gaspoz, S. Molliex, A. Antoniadis, T. Busso, F. Roche, F. Costes, L. Quintin, J. R. Lacour, and J. C. Barthelemy, "Wavelet transform to quantify heart rate variability and to assess its instantaneous changes," *J. Appl. Physiol*, vol. 86, no. 3, pp. 1081-1091, Mar.1999.

[84] K. Tanaka and A. R. Hargens, "Wavelet packet transform for R-R interval variability," *Med. Eng Phys.*, vol. 26, no. 4, pp. 313-319, May2004.

[85] E. Toledo, O. Gurevitz, H. Hod, M. Eldar, and S. Akselrod, "Wavelet analysis of instantaneous heart rate: a study of autonomic control during thrombolysis," *Am. J. Physiol Regul. Integr. Comp Physiol*, vol. 284, no. 4, p. R1079-R1091, Apr.2003.

CHAPTER III

SPIKE DETECTION IN HUMAN MUSCLE SYMPATHETIC NERVE ACTIVITY USING THE KURTOSIS OF STATIONARY WAVELET TRANSFORM COEFFICIENTS

Abstract

The accurate assessment of autonomic sympathetic function is important in the diagnosis and study of various autonomic and cardiovascular disorders. Sympathetic function in humans can be assessed by recording the muscle sympathetic nerve activity, which is characterized by synchronous neuronal discharges separated by periods of neural silence dominated by colored Gaussian noise. The raw nerve activity is generally rectified, integrated, and quantified using the integrated burst rate or area. We propose an alternative quantification involving spike detection using a two-stage stationary wavelet transform (SWT) de-noising method. The SWT coefficients are first separated into noise-related and burst-related coefficients on the basis of their local kurtosis. The noise-related coefficients are then used to establish a threshold to identify spikes within the bursts. This method demonstrated better detection performance than an unsupervised amplitude discriminator and similar wavelet-based methods when confronted with simulated data of varying burst rate and signal to noise ratio. Additional validation on data acquired during a graded head-up tilt protocol revealed a strong correlation between the mean spike rate and the mean integrate burst rate (r=0.85) and burst area rate (r=0.91). In conclusion, the kurtosis-based wavelet de-noising technique is a potentially useful method of studying sympathetic nerve activity in humans.

Introduction

The autonomic nervous system helps to regulate a number of important systems throughout the body. One of its primary roles is to maintain cardiovascular function which includes regulation of blood pressure, heart rate, and contractility. Accurate assessment of autonomic function is important in the study and diagnosis of disorders such as essential hypertension [1-3], orthostatic intolerance [4], and congestive heart failure [5]. Autonomic sympathetic function can be assessed in humans by direct recordings of the muscle sympathetic nerve activity (MSNA) [6].

The general appearance of the human MSNA has been described as heartbeat-synchronous discharges from a group of sympathetic neurons, separated by periods of neural silence [7], (Fig. 1). These bursts of activity are coupled to changes in the blood pressure and cardiac output through the baroreceptor reflex [8-10]. The most widely used MSNA processing method involves using an R-C circuit to rectifying and integrate the neurogram to achieve its envelope [3;11], a signal known as the integrated-MSNA [12]. At that point, bursts are identified and sympathetic activity can be quantified in terms of burst frequency (bursts/min), burst incidence (bursts/100 heart beats) or burst area rate (arbitrary units^2/min) [13;14].

Quantification of the MSNA using multiunit bursts has its limitations. For instance, none of the burst parameters is capable of conveying whether a large burst is generated by a few large amplitude sympathetic spikes (or artifacts) or many small amplitude spikes firing in rapid succession. Also, the amount of pass band noise integrated into each burst is dependent on the signal-to-noise ratio (SNR) of each recording, making it difficult to compare the arbitrary unit burst amplitudes and areas across subjects.

An alternative solution to the MSNA quantification problem is to implement a spike detection algorithm. In the past, this has proved difficult due to the traditionally low SNR found in most recordings, a consequence of the monopolar recording arrangement and high levels of contamination from environmental and bioelectric noise. The properties of this noise can be identified during Phase IV of the Valsalva Maneuver (VM) when mean blood pressure "overshoots" basal levels and MSNA is suppressed via baroreceptor feedback (Fig. 1C) [15]. The amplitude distribution of the noise is nearly Gaussian and its frequency content is colored as a result of hardware-based filtering.

Automated wavelet-based methods have been successful in detecting neural and classifying spikes in colored, Gaussian noise [16-19]. In particular, a wavelet-based spike detection method has been shown to outperform common, automated amplitude discriminators in the detection of human sympathetic spikes under varying signal to noise ratios [12]. However, the parameters of this algorithm were optimized from recordings during a supine resting state, and its detection performance was not examined at higher or lower burst rates [12]. A sympathetic spike detector whose performance is robust to changes in burst rate is important in the study of various autonomic syndromes [4;20-22] as well as in the analysis of various physiological and pharmacological interventions used to augment or suppress sympathetic

activity during clinical investigations [10;23]. Consequently, the properties of this technique should be studied during varying burst rates.

The wavelet transform is capable of decomposing a signal into a set of wavelet coefficients which preserve its temporal structure, but distributes its energy amongst several frequency sub-bands. Following this decomposition, a threshold is generally applied to the wavelet coefficients to eliminate all small, noise-related coefficients and retain larger spike-related coefficients [24]. Most standard wavelet threshold algorithms consider *all* of the coefficients while estimating the noise-threshold, i.e. those associated with both the signal and the noise [25]. However, it may be more beneficial to initially separate the wavelet coefficients purely derived from the noise from those which contain signal-plus-noise prior to thresholding [18]. In the MSNA signal, this requires identification of the wavelet coefficients related to the neural bursts and those related to the areas between bursts.

As demonstrated in Figure 1, the amplitude distribution of the noise related regions of the MSNA are Gaussian, a property which is preserved during wavelet transformation [24]. During periods of moderate (Fig 1A, baseline) and high (Fig 1B, VM Phase II) burst rates, the tails of the distribution become progressively heavier, meaning a Gaussian fit is no longer accurate. Local deviations from Gaussinity similar to those caused by MSNA bursts have been shown to be detectable using higher-order statistics (moments and cumulants higher than order two) [26;27]. In particular, the kurtosis of wavelet coefficients has been employed to detect non-Gaussian perturbation in cosmologic data [28;29]. However, to our knowledge, this technique has not been applied to neural signals.

We propose to use the local kurtosis of the wavelet coefficients as part of a spike detection scheme for human muscle sympathetic nerve activity. Due to the bursting nature of the MSNA, the local kurtosis will be used to classify wavelet coefficients as belonging to a pure noise segment or a burst segment containing signal plus noise. The noise-related coefficients will then be used to establish a threshold which can subsequently be applied to the burst-related coefficients. The parameters of this procedure will be optimized using simulated MSNA burst data and later validated using both simulated data and recordings made during a graded head up tilt protocol.

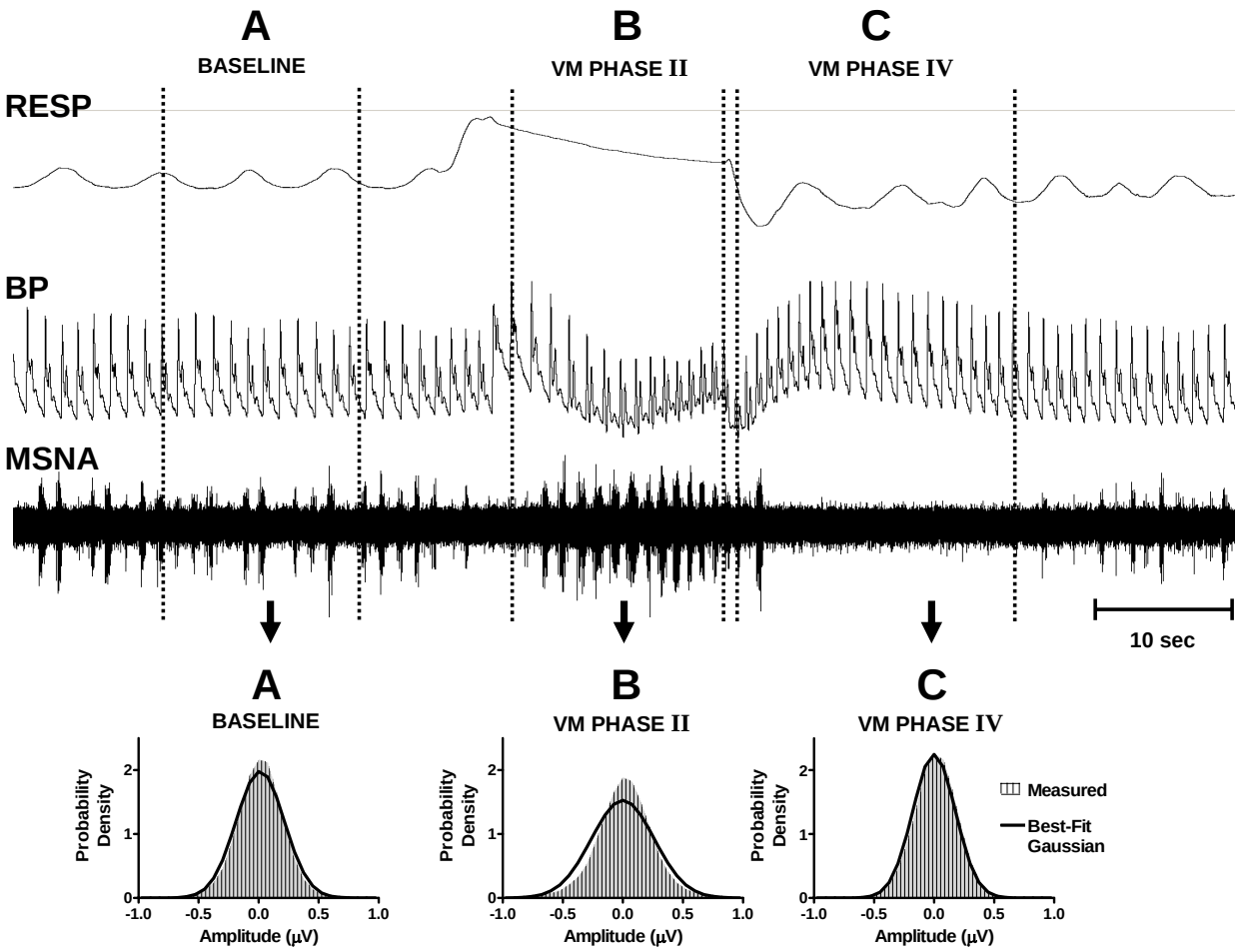

Figure 1. Tracings of the respiration (RESP), blood pressure (BP), and raw muscle sympathetic nerve activity (MSNA) during Valsalva Maneuver. During baseline (period A), MSNA burst activity is at a basal rate, and the recorded amplitudes are close to Gaussian (lower left panel). During Phase II of the Valsalva Maneuver (B), BP drops rapidly causing a significant rise in the and MSNA burst rate. The MSNA amplitudes are no longer fit by a Gaussian (lower middle panel). In Phase IV of the Valsalva Maneuver (C), BP overshoots it baseline values and MSNA ceases. This is assumed to be neural noise and is well fit by a Gaussian distribution (lower right panel).

Methods

Instrumentation and Recording Conditions

MSNA was recorded from the peroneal nerve [30]. A unipolar tungsten electrode with uninsulated tip diameter 1 to 5 μm and shaft diameter 200 μm (Frederick Haer and Co, Bowdoinham, MA, USA) was inserted into the muscle nerve fascicles of the peroneal nerve at the fibular head for multi-unit recordings. Raw nerve activity was amplified with a total gain of 100 000, band pass filtered from 0.7 to 2 kHz (662C-3 Nerve Traffic Analysis System, University of Iowa, Iowa City, USA), and recorded. The filtered nerve signal was also placed

through an R-C integrating circuit with a 0.1 sec time constant and the output (integrated MSNA) was simultaneously recorded. Satisfactory recordings of muscle sympathetic nerve activity were defined by (1) heart pulse synchronicity; (2) facilitation during Valsalva straining and suppression during the hypertensive overshoot after release; (3) increases in response to breath-holding; and (4) no change during tactile or auditory stimulation [11].

The continuous blood pressure (BP) waveform was measured by photoplethysmographic-based volume clamp method [31] with a finger cuff on the middle finger of the non-dominant hand (Finapres, Ohmeda, Englewood, CO, USA). Respiration was measured using a pneumobelt (Pneumotrace II; UFI, Morro Bay, CA). All data were acquired at 5000 Hz, 14 bit resolution using the Windaq data acquisition system (DI-720, DATAQ Instruments, Akron OH) and analyzed offline with custom software written in the PV Wave (Visual Numerics Inc., Houston, TX) and MATLAB (Mathworks; Natick, MA) environments.

Signal Processing

A brief discussion on wavelet-based signal processing is given in the following section. A more comprehensive review can be found in Appendix A.

Wavelet Decomposition The initial sympathetic spike detection technique proposed by *Diedrich et. al.* (2003) used the discrete wavelet transform (DWT) to decompose the nerve signal into several frequency sub-bands of wavelet coefficients. However, the DWT lacks translation invariance, which can be detrimental in the de-noising [24] and detection [32] of transient neural spikes. Alternatively, the stationary wavelet transform (SWT) is translation invariant, and has been shown to improve sympathetic spike detection in mice [33].

The SWT decomposition process [34] is described by Eq. 1 and 2. A signal, *f*, is projected onto a dyadically-spaced set of scales, or levels (*j*), using a set of *level dependent quadrature mirror decomposition filters,* h_j and g_j, that have respective band-pass and low-pass properties specific to each wavelet basis [35]. The broad scale, or *approximation*, coefficients, a_j^{SWT}, are convolved separately with g_j and h_j. This process splits the a_j^{SWT} frequency information roughly in half, partitioning it into a set of fine scale, or *detail* coefficients, d_{j+1}^{SWT}, and a coarser set of approximation coefficients, a_{j+1}^{SWT}. During the next level of processing, a zero is placed in between each consecutive value found in the g_j and h_j filters

(i.e. up-sampling by two) to achieve the g_{j+1} and h_{j+1} filters. This procedure can be iteratively continued until the desired level of decomposition, *j=J*, is obtained. Note that the algorithm is initiated by setting $a_0^{SWT} = f$.

$$a_{j+1}^{SWT}(k) = \sum_n h_j(n-k) a_j^{SWT}(k) \quad \textbf{(1)}$$

$$d_{j+1}^{SWT}(k) = \sum_n g_j(n-k) a_j^{SWT}(k) \quad \textbf{(2)}$$

The a_j^{SWT} coefficients can be reconstructed from a_{j+1}^{SWT} and d_{j+1}^{SWT} by convolving each with the respective reconstruction filter, $h_j(-n)$ or $g_j(-n)$, and summing (Eq. 3). Note that each reconstruction filter is also level dependent and includes 2^j-1 zeros between each filter coefficients. This process can be iteratively continued until the original signal, *f*, is recovered.

$$a_j^{SWT}(k) = \sum_n h_j(k-n) a_{j+1}^{SWT}(n) + \sum_n g_j(k-n) d_{j+1}^{SWT}(n) \quad \textbf{(3)}$$

Wavelet Thresholding Most wavelet based spike detection algorithms include some modified form of a process known as wavelet de-noising [25]. In this process, a nerve signal with additive noise, f, is decomposed using the wavelet transform and a threshold is applied to each of the detail coefficient levels. All coefficients with an absolute value greater than the threshold are thought to be part of an action potential and those below the threshold are presumably derived from noise. The noise coefficients can be set to zero and a noise-free signal can then be reconstructed and used for AP detection [12].

Several standard thresholds have been derived for wavelet de-noising [25;36]. In the case of correlated or colored noise, the standard deviation of the noise changes with each level and consequently requires a robust, level-dependent estimate, σ_j (Eq. 4),

$$\sigma_j = median\left(\left|d_j - \bar{d}_j\right|\right) / 0.6745 \quad \textbf{(4)}$$

which is later used in the calculation of the *standard colored noise threshold*, T_j^S (Eq. 5) [36].

$$T_j^S = \sigma_j \sqrt{2\log_e(N)} \quad \textbf{(5)}$$

A modified form of Eq. 5 has been shown to yield better detection performance in human sympathetic nerve activity [12]. We will refer to this as the *modified colored noise threshold*, T_j^M . It is displayed in Eq. 6

$$T_j^M = 0.8\sigma_j\sqrt{2\log_e(N)} \quad \textbf{(6)}$$

The performance of both the standard and modified colored noise thresholds will be assessed using simulation.

Wavelet Basis and Level Selection It has been observed that not all wavelet levels are necessary for spike detection and additional levels could actually hinder the performance of wavelet based detectors [32]. In the human MSNA, we have found that sympathetic activation during physiological interventions, such as a head-up tilt (HUT) protocol, causes increases in the MSNA power spectral density (PSD) between approximately 400 and 2500 Hz (Fig. 2A). This frequency range approximately corresponds to wavelet levels 1 to 3 for a signal sampled at 5 kHz. However, the wavelet coefficient standard deviation of levels 2 and 3 (σ_2 and σ_3) appear to have the most pronounced increases during HUT while σ_1 does not appear to respond to mild sympathetic activation, for instance 30^o HUT (Fig. 2B). We have therefore chosen only to use wavelet levels 2 and 3 while designing and testing the spike detection protocol. Symlet 7 was chosen as the wavelet basis because its morphology is similar to a sympathetic spike (Fig. 4D) [12].

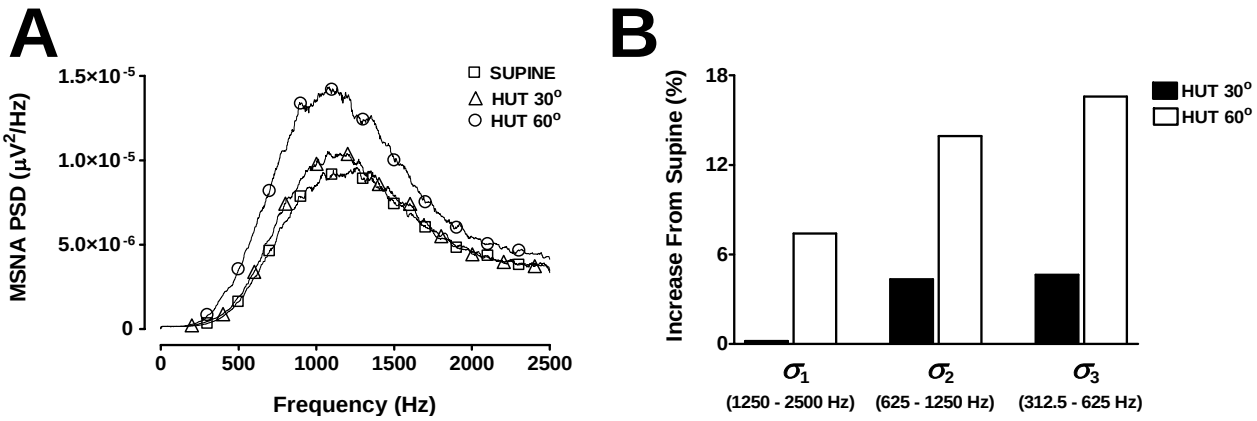

Figure 2. Power spectral density (PSD) **(A)** and percent increase in wavelet level standard deviations (σ_j) **(B)** of human muscle sympathetic nerve activity (MSNA) during different stages of a graded head up tilt (HUT) protocol. Increasing the angle of tilt further activates the sympathetic nervous system, and increases the power in the frequency range between 400 and 2500 Hz. Wavelet levels 2 and 3 appear to have the most dynamic response to the sympathetic activation. The approximate frequency range of each wavelet level is also displayed.

Local Kurtosis Estimate The local (or sliding) kurtosis computed over N_k detail coefficients of level j, expressed as K_j, was estimated using the following equation:

$$K_j(k) = \frac{1}{N_K}\sum_{n=0}^{N_K-1}\left(d_j(n-k)-m_j(k)\right)^4 \Bigg/ \left(\frac{1}{N_K}\sum_{n=0}^{N_K-1}\left(d_j(n-k)-m_j(k)\right)^2\right)^2 \quad \textbf{(7)}$$

where m_j is an estimate of the local mean of N_k level j coefficients, calculated using:

$$m_j(k) = \frac{1}{N_K}\sum_{n=0}^{N_K-1} d_j(n-k) \quad \textbf{(8)}$$

The kurtosis of a Gaussian sequence is always 3, regardless of the mean or variance of the distribution. We expect the kurtosis of the burst related coefficients to be greater than 3 due to the presence of action potentials with large positive and negative values.

Once the kurtosis sequence was computed, wavelet de-noising took place in two stages. In stage 1, a kurtosis threshold, T_K, was established. All kurtosis values below T_K were classified as coming from noise while kurtosis values above T_K were assumed to be burst-related. During stage 2, the noise coefficients were used to estimate the noise standard deviation, σ_j, as shown in Eq. 7. All detail coefficients located within an identified burst segment and whose absolute value was greater than $3.5\sigma_j$ were retained, while all other coefficients were set to zero. The de-noised signal was then reconstructed and action potentials were detected using a simple peak detection scheme that locates maxima above 99% of the signal energy, as described previously [12]. An example of the two-stage kurtosis de-noising scheme applied to a representative MSNA recording is displayed in Fig. 3. The optimal values for N_K and T_K were determined through simulation, as described below in Section 2.3.1.

Simulations

Simulated signals were constructed with templates extracted from recordings with sufficiently high signal to noise ratio in 8 healthy subjects during periods of sympathetic activation (head-up tilt) (Fig. 4D). Noise was extracted from each recording during Phase IV of the Valsalva maneuver, as shown in Figure 1. Since the length of the noise was generally too short for an appropriate simulation (< 15 sec), a 50 order autoregressive (AR) model was created using the Burg method [37] and subsequently applied to a sequence of Gaussian random numbers 60 seconds in length. Prior to AR filtering the Gaussian random numbers have a white noise power spectral density (PSD) and normalized autocorrelation function (NACF). But after

filtering, the NACF and PSD of the simulated noise were shown to closely approximate those of the recorded noise (Fig. 4B-4C). The overall shape of the Gaussian sequence probability density distribution is not affected by the AR filter (Fig. 4A).

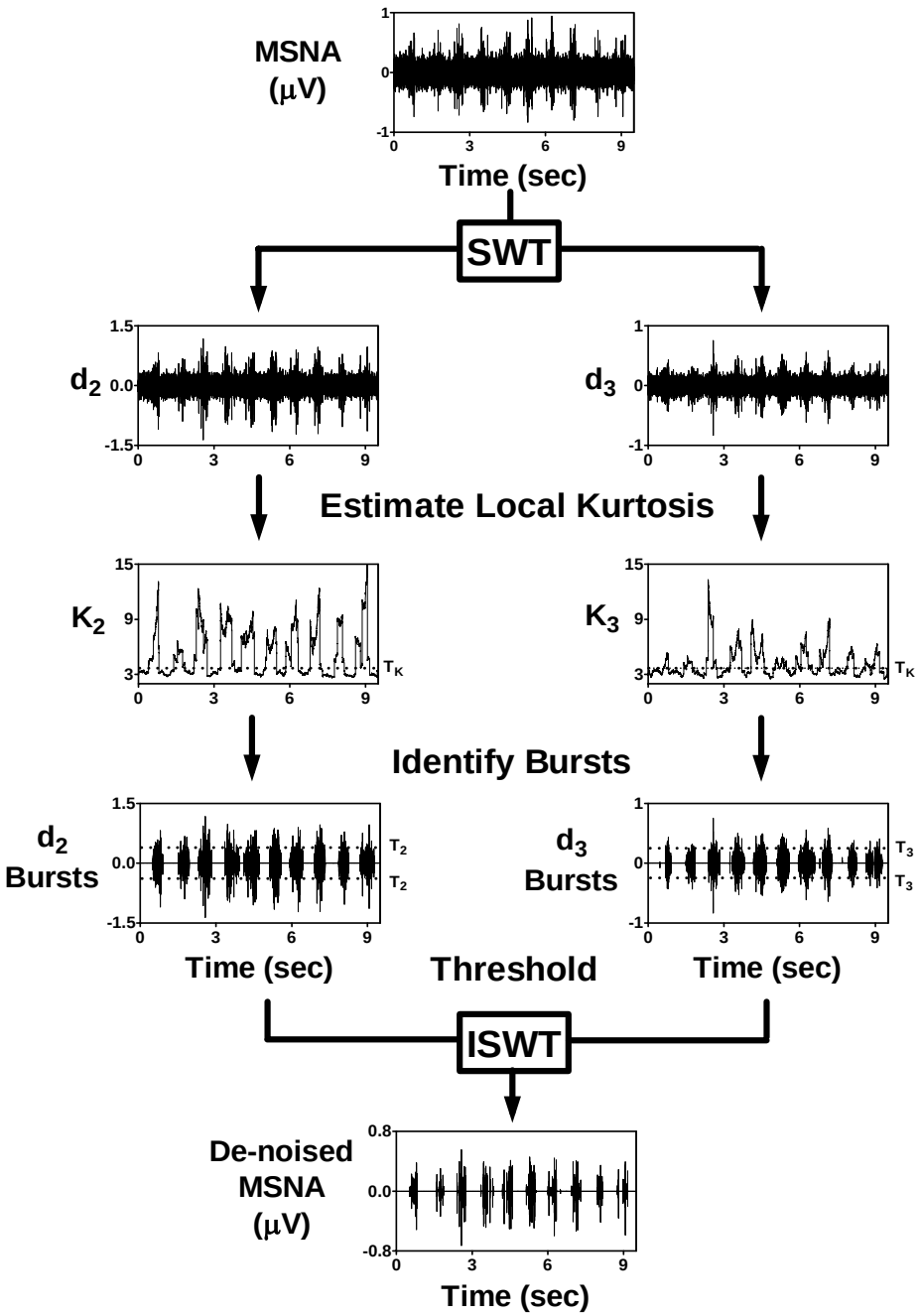

Figure 3. Two-stage kurtosis de-noising example. The MSNA is decomposed using the SWT. A moving kurtosis estimate is made of the detail coefficients (d_2 and d_3). The coefficients are grouped into noise-related (K_2 and $K_3<T_K$) and burst-related (K_2 and $K_3>T_K$). The noise-related coefficients are used to estimate noise level (σ_2 and σ_3) and burst-related coefficients undergo thresholding. The de-noised signal is reconstructed with the ISWT.

The templates were then randomly inserted into neural noise in burst fashion. The burst position, burst duration, and spike placement within each burst were all randomly assigned according to separate Poisson random variables. The average burst duration and spike rate within each burst were fixed at 0.8 seconds and 60 spikes/sec, respectively. Each simulation was assigned either a low (5 burst/min), moderate (25 bursts/min), or high (50 bursts/min) mean burst rate. The signal to noise ratio (SNR) of the simulations was altered from 6 (high signal quality) to 1 (poor signal quality). The SNR was defined as the ratio between the absolute peak amplitude of the action potential and the standard deviation of the noise, as defined elsewhere [12;18].

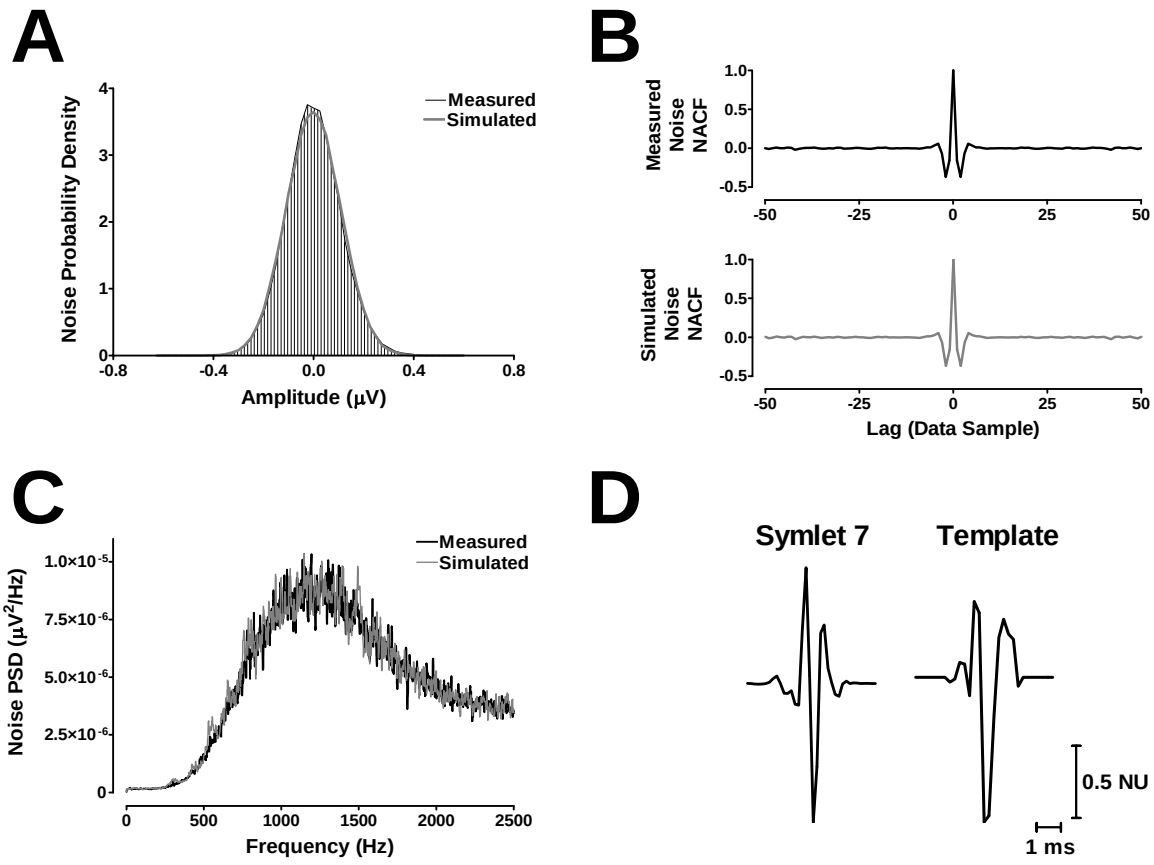

Figure 4. Simulation elements. **(A)** Histograms of the neural noise recorded during Phase IV of the Valsalva Maneuver (Measured, black) and random simulated noise after application of an AR filter (Simulated, gray). Both demonstrate a normal probability density. **(B)** The normalized autocorrelation function (NACF) of the measured (top, black) and simulated noise (bottom, gray). **(C)** The power spectral density (PSD) of the measured (black) and simulated (gray) noise. **(D)** The Symlet 7 wavelet (left) and two representative template action potentials (right) displayed in normalized units (NU).

Kurtosis Method Optimization The parameters of the kurtosis-based wavelet de-noising were optimized using the simulated data described above. The value for the kurtosis threshold, T_K, was varied from 2.8 to 5 and the number of samples in each kurtosis calculation, N_K, was varied from 250 to 4000 samples. The optimum T_K and N_K values for each burst rate and each SNR were defined as those which resulted in the maximum difference between the average percentage of correctly identified burst area and the percentage of the remaining area falsely identified as burst related. The optimum T_K and N_K values were averaged across all subjects, burst rates, and SNRs. The average T_K and N_K optimums were then used in the tests of spike detection performance and the validation discussed below.

Evaluation of Detection Performance The simulated signals were also used to test the performance of several wavelet-based algorithms and an unsupervised amplitude discriminator. The amplitude discriminator detected all peaks with an absolute value greater than 3.5 times the standard deviation of the signal, as discussed elsewhere [38]**.** The three wavelet algorithms each used different de-noising methods which included the standard wavelet threshold (SWTS, Eq. 5), the modified threshold (SWTM, Eq. 6), and the two-stage kurtosis method (SWTK). Both the amplitude discriminator and wavelet detection methods used a 3 msec time-window, which was observed to be the maximum duration of a human sympathetic spike. The detection performance evaluation was repeated 12 separate times for each subject, yielding 96 trials for each SNR and mean burst rate. The performance of each method was quantified using the percent of correctly detected action potentials (PCD, Eq. 9) and the percent of false alarms (PFA, Eq. 10).

$$PCD = \frac{N_{CD}}{N_{AP}} \times 100 \quad \textbf{(9)}$$

$$PFA = \frac{N_{FA}}{N_{CD}} \times 100 \quad \textbf{(10)}$$

N_{CD} is the number of correctly detected APs, N_{AP} is the number of APs inserted into the simulation, and N_{FA} is the number of false alarms.

Since the original method of MSNA spike detection employed the discrete wavelet transform (DWT), the performance of similar DWT methods were also compared to each of the SWT-based detection methods using the simulated human MSNA data. The results of this comparison can be found in APPENDIX B.

Validation using Graded Head-Up Tilt Protocol

Seven healthy subjects (6 males and 1 female, age 23 to 47) were recruited from the Vanderbilt University General Clinical Research Center volunteer database. All subjects underwent extensive physical examination and abstained from all drugs for at least 72 hours prior to the study. The subjects were secured to a tilt table with straps and instructed to remain relaxed and quiet throughout all studies. After 15 minutes of supine rest the subjects were tilted by 15° increments every 5 minutes until an angle of 60° was reached. The parameters of the integrated MSNA bursts and the MSNA spike rates were later computed offline and compared using linear regression. The Pearson correlation coefficient (r) was used to quantify the goodness of fit. All studies were conducted at Vanderbilt University General Clinical Research Center and all procedures were approved by the local institutional review board.

Results

Kurtosis Method Optimization

The results of the search for the optimal number of samples in each kurtosis calculation, N_K, and the optimal kurtosis threshold, T_K, are displayed in Figure 5. Each point represents the mean for each subject across all burst rates and SNR values. The group means were found to be $T_K = 3.7$ and $N_K = 961$.

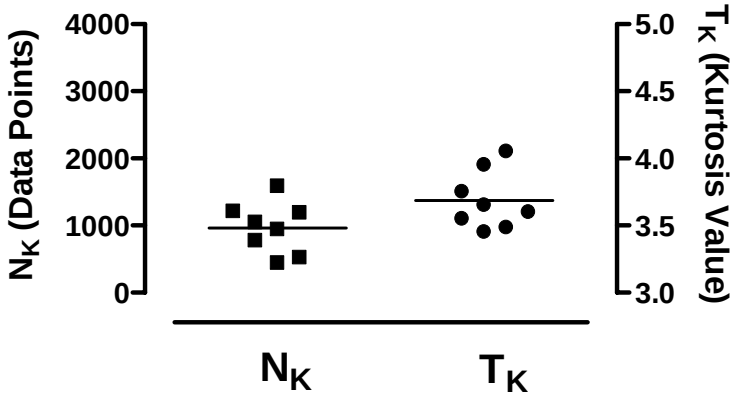

Figure 5. Results of kurtosis method optimization. The optimal sample number for kurtosis calculation (N_K, left) and optimal kurtosis threshold (T_K, right) were determined through simulation. Each point is the mean for each subject across signal to noise ratios from 1 to 6 and bursts rates of 5, 25, and 50 bursts/min.

These values were used in the evaluation of the detection performance and the validation during baroreflex testing.

Evaluation of Detection Performance

The detection performance of each of the four methods is displayed in Figure 6. While the standard wavelet threshold (SWTS) has the lowest percentage of false alarms (PFA) during all simulations, its percent of correctly detected action potentials (PCD) is also lowest. The modification to the standard threshold (SWTM), suggested by *Diedrich et al.*, results in a higher PCD and the PFA remains low (<10%) for SNR>2 during moderate (25 bursts/min) and high (50 bursts/min) burst rates. However, during low burst rates (5 bursts/min), the PFA is greater than 15% at a SNR of 3.25 and steadily increases as SNR drops. The two-stage kurtosis de-noising (SWTK) demonstrates the highest PCD for SNR>2 during all burst rates and its PFA is similar to that of the modified wavelet threshold at burst rates of 25 and 50 bursts/min and lower during the 5 burst/min simulations. The amplitude discriminator has a PFA that is similar to or greater than all other detection methods during all simulations and its PCD is lower than that of the modified and kurtosis-based wavelet thresholding methods.

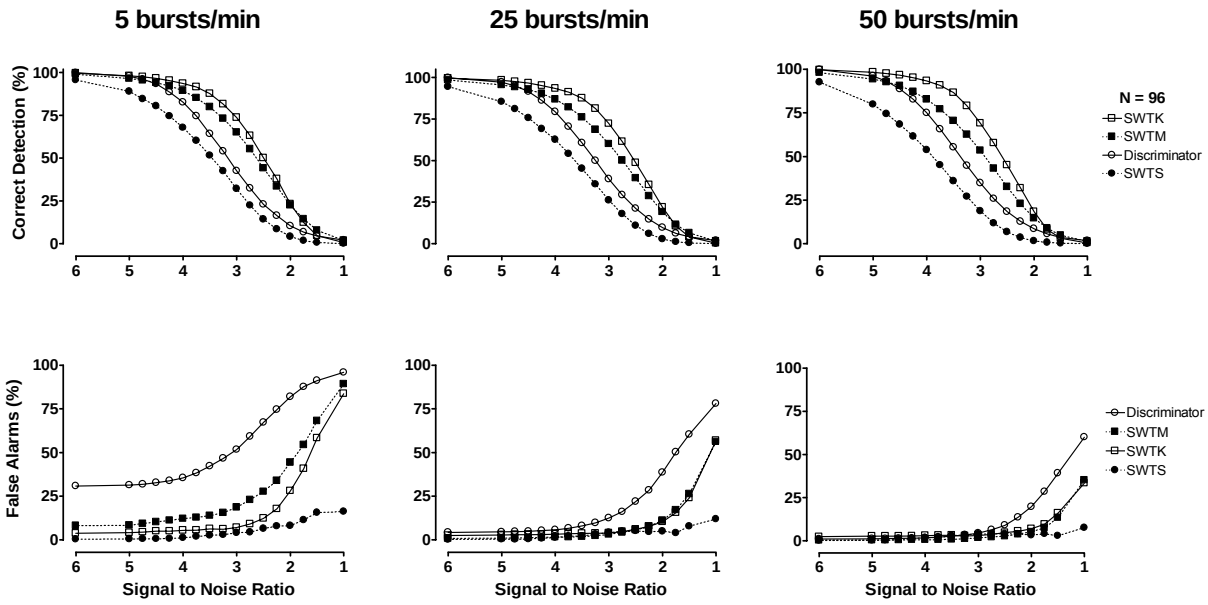

Figure 6. Mean results for simulations with varied noise levels and mean burst rates. The simulations tested the performance of an unsupervised amplitude discriminator (Discriminator), SWT decomposition with standard (SWTS) and modified (SWTM) colored noise thresholds, SWT decomposition with 2-stage kurtosis threshold (SWTK). Each point on each curve represents the mean result of 96 simulations.

Validation using Graded Head-Up Tilt Protocol

Figure 7 demonstrates that a good correlation exists between the spike rates detected using the two-phase kurtosis method and the commonly used integrated burst rate (Fig 7A, r = 0.85) and burst area rate (Fig. 7B, r = 0.91) parameters. The spike rate, burst rate (Fig 7C), and burst area rate (Fig. 7D) also demonstrate similar increasing trends as the head-up tilt angle is increased and the sympathetic nervous system is activated.

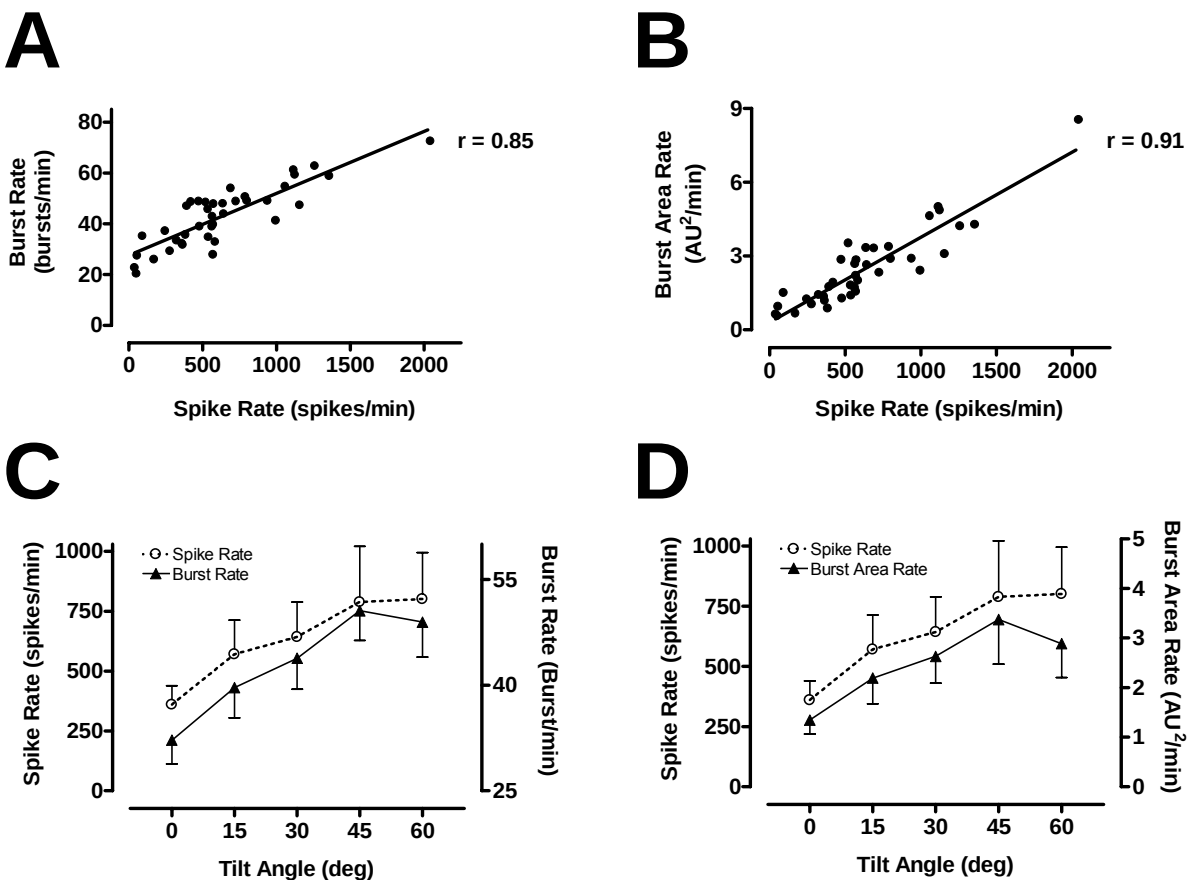

Figure 7. Comparison of spike detection and burst parameters during a head-up tilt (HUT) protocol. The mean spike rate shows a good correlation to the mean burst rate **(A)** and burst area rate **(B)**. The mean spike rate demonstrates the same general increasing pattern as the mean burst rate **(C)** and mean burst area rate **(D)** as tilt angle is increased.

Discussion

We have demonstrated a novel spike detection scheme for human muscle sympathetic nerve activity that uses the local kurtosis of the stationary wavelet transform coefficients to identify pure noise coefficients, which are used to estimate a noise threshold, and signal-plus-noise (burst–related) coefficients, which undergo thresholding. This method was shown to

outperform a similar modified-wavelet technique specifically designed for the MSNA, which was not previously evaluated at varying burst rates [12]. It was also shown to have better overall detection performance than an unsupervised amplitude discriminator and a higher percent of correctly detected action potentials than standard wavelet thresholding. The mean spike rates detected using the two-phase kurtosis de-noising method during a graded head-up tilt protocol were also shown to be highly correlated to commonly used integrated burst rate ($r = 0.85$) and burst area rate ($r = 0.91$) parameters. These correlations were improved from than those previously reported with the modified wavelet threshold ($r = 0.79$ and $r = 0.52$, respectively) [12]. The spike rates, burst rates, and burst area rates also displayed similar increasing responses to increased tilt angle.

Limitations

In this study, we have focused our optimization and evaluations on recordings of the human muscle sympathetic nerve activity. This detection technique may be applicable to other neural or bioelectric signals with bursting characteristics, but this has not yet been investigated. In the case of the MSNA, the kurtosis-based wavelet de-noising method was found to possess reasonably accurate detection performance for signal-to-noise ratios greater than three independent of the burst rate, with over 70% of the action potentials correctly identified and less than 10% false alarms. However, detections made using this method, or any other method tested here, on signals with SNR<3 may not be reliable. Also, the kurtosis-based wavelet de-nosing method may not detect levels of tonic activity that occurs between bursts. But, the initial separation of noise segments using kurtosis may be useful in a hypothesis testing framework, as suggested earlier [18].

Conclusions

Application of this spike detection technique may be useful in the diagnosis and study of various peripheral neuropathies and disorders of the autonomic nervous system. Specifically, detection of sympathetic spikes, as opposed to bursts, allows for the possibility of subsequent, automated sorting of spikes into classes derived from individual neurons [12]. Single-unit recordings have identified important differences in diseases such as congestive heart failure and hypertension which were not demonstrated in the multiunit burst rate [39-41]. Since these single

unit recordings are extremely difficult to achieve and sustain manually [42], automated spike detection and classification methods will be useful in this area. In conclusion, the kurtosis-based wavelet de-noising technique is a potentially useful method of studying sympathetic nerve activity in humans.

Acknowledgements

This work was supported in part by National Institutes of Health grants RR00095, and 1PO1 HL56693. We thank Sachin Y Paranjape, Indu Taneja, and Bonnie Black for the support of this study.

References

[1] S. Gudbjornsdottir, P. Lonnroth, Y. B. Sverrisdottir, B. G. Wallin, and M. Elam, "Sympathetic nerve activity and insulin in obese normotensive and hypertensive men," *Hypertension*, vol. 27, no. 2, pp. 276-280, Feb.1996.

[2] A. L. Mark, "The sympathetic nervous system in hypertension: a potential long-term regulator of arterial pressure," *J Hypertens. Suppl*, vol. 14, no. 5, p. S159-S165, Dec.1996.

[3] B. G. Wallin and G. Sundlof, "A quantitative study of muscle nerve sympathetic activity in resting normotensive and hypertensive subjects," *Hypertension*, vol. 1, no. 2, pp. 67-77, Mar.1979.

[4] R. Furlan, G. Jacob, M. Snell, D. Robertson, A. Porta, P. Harris, and R. Mosqueda-Garcia, "Chronic orthostatic intolerance: a disorder with discordant cardiac and vascular sympathetic control," *Circulation*, vol. 98, no. 20, pp. 2154-2159, Nov.1998.

[5] van de Borne P., N. Montano, M. Pagani, R. Oren, and V. K. Somers, "Absence of low-frequency variability of sympathetic nerve activity in severe heart failure," *Circulation*, vol. 95, no. 6, pp. 1449-1454, Mar.1997.

[6] K. E. Hagbarth and A. B. Vallbo, "Pulse and respiratory grouping of sympathetic impulses in human muscle- nerves," *Acta Physiol Scand.*, vol. 74, no. 1, pp. 96-108, Sept.1968.

[7] B. G. Wallin and J. Fagius, "Peripheral sympathetic neural activity in conscious humans," *Annu. Rev. Physiol*, vol. 50, pp. 565-576, 1988.

[8] N. Charkoudian, M. J. Joyner, C. P. Johnson, J. H. Eisenach, N. M. Dietz, and B. G. Wallin, "Balance between cardiac output and sympathetic nerve activity in resting humans: role in arterial pressure regulation," *J Physiol*, vol. 568, no. Pt 1, pp. 315-321, Oct.2005.

[9] R. Furlan, A. Porta, F. Costa, J. Tank, L. Baker, R. Schiavi, D. Robertson, A. Malliani, and R. Mosqueda-Garcia, "Oscillatory patterns in sympathetic neural discharge and cardiovascular variables during orthostatic stimulus," *Circulation*, vol. 101, no. 8, pp. 886-892, Feb.2000.

[10] M. Pagani, N. Montano, A. Porta, A. Malliani, F. M. Abboud, C. Birkett, and V. K. Somers, "Relationship between spectral components of cardiovascular variabilities and direct measures of muscle sympathetic nerve activity in humans," *Circulation*, vol. 95, no. 6, pp. 1441-1448, Mar.1997.

[11] W. Delius, K. E. Hagbarth, A. Hongell, and B. G. Wallin, "General characteristics of sympathetic activity in human muscle nerves," *Acta Physiol Scand.*, vol. 84, no. 1, pp. 65-81, Jan.1972.

[12] A. Diedrich, W. Charoensuk, R. J. Brychta, A. C. Ertl, and R. Shiavi, "Analysis of raw microneurographic recordings based on wavelet de-noising technique and classification algorithm: wavelet analysis in microneurography," *IEEE Trans. Biomed. Eng*, vol. 50, no. 1, pp. 41-50, Jan.2003.

[13] Y. Sugiyama, T. Matsukawa, H. Suzuki, S. Iwase, A. S. Shamsuzzaman, and T. Mano, "A new method of quantifying human muscle sympathetic nerve activity for frequency domain analysis," *Electroencephalogr. Clin Neurophysiol.*, vol. 101, no. 2, pp. 121-128, Apr.1996.

[14] G. Sundlof and B. G. Wallin, "The variability of muscle nerve sympathetic activity in resting recumbent man," *J Physiol (Lond)*, vol. 272, no. 2, pp. 383-397, Nov.1977.

[15] R. Mosqueda-Garcia, "Evaluation of autonomic failure," in *The Autonomic Nervous System*. G. Burnstock, Ed. Luxembourg: Harwood Academic Press, 1995, pp. 25-59.

[16] J. C. Letelier and P. P. Weber, "Spike sorting based on discrete wavelet transform coefficients," *J Neurosci Methods*, vol. 101, no. 2, pp. 93-106, Sept.2000.

[17] H. Nakatani, T. Watanabe, and N. Hoshimiya, "Detection of nerve action potentials under low signal-to-noise ratio condition," *IEEE Trans. Biomed. Eng*, vol. 48, no. 8, pp. 845-849, Aug.2001.

[18] Z. Nenadic and J. W. Burdick, "Spike detection using the continuous wavelet transform," *IEEE Trans. Biomed. Eng*, vol. 52, no. 1, pp. 74-87, Jan.2005.

[19] K. G. Oweiss and D. J. Anderson, "Spike sorting: a novel shift and amplitude invariant technique," *NEUROCOMPUTING NEUROCOMPUTING*, vol. 44-46, pp. 1133-1139, June2002.

[20] G. Grassi, G. Seravalle, B. M. Cattaneo, G. B. Bolla, A. Lanfranchi, M. Colombo, C. Giannattasio, A. Brunani, F. Cavagnini, and G. Mancia, "Sympathetic activation in obese normotensive subjects," *Hypertension*, vol. 25, no. 4 Pt 1, pp. 560-563, Apr.1995.

[21] G. Grassi, B. M. Cattaneo, G. Seravalle, A. Lanfranchi, and G. Mancia, "Baroreflex control of sympathetic nerve activity in essential and secondary hypertension," *Hypertension*, vol. 31, no. 1, pp. 68-72, 1998.

[22] R. Mosqueda-Garcia, R. Furlan, R. Fernandez-Violante, T. Desai, M. Snell, Z. Jarai, V. Ananthram, R. M. Robertson, and D. Robertson, "Sympathetic and baroreceptor reflex function in neurally mediated syncope evoked by tilt," *J Clin Invest*, vol. 99, no. 11, pp. 2736-2744, June1997.

[23] J. Jordan, J. Tank, J. R. Shannon, A. Diedrich, A. Lipp, C. Schroder, G. Arnold, A. M. Sharma, I. Biaggioni, D. Robertson, and F. C. Luft, "Baroreflex buffering and susceptibility to vasoactive drugs," *Circulation*, vol. 105, no. 12, pp. 1459-1464, Mar.2002.

[24] B. Silverman, "Wavelets in statistics: beyond the standard assumptions," *PHILOS T ROY SOC A*, vol. 357, no. 1760\, pp. 2459-2473, 1999.

[25] D. L. Donoho, "De-Noising by Soft-Thresholding," *Ieee T Inform Theory*, vol. 41, no. 3, pp. 613-624, 1995.

[26] O. N. Gerek and D. G. Ece, "Power-quality event analysis using higher order cumulants and quadratic classifiers," *Power Delivery, IEEE Transactions on*, vol. 21, no. 2, pp. 883-889, 2006.

[27] Nikias C.L. and Petropulu A.P., *Higher-Order Spectra Analysis: A Nonlinear Signal Processing Framework*. Englewood Cliffs, NJ: Prentice Hall, 1993.

[28] Vielva P., Martinez-Gonzalez E., Barreiro R.B., Sanz J.L., and Cayon L., "Detection of non-Gaussinity in the *Wilkinson Microwave Anisotopy Probe* first-year data using spherical wavelets," *The Astrophysical Journal*, vol. 609, no. 1, pp. 22-34, July2004.

[29] Jin J, Starck J.L., Donoho D.L., Aghanim N., and Forni O., "Cosmological non-Gaussian signature detection: comparing performace of statistical tests," *EURASIP Journal on Applied Signal Processing*, vol. 15, pp. 2470-2485, 2005.

[30] A. B. Vallbo, K. E. Hagbarth, H. E. Torebjork, and B. G. Wallin, "Somatosensory, proprioceptive, and sympathetic activity in human peripheral nerves," *Physiol Rev.*, vol. 59, no. 4, pp. 919-957, Oct.1979.

[31] J. Penaz, "Photoelectric measurement of blood pressure, volume and flow in the finger," *Digest of the 10th international conference on medical and biological engineering - Dresden.*, p. 104, 1973.

[32] K. H. Kim and S. J. Kim, "A wavelet-based method for action potential detection from extracellular neural signal recording with low signal-to-noise ratio," *IEEE Trans. Biomed. Eng*, vol. 50, no. 8, pp. 999-1011, Aug.2003.

[33] R. J. Brychta, S. Tuntrakool, M. Appalsamy, N. R. Keller, C. Finney, D. Robertson, R. Shiavi, and A. Diedrich, "Spike detection in mouse renal sympathetic nerve activity using the stationary wavelet transform with automated noise level estimation," *IEEE Trans Biomed Eng*, 2006.

[34] S. Mallat, "Zero-Crossings of a Wavelet Transform," *Ieee T Inform Theory*, vol. 37, no. 4, pp. 1019-1033, 1991.

[35] S. G. Mallat, "A Theory for Multiresolution Signal Decomposition - the Wavelet Representation," *Ieee T Pattern Anal*, vol. 11, no. 7, pp. 674-693, 1989.

[36] I. Johnstone and B. Silverman, "Wavelet threshold estimators for data with correlated noise," *J of the Royal Statistical Society*, vol. 59, no. 2, pp. 319-351, 1997.

[37] R. G. Shiavi, *Introduction to Applied Statistical Signal Analysis*, 2nd ed. San Diego: Academic Press, 1999.

[38] C. Pouzat, O. Mazor, and G. Laurent, "Using noise signature to optimize spike-sorting and to assess neuronal classification quality," *J Neurosci Meth*, vol. 122, no. 1, pp. 43-57, 2002.

[39] V. G. Macefield and B. G. Wallin, "Firing properties of single vasoconstrictor neurones in human subjects with high levels of muscle sympathetic activity," *J Physiol (Lond)*, vol. 516 (Pt 1), pp. 293-301, Apr.1999.

[40] V. G. Macefield, B. Rundqvist, Y. B. Sverrisdottir, B. G. Wallin, and M. Elam, "Firing properties of single muscle vasoconstrictor neurons in the sympathoexcitation associated with congestive heart failure," *Circulation*, vol. 100, no. 16, pp. 1708-1713, Oct.1999.

[41] D. A. Mary and J. B. Stoker, "The activity of single vasoconstrictor nerve units in hypertension," *Acta Physiol Scand.*, vol. 177, no. 3, pp. 367-376, Mar.2003.

[42] B. G. Wallin, "Sympathetic Microneurography," in *Primer on the Autonomic Nervous System*, 2 ed. D. Robertson, Ed. Oxford, UK: Elsevier, 2004, pp. 224-227.

CHAPTER IV

WAVELET METHODS FOR SPIKE DETECTION IN MOUSE RENAL SYMPATHETIC NERVE ACTIVITY

Abstract

Abnormal autonomic nerve traffic has been associated with a number of peripheral neuropathies and cardiovascular disorders prompting the development of genetically altered mice to study the genetic and molecular components of these diseases. Autonomic function in mice can be assessed by directly recording sympathetic nerve activity. However, murine sympathetic spikes are typically detected using a manually adjusted voltage threshold and no unsupervised detection methods have been developed for the mouse. Therefore, we tested the performance of several unsupervised spike detection algorithms on simulated murine renal sympathetic nerve recordings, including an automated amplitude discriminator and wavelet based detection methods which used both the discrete wavelet transform (DWT) and the stationary wavelet transform (SWT) and several wavelet threshold rules. The parameters of the wavelet methods were optimized by comparing basal sympathetic activity to postmortem recordings and recordings made during pharmacological suppression and enhancement of sympathetic activity. In general, SWT methods were found to outperform amplitude discriminators and DWT methods with similar wavelet coefficient thresholding algorithms when presented with simulations with varied mean spike rates and signal to noise ratios. A SWT method which estimates the noise level using a “noise-only” wavelet scale and then selectively thresholds scales containing the physiologically important signal information was found to have the most robust spike detection. The proposed noise level estimation method was also successfully validated during pharmacological interventions.

Introduction

The autonomic nervous system has a broad range of functions, including the regulation of blood pressure, cardiac function, visceral function, and renal output. Abnormal autonomic function has been associated with such profound disorders as essential hypertension [1-3], obesity [1, 4], chronic renal disease [5], diabetes [6, 7], orthostatic intolerance [8], and congestive heart failure [9]. The many recent insights into the murine genome have motivated

scientists to develop transgenic and gene targeted mouse models to better understand the genetic and molecular components of these diseases [10-15]. One method of assessing autonomic sympathetic function is to directly record renal sympathetic nerve activity (RSNA). Measurement of the RSNA in mice has been recently introduced [16-19] and there is some debate as to how it should be objectively quantified. The low amplitude, multiunit sympathetic action potentials (AP) recorded from the renal nerve are significantly corrupted by high levels of bioelectric, mechanical, and environmental noise. Contamination from biological noise sources is particularly common in mice because many of the electrically active organs are in close proximity to the recording electrode due to the small frame of the animal.

Currently, the murine RSNA is quantified using two general strategies: (1) integrating the nerve signal over short periods of 5 to 10 seconds [16] or (2) using a hardware amplitude discriminator to detect APs [17-19]. The integration method is computationally efficient, but also indiscriminately integrates artifacts and noise and makes no correction for differences in AP amplitudes. For instance, several large amplitude APs with a low firing rate may produce the same value as many small APs with a high firing rate. The second approach using amplitude discrimination involves manually adjusting a voltage threshold trigger until the threshold exceeds the level of the noise. All signal amplitudes that exceed the threshold are detected as spikes [20]. The level of the murine RSNA threshold is typically established as the voltage at which no spikes are detected following a bolus injection of a pharmacological agent known to increase blood pressure and suppress the heart rate and RSNA via the baroreceptor-reflex, such as phenylephrine (PHE), [17, 18] (Fig 1). Similarly, investigators studying the rat RSNA have used the highest voltage in the postmortem recording as a threshold for a subsequent off-line amplitude discrimination procedure [21]. Postmortem activity has also been used to correct total activity recorded during the experiment to obtain an estimate of the true neural activity in mice [19].

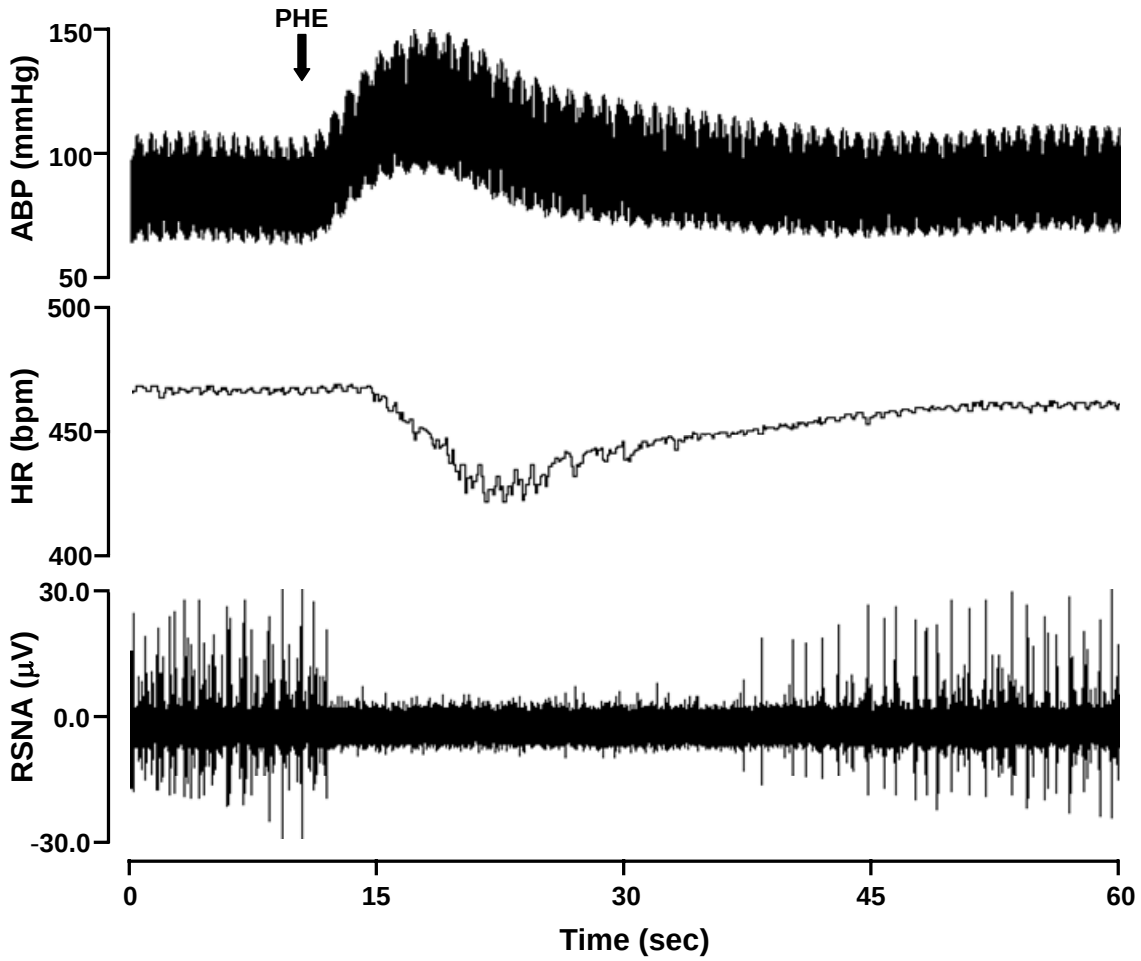

Figure 1. Representative affects of phenylephrine bolus injection on murine arterial blood pressure (ABP), heart rate (HR), and renal sympathetic nerve activity (RSNA).

Both amplitude discrimination methods currently used in the processing of small animal RSNA signals have specific limitations. Selecting a threshold based on the maximum voltage level during baroreflex mediated decrease of sympathetic nerve activity necessitates having to perform pharmacological tests during each experimental protocol and it does not account for incomplete RSNA suppression due to the presence of baroreflex independent nerve activity. Further, this procedure can not be applied in mouse models that exhibit baroreflex dysfunction. A threshold procedure that uses the maximum voltage of the postmortem nerve recording can only be used for off-line analysis, may not be accurate due to changes in needle position throughout the recording, and does not take into account bioelectric noise present during the living state. The postmortem noise level is usually lower than the living state noise level due additional physiological activities and biological noise in the living animal. Threshold estimation

following PHE bolus in the living mouse or after death can produce substantially different spike detection results, as illustrated in Fig. 2.

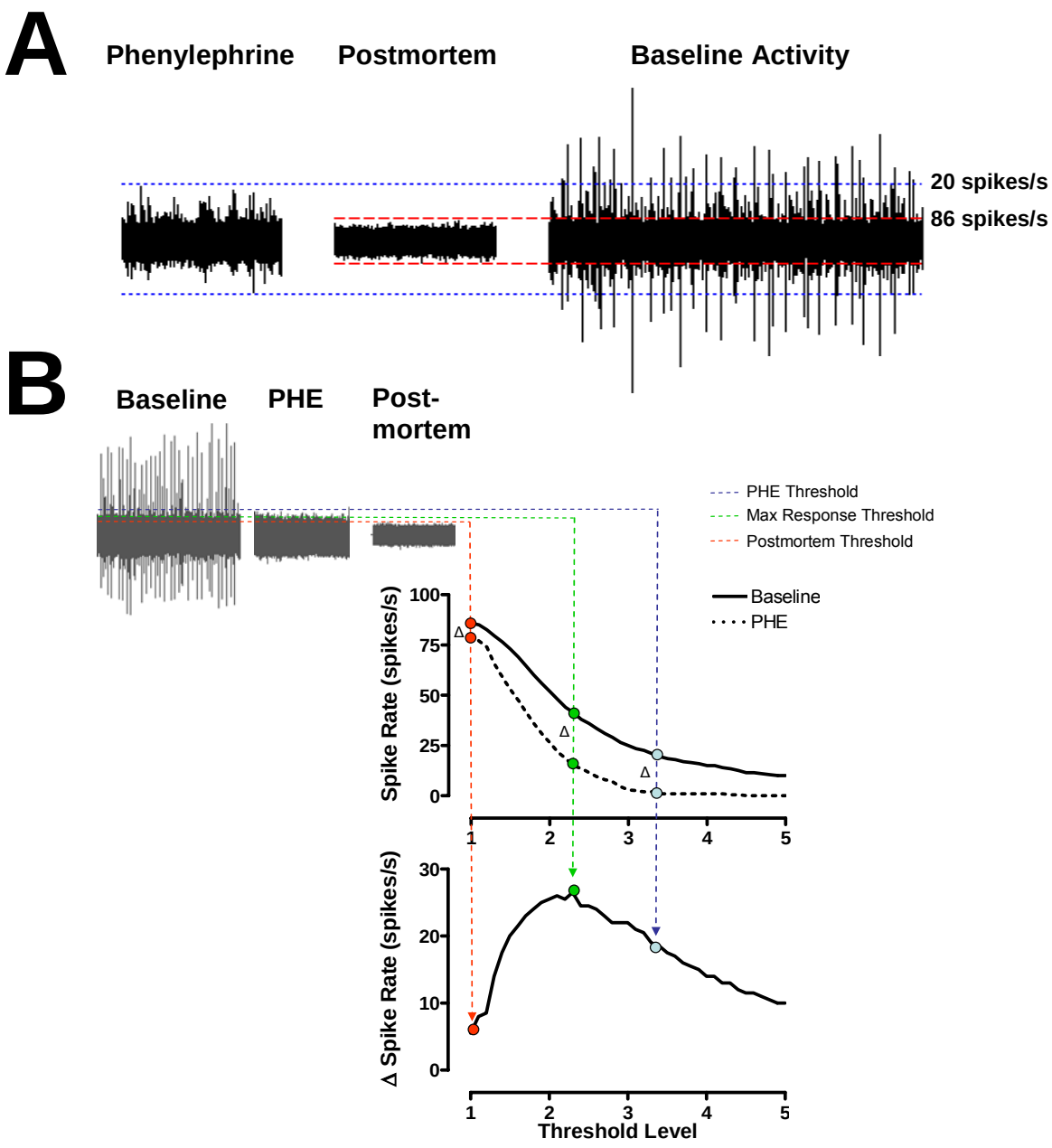

Figure 2. (A) Noise threshold estimates using recordings during baroreflex mediated suppression of RSNA using phenylephrine (PHE) bolus injection (left) and postmortem recordings (middle) in the same mouse. **(B)** The threshold value which yields the maximum change in spike rate from PHE to baseline (max Δ spike rate) is termed the optimal threshold level (green broken line). The nerve signal recorded during PHE bolus (red broken lines) overestimates the noise level and the postmortem recording (blue broken lines) underestimates the noise level.

Hardware amplitude discriminators also have several obvious general drawbacks. To begin, they require manual threshold selection which can be both tedious and subjective. Additionally, they only take into account the amplitude and duration of the waveform and disregard other potentially useful attributes such as shape and frequency content. Over the past several decades, a number of spike detection algorithms have taken advantage of these properties and improved upon the classic hardware amplitude discriminator approach, as discussed in several comprehensive reviews [22, 23]. Notable contributions to this field include the unsupervised amplitude discriminator, power or energy detectors, and the matched filter [24, 25]. Unsupervised amplitude discriminators typically establish a threshold by multiplying the standard deviation of the signal by some predetermined factor [26]. Power detectors compute the sum of squared amplitude using a sliding window and also use the standard deviation of the signal to create a threshold [24]. The accuracy these methods has been shown to decrease significantly at low signal to noise ratios (SNR) [24]. Matched filters generally increase the SNR of a signal by correlating signal amplitudes with template waveforms identified from the signal, particularly when a prewhitening filter is used [24, 25]. This process requires manual identification of the templates for each signal analyzed and is difficult to automate due to the changes in action potential shapes that occur with different spatial relationships between the electrode and neurons [27].

Recently, use of the wavelet transform has become popular in multiunit AP discrimination [28-37]. Wavelet decomposition effectively filters the nerve signal into several frequency sub-bands while preserving its temporal structure. Each sub-band of wavelet processing decorrelates successive noise-related values and compares progressively more dilated versions of a general spike shape to each point in the signal, which is similar to a generalized group of matched filters coupled with prewhitening filters [31]. This process can ease the detection of APs by separating the signal and noise using their distinct time-frequency signatures. Several of these wavelet processing techniques are primarily concerned with the classification of APs from different cells [29, 30, 32, 36, 37], a process which follows detection and can be aided by an accurate detection algorithm that limits the number of false alarms detected. Oweiss, *et al* [35] presented a wavelet method that uses information from several electrode channels but is not applicable to single channel, bipolar recordings of the renal nerve activity in mice. However, others have demonstrated that wavelet methods are suitable for

unsupervised de-noising and detection of single channel, multiunit data with low signal-to-noise ratio [28, 31, 33, 34]. In particular, wavelet-based processing has been demonstrated to be effective in the detection of human sympathetic APs [28], suggesting that a wavelet detection method could be applied to the mouse sympathetic nerve activity.

In general, two wavelet decomposition techniques have been used for spike detection, the discrete wavelet transform (DWT) and the stationary wavelet transform (SWT). These techniques have different limitations. The DWT lacks translation invariance [38-43] while the SWT expands the amount of data by over-representing signals in the wavelet domain (for details see section IIA). However, a formal comparison between the use of the DWT and SWT in spike detection has not yet been presented.

The primary aim of this paper is to develop an automated, wavelet-based method for spike detection in recordings of renal nerve activity specifically for mice. The parameters of this method will be determined using pharmacological interventions and simulated data, but will be applicable to other data sets. The accuracy of several different wavelet decomposition techniques and wavelet threshold algorithms will be compared to one another and to a general automated amplitude discriminator detection method.

Background

A brief description of the wavelet-based signal processing involved in decomposition, de-noising, and detection of action potentials is presented in the sections below. For a more detail review, please see Appendix A.

Signal Decomposition with the Discrete and Stationary Wavelet Transform

Several wavelet techniques have been introduced to project a signal, *f*, onto a set of dyadically-spaced scales on a time-frequency grid [44, 45] and have successfully been applied in the field of neuroscience [32, 46]. The two main discrete wavelet methods are known generally as the discrete wavelet transform (DWT) and the stationary wavelet transform (SWT). Both methods use a *mother wavelet*, Ψ, which can be translated and dilated according to the following equation (Matlab notation):

$$\psi_{j,k}(t) = 2^{j/2}\Psi\left(2^{j}t - k\right) \qquad j,k \in Z \qquad \textbf{(1)}$$

where $\psi_{j,k}$ corresponds to the *wavelet function* at wavelet level *j* and temporal translation *k*. An increase in the wavelet *level* from *j* to *j*+1 results in a more dilated wavelet function, $\psi_{j+1,k}$, with a center frequency and bandwidth that is roughly half that of $\psi_{j,k}$.

The fast DWT algorithm proposed by Mallat (1989) decomposes *f* using a set of *quadrature mirror decomposition filters*, g_0 and h_0, that have respective band-pass and low-pass properties specific to each mother wavelet [45]. Equations (2) and (3) describe the DWT decomposition process. The broad scale, or *approximation*, coefficients a_j^{DWT} are convolved separately with g_0 and h_0 and the result is down-sampled by two. This process splits the a_j^{DWT} frequency information roughly in half, partitioning it into a set of fine scale, or *detail* coefficients d_{j+1}^{DWT} and a coarser set of approximation coefficients a_{j+1}^{DWT}. This procedure can be iteratively continued until the desired level of decomposition, *j=J*, is obtained. Note that the algorithm is initiated by setting $a_0^{DWT} = f$.

$$a_{j+1}^{DWT}(k) = \sum_n h_0(n-2k) a_j^{DWT}(k) \quad \textbf{(2)}$$

$$d_{j+1}^{DWT}(k) = \sum_n g_0(n-2k) a_j^{DWT}(k) \quad \textbf{(3)}$$

The a_j^{DWT} coefficients can be reconstructed from a_{j+1}^{DWT} and d_{j+1}^{DWT} by placing a zero between each consecutive value found in a_{j+1}^{DWT} and d_{j+1}^{DWT} (e.g. up-sampling by two), convolving the results with the respective reconstruction filter, $h_0(-n)$ or $g_0(-n)$, and summing. This process can be iteratively continued until the original signal, *f*, is recovered.

$$a_j^{DWT}(k) = \sum_n h_0(k-2n) a_{j+1}^{DWT}(n) + \sum_n g_0(k-2n) d_{j+1}^{DWT}(n) \quad \textbf{(4)}$$

Down-sampling the DWT coefficients between each level acts to halve their effective sample frequency and halve the effective corner frequencies of the h_0 and g_0 filters for the next level of processing. Therefore, identical filters can be used for each step of the DWT procedure. The DWT has two main advantages: (1) Each step of the DWT requires half as many computations as the previous step, and (2) The total number of DWT coefficients never exceeds *N*, the length of the original signal. A number of AP detection and classification algorithms currently use this decomposition technique [28, 32, 33, 35].

One complication that arises from the level-to-level decimation of the DWT coefficients, however, is a lack of *translation invariance* in the DWT representation of the signal [38-43]. Dyadically down-sampling the approximation and detail coefficients from *f*(*n*) leads to a completely different set of DWT coefficients than down-sampling the coefficients from its shifted version, *f*(*n+1*). Similarly, choosing to retain the odd wavelet coefficients during the dyadic down-sampling will result in a different outcome than retaining the even wavelet coefficients [38-43].

As a result of the shift variability of the DWT, several authors have used translation invariant decomposition techniques, such as the continuous wavelet transform or stationary wavelet transform (SWT), for the purpose of detecting action potentials [31, 34]. In contrast to the DWT, the SWT up-samples the decomposition filters by inserting zeros between every other filter coefficient and, consequently, avoids the translational variance problem caused by decimation [47]. Therefore, the SWT uses a set of *level dependent decomposition filters*, h_j and g_j, which are the h_0 and g_0 filters with 2^j-1 zeros between each discrete filter coefficient. The SWT approximation and detail coefficients can then be computed using Eq. (5) and (6).

$$a_{j+1}^{SWT}(k) = \sum_n h_j(n-k) a_j^{SWT}(k) \quad \textbf{(5)}$$

$$d_{j+1}^{SWT}(k) = \sum_n g_j(n-k) a_j^{SWT}(k) \quad \textbf{(6)}$$

The SWT reconstruction process is similar to that of the DWT, although the reconstruction filters are level dependent an include 2^j-1 zeros between each filter coefficients. This reconstruction process is described in Eq. (7).

$$a_j^{SWT}(k) = \sum_n h_j(k-n) a_{j+1}^{SWT}(n) + \sum_n g_j(k-n) d_{j+1}^{SWT}(n) \quad \textbf{(7)}$$

Inserting zeros between the filter coefficients allows the SWT to analyze every possible shift of the signal while the effective sample rate at each wavelet level remains unchanged. In the frequency domain, up-sampling acts to halve the corner frequency of both the low-pass and high-pass decomposition filters, resulting in the same bandwidth decomposition as is found in the DWT. The result is a redundant, or over-complete, set of detail and approximation coefficients [39]. The drawbacks of the SWT algorithm include its increased computational complexity and the increased number of wavelet coefficients it generates. The general differences between the

DWT and SWT are described in detail elsewhere [38-43]. Specific differences between DWT- and SWT-based spike detection in murine renal nerve recordings will be compared in this paper.

Wavelet-Based Spike Detection

Most wavelet based spike detection algorithms include some modified form of a process known as *wavelet de-noising* [48]. In this process, a nerve signal with additive noise, *f*, is decomposed using either the DWT or SWT and a threshold is applied to each of the detail coefficient levels. All coefficients with an absolute value greater than the threshold are thought to be part of an action potential and those below the threshold are presumably derived from noise. The noise coefficients can be set to zero and a noise-free signal can then be reconstructed and used for AP detection [28].

Several standard methods of deriving thresholds for wavelet de-noising have been suggested [48, 49]. A *single level noise estimation threshold* is typically used in the case of stationary white noise with an unknown variance (σ_W^2). In this case, the standard deviation of the noise related coefficients in all detail coefficient levels is equal to σ_W and is usually estimated using the level 1 detail coefficients (Eq. 8) [48]. The corresponding threshold, T_w, can be applied to all levels of detail coefficients (Eq. 9). In Eq. 8, the standard deviation of the noise is estimated using the median absolute deviation from zero (MAD) of the level 1 detail coefficients divided by the 75th percentile of the standard normal distribution, 0.6745. This method of estimating the standard deviation is typically used in wavelet de-noising because it less sensitive to outliers than the traditional calculation of the sample standard deviation [50]. In Eq. 9, *N* is the number of points in the signal and $\bar{d}_1$ is the sample mean of the level 1 detail coefficients.

$$\sigma_W = \frac{median\left(\left|d_1 - \bar{d}_1\right|\right)}{0.6745} \quad \textbf{(8)}$$

$$T_W = \sigma_W \sqrt{2\log_e(N)} \quad \textbf{(9)}$$

In the case of correlated or colored noise, such as 1/*f* noise, the standard deviation of the noise is level dependent [49, 51]. This type of noise requires a standard *level dependent noise estimation threshold*, T_j^S, which uses a level dependent noise level estimate, σ_j (Eq. 10 and 11) [49].

$$\sigma_j = \frac{median\left(\left|d_j - \bar{d}_j\right|\right)}{0.6745} \quad \textbf{(10)}$$

$$T_j^S = \sigma_j \sqrt{2\log_e(N)} \quad \textbf{(11)}$$

Recently, Kim and Kim (2003) also made the observation that not all of the wavelet levels are necessary for spike detection, and additional levels could actually confound the detection process [31]. We have therefore elected to test both of these wavelet threshold techniques on the mouse RSNA signal using wavelet levels that contain physiologically important information, which will be described in a later section. We will demonstrate that a spike detector which uses the SWT and a single-level noise estimation threshold on select wavelet levels is more robust against changes in spike rate and signal to noise ratio than an unsupervised amplitude discriminator or other wavelet-based methods.

Methods

Animal Experiments

Recordings from the renal nerve of 16 healthy C57BL/6J strain wild-type (10.1±0.1 month; 31±0.4g) were used to determine the optimal parameters for wavelet based spike detection. All protocols were approved by the Vanderbilt University Institutional Animal Care and Use Committee. Mice were anesthetized with 1.5% Isofluoran (in 100% Oxygen). Body temperature was maintained at 36-37°C with an isothermal pad (Braintree Scientific, Inc., Braintree, MA). A bipolar stainless steel wire electrode pair (electrode distance 1-1.5 mm, MedWire Corp, NY,) was hooked onto renal nerve of the left kidney. After adjusting the electrodes to obtain optimal signal quality, the electrodes were secured with silicone adhesive gel (QuickSeal, World Precision Instruments, Sarasota, FL) to ensure a relatively constant distance relationship between the neuron and electrode throughout the recording. The nerve signal was high pass filtered (300Hz) and amplified (gain 100,000) by a differential amplifier (ISO-80, World Precision Instruments, Sarasota, FL). Blood pressure was measured through a catheter in right femoral artery (Micro-Renathane, Braintree Scientific Inc, MA; PE-50, Becton Dickinson, Signapore) connected to a pressure transducer (DTX Plus-4812, Becton-Dickinson, Signapore) and carrier amplifier (13-4615-35, Gould Instruments, Cleveland, OH). Drugs were administered through a venous catheter (Micro-Renathane, MRE-025, Braintree Scientific Inc., MA) with an

infusion pump (CMA/100, CMA, Sweden). Heart rate, blood pressure, and renal sympathetic nerve traffic were recorded for 5 min to determine baseline levels and then during intravenous administration of phenylephrine (30 μg/kg, 40 μg/kg) or sodium nitroprusside (30 μg/kg, 40 μg/kg), bolus injection. 1 min baseline and 2 min after bolus injection was recorded. At the end of experiment, animals were euthanized with an overdose of urethane bolus and the renal nerve signal was recorded postmortem. The signals were recorded using a WINDAQ data acquisition system (DI410, DATAQ, Acron, OH) with 14 Bit resolution at 10,000 Hz sample frequency. The data were processed off-line using customized software written in the Matlab environment (The MathWorks, Inc., Natick, MA).

Determination of the Physiologically Important Frequency Range

The physiological frequency range of the baroreflex-related mouse RSNA was determined as the range of frequencies over which the most dominant changes in a) average power spectral density, and b) wavelet level variance were observed during baroreflex mediated pharmacological suppression and enhancement of the RSNA and after death, when no vital activity is present. These observations were used to determine which frequency range and wavelet levels are important for the detection of spikes in the mouse RSNA.

Changes in power spectral density The Welch Periodogram method [52] was used to compute estimates of the power spectral density (PSD) in the mouse RSNA recorded during periods of baseline, NTP bolus injection (increase of nerve activity), PHE bolus injection (suppression of nerve activity), and postmortem (no vital activity) in 9 mice. Twenty-second signals recorded during each physiologic intervention were divided into 1-second segments that overlapped by 50%. Each segment was detrended, multiplied by a Hamming window, and zero-padded. The power was estimated as the area under the PSD curve and normalized by the baseline variance. Spectral smoothing was then performed using a 20 point moving average. The frequency range over which the maximum changes in PSD occurred was determined to be the physiologically important range.

Changes in wavelet level standard deviation The standard deviation of each level of detail coefficients and in the signal itself was calculated using the median absolute deviation from zero (MAD) divided by 0.6745 (Eq. 10) in all subsequent SWT, DWT, and amplitude discriminator methods. Changes in the standard deviation from baseline to phenylephrine (PHE) and

postmortem periods were also assessed in the signal and each of the detail coefficient levels. All signal coefficient values were normalized to the respective baseline signal variance. The Mann-Whitney or Wilcoxon test with a significance level of 0.05 was used for statistical analysis.

Simulated Signal Construction

Simulated signals were constructed with templates extracted from the baseline periods of 6 RSNA recordings with sufficiently high signal to noise ratios (Fig. 3). The templates were then randomly inserted into neural noise taken from the postmortem recordings with a length of one minute. The interspike intervals were randomly assigned according to a Poisson distribution [53] with a minimum refractory period of 10 msec between spikes. Each simulation was assigned either a low (10 spike/sec), medium (30 spike/sec), or high mean spike rate (60 spike/sec). The signal to noise ratio (SNR) of the simulations was altered from 5 (high signal quality) to 1 (poor signal quality). The SNR was defined as the ratio between the absolute peak amplitude of the action potential and the standard deviation of the noise, as defined elsewhere [28, 34].

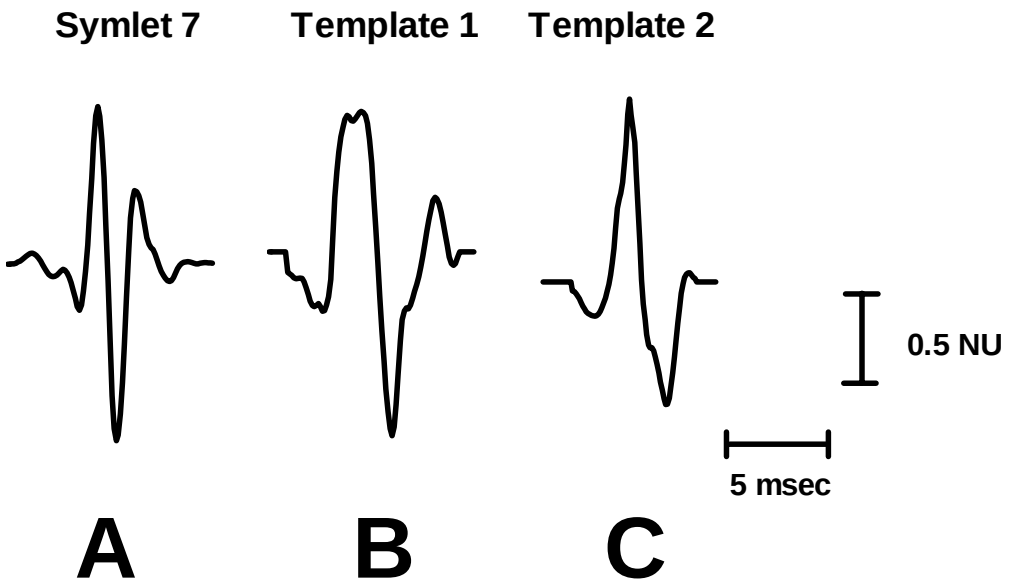

Figure 3. The symlet 7 wavelet (A) and two representative mouse sympathetic action potential templates, (B) and (C), used in the simulations. Amplitudes are displayed in units normalized to the largest absolute value in each waveform (Normalized Units; NU).

The simulated signals were used to test the performance of several wavelet-based algorithms and an unsupervised amplitude discriminator, diagramed in Fig. 4. Four wavelet

algorithms were tested using the following combinations: (1) SWT decomposition with a single level noise estimation threshold (SWTS), (2) SWT decomposition with a level dependent noise estimation threshold (SWTD), (3) DWT decomposition with a single level noise estimation threshold (DWTS), and (4) DWT decomposition with a level dependent noise estimation threshold (DWTD). The decomposition methods and thresholds were discussed in detail in Section IIA and IIB, respectively. Each of the wavelet techniques used the same mother wavelet, symlet 7 (Fig. 3), due to its morphological similarities to an average sympathetic spike and because it has been shown to impose less distortion on sympathetic spikes during de-noising than other commonly used wavelets, such as Daubechies 4 [28]. Each simulated signal was decomposed into 5 levels of detail coefficients and 1 level of approximation coefficients. Five was chosen as the maximum decomposition level because levels higher than 5 were found to contain primarily noise. Only wavelet levels that were deemed to have physiological significance to the mouse RSNA spikes (determined later in Section IVA) were used in the thresholding process, and all other wavelet coefficients were set to zero. After the signal is decomposed and thresholded, the de-noised signal was reconstructed and the action potentials were detected using a simple peak detection scheme that locates maxima above 99% of the signal energy, as described previously [28]. The unsupervised amplitude discriminator detected all absolute values greater than three times the standard deviation of the signal as discussed elsewhere [26]. Both the amplitude discriminator and the wavelet detection used a window length of 6 msec, which was observed to be the maximum duration of a mouse RSNA spike.

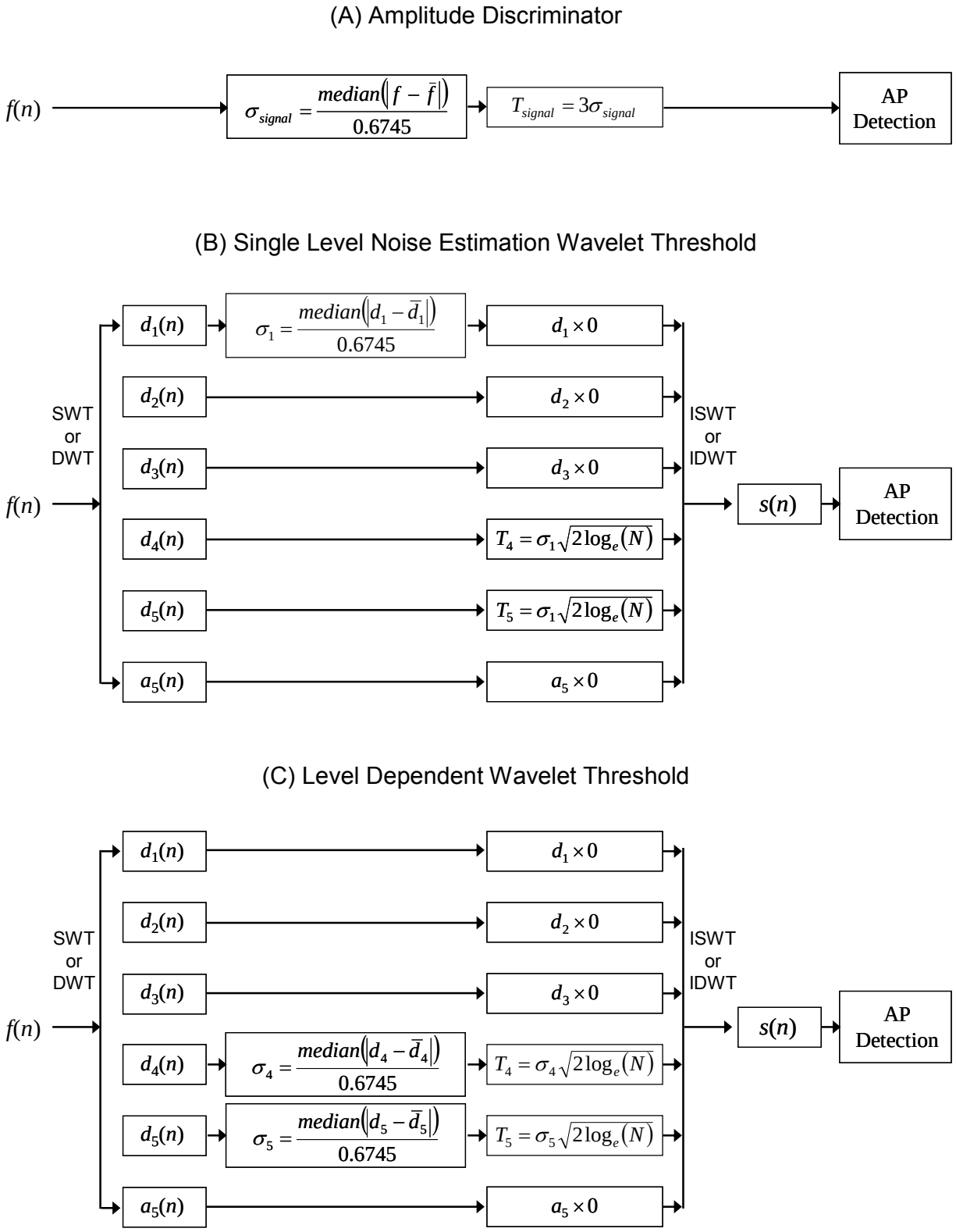

Figure 4. Block diagram of all detection methods. **(A)** Unsupervised amplitude discriminator. **(B)** Single level noise estimation wavelet threshold used with either the stationary (SWT) or discrete wavelet transform (DWT). **(C)** Level dependent noise estimation wavelet threshold used with the SWT or DWT.

The performances of the five methods were quantified using the percent of correctly detected APs (PCD) and the percent of false alarms (PFA).

$$PCD = \frac{N_{CD}}{N_{AP}} \times 100 \quad \textbf{(12)}$$

$$PFA = \frac{N_{FA}}{N_{CD}} \times 100 \quad \textbf{(13)}$$

N_{CD} is the number of correctly detected APs, N_{AP} is the number of APs inserted into the simulation, and N_{FA} is the number of false alarms.

Verification of Threshold Using Physiological Data

A physiologic verification of the threshold was performed using pharmacologic data in mice. PHE increases blood pressure and induces a baroreflex mediated suppression of RSNA, as demonstrated in Figure 1. Rather than using the maximum absolute voltage level during baroreflex mediated decrease of sympathetic nerve activity (Fig 2A), we determined which thresholds would yield the maximum change in the detected spike rate from a baseline period to the period following a PHE bolus injection by systematically varying the threshold level and recording the corresponding maximum delta spike rate. Figure 2B demonstrates that the "optimal" amplitude discriminator threshold determined by the maximum response is neither the maximum voltage level during PHE depression nor the postmortem noise level but an intermediate value (Fig 2B).

We applied the "maximum response optimization" approach to determine the optimal threshold value for each wavelet level that comprised the RSNA frequency range. In detail, renal nerve recordings that contained 60 seconds of baseline activity followed by approximately 60 seconds of reduced nerve activity after PHE bolus injection were decomposed using the stationary wavelet transform. A systematic search for the optimal threshold value was then performed on each detail coefficient level found to hold physiologically important information. For all combinations of threshold values (which varied from 0 to $5\sigma_j$ for each wavelet level of interest) the detail coefficients with an absolute value above the threshold were unmodified. All other coefficients were set to zero. The signal was then reconstructed and spikes were detected using the same procedure described in Section IIIC. The spike-rate was then computed using a

one-second sliding window. The criterion used to determine the optimal combination of thresholds was defined as the maximum difference between the median spike rate during baseline and the minimum spike rate after PHE bolus injection. The optimal threshold values were then compared to those used in the single level noise estimation thresholding scheme. Data from all 16 mice were used during this verification.

Results

Determination of Physiologically Important Frequency Range

Changes in power spectral density The average normalized power spectral density (PSD) of the renal nerve activity during periods of baseline, NTP bolus injection, PHE bolus injection, and postmortem is depicted in Figure 5A. Power in the range of 100 Hz to 1000 Hz was dominant during all interventions in the living animal but was significantly abolished postmortem. The power in this range was increased after NTP bolus injection and decreased after PHE bolus injection. Complete suppression of renal nerve activity was not always achieved during the highest dose of PHE, but this residual activity is abolished in the euthanized animal. This suggests the presence of other renal nerve activity independent of the baroreflex (as presented in Fig. 2). Above 1000 Hz, the average power remains relatively consistent during the baseline, postmortem, PHE and NTP recordings, indicating that these levels are unaffected by the RSNA and contain mostly noise.

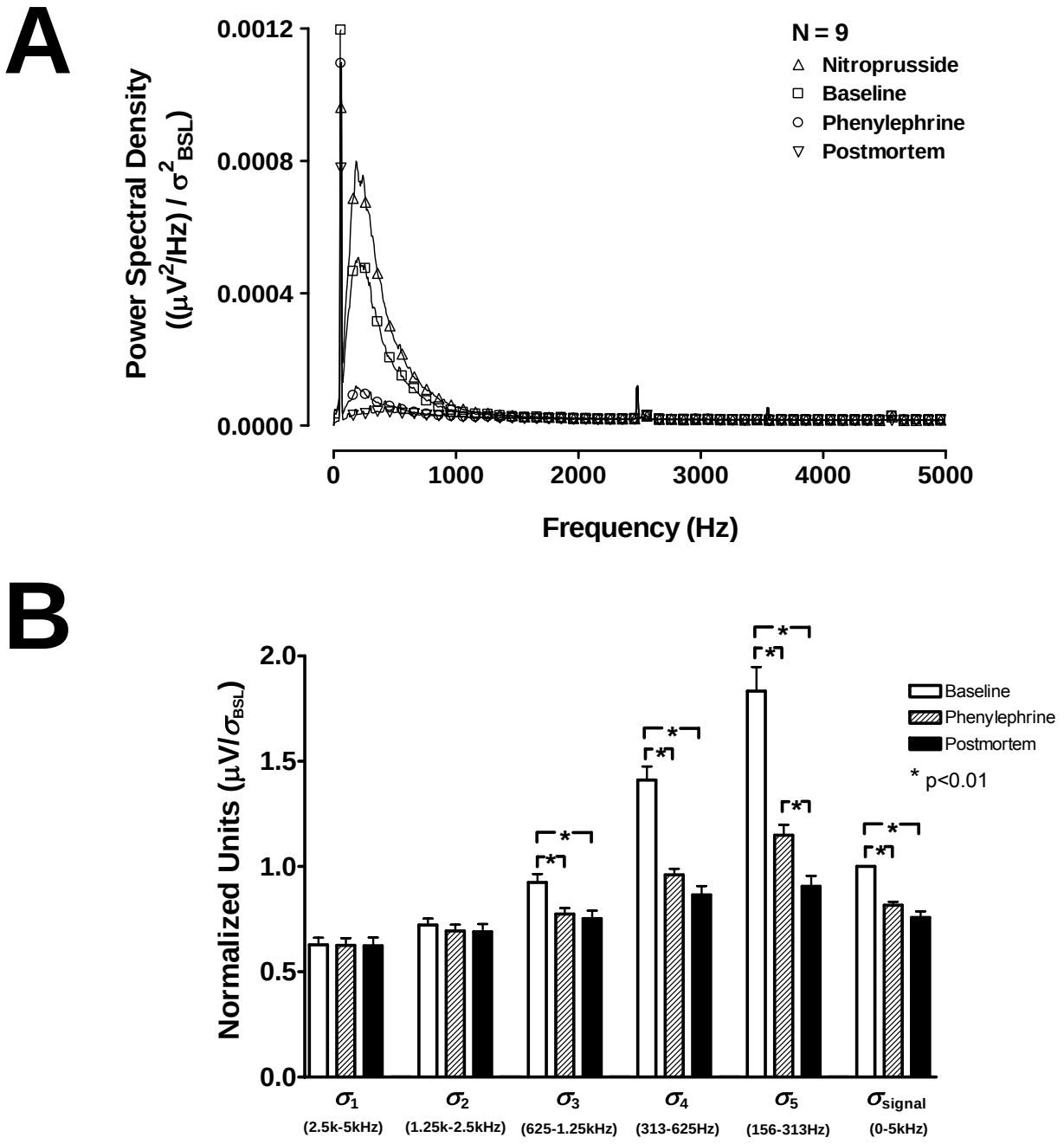

Figure 5. (A) Average normalized PSD of renal nerve recordings during nitroprusside (Δ), baseline (□), phenylephrine (O), and postmortem (∇) periods. **(B)** Normalized standard deviations of the detail coefficient levels and the signal during baseline (white), after phenylephrine bolus injection (hatched), and postmortem (black). The changes in the standard deviation of detail levels 1 and 2 (σ_1 and σ_2) are minimal, but changes in the standard deviations of the level 3, 4, and 5 detail coefficients (σ_3 - σ_5) and the signal (σ_{signal}) are significant during phenylephrine and postmortem.

Changes in wavelet level standard deviation To demonstrate the relationship between the power spectral density and the variance of the wavelet coefficients and determine the wavelet

levels with physiologically important information, the change in the detail coefficient standard deviations (σ_1 – σ_5 for detail levels 1 – 5) from baseline to post-PHE bolus injection and postmortem periods were compared (Fig 5B). The level 3, 4, and 5 SWT detail coefficients have approximate respective frequency ranges of 625 – 1250 Hz, 313 – 625 Hz, and 156 – 313 Hz for data collected at 10,000 samples/sec. The power in these frequency ranges demonstrated the most pronounced changes during the pharmacological interventions and after death (Fig. 5A). Consequently, the standard deviation of these detail levels (σ_3-σ_5) were found to drop significantly during PHE and postmortem ($p<0.01$, Fig. 5B). The level 1 and 2 detail coefficients have approximate frequency ranges of 2500 – 5000 Hz and 1250-2500 Hz, respectively. The power in these frequency ranges did not change significantly during any of the interventions (Fig. 5A), nor did σ_1 and σ_2 (Fig. 5B). The standard deviation of the signal (σ_{signal}) also undergoes a significant decline during these periods ($p<0.01$).

The detail coefficients can now be separated into levels that contain the RSNA signal plus noise and levels which contain noise only. Since both the power in the frequency ranges of the level 4 and 5 detail coefficients and the standard deviation of the coefficients themselves demonstrate significant changes during pharmacological tests and after death, they are assumed to contain the majority of the information associated with sympathetic spikes. Thus, only the level 4 and 5 detail coefficients will be subject to thresholding in each of the wavelet methods mentioned in Section IIIC during the simulations. All wavelet coefficients that either fall below the threshold or are found in other levels, including the level 5 approximation coefficients, will be considered noise-related and set to zero. The level 3 detail coefficients were not included in the threshold operation because the changes in spectral power and standard deviation in this level during pharmacological tests and postmortem were not as pronounced and could result in a significant number of false alarms in signals with very low signal to noise ratios. The standard deviation of the level 1 detail coefficients, σ_1, will be used in the single level noise estimation threshold (as shown in Eq. 8 and 9) because it was shown to remain constant throughout the pharmacological interventions and postmortem.

Simulation Results

The detection performance of the unsupervised amplitude discriminator, SWTS, SWTD, DWTS, and DWTD is described in Fig. 6. The percent of correctly detected spikes (PCD, top)

and percent of false alarms (PFA, bottom) are displayed for low (left), medium (middle), and high mean spike rates at various signal to noise ratios (Fig. 6).

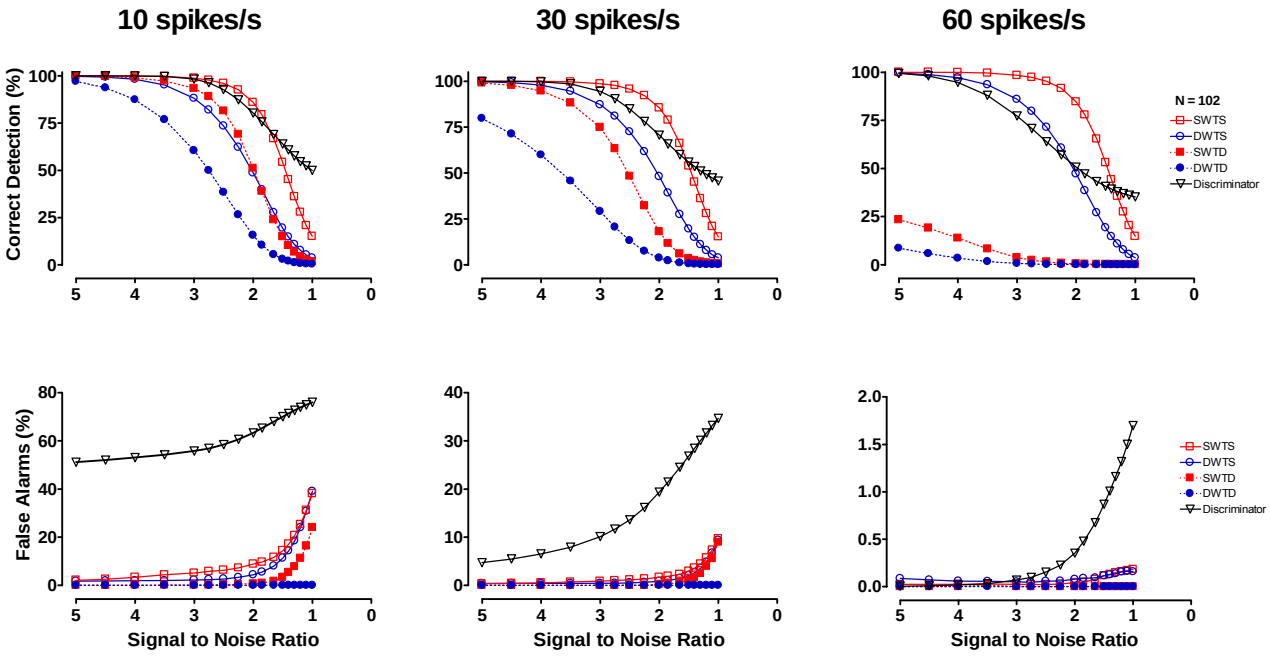

Figure 6. Mean results for simulations with varied noise levels and mean spike rates. The simulations tested the performance of an unsupervised amplitude discriminator, SWT decomposition with thresholds based on single level (SWTS) and level dependent (SWTD) noise estimation, and DWT decomposition with thresholds based on single level (DWTS) and level dependent (DWTD) noise estimation. Each point on each curve represents the mean result of 102 simulations.

The detection performance of the amplitude discriminator method was found to be highly dependent on the mean spike rate (Fig. 6). It demonstrated a high percent of correct detections for signals with low and medium spike rates, but also detected the highest percent of false alarms during most SNRs and mean spike rate situations in these simulated signals.

The detection performance of the SWT and DWT methods with level dependent noise estimation (SWTD and DWTD) also demonstrated a large dependence on the mean spike rate (Fig. 6). As spike rate increased, the percent of correct detections of the methods with level dependent noise estimation began to drop off at higher values of SNR. The SWT and DWT methods with single level noise estimation thresholds (SWTS and DWTS) show much more consistent patterns in their percent of correct detections during changes in mean spike rate. The single level noise estimation methods also generally had a higher percent of false alarms than

their level dependent counter parts, but the percent of false alarms for all wavelet methods was below 15% for all SNRs greater than 1.5 during all mean spike rate scenarios.

The SWT methods correctly identified a higher percentage of the inserted action potentials than the DWT methods with the same threshold criteria for all SNRs and mean spike rates (e.g. SWTS>DWTS and SWTD>DWTD). The percent of false alarms was similar for SWT and DWT methods with the same threshold criteria. The SWTS method (stationary wavelet transform with a single level noise estimation criteria) seemed to exhibit the most consistent performance on the simulated murine sympathetic nerve recordings. The percent of correct detections for this spike detection method remained above 75% and the percent of false alarms remained below 10% for all spike rates and all SNRs above 1.8. Although the discriminator had a higher percent of correct detections than the SWTS at very low signal to noise ratios (SNR<1.6), it also detected a significantly higher percent of false alarms during these SNRs as well.

Threshold Verification Using Physiological Data

Renal nerve recordings that contained 60 seconds of baseline activity followed by approximately 60 seconds of reduced activity after PHE bolus injection were used to determine the optimal threshold value in each wavelet level that comprised the RSNA frequency range. The threshold in each of the wavelet levels of interest, levels 4 (T_4) and 5 (T_5), was systematically varied until the threshold combination which produced the maximum difference between the median detected spike rate during baseline and the minimum detected spike rate after administration of the PHE bolus was determined (T_4^{opt} and T_5^{opt}). Figure 7A demonstrates a representative example of the results of this search normalized by σ_1 the standard deviation of the level 1 detail coefficients. From Eq. 9 we can see that $T_W/\sigma_W = \sqrt{2\log_e(N)}$. For the signals used in this section, $N = 120\,\text{sec} \times 10{,}000\text{Hz}$ and $\sqrt{2\log_e(N)} \approx 5.29$. In Fig. 7A, the maximum delta spike rate (T_4^{opt}/σ_1 and T_5^{opt}/σ_1, the dark red region) is near the single level noise estimation threshold, i.e. $T_4/\sigma_1 = T_5/\sigma_1 \approx 5.29$ (the white circle).

The threshold values T_4^{opt} and T_5^{opt} were determined for 16 mice and normalized using the single level noise normalization, i.e. dividing by σ_1 (Fig. 7B). The average normalized values for both level 4 and 5 are near the standard value of 5.29.

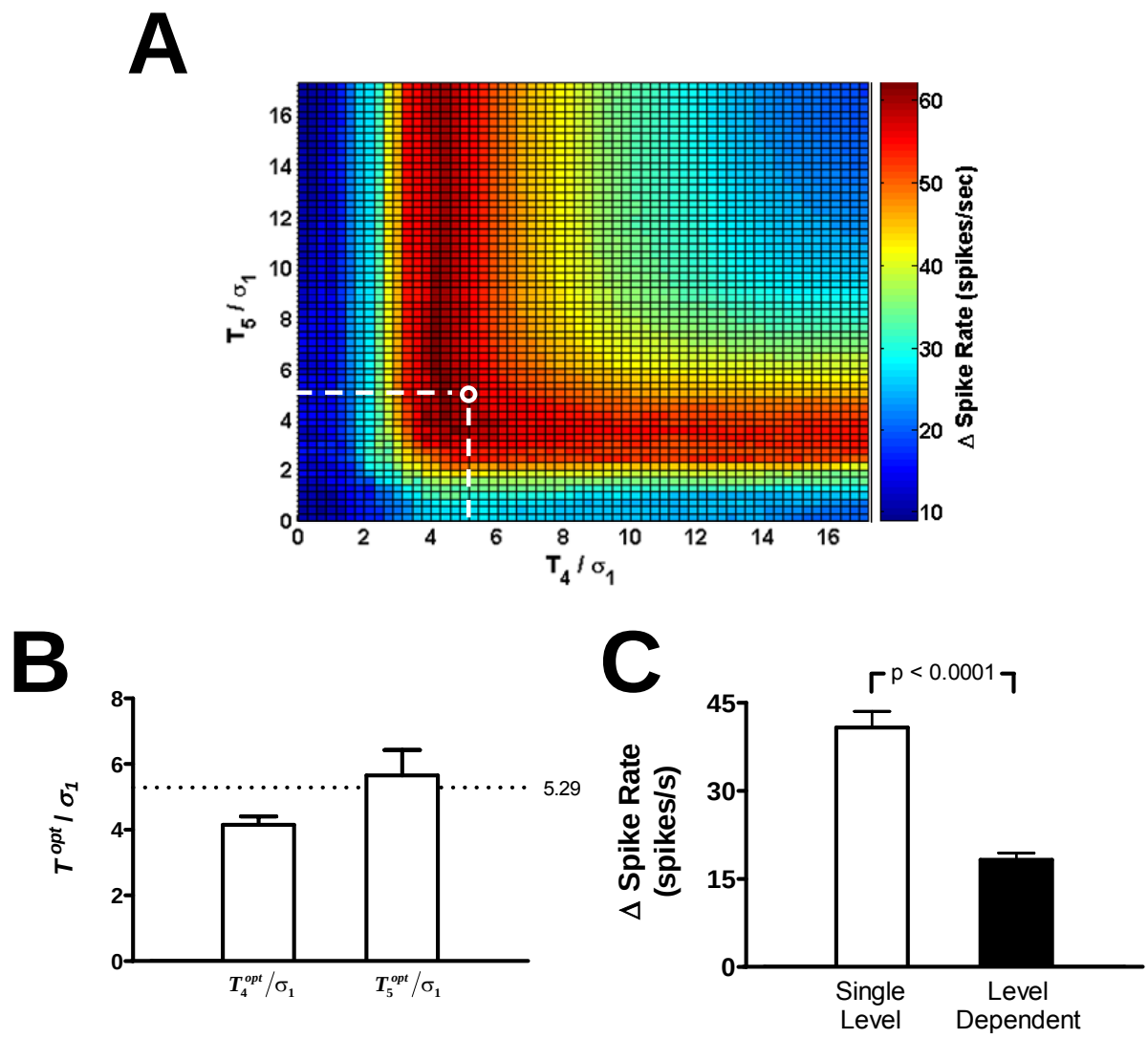

Figure 7. (A) Representative example of the search for the optimal threshold combination for the level 4 and 5 detail coefficients (T_4 and T_5) normalized by the standard deviation of the level 1 detail coefficients. **(B)** The mean values for the normalized T_4^{opt} and T_5^{opt} for 16 mice. In both cases, the maximum response thresholds come close to the standard value calculated from Eq. 8 (5.29; white circle in (A) and broken line in (B)). **(C)** Mean changes in the detected spike rate from baseline to after PHE bolus injection (Δ spike rate) using two different SWT threshold algorithms. The single level noise estimation threshold (white) detected a significantly greater response to the PHE bolus than the level dependent noise estimation threshold (black). Error bars indicate SE.

The SWT methods using the single level and level dependent noise estimation thresholds were both used to detect the change in the detected spike rate from baseline to after PHE bolus injection in the same 16 mouse renal nerve recordings (Fig. 7C). The single level noise estimation threshold detected a significantly greater response to the PHE bolus than the level dependent noise estimation threshold.

Discussion

The aim of this paper was to devise an automated spike detection system specifically for mouse renal sympathetic nerve activity which could be used as an alternative to the currently used approaches of RSNA integration and hardware amplitude discriminators. Although we have only presented data for this specific neural signal, this type of optimization process and some of the results may be applicable to other types of neural data. We have shown that wavelet methods had a more robust performance than amplitude discriminators when presented with simulated mouse sympathetic nerve signals with different spike rates and signal to noise ratios. Additionally, the DWT methods, which lack translation invariance, were outperformed by translation invariant SWT methods with the same threshold criteria. The single level noise estimation threshold criteria was also shown to be less dependent on changes in mean spike rate in simulated mouse renal nerve recordings than level dependent noise estimation threshold algorithms. The choice of a single level noise estimate was also close to the maximum response thresholds determined using the physiological PHE bolus data.

Johnstone and Silverman (1997) demonstrated that the SWT has better de-noising performance than the DWT for data contaminated with neurophysiological noise [49]. They have also suggested that the limitations of the DWT are more apparent for signals with low signal-to-noise ratios (SNR) and sharp discontinuities [49]. Murine RSNA action potentials posses these characteristics and, consequently, a spike detection procedure based on the DWT is less effective than one which uses the SWT. The simulated scenario in Fig. 8 demonstrates how the translation variability found in the DWT reduces the likelihood of an RSNA action potentials being detected. Each peak in the RSNA action potential occupies a very short period, approximately 1 msec, or 10 points of a signal sampled at 10,000 Hz. After 2 levels of decimation, less than 2 or 3 peak points remain. In the simulated RSNA signal depicted in Figure 8, down-sampling by eliminating odd and even coefficients significantly alters the DWT representation and, as a

result, the detection performance of the DWT algorithm. The SWT, however, is able to detect both APs. This would account for the lower percentage of correctly detected action potentials in the DWT based detection algorithms in our simulations and may play a role in any DWT based detection or discrimination of neural data.

One key feature common to both wavelet and amplitude discriminator based detection methods is a threshold rule based on some estimate of the noise level. A robust threshold rule should accurately reflect the noise level but should be unaffected by changes in spike rate or spike amplitude. In the case of the murine RNSA, the spike rate can be non-stationary, particularly when different pharmacological agents are introduced. Both the automated amplitude discriminator and the wavelet methods with a level dependent noise threshold, however, were significantly affected by changes in spike rate. For example, the standard deviation of the level 4 and 5 detail coefficients change significantly during the PHE and postmortem recordings, and these changes are presumed to be primarily caused by changes in the mean spike rate during these states (Fig. 5B). We have also observed that the standard deviation of simulated signals (σ_{signal}) and the standard deviation of their detail levels in the frequency range of the RSNA spikes (σ_4 and σ_5) increase with spike rate. For instance, simulated signals with identical noise and mean spike rates of 0, 35, and 75 spikes/s resulted in σ_{signal} of 0.25, 0.295, and 0.365 normalized unit (NU) and σ_5 of 0.25, 0.43 and 1.12 NU. However, the standard deviation of the level 1 detail coefficients, σ_1, remained almost constant (0.25, 0.253, 0.256 NU) for all spike rates. Therefore, a threshold selection rule that relates the noise level of the level 1, or “noise-only”, detail coefficients to the threshold for the level 4 and 5, or “signal concentrated”, detail coefficients, such as the single level noise threshold rule, may be more appropriate detection in nerve signals with highly variable mean spike rates. The maximum response thresholds determined with the PHE bolus data also suggested that the use of the single level noise estimation threshold was more suitable than the use of a level dependent noise estimation threshold (Fig. 7).

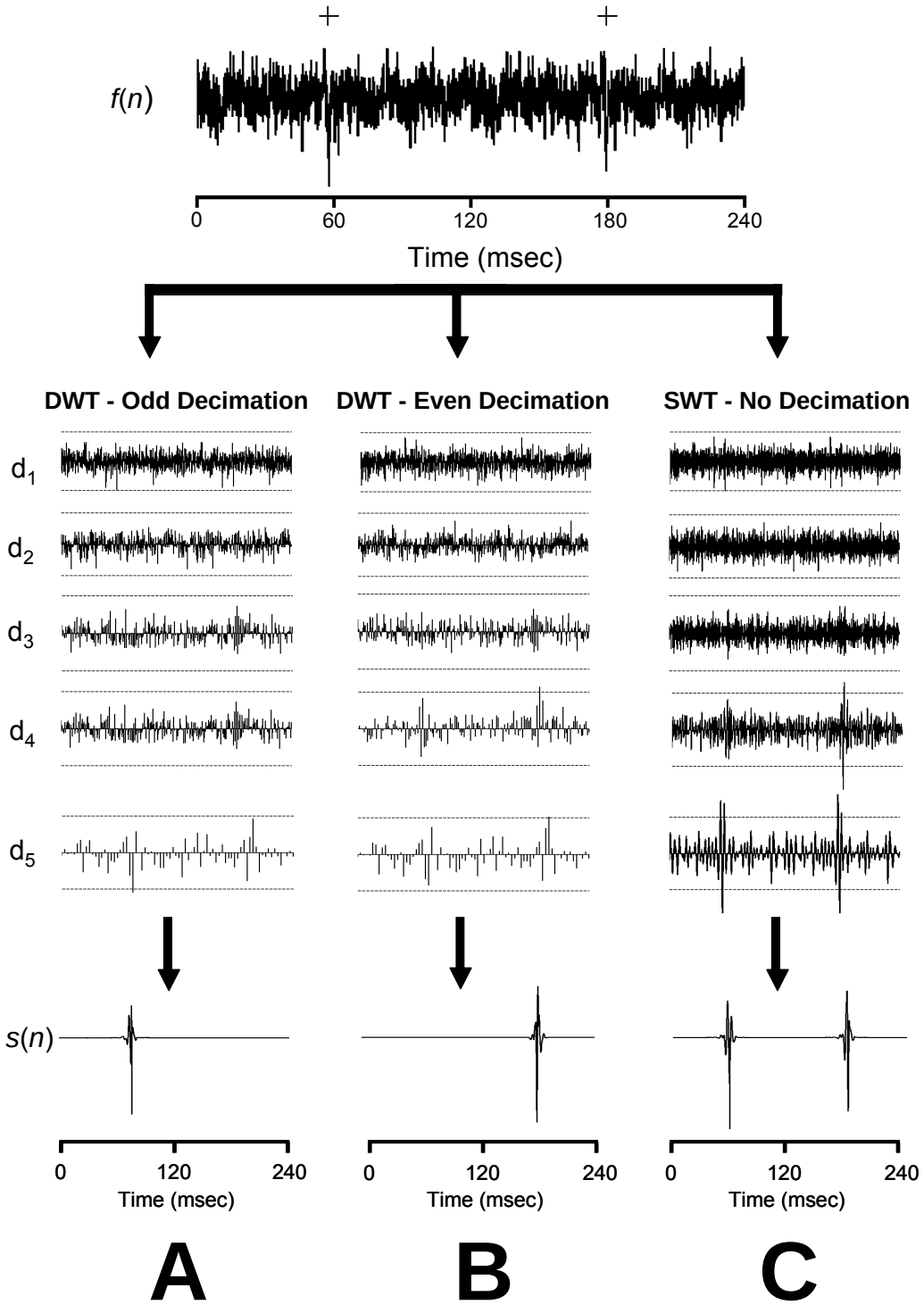

Figure 8. Detection performance using the DWT and SWT de-noising. The top row contains a simulated signal, $f(n)$, containing 2 APs (+). The middle rows contain detail coefficient for levels 1-5 ($d_1 - d_5$) obtained using either the DWT with odd down-sampling **(A)**, the DWT with even down-sampling **(B)**, or the SWT **(C)**. Broken lines in $d_1 - d_5$ are standard thresholds (Eq 8 and 9) and the bottom row is the reconstructed noise-free spike train, $s(n)$. Decimating the odd coefficients eliminates the detail coefficients that represent the second AP, while even decimation abolishes the first AP. Both APs are detected using the SWT method because it does not down-sample the detail coefficients.

In light of these findings, we advocate the use of an SWT algorithm with a single level noise estimation threshold for the detection of action potentials in the murine RSNA. This method was shown to be the most robust when presented with variable spike rates and signal to noise ratios. Several previous publications have used the wavelet transform for the specific purpose of spike detection in similar multiunit neural data [28, 31, 33, 34, 54]. Kim, *et al.* (2003) suggested a novel AP detection method for nerve recordings with low SNR which combined selected scales of the SWT using point-wise multiplication and smoothing with a Bartlett window [31] and Olkkonen, *et al.* (2006) demonstrated a Hilbert assisted DWT to improve SNR in nerve signals [54]. However, neither author discusses a method to objectively automate a threshold selection process. Both Nakatani, *et al* [33] and Diedrich, *et al* [28] demonstrated automated methods for colored, normally distributed neural noise. Each implemented a level dependent threshold by extrapolating the parameters of the noise distribution by fitting a Gaussian to the central quantiles of the detail coefficient amplitudes at each wavelet level. This method assumes that the contribution of the AP waveforms to the central quantiles of the distribution is negligible, an assumption that is valid for lower spike rates but fails for higher spike rates. Both authors do not test their technique under conditions of variable spike rates.

Nenadic, *et al* [34] uses the continuous wavelet transform (CWT) and a level dependent threshold to make an initial separation of signal and noise for the purpose of parameter estimation prior to hypothesis based spike detection. This technique is validated using simulations with different spike rates and SNR. Our results demonstrate that the level dependent threshold drastically over estimates wavelet noise levels at high spike rates, resulting in significant missed detections (Fig. 6). The discrepancy of these results may lie in the type of neural data used. The former study involved recordings from CNS neurons with a relatively high conduction velocity, whereas our recordings were derived from unmyelinated peripheral neurons with a slower conducting speed (Fig 3). The longer duration of the sympathetic APs yields more high amplitude points per unit time for each spike, which has a dramatic affect on the level dependent noise estimate, particularly at high firing rates. Although the noise in both the signal and simulations used here are colored, the single level noise estimation threshold was useful because it relates the noise level in a wavelet band that is unrelated to the physiological signal information to the wavelet levels that contain signal plus noise and avoids overestimating the threshold in these levels at high firing rates.

Applications

Spike detection using the single-level noise estimation threshold coupled with SWT decomposition was applied to RSNA recordings from several transgenic mouse populations, including norepinephrine transporter (NET) deficient and regulator G-protein-2 (RGS-2) deficient mice. Using the wavelet-based spike detection, we were able to confirm that a baseline drop in sympathetic activity mimicking that observed during pharmacological NET blockade in humans also occurred in the NET deficient mice. Similarly, the regulator of G-protein signaling 2 (RGS2) is known to play a role in the maintenance of vascular tone and sympathetic regulation. Mice deficient in this enzyme were also shown to have significantly lower than normal sympathetic spike rates using wavelet spike detection. Further details of these analyses and results can be found in Appendix C.

Limitations

One significant limitation to using the SWT as opposed to the amplitude discriminator or the DWT is the increase in computational complexity. While the amplitude discriminator requires no transformation, the DWT requires $O(N)$ operations and the SWT requires $O(N \log(N))$ operations [40], which may pose a problem when applying such a method to more complex problems, such as nerve signals recorded from a multielectrode array. However, the SWT requires less computational complexity than the CWT, an $O(N^2)$ process which has been used in previous spike detection methods [34]. A second limitation is the assumption that all of the recorded APs will have a shape similar to the symlet 7 wavelet or one of its dilations at higher wavelet levels. Although the waveforms identified in our recordings were relatively similar to those depicted in Fig. 3, different neuron-electrode geometries have been observed to result in very different AP morphologies [27] and this should be considered when implementing such a method. In this study we focused on the detection of APs and chose not to examine the sorting of waveforms, which is typically handled following detection. As a consequence, the amount of AP overlap in the simulations was limited. Significant AP overlap may cause multiple, overlapped APs to be detected as 1 AP. In this case an additional waveform classifier would be required to separate the overlapped waveforms. This has been proposed previously [28].

Extension of this method to other types of neural data and signals with transient spikes would require a similar form of optimization process and simulated data to objectively assess detection quality. The optimization process described here could be difficult without the use of either pharmacological or postmortem recordings. However, physiological interventions may be used in order to characterize the

noise process contaminating other neural data. For instance, in the case of the human muscle sympathetic nerve activity (MSNA), a noise component may be obtained during Phase IV of the Valsalva maneuver which is characterized by an increase in blood pressure beyond baseline levels and, consequently, a dramatic reduction in sympathetic nerve activity in healthy subjects [55]. The wavelet levels used in this optimization may also differ for other signals. The APs found in the MSNA, for example, have a similar shape to murine RSNA spikes, but have a much shorter duration [28]. As a result, the power of the MSNA spikes was found to be concentrated between 700 and 2000 Hz [28], and would require thresholding of the level 2 and 3 wavelet coefficients for 10kHz recordings.

Conclusions

An automated spike detection method for mouse sympathetic nerve activity would eliminate the need for establishing a subjective manual threshold or using integrated nerve activity. Furthermore, unsupervised spike detection allows for the possibility of AP classification and subsequent single-unit analysis of sympathetic nerve activity, which has been shown to hold useful information [56-60]. In conclusion, spike detection using the SWT is a potentially useful tool in the study of autonomic dysfunction in mice and may have implications for the study of various cardiovascular disorders.

Acknowledgements

This work was supported in part by National Institutes of Health grants M01 RR00095, 1R41-AG19576-01A1, and 1PO1 HL56693.

References

[1] S. Gudbjornsdottir, P. Lonnroth, Y. B. Sverrisdottir, B. G. Wallin, and M. Elam, "Sympathetic nerve activity and insulin in obese normotensive and hypertensive men," *Hypertension*, vol. 27, pp. 276-80, 1996.

[2] A. L. Mark, "The sympathetic nervous system in hypertension: a potential long-term regulator of arterial pressure," *J Hypertens Suppl*, vol. 14, pp. S159-65, 1996.

[3] B. G. Wallin and G. Sundlof, "A quantitative study of muscle nerve sympathetic activity in resting normotensive and hypertensive subjects," *Hypertension*, vol. 1, pp. 67-77, 1979.

[4] B. Andersson, M. Elam, B. G. Wallin, P. Bjorntorp, and O. K. Andersson, "Effect of energy-restricted diet on sympathetic muscle nerve activity in obese women," *Hypertension*, vol. 18, pp. 783-9, 1991.

[5] I. H. Klein, G. Ligtenberg, J. Neumann, P. L. Oey, H. A. Koomans, and P. J. Blankestijn, "Sympathetic nerve activity is inappropriately increased in chronic renal disease," *J Am Soc Nephrol*, vol. 14, pp. 3239-44, 2003.

[6] R. J. Huggett, E. M. Scott, S. G. Gilbey, J. B. Stoker, A. F. Mackintosh, and D. A. Mary, "Impact of type 2 diabetes mellitus on sympathetic neural mechanisms in hypertension," *Circulation*, vol. 108, pp. 3097-101, 2003.

[7] R. J. Huggett, E. M. Scott, S. G. Gilbey, J. Bannister, A. F. Mackintosh, and D. A. Mary, "Disparity of autonomic control in type 2 diabetes mellitus," *Diabetologia*, vol. 48, pp. 172-9, 2005.

[8] R. Furlan, G. Jacob, M. Snell, D. Robertson, A. Porta, P. Harris, and R. Mosqueda-Garcia, "Chronic orthostatic intolerance: a disorder with discordant cardiac and vascular sympathetic control," *Circulation*, vol. 98, pp. 2154-9, 1998.

[9] P. van de Borne, N. Montano, M. Pagani, R. Oren, and V. K. Somers, "Absence of low-frequency variability of sympathetic nerve activity in severe heart failure," *Circulation*, vol. 95, pp. 1449-54, 1997.

[10] M. Bader, "Mouse knockout models of hypertension," *Methods Mol Med*, vol. 108, pp. 17-32, 2004.

[11] V. Gross, J. Tank, M. Obst, R. Plehm, K. J. Blumer, A. Diedrich, J. Jordan, and F. C. Luft, "Autonomic nervous system and blood pressure regulation in RGS2-deficient mice," *Am J Physiol Regul Integr Comp Physiol*, vol. 288, pp. R1134-42, 2005.

[12] B. J. Janssen and J. F. Smits, "Autonomic control of blood pressure in mice: basic physiology and effects of genetic modification," *Am J Physiol Regul Integr Comp Physiol*, vol. 282, pp. R1545-64, 2002.

[13] E. Popova, M. Bader, and A. Krivokharchenko, "Production of transgenic models in hypertension," *Methods Mol Med*, vol. 108, pp. 33-50, 2004.

[14] P. C. Usera, S. Vincent, and D. Robertson, "Human phenotypes and animal knockout models of genetic autonomic disorders," *J Biomed Sci*, vol. 11, pp. 4-10, 2004.

[15] N. R. Keller, A. Diedrich, M. Appalsamy, S. Tuntrakool, S. Lonce, C. Finney, M. G. Caron, and D. Robertson, "Norepinephrine transporter-deficient mice exhibit excessive tachycardia and elevated blood pressure with wakefulness and activity," *Circulation*, vol. 110, pp. 1191-6, 2004.

[16] G. Y. Ling, W. H. Cao, M. Onodera, K. H. Ju, H. Kurihara, Y. Kurihara, Y. Yazaki, M. Kumada, Y. Fukuda, and T. Kuwaki, "Renal sympathetic nerve activity in mice:

comparison between mice and rats and between normal and endothelin-1 deficient mice," *Brain Res*, vol. 808, pp. 238-49, 1998.

[17] X. Ma, M. W. Chapleau, C. A. Whiteis, F. M. Abboud, and K. Bielefeldt, "Angiotensin selectively activates a subpopulation of postganglionic sympathetic neurons in mice," *Circ Res*, vol. 88, pp. 787-93, 2001.

[18] X. Ma, F. M. Abboud, and M. W. Chapleau, "A novel effect of angiotensin on renal sympathetic nerve activity in mice," *J Hypertens*, vol. 19, pp. 609-18, 2001.

[19] W. Zhang, J. L. Li, M. Hosaka, R. Janz, J. M. Shelton, G. M. Albright, J. A. Richardson, T. C. Sudhof, and R. G. Victor, "Cyclosporine A-induced hypertension involves synapsin in renal sensory nerve endings," *Proc Natl Acad Sci U S A*, vol. 97, pp. 9765-70, 2000.

[20] M. Bak and E. Schmidt, "Improved Time-Amplitude Window Discriminator," *IEEE Transactions on Biomedical Engineering*, vol. 24, pp. 486-489, 1977.

[21] W. G. Haynes, D. A. Morgan, S. A. Walsh, A. L. Mark, and W. I. Sivitz, "Receptor-mediated regional sympathetic nerve activation by leptin," *J Clin Invest*, vol. 100, pp. 270-8, 1997.

[22] E. N. Brown, R. E. Kass, and P. P. Mitra, "Multiple neural spike train data analysis: state-of-the-art and future challenges," *Nat Neurosci*, vol. 7, pp. 456-61, 2004.

[23] M. S. Lewicki, "A review of methods for spike sorting: the detection and classification of neural action potentials," *Network-Computation in Neural Systems*, vol. 9, pp. R53-R78, 1998.

[24] I. Bankman, K. Johnson, and W. Schneider, "Optimal detection, classification, and superposition resolution in neural wave-form recordings," *IEEE Transactions on Biomedical Engineering*, vol. 40, pp. 836-841, 1993.

[25] S. Gozani and J. Miller, "Optimal discrimination and classification of neuronal action-potential wave-forms from multiunit, multichannel recordings using software-based linear filters," *IEEE Transactions on Biomedical Engineering*, vol. 41, pp. 358-372, 1994.

[26] C. Pouzat, O. Mazor, and G. Laurent, "Using noise signature to optimize spike-sorting and to assess neuronal classification quality," *Journal of Neuroscience Methods*, vol. 122, pp. 43-57, 2002.

[27] R. Segev, J. Goodhouse, J. Puchalla, and M. Berry, "Recording spikes from a large fraction of the ganglion cells in a retinal patch," *NATURE NEUROSCIENCE*, vol. 7, pp. 1155-1162, 2004.

[28] A. Diedrich, W. Charoensuk, R. J. Brychta, A. C. Ertl, and R. Shiavi, "Analysis of raw microneurographic recordings based on wavelet de-noising technique and classification

algorithm: Wavelet analysis in microneurography," *IEEE Transactions on Biomedical Engineering*, vol. 50, pp. 41-50, 2003.

[29] E. Hulata, R. Segev, Y. Shapira, M. Benveniste, and E. Ben-Jacob, "Detection and sorting of neural spikes using wavelet packets," *Physical Review Letters*, vol. 85, pp. 4637-4640, 2000.

[30] E. Hulata, R. Segev, and E. Ben-Jacob, "A method for spike sorting and detection based on wavelet packets and Shannon's mutual information," *Journal of Neuroscience Methods*, vol. 117, pp. 1-12, 2002.

[31] K. Kim and S. Kim, "A wavelet-based method for action potential detection from extracellular neural signal recording with low signal-to-noise ratio," *IEEE Transactions on Biomedical Engineering*, vol. 50, pp. 999-1011, 2003.

[32] J. Letelier and P. Weber, "Spike sorting based on discrete wavelet transform coefficients," *Journal of Neuroscience Methods*, vol. 101, pp. 93-106, 2000.

[33] H. Nakatani, T. Watanabe, and N. Hoshimiya, "Detection of nerve action potentials under low signal-to-noise ratio condition," *IEEE Transactions on Biomedical Engineering*, vol. 48, pp. 845-849, 2001.

[34] Z. Nenadic and J. Burdick, "Spike detection using the continuous wavelet transform," *IEEE Transactions on Biomedical Engineering*, vol. 52, pp. 74-87, 2005.

[35] K. Oweiss and D. Anderson, "Noise reduction in multichannel neural recordings using a new array wavelet denoising algorithm," *Neurocomputing*, vol. 38, pp. 1687-1693, 2001.

[36] K. Oweiss and D. Anderson, "Spike sorting: a novel shift and amplitude invariant technique," *Neurocomputing*, vol. 44, pp. 1133-1139, 2002.

[37] G. Zouridakis and D. C. Tam, "Identification of reliable spike templates in multi-unit extracellular recordings using fuzzy clustering," *Computer Methods and Programs in Biomedicine*, vol. 61, pp. 91-98, 2000.

[38] R. R. Coifman and D. L. Donoho, "Translation-Invariant De-Noising," *Lecture Notes on Statistics*, vol. 103, pp. 125-150, 1995.

[39] M. Lang, H. Guo, J. Odegard, C. Burrus, and R. Wells, "Noise reduction using an undecimated discrete wavelet transform," *IEEE Signal Processing Letters*, vol. 3, pp. 10-12, 1996.

[40] J. Liang and T. W. Parks, "A translation-invariant wavelet representation algorithm with applications," *IEEE Transactions on Signal Processing*, vol. 44, pp. 225-232, 1996.

[41] J. Pesquet, H. Krim, and H. Carfantan, "Time-invariant orthonormal wavelet representations," *IEEE Transactions on Signal Processing*, vol. 44, pp. 1964-1970, 1996.

[42] B. Silverman, "Wavelets in statistics: beyond the standard assumptions," *Philosophical Transactions of the Royal Society of London Series A-Mathematical Physical and Engineering Sciences*, vol. 357, pp. 2459-2473, 1999.

[43] E. P. Simoncelli, W. T. Freeman, E. H. Adelson, and D. J. Heeger, "Shiftable Multiscale Transforms," *IEEE Transactions on Information Theory*, vol. 38, pp. 587-607, 1992.

[44] A. Cohen and J. Kovacevic, "Wavelets: The mathematical background," *Proceedings of the IEEE*, vol. 84, pp. 514-522, 1996.

[45] S. G. Mallat, "A Theory for Multiresolution Signal Decomposition - the Wavelet Representation," *IEEE Transactions on Pattern Analysis and Machine Intelligence*, vol. 11, pp. 674-693, 1989.

[46] V. Samar, A. Bopardikar, R. Rao, and K. Swartz, "Wavelet analysis of neuroelectric waveforms: A conceptual tutorial," *Brain and Language*, vol. 66, pp. 7-60, 1999.

[47] S. Mallat, "Zero-Crossings of a Wavelet Transform," *IEEE Transactions on Information Theory*, vol. 37, pp. 1019-1033, 1991.

[48] D. L. Donoho, "De-Noising by Soft-Thresholding," *IEEE Transactions on Information Theory*, vol. 41, pp. 613-627, 1995.

[49] I. Johnstone and B. Silverman, "Wavelet threshold estimators for data with correlated noise," *Journal of the Royal Statistical Society Series B - Methodological*, vol. 59, pp. 319-351, 1997.

[50] F. Hampel, *Robust Statistics: the Approach Based on Influence Functions.* New York: John Wiley & Sons, 1986.

[51] G. Wornell, "Wavelet-Based Representations for the 1/f Family of Fractal Processes," *Proceedings of the IEEE*, vol. 81, pp. 1428-1450, 1993.

[52] P. Welch, "Use of fast fourier transform for estimation of power spectra - A method based on time averaging over short modified periodograms," *IEEE Transactions on Audio and Electroacoustics*, vol. AU15, pp. 70-73, 1967.

[53] G. Strangman, "Detecting synchronous cell assemblies with limited data and overlapping assemblies," *Neural Comput*, vol. 9, pp. 51-76, 1997.

[54] H. Olkkonen, P. Pesola, J. Olkkonen, and H. Zhou, "Hilbert transform assisted complex wavelet transform for neuroelectric signal analysis," *J Neurosci Methods*, vol. 151, pp. 106-13, 2006.

[55] R. Mosqueda-Garcia, "Evaluation of Autonomic Failure," in *Disorders of the Autonomic Nervous System*, vol. 5, *The Autonomic Nervous System*, D. Robertson and I. Biaggioni, Eds., 1 ed. Luxembourg: Harwood Academic Publishers, 1995, pp. 25-59.

[56] J. P. Greenwood, J. B. Stoker, and D. A. Mary, "Single-unit sympathetic discharge: quantitative assessment in human hypertensive disease," *Circulation*, vol. 100, pp. 1305-10, 1999.

[57] V. G. Macefield and B. G. Wallin, "The discharge behaviour of single sympathetic neurones supplying human sweat glands," *Journal of the Autonomic Nervous System*, vol. 61, pp. 277-286, 1996.

[58] V. G. Macefield and B. G. Wallin, "Firing properties of single vasoconstrictor neurones in human subjects with high levels of muscle sympathetic activity," *Journal of Physiology-London*, vol. 516, pp. 293-301, 1999.

[59] V. G. Macefield and B. G. Wallin, "Respiratory and cardiac modulation of single sympathetic vasoconstrictor and sudomotor neurones to human skin," *Journal of Physiology-London*, vol. 516, pp. 303-314, 1999.

[60] V. G. Macefield, M. Elam, and B. G. Wallin, "Firing properties of single postganglionic sympathetic neurones recorded in awake human subjects," *Autonomic Neuroscience-Basic & Clinical*, vol. 95, pp. 146-159, 2002.

CHAPTER V

A SIMPLIFIED TWO COMPONENT MODEL OF BLOOD PRESSURE FLUCTUATION

Abstract

We propose a simple moving average (MA) model which uses the low frequency (LF) component of the peroneal muscle sympathetic nerve spike rate and the high frequency (HF) component of respiration to describe the low frequency neuro-vascular fluctuations and the high frequency mechanical oscillations in systolic blood pressure (SBP), respectively. This method was validated on data from eight healthy subjects (age 23-47, 6 males) during a graded tilt (15° increments each 5 min until 60°). The LF_{SBP} had a strong baroreflex mediated feedback correlation with $LF_{Spike\ Rate}$ ($r=-0.69\pm0.05$) but also a strong feed-forward relation to $LF_{Spike\ Rate}$ ($r=0.58\pm0.03$ with LF_{SBP} delay $\tau=5.625\pm0.15$s). $HF_{Spike\ Rate}$ and HF_{SBP} were not significantly correlated. Conversely, the HF components of respiration and SBP are highly correlated ($r=-0.79\pm0.04$) while their LF components have a significantly lower correlation ($r=0.45\pm0.08$). The mean correlation coefficients between the measured LF_{SBP} and the LF_{SBP} predicted from the model was $r=0.74\pm0.03$ in the supine position, and this value did not change significantly during tilt. The mean correlation between the measured HF_{SBP} and the predicted HF_{SBP} was $r=0.89\pm0.02$ while supine. The R^2 values for the regression analysis of the predicted and measured LF and HF powers indicate that 78 and 91 percent of the variability in power can be explained by the linear relationship $LF_{Spike\ Rate}$ to LF_{SBP}, and HF_{Resp} to $HF_{SBP.}$ We report a simple two component model using neural sympathetic and mechanical respiratory inputs which can explain the majority of BP fluctuation at rest and during orthostatic stress in healthy subjects.

Introduction

Various rhythmic oscillations found in the human blood pressure (BP) have been proposed to reflect the action of different physiological mechanisms on BP regulation. For instance, it has been suggested that very low frequency trends (VLF, period >25 sec, frequency <0.04 Hz) in BP represent the influence of hormonal and thermo-regulation and that high frequency fluctuations (HF, 0.15-0.4 Hz) mark the effect of respiration on BP. A more hotly debated issue is the idea that low frequency (LF, 0.04-0.14 Hz) BP oscillations occurring with a

10-second periodicity, generally referred to as the Traube-Hering-Mayer waves, reflect sympathetically-mediated vasomotor BP modulation. It has been proposed that the origin of these waves is a resonance phenomenon of the baroreflex pathway [1], and the LF power has been used as a marker of sympathetic activity [2-4], although this practice still remains controversial [5;6].

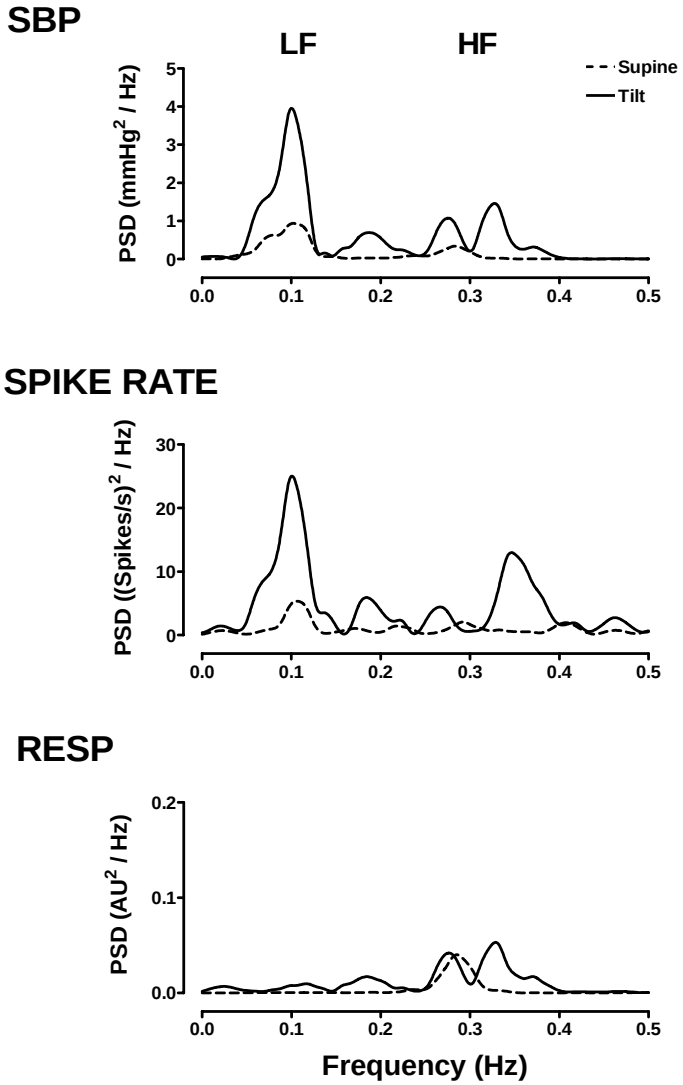

Figure 1. Spectral characteristic of systolic blood pressure (SBP, upper panel), sympathetic spike rate, and respiration (RESP) during resting supine (broken line) and 60 deg head up tilt position (black solid line) in a representative subject.

Several lines of indirect evidence have been used to associate the oscillations in BP with oscillations in these other physiological rhythms. For example, physiological maneuvers have

identified changes in the oscillatory patterns of the sympathetic nerve activity and respiration which correspond to those seen in the BP during sympathetic activation [7]. Figure 1 demonstrates that, during head-up tilt: *a)* LF oscillations are evident in the nerve activity and BP; *b)* the HF oscillations are expressed in each of the three signals -- respiration, BP, and nerve activity; and *c)* relative changes in the LF of spike rate and the HF of respiration are also reflected in the BP.

Similarly, pharmacological interventions and the study of autonomic pathologies have also provided indirect support to the idea that the sympathetic activity and respiration contribute to the oscillations in BP. The LF_{BP} oscillations are attenuated during ganglionic blockade in healthy subjects [8-10] and are absent in pure autonomic failure patients with peripheral sympathetic nerve lesions [8;11], suggesting a sympathetic origin for this rhythm. On the other hand, HF_{BP} fluctuations have been unaffected by ganglionic blockade [8-10] and is still present after thoracic sympathectomy in transplant patients [12]. Additionally, the neuro-vascular interface has been suggested to possess low-pass characteristics which effectively filter out the HF components of the sympathetic activity [1;13-15]. These findings indicate that the HF_{BP} rhythm is not neurally mediated, but instead largely the result of the mechanical interaction between the BP and the respiration or cardiac output.

Although much indirect evidence exists, a mathematical model may provide a more direct description of the relationship between the BP oscillations and fluctuations found in other cardiovascular parameters. A number of models have been developed to help explain the fluctuations in human BP using heart rate, blood pressure and respiration [1;16-18]. One limitation of these models is that they do not include sympathetic activity as a direct input parameter. Modeling of BP fluctuations from sympathetic activity has been successfully applied in animals [19-21]. However, a model developed by Myers, et al. (2001) for human BP fluctuations using integrated sympathetic activity as an input parameter yielded less accurate results [5]. But this model was primarily concerned with explaining the LF component of BP; utilized integrated burst areas with arbitrary units to quantify sympathetic activity, rather than the spike rates typically found in animal models; and involved euglycemic clamping to enhance sympathetic activation, a procedure which induces vasodilation through increased insulin release and may alter the neuro-vascular coupling [22].

We propose a different mathematical model which combines subbands of the sympathetic spike rate and respiration to explain the LF and HF oscillations in human blood pressure. A technique to detect action potentials in raw human sympathetic nerve recordings has been recently introduced and can be used to form a spike rate density series to quantify sympathetic activity [23;24]. Using the spike rate density along with measured respiratory patterns, we will examine the accuracy of a two component linear model which attempts to describe the low frequency neuro-vascular interaction and the high frequency mechanical effects of respiration on the fluctuations in human BP.

Methods

Subjects and Clinical Conditions

Eight healthy subjects (6 males and 2 females, age 23 to 47) were recruited from the Vanderbilt University General Clinical Research Center volunteer database. All subjects underwent extensive physical examination and did not have any signs of cardiovascular disease or history of syncope prior to the study. The subjects abstained from all drugs, including caffeine and nicotine, for at least 72 hours prior to testing. Their body mass index was 26±1.7 kg/m2, resting HR was 61±2 bpm, and BP was 111±2 / 65±2 mm Hg.

Protocol

The subjects were secured to a tilt table with straps. Subjects were instructed to remain relaxed and quiet throughout all studies and were monitored for any signs of presyncope during all tests [25]. After 15 minutes of supine rest the subjects were tilted by 15° increments every 5 minutes until an angle of 60° was reached. All studies were conducted at Vanderbilt University General Clinical Research Center and all procedures were approved by the local institutional review board.

Instrumentation

The following variables were measured: electrocardiogram (ECG), blood pressure, respiration, and muscle sympathetic nerve activity (MSNA). The electrocardiogram (ECG) of lead II was recorded with a Gould ECG/Biotach amplifier (Gould Electronics, Cleveland, OH,

USA). The continuous finger blood pressure (BP) waveform was measured by photoplethysmographic-based volume clamp method [26] with a finger cuff on the middle finger of the non-dominant hand (Finapres, Ohmeda, Englewood, CO, USA) and verified using brachial BP obtained by automated auscultometric device (Dinamap blood pressure monitor, model 1846SX, Critikon, Tampa, FL) on the contralateral arm. The hand with the Finapres sensor was fixed at heart level. Respiration was measured by a pneumobelt (Pneumotrace II; UFI, Morro Bay, CA).

Microneurography MSNA was recorded from the peroneal nerve [27]. Recording was done randomly in either of the legs. A unipolar tungsten electrode with uninsulated tip diameter 1 to 5 μm and shaft diameter 200 μm (Frederick Haer and Co, Bowdoinham, MA, USA) was inserted into the muscle nerve fascicles of the peroneal nerve at the fibular head for multi-unit recordings. Raw nerve activity was amplified with a total gain of 100 000, band pass filtered from 0.7 to 2 kHz (662C-3 Nerve Traffic Analysis System, University of Iowa, Iowa City, USA). Satisfactory recordings of muscle sympathetic nerve activity were defined by (1) heart pulse synchronicity; (2) facilitation during Valsalva straining and suppression during the hypertensive overshoot after release; (3) increases in response to breath-holding; and (4) no change during tactile or auditory stimulation [28].

Data Preprocessing

Data were acquired at 5000 Hz, 14 bit resolution using the Windaq data acquisition system (DI-720, DATAQ Instruments, Akron OH) and analyzed offline with custom software written in the PV Wave (Visual Numerics Inc., Houston, TX) and MATLAB (Mathworks; Natick, MA) environments. QRS detection was performed using a modified Pan-Tompkins algorithm [29]. Systolic and diastolic values in the continuous blood pressure recordings were automatically identified as the maxima and minima for each cardiac cycle. All detections were visually verified.

Action potential spikes were detected in raw MSNA recordings using a modified form of a technique described elsewhere [24;30]. The MSNA was decomposed into 4 bands of wavelet detail coefficients using a stationary wavelet transform (SWT) with the Symlet 7 wavelet. Regions dominated by normally distributed noise in each band were identified as those which had a kurtosis less than 4. A kurtosis value of 3 indicates an ideal Gaussian distribution and

signal episodes with spike activity have usually higher kurtosis values. All coefficients with an absolute value less than 4 times the standard deviation of the identified noise regions were set to zero and the de-noised signal was reconstructed using the inverse SWT. Action potential spikes were then automatically detected from the de-noised signal using a peak detector with a 3 msec time window.

We analyzed diastolic (DBP), systolic (SBP), and mean blood pressure (MBP) series, continuous respiration, and detected MSNA spikes over 200 second periods after a stabilization of 100 sec for supine, 15, 30, 45, and 60 degrees of head-up tilt. Diastolic, systolic, and mean blood pressure variability series were formed by linearly interpolating the detected values onto regular intervals of 200 msec (5 Hz). The detected MSNA spikes were used to form a spike rate series using a previously described method [23;31]. Briefly, a binary spike train was formed by inserting delta functions into a 5 kHz sampled series at the detected spike times. The spike train was converted to a spike rate series by convolving with a Gaussian filter with a 3 Hz cutoff frequency [23]. The spike rate signal was decimated by iteratively convolving with an anti-aliasing Gaussian filter with a corner frequency of 0.4 times the current sample rate and down-sampling by two until a sample rate of 4.88 Hz was reached. The resultant series was linearly interpolated at 5 Hz. The respiration signal was also decimated to 5 Hz after application of an eighth-order, anti-aliasing, Chebyshev Type I lowpass filter with a corner frequency of 2 Hz. Each series was detrended by removing the mean offset plus the very low frequency (VLF) components (0-0.04 Hz) by filtering with a high-pass, finite impulse response filter with a corner frequency of 0.04 Hz prior to any analysis or comparisons.

Low frequency (LF) and high frequency (HF) time series were formed using a set of band pass filters based on the Meyer wavelet, a modulated sinusoid with compact support [32], with approximate respective pass bands of 0.04 - 0.15 Hz (LF) and 0.15 - 0.5 Hz (HF). Details of wavelet filtering can be found elsewhere [33].

Data Analysis

To study the relationship between each blood pressure series (SBP, DBP, and MBP) and the MSNA spike rate and respiration, time-based cross-correlations were performed. In general, during the cross-correlation procedure one time series, *x*, was time-delayed between τ_{start} and τ_{end} seconds while the other series, *y*, remained stationary. After each delay, a correlation was

performed between the two series. First, the low frequency components of each series were compared, using the $LF_{Spike\ Rate}$ and LF_{RESP} as *x* and the LF_{SBP}, LF_{DBP}, and LF_{MBP} as *y*. The procedure was then repeated using the HF components of each series. For the $HF_{Spike\ Rate}$ and the respiratory series, the maximum absolute correlation was recorded for time delays between τ_{start} = 10 sec and τ_{end} = 0 sec, meaning that our only interest was the relationship in which changes respiration and $HF_{Spike\ Rate}$ preceded changes in the BP. For the $LF_{Spike\ Rate}$ and the low frequency components of the blood pressure series, two relationships were investigated. The minimum negative cross-correlation value was termed the baroreflex-feedback relationship and studied within the period of τ_{start} = 2 sec and τ_{end} = -2 sec. In this case, a negative time delay (e.g. τ = -2 sec) would indicate that the spike rate is advanced in time. The positive maximum cross-correlation value was termed the feed-forward relationship and studied within the period of τ_{start} = 10 and τ_{end} = 0 sec.

Prior to modeling the BP fluctuations, the $LF_{Spike\ Rate}$ was delayed in time by an amount equal to the feed-forward delay and the HF_{RESP} was delayed by an amount equal to the time-shift which produced the maximum absolute correlation to the HF_{BP}.

Data Predictive Modeling

A two component, moving average (MA), linear model was used to predict the fluctuations in blood pressure using the low frequency oscillations in sympathetic nerve activity and the high frequency fluctuations in the respiration. First, the low frequency model (LF model) predicts the current value of the low frequency BP series (LF_{BP}) using moving average model in which the output is a linear combination of *P* previous values of the low frequency components of the spike rate series ($LF_{Spike\ Rate}$).

$$LF_{BP}(n) = \sum_{p=0}^{P-1} a(p) LF_{Spike\ Rate}(n-p) \qquad (9)$$

Similarly, the high frequency model (HF model) predicts the current value of the high frequency BP series (HF_{BP}) using a linear combination of *K* previous values from the high frequency respiration series (HF_{RESP}).

$$HF_{BP}(n) = \sum_{k=0}^{K-1} b(k) HF_{RESP}(n-k) \qquad (2)$$

The proposed total model, as shown in Figure 2, is a summation of the outputs of the LF and HF models and predicts the current value of the detrended blood pressure series.

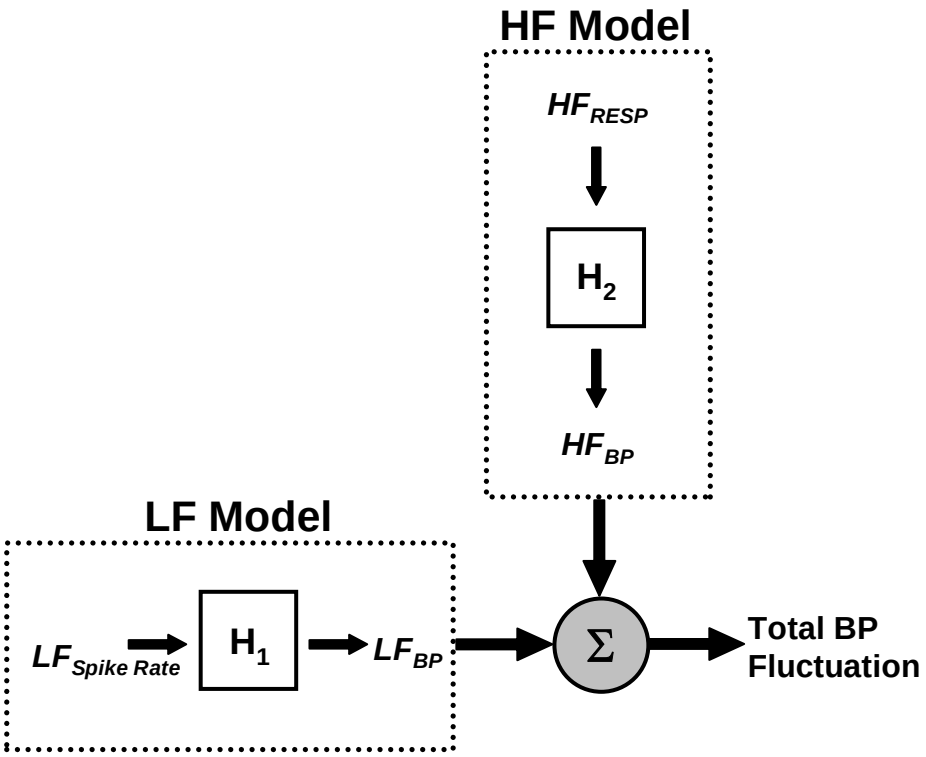

Figure 2. Block diagram of the components used to predict the fluctuations in the blood pressure (BP). H_1 is a moving average (MA) model to convert the low frequency (LF) spike rate to the LF-SBP and H_2 is the MA model to convert high frequency (HF) respiration (RESP) to HF-BP. The sum of the LF and HF model predict the total BP fluctuation.

The coefficients for each model were computed using the Steiglitz-McBride method [34] and the optimal values for *P* or *K* (model order) was selected as the value which minimized the final prediction error (FPE) [35] with a maximum order of 25 coefficients, or 5 seconds of past data. The model is based on equidistant data because of the continuous nature of the spike rate and respiratory input signal.

$$FPE(P) = \sigma_E^2 \frac{N+P+1}{N-P-1} \tag{3}$$

Where σ_E^2 is the mean squared error between the model and true output, *N* is the total number of points in the signal, and *P* is the current model order. This modeling technique was applied to components of the signals recorded during a baseline period and over increasing orthostatic load during graded head-up tilt. The values predicted by each model were compared to the

corresponding measured values using point-by-point linear regression analysis and by comparing their power spectral density (PSD) in specific frequency ranges.

Power Spectral Density

The Welch Periodogram method [36] will be used to compare the estimated power spectral density (PSD) in the measured BP series to that of the BP series predicted by the total model. The two hundred-second signals, which were recorded and predicted during each angle of tilt, were divided into 60-second segments that overlapped by 50%. Each segment was detrended, multiplied by a Hamming window, and zero-padded to the next power of two. The power in the low (0.04-0.15 Hz) and high (0.15-0.5 Hz) frequency ranges was estimated as the area under the PSD curve.

Statistics

Regression analysis was performed using a linear least squares fit and the Pearson correlation coefficient (r) or the coefficient of determination (R^2) was used to quantify the goodness of fit. The Wilcoxon signed ranks test was used to test for significant differences in the correlation between the components of three different BP series (SBP, DBP, and MBP) and the components of the sympathetic spike rate and respiration. This test was also used to determine if significant differences existed between measured and model-predicted BP values at different degrees of head up tilt. A probability value of 0.05 was defined as the significance level. Unless otherwise noted, all data are reported as means ± SEM.

Results

Correlations between Oscillatory Components

Figure 3 displays a representative temporal relationship between SBP and MSNA spike rate. The sample-to-sample correlation between the unfiltered SBP and spike rate does not reveal an inherent linear relationship between the two series (r=-0.37; Fig. 3A, bottom panel). However, their LF components appear to have two distinct relationships. Shifting the $LF_{Spike\ Rate}$ series back in time by 0.4 sec results in a strong negative correlation to the LF_{SBP} (r=-0.87; Fig. 3B, bottom panel), which indicates the strength of the baroreflex mediated feedback (high spike rates

occurring during low blood pressures). Shifting the $LF_{Spike\ Rate}$ series back in time by 5.2 sec yields a strong positive correlation to the LF_{SBP}, (r=0.70; Fig. 3C, bottom panel). This suggests the existence of a feed-forward relationship between the two series, meaning that an increase in $LF_{Spike\ Rate}$ will produce a corresponding increase in the LF_{BP}.

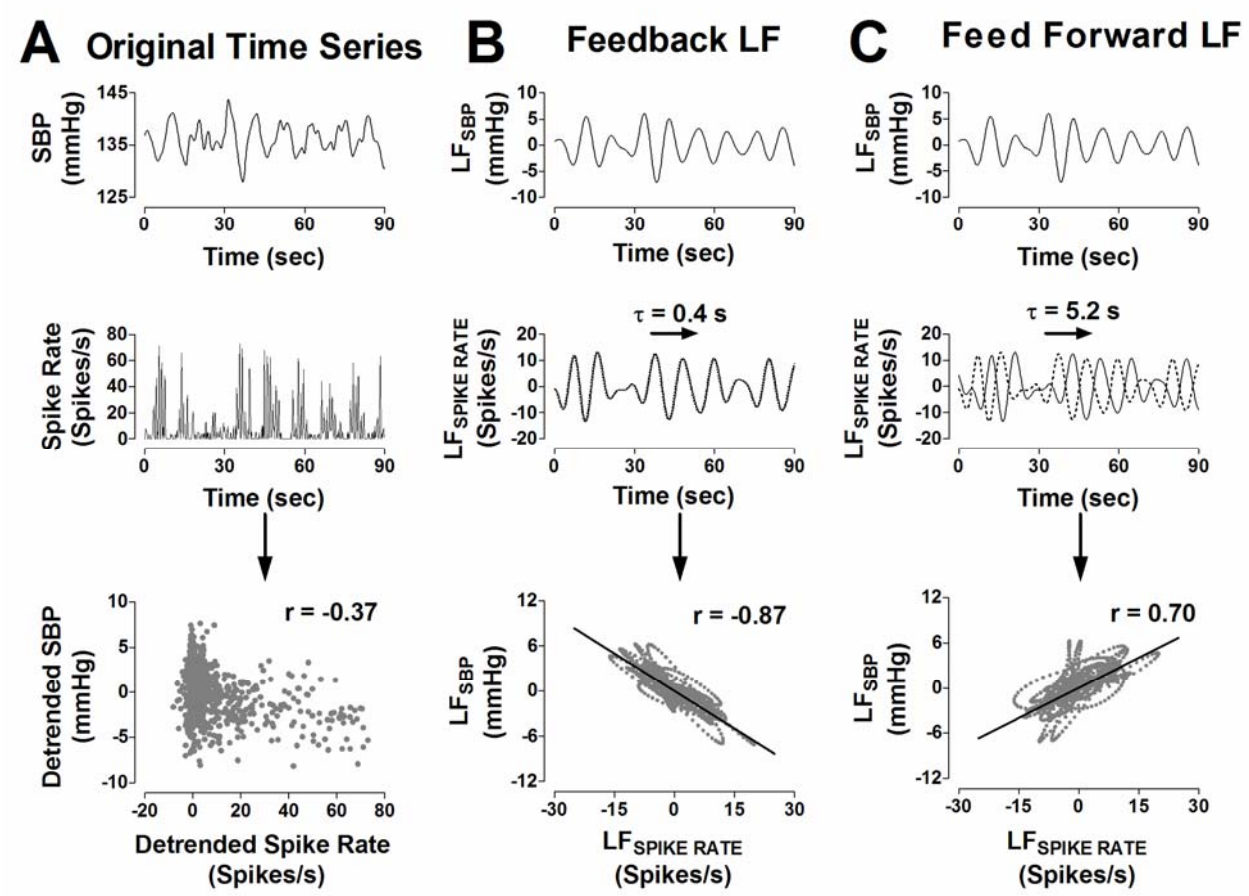

Figure 3. (A) Correlation between systolic blood pressure (SBP) and spike rate time series. **(B)** Baroreflex mediated feedback relationship between the low frequency (LF) components of SBP and spike rate. **(C)** Feed forward relationship between the LF components of the SBP and spike rate. The unshifted LF-spike rate time series are shown with broken lines.

A similar relationship can be found between the SBP, the respiration, and their high frequency components (Fig. 4). The unfiltered time series have a lower correlation coefficient (r=-0.41; Fig. 4A, bottom panel), but after the application of an HF-band wavelet filter, the sample-to-sample correlation improves significantly (r=-0.86; Fig. 4B, bottom panel).

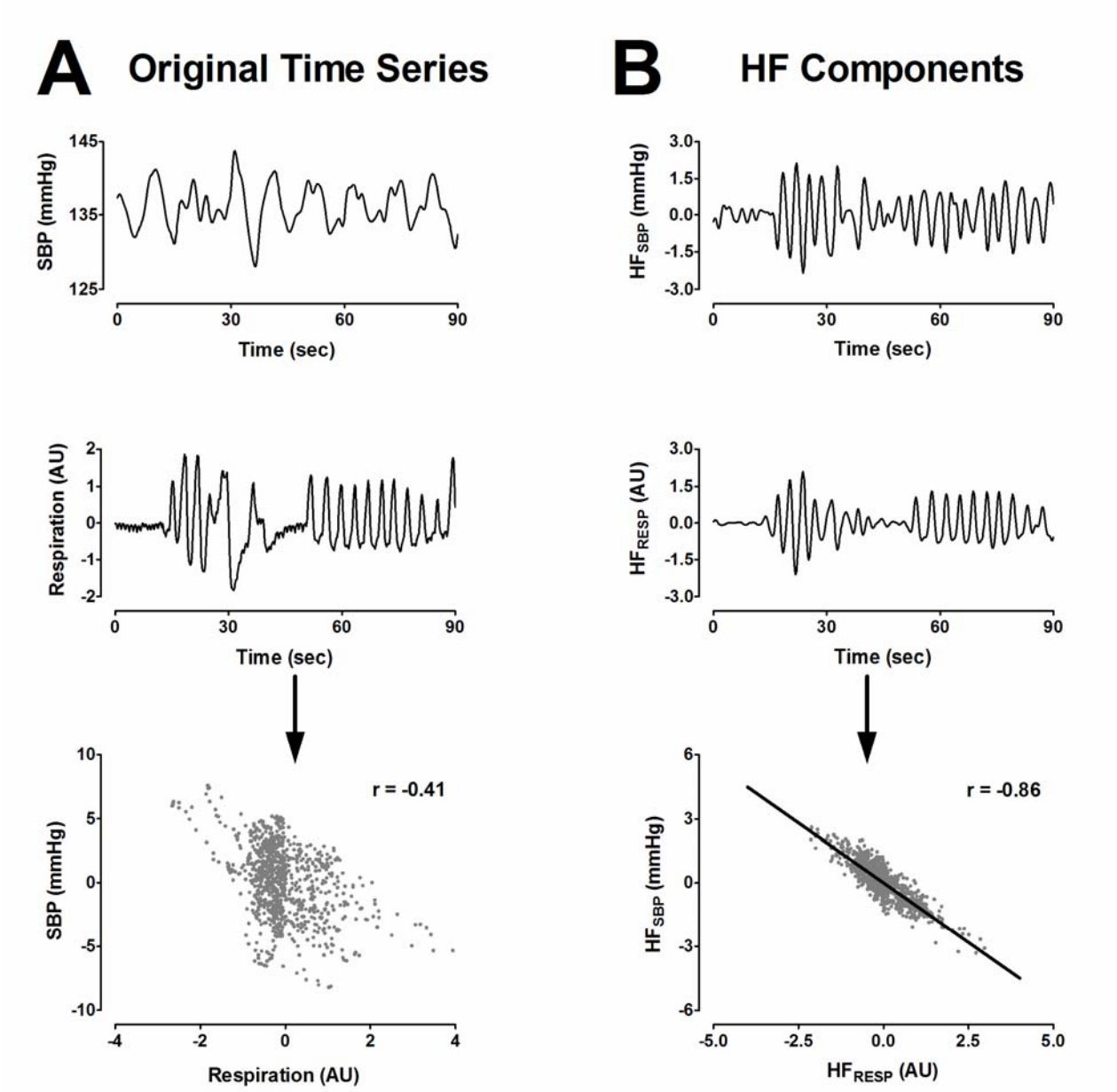

Figure 4. (A) Correlation between systolic blood pressure (SBP) and respiration (RESP) time series. **(B)** Correlation between the high frequency (HF) components of each time series.

A complete correlation analysis was performed between the LF and HF components of the SBP, MSNA spike rate, and respiration for all eight subjects during the baseline period (Fig. 5). The baroreflex mediated feedback correlation (r=-0.69±0.05) was significantly greater than the feed-forward relationship (r=0.58±0.03; Fig 5, top left panel) between the LF_{SBP} and the $LF_{Spike\ Rate}$. However, the feed-forward time delay (τ=5.625±0.15s, increases in spike rate lead to increases in blood pressure) was used in favor of the feedback time delay (τ=0.375±0.10s, spike

rate decrease occurs with blood pressure increase) in the predictive model because the intention of this model is to predict LF changes in blood pressure from the LF changes in spike rate. The $HF_{Spike\ Rate}$ and the HF_{SBP} were not found to be significantly correlated (r=-0.22±0.04; Fig 5, top right panel). Conversely, the HF components of the respiration and SBP are highly correlated (r=-0.79±0.04; Fig 5, bottom right panel) while their LF components have a significantly lower and less consistent correlation across subjects (r=0.45±0.08; Fig 5, bottom left panel).

When the correlation analysis was repeated using the DBP and MBP, the feedback and feed-forward correlations to the $LF_{Spike\ Rate}$ did not differ significantly from those of SBP ($p>0.05$ in each case). The LF_{SBP} (r=-0.58±0.03; τ=5.625±0.15s), LF_{DBP} (r=0.62±0.05; τ=5.1±0.14s), and LF_{MBP} (r=0.62±0.04; τ=4.8±0.17s) also had statistically similar feed-forward correlations to the $LF_{Spike\ Rate}$. However, the correlation between the HF_{RESP} and the HF component of the DBP and MBP were significantly less than that between the HF_{RESP} and the HF_{SBP} ($p<0.01$ in both cases). Consequently, the LF and HF components of the SBP will serve as the output of the predictive model in the subsequent sections.

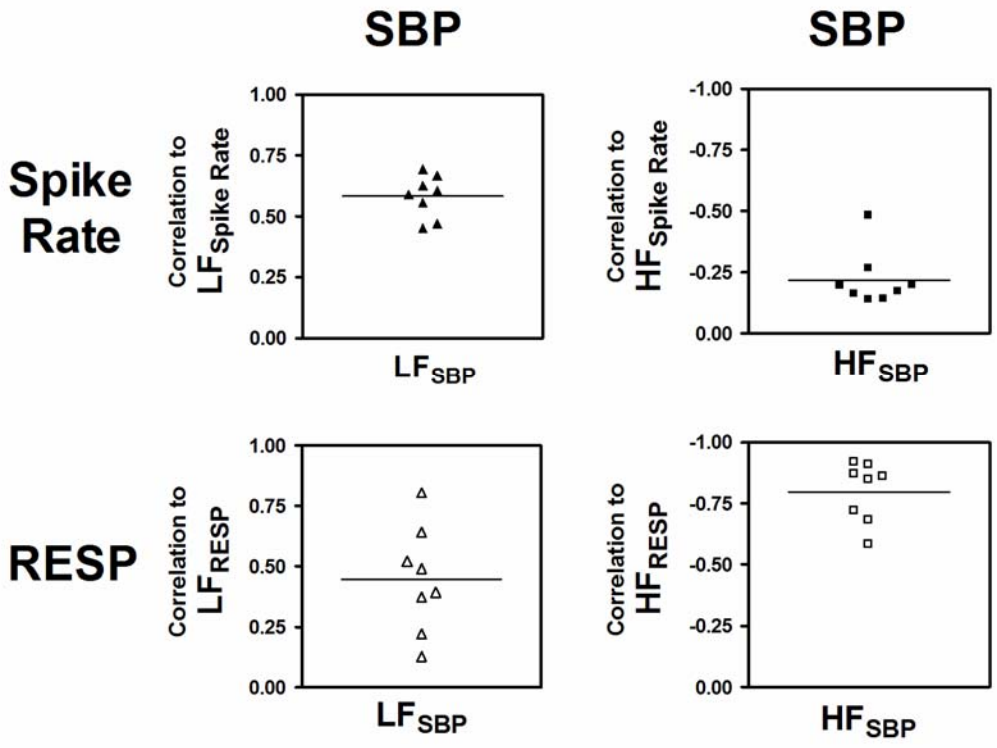

Figure 5. Correlations between low frequency (LF, left column) and high frequency (HF, right column) components of systolic blood pressure (SBP) and the LF and HF components of spike rate (top) or respiration (bottom) during baseline conditions.

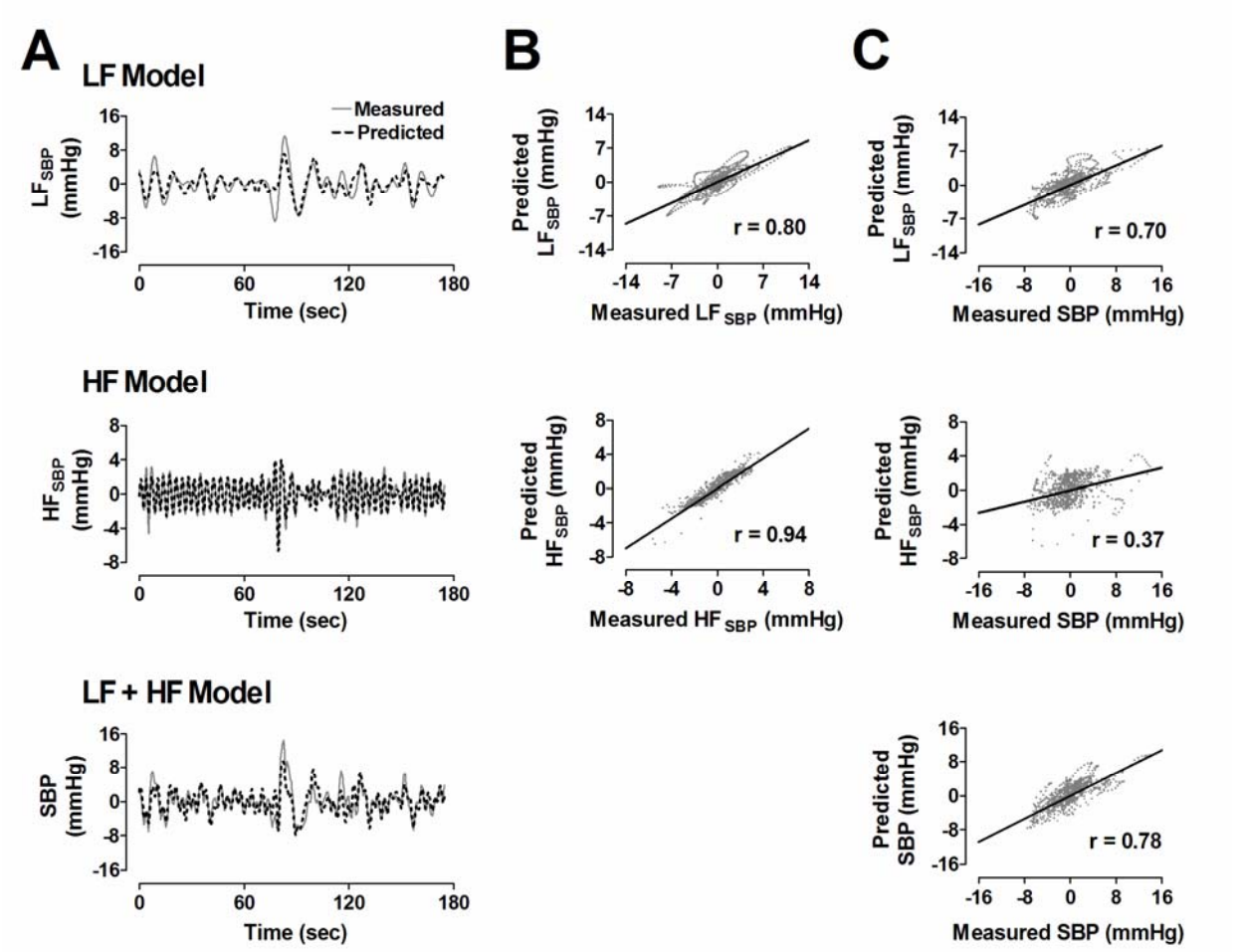

Figure 6. (A) Measured (gray solid line) and model predicted (broken black line) time series for the low frequency component (LF, top), high frequency component (HF, middle), and total (LF+HF, bottom) detrended systolic blood pressure (SBP). **(B)** Correlations between the measured and predicted LF and HF time series in (A). **(C)** Correlations between the predicted time series in (A) and the measured total SBP. LF-spike rate and HF-respiration were used as the LF and HF model inputs, respectively (See Fig. 2).

Predictive Modeling during Resting Supine Position

The LF model (Fig. 2) used past values of the $LF_{Spike\ Rate}$ to predict the current values of the LF_{SBP}. The results of this model during baseline are displayed in Figure 6A. The oscillations in the predicted LF_{SBP} are shown to follow those found in the measured LF_{SBP} (Fig. 6A, top panel) and the two series have a strong linear correlation (r=0.80; Fig. 6B, top panel). The HF model (Fig. 2) used past values of the HF_{RESP} time series to predict the current values of the HF_{SBP} series. This model also demonstrates an ability to follow the measured HF_{SBP} (Fig. 6A, middle panel) and the measured and predicted sequences show a high positive correlation (r=0.94; Fig. 6B, middle panel). When the output of the LF and HF models were summed, the

resultant series was able to predict the total fluctuations found in the SBP (Fig. 6A, bottom panel). As shown in Fig 6C, the sum of the LF and HF models produces a greater correlation to the measured SBP (r=0.78; bottom panel) than either the individual LF (r=0.70; top panel) or HF (r=0.37; middle panel) models. (Statistical analyses for the supine model are discussed in the following section).

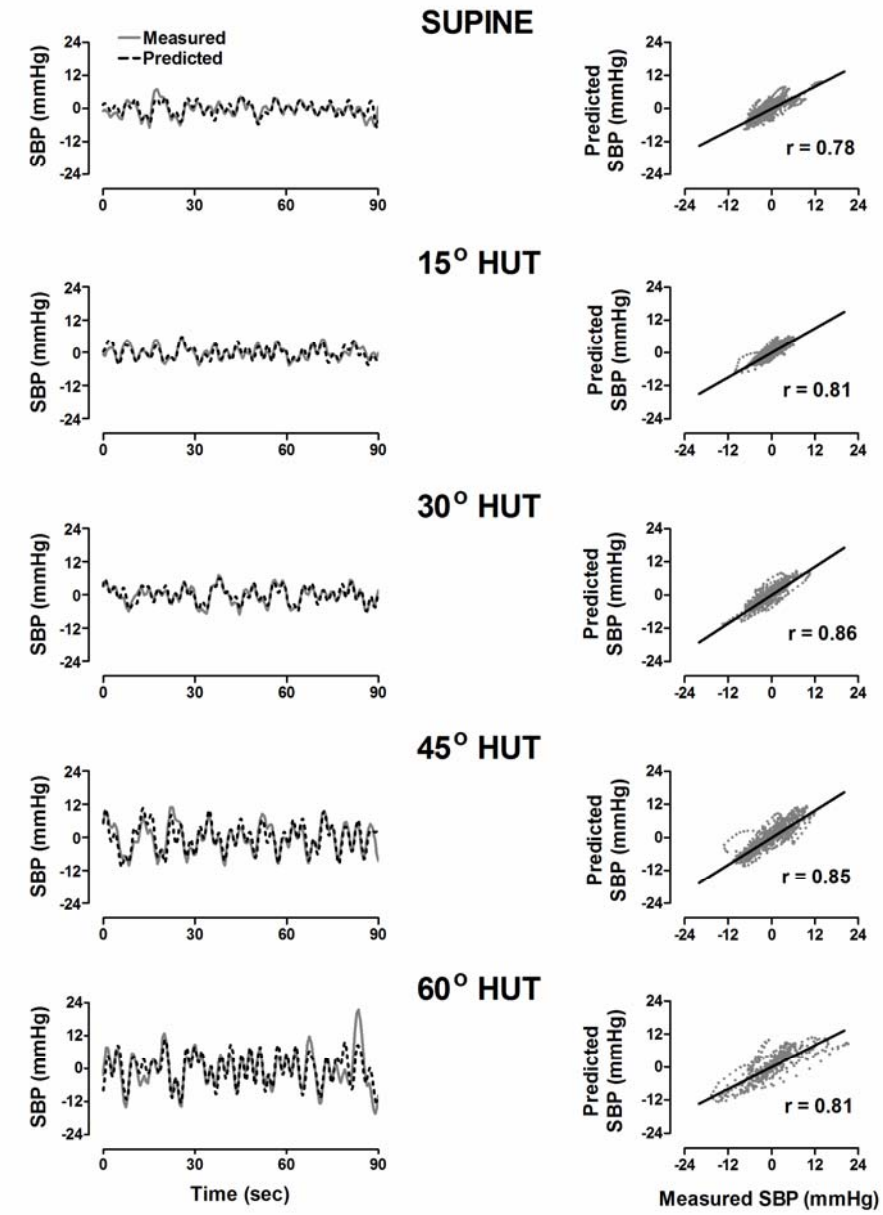

Figure 7. Measured (gray solid line) and model predicted (broken black line) detrended systolic blood pressure during supine, 15, 30, 45, and 60 degree head up tilt (HUT, left panels) Correlations between the measured and predicted time series are shown in the right panels.

Predictive Modeling during Orthostatic Stress

The LF, HF, and total models were also tested over increasing degrees orthostatic stress during head-up tilt (HUT) (Fig. 7). The left column of Figure 7 shows that the model is effective in predicting the total oscillations in the SBP components. The right column demonstrates that the correlation between measured and predicted SBP fluctuations remains strong during increasing orthostatic load.

The mean value of the correlation coefficients between the measured LF_{SBP} and the model predicted LF_{SBP} for eight subjects during resting supine position was r=0.74±0.03 and this value did not change significantly during increased orthostatic load ($p>0.05$ in all cases). The average order used for the LF model ranged between 14 and 19 coefficients (from 2.8 to 3.8 sec of past data) but did not differ significantly ($p>0.05$) over all degrees of HUT. The mean correlation for the measured HF_{SBP} and the predicted HF_{SBP} was r=0.89±0.02 during supine baseline. This correlation became significantly reduced during 30^o (r=0.68±0.04; $p<0.01$) and 45^o (r=0.74±0.06; $p<0.05$) of HUT but was not statistically different from baseline at 15^o or 60^o of HUT. The average HF model order varied between 14 and 18 coefficients (from 2.8 to 3.6 sec of past data) but did not differ significantly ($p>0.05$) over all degrees of HUT. Figure 8 displays the correlation between total measured fluctuations in SBP and the SBP fluctuations predicted by the model during supine and graded tilt conditions. The mean correlation between the measured and model predicted SBP fluctuation during each degree of tilt fell within the range of r=0.68 and r=0.79 and were not statistically different from one another. Note that three subjects fainted during 60^o HUT and were not included in the results at this tilt angle.

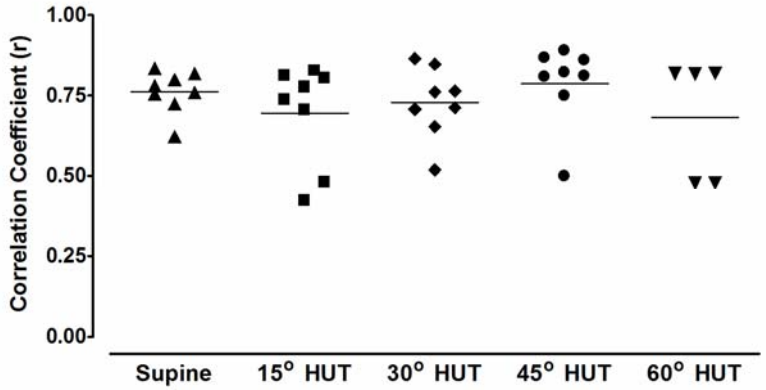

Figure 8. Correlations between measured and model predicted systolic blood pressure (SBP) during supine, 15, 30, 45, and 60 degree head up tilt (HUT).

The relationship between the LF and HF power of the measured and predicted SBP signals for each subject during each degree of HUT is shown in Figure 9. The slope of both regression lines is near 1 (0.9 for LF power and 1.1 for HF power) and the y-intercepts are 0, indicating a close identity of the model and measured values. The respective R^2 values for the regression analysis of the LF and HF powers indicate that 78 and 91 percent of the variability in power can be explained by the linear relationship.

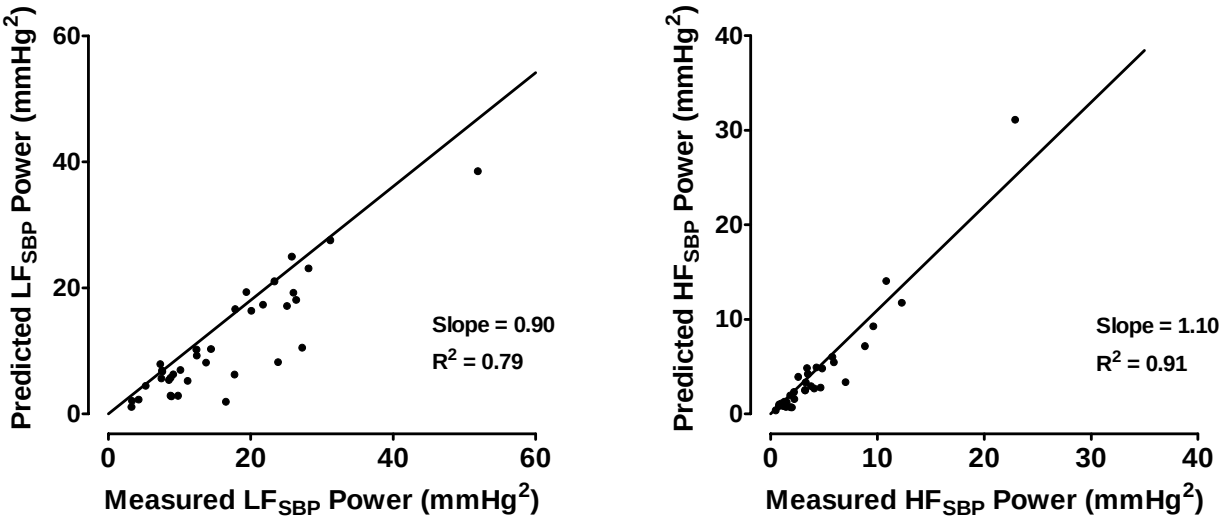

Figure 9. Cumulative relationship between the low frequency (LF, left panel) and high frequency (HF, right panel) power derived from the measured and model predicted systolic blood pressure (SBP) series during supine, 15, 30, 45, and 60 degree head up tilt (HUT).

One Order versus Optimal Order Model.

When a simple slope model (model order = 0, 1 coefficient) was used to predict the components of the SBP from the components of the spike rate and respiration, the correlation between the measured and predicted values still indicated a strong linear relationship (mean r = 0.60 for total model), but the correlations were significantly less than those computed using the optimal model order defined by the minimum final prediction error (FPE, $p<0.01$). Similarly, when optimal model coefficients determined from the baseline period were used to predict the components of the SBP from those of the MSNA spike rate and respiration during the graded tilt, the correlation was significantly lower than those obtained using the optimal models for each recording ($p<0.01$ in all cases).

Discussion

In this study, we report three main findings: *1)* The LF_{BP} has a strong, linear, temporal correlation to the $LF_{Spike\ Rate}$, *2)* The HF_{SBP} and HF_{RESP} also have a strong temporal correlation, and *3)* A large portion of the fluctuations in blood pressure can be explained using the $LF_{Spike\ Rate}$ and HF_{RESP} as the inputs to linear, moving average models.

Relationship Between LF_{SBP}-$LF_{Spike\ Rate}$

A great deal of indirect evidence exists which supports the hypothesis that low frequency changes in the MSNA contribute to the low frequency changes in blood pressure. For example, the LF_{SBP} has been shown to increases during periods of sympathetic activation, including orthostatic stress, such as LBNP [37-39] and upright tilt [7;40], infusion of vasoactive drugs such as nitroprusside [38], and hypovolemia [41]. Similarly, LF_{SBP} power has been shown to decrease significantly during ganglionic blockade in normal subjects [8-10] and in patients with essential hypertension and multiple system atrophy [8], indicating that it is largely mediated by the sympathetic nervous system. Finally, the LF_{SBP} and LF_{MSNA} power have been shown to have corresponding increases during head up tilt [7] and nitroprusside infusion, while both decrease during phenylephrine infusion [42].

Conversely, a previous model of the human BP by *Myers, et al* (2001) reported that the sympathetic activity contributes little to the low frequency BP oscillations [5]. In the present work, however, we have demonstrated a strong temporal forward and feedback correlation between the low frequency fluctuations in SBP and the low frequency changes in MSNA spike rate in healthy humans during resting conditions. The relationship also improves when past values of the $LF_{Spike\ Rate}$ are incorporated to predict the current value of the LF_{SBP} (Fig. 6; top row) and this is unaffected by increased orthostatic load.

The discrepancy in these results may be explained by several differences in protocol. First, the previous model used normalized arbitrary units of integrated sympathetic burst area to form a sympathetic activity series, while our process involved detected sympathetic action potentials. The action potential detection is not based on arbitrary units and is less sensitive to the pass-band noise and artifacts that influence the burst area. Next, we used a physiological maneuver (head-up tilt) rather than vasoactive or metabolic drugs to induce an increased sympathetic state. These pharmacological agents may block or reduce the ability of the

vasculature to accept modulatory sympathetic input, particularly at high doses when operating on the non-linear portion of the baroreflex curve. Finally, the authors elected to use 0.05 – 0.20 Hz as the LF frequency range, which is broader than the range recommended by the Autonomic Task Force (0.04-0.15 Hz) [43], although breathing was controlled at a higher frequency (0.25 Hz) [5].

Interestingly, *Myers, et al.* also identified the strongest linear relationship between the LF_{SBP} and the LF_{MSNA} near 0 sec, which results in a highly negative correlation between the two (MSNA is high at low BP, and vice versa). In the present work, we have termed this the baroreflex "feedback" relationship, although the change in LF_{MSNA} often precedes or occurs concurrently with changes in LF_{SBP} (average τ=-0.375). We hypothesize that this could be a sympathetic response to the change in blood pressure (first deviation) rather than the absolute blood pressure itself [44]. This is supported by animal studies which have shown baroreceptors afferents respond strongly to changes in pressure [45].

The authors of this previous model of LF_{SBP} using LF_{MSNA} chose to use this inverse, feedback relationship as the input to their model, which necessitated the use of a negative model coefficient [5]. Instead, we have elected to use the feed-forward relationship, defined as the maximum *positive* cross-correlation between $LF_{Spike\ Rate}$ and LF_{SBP} (high values of MSNA ultimately leading to high values in BP). The feed-forward time dealy was found to be approximately 5.6 sec, meaning a peak in the LF_{SBP} occurred 5.6 sec after a peak in the $LF_{Spike\ Rate}$. This finding supports the hypothesis that smooth muscle of the vasculature is slow to respond to an increase in sympathetic activity (~5sec delay) [1;46;47]. However, when the feedback relationship is used as the input to the LF model, it results in significantly higher correlations between the measured and predicted LF_{SBP} ($r=0.744\pm0.03$ vs $r=0.81\pm0.03$, $p<0.025$ for the mean feed-forward and feed back time shifts, respectively).

Relationship Between HF_{SBP} and HF_{RESP}

Oscillations in the blood pressure corresponding to respiratory rhythms have been well documented using spectral methods [48-50]. The high frequency range of the blood pressure variability contains the range of frequencies associated with normal breathing rhythms. Ganglionic blockade has little or no affect on the HF_{BP}, suggesting that these oscillations are

unrelated to the sympathetic activity and primarily due to changes in intrathoracic pressure caused by the mechanical aspects of respiration [8-10].

Here we report similar findings. We show that the temporal correlation between the HF_{SBP} and the $HF_{Spike\ Rate}$ is low (r=-0.22±0.04), meaning that vessels act as a neural low pass filter [14] blocking the transmission of the HF oscillations in MSNA to the arterial pressure. On the other hand, the respiration has a strong mechanical influence on the blood pressure, evidenced by the high temporal correlation (r=-0.79±0.04) between the HF_{SBP} and HF_{RESP} during supine, resting conditions.

The HF_{SBP} was found to have a significantly higher correlation to the HF_{RESP} than either the high frequency component of the diastolic (r=-0.45±0.06) or mean (r=0.56±0.08) BP during resting conditions. This is consistent with the model proposed by Saul, et. al. (1991) which described that the mechanical affects of breathing would have a larger impact on the SBP than DBP due to the increased capacitance offered by the ventricles during systole [47].

Predictive Model

We have described how the fluctuations in the SBP can be predicted by summing an optimized linear combination of past LF spike rate values, which predict the LF_{SBP}, and past HF_{RESP} values, which predict the HF_{SBP}. Using this approach, we were able to generate predicted SBP fluctuation series that had good correlations to the measured values during baseline and graded HUT conditions. The relationship between the power of the predicted and measured SBP also indicated that the models were able to explain a large majority of the fluctuations.

The optimized models produced predicted values that were more strongly correlated to the measured SBP fluctuations than a simple slope model, suggesting that some past information from the respiration and sympathetic spike rate contributes to the fluctuations in the SBP. Also, when model coefficients computed during baseline were used to predict the SBP oscillations during varying degrees of HUT, the correlations between measured and predicted SBP values were reasonable, but significantly less than those predicted with the optimal models for each recording. This indicates that the relationship between the BP, sympathetic activity, and respiration changes during orthostatic load and cannot completely be explained by models created during baseline conditions.

Limitations

Very low frequency (0.004-0.04 Hz) fluctuations were excluded from the present model mainly because the length of each segment analyzed was too short (~200 sec) to accurately calculate the influence of oscillations at this frequency range on the SBP. In this study, all subjects maintained a spontaneous breathing rate above 0.15 Hz (in the HF range), however respiratory frequencies lower than 0.15 Hz would cause additional respiratory input in the LF range and an LF model based solely on the $LF_{Spike\ Rate}$ could not accurately predict changes in the LF_{SBP}. The present model only takes into account open-loop properties of the baroreflex system and ignores its closed-loop properties, i.e. feedback from the baroreceptors, which may also contribute to changes in BP and spike rate fluctuations [51]. Finally, although indirect measures of cardiac output (i.e. RR interval) have been shown to contribute to the fluctuations in BP [5] and more direct measures (acetyline rebreathing) have been correlated to changes in mean human sympathetic activity [52] its effect on BP fluctuation was not taken into account in this model. The addition of cardiac output as an input may help to explain the remaining variability in the BP oscillations.

In conclusion, we have shown that a simple two component model of neural sympathetic and mechanical respiratory input can explain the majority of blood pressure fluctuation during resting condition and orthostatic stress in healthy subject.

Acknowledgements

This work was supported in part by National Institutes of Health grants RR00095, and 1PO1 HL56693. We thank Sachin Y Paranjape, Indu Taneja, and Bonnie Black for the support of this study.

References

[1] R. W. DeBoer, J. M. Karemaker, and J. Strackee, "Hemodynamic fluctuations and baroreflex sensitivity in humans: a beat- to-beat model," *Am. J Physiol*, vol. 253, no. 3 Pt 2, p. H680-H689, Sept.1987.

[2] M. Pagani, D. Lucini, O. Rimoldi, R. Furlan, S. Piazza, A. Porta, and A. Malliani, "Low and high frequency components of blood pressure variability," *Ann. N. Y. Acad. Sci.*, vol. 783, pp. 10-23, Aug.1996.

[3] M. Pagani, N. Montano, A. Porta, A. Malliani, F. M. Abboud, C. Birkett, and V. K. Somers, "Relationship between spectral components of cardiovascular variabilities and direct measures of muscle sympathetic nerve activity in humans," *Circulation*, vol. 95, no. 6, pp. 1441-1448, Mar.1997.

[4] M. Pagani and D. Lucini, "Sympathetic contribution to blood pressure variability," *Fundam. Clin. Pharmacol.*, vol. 12 Suppl 1, pp. 42s-47s, 1998.

[5] C. W. Myers, M. A. Cohen, D. L. Eckberg, and J. A. Taylor, "A model for the genesis of arterial pressure Mayer waves from heart rate and sympathetic activity," *Auton. Neurosci.*, vol. 91, no. 1-2, pp. 62-75, Aug.2001.

[6] J. A. Taylor, T. D. Williams, D. R. Seals, and K. P. Davy, "Low-frequency arterial pressure fluctuations do not reflect sympathetic outflow: gender and age differences," *Am. J Physiol*, vol. 274, no. 4 Pt 2, p. H1194-H1201, Apr.1998.

[7] R. Furlan, A. Porta, F. Costa, J. Tank, L. Baker, R. Schiavi, D. Robertson, A. Malliani, and R. Mosqueda-Garcia, "Oscillatory patterns in sympathetic neural discharge and cardiovascular variables during orthostatic stimulus," *Circulation*, vol. 101, no. 8, pp. 886-892, Feb.2000.

[8] A. Diedrich, J. Jordan, J. Tank, J. R. Shannon, R. Robertson, F. C. Luft, D. Robertson, and I. Biaggioni, "The sympathetic nervous system in hypertension: assessment by blood pressure variability and ganglionic blockade," *J. Hypertens.*, vol. 21, no. 9, pp. 1677-1686, Sept.2003.

[9] A. Nakata, S. Takata, T. Yuasa, A. Shimakura, M. Maruyama, H. Nagai, S. Sakagami, and K. Kobayashi, "Spectral analysis of heart rate, arterial pressure, and muscle sympathetic nerve activity in normal humans," *Am. J. Physiol*, vol. 274, no. 4 Pt 2, p. H1211-H1217, Apr.1998.

[10] R. Zhang, K. Iwasaki, J. H. Zuckerman, K. Behbehani, C. G. Crandall, and B. D. Levine, "Mechanism of blood pressure and R-R variability: insights from ganglion blockade in humans," *J. Physiol*, vol. 543, no. Pt 1, pp. 337-348, Aug.2002.

[11] R. Furlan, S. Piazza, M. Bevilacqua, M. Turiel, G. Norbiato, F. Lombardi, and A. Malliani, "Pure Autonomic Failure: complex abnormalities in the neural mechanisms regulating the cardiovascular system," *J Auton. Nerv. Syst.*, vol. 51, no. 3, pp. 223-235, Mar.1995.

[12] R. Kingma, B. J. TenVoorde, G. J. Scheffer, J. M. Karemaker, A. J. Mackaay, K. H. Wesseling, and J. J. de Lange, "Thoracic sympathectomy: effects on hemodynamics and baroreflex control," *Clin Auton. Res*, vol. 12, no. 1, pp. 35-42, Feb.2002.

[13] T. Kawada, M. Sugimachi, T. Sato, H. Miyano, T. Shishido, H. Miyashita, R. Yoshimura, H. Takaki, J. Alexander, Jr., and K. Sunagawa, "Closed-loop identification of carotid sinus baroreflex open-loop transfer characteristics in rabbits," *Am. J. Physiol*, vol. 273, no. 2 Pt 2, p. H1024-H1031, Aug.1997.

[14] T. Yingthawornsuk, T. Kawada, T. Sato, M. Inagaki, K. Sunagawa, J. Cox, R. Shiavi, and A. Diedrich, "Identification of open-loop transfer functions in closed-loop baroreflex system using randomized breathing in humans," *Computers in Cardiology*, vol. 29, pp. 461-464, 2002.

[15] H. M. Stauss, E. A. Anderson, W. G. Haynes, and K. C. Kregel, "Frequency response characteristics of sympathetically mediated vasomotor waves in humans," *Am. J. Physiol*, vol. 274, no. 4 Pt 2, p. H1277-H1283, Apr.1998.

[16] R. Mukkamala, J. M. Mathias, T. J. Mullen, R. J. Cohen, and R. Freeman, "System identification of closed-loop cardiovascular control mechanisms: diabetic autonomic neuropathy," *Am. J Physiol*, vol. 276, no. 3 Pt 2, p. R905-R912, Mar.1999.

[17] T. J. Mullen, M. L. Appel, R. Mukkamala, J. M. Mathias, and R. J. Cohen, "System identification of closed-loop cardiovascular control: effects of posture and autonomic blockade," *Am. J Physiol*, vol. 272, no. 1 Pt 2, p. H448-H461, Jan.1997.

[18] J. A. Taylor and D. L. Eckberg, "Fundamental relations between short-term RR interval and arterial pressure oscillations in humans," *Circulation*, vol. 93, no. 8, pp. 1527-1532, Apr.1996.

[19] Y. Ikeda, T. Kawada, M. Sugimachi, O. Kawaguchi, T. Shishido, T. Sato, H. Miyano, W. Matsuura, J. Alexander, Jr., and K. Sunagawa, "Neural arc of baroreflex optimizes dynamic pressure regulation in achieving both stability and quickness," *Am. J. Physiol*, vol. 271, no. 3 Pt 2, p. H882-H890, Sept.1996.

[20] T. Kawada, T. Sato, M. Inagaki, T. Shishido, T. Tatewaki, Y. Yanagiya, C. Zheng, M. Sugimachi, and K. Sunagawa, "Closed-loop identification of carotid sinus baroreflex transfer characteristics using electrical stimulation," *Jpn. J. Physiol*, vol. 50, no. 3, pp. 371-380, June2000.

[21] B. Chapuis, E. Vidal-Petiot, V. Orea, C. Barres, and C. Julien, "Linear modelling analysis of baroreflex control of arterial pressure variability in rats," *J. Physiol*, vol. 559, no. Pt 2, pp. 639-649, Sept.2004.

[22] S. N. Davis, C. Shavers, F. Costa, and R. Mosqueda-Garcia, "Role of cortisol in the pathogenesis of deficient counterregulation after antecedent hypoglycemia in normal humans," *J Clin. Invest*, vol. 98, no. 3, pp. 680-691, Aug.1996.

[23] Brychta RJ, Charoensuk W, L. Bernardi, R. Furlan, Shiavi R, and A. Diedrich, "Spectral analysis of multiunit action potential trains of muscle sympathetic nerve activity in humans," *Computers in Cardiology*, vol. 29, pp. 457-460, 2002.

[24] A. Diedrich, W. Charoensuk, R. J. Brychta, A. C. Ertl, and R. Shiavi, "Analysis of raw microneurographic recordings based on wavelet de-noising technique and classification algorithm: wavelet analysis in microneurography," *IEEE Trans. Biomed. Eng*, vol. 50, no. 1, pp. 41-50, Jan.2003.

[25] D. E. Watenpaugh, G. A. Breit, T. M. Buckley, R. E. Ballard, G. Murthy, and A. R. Hargens, "Human cutaneous vascular responses to whole-body tilting, Gz centrifugation, and LBNP," *J Appl Physiol*, vol. 96, no. 6, pp. 2153-2160, 2004.

[26] J. Penaz, "Photoelectric measurement of blood pressure, volume and flow in the finger," *Digest of the 10th international conference on medical and biological engineering - Dresden.*, p. 104, 1973.

[27] A. B. Vallbo, K. E. Hagbarth, H. E. Torebjork, and B. G. Wallin, "Somatosensory, proprioceptive, and sympathetic activity in human peripheral nerves," *Physiol Rev.*, vol. 59, no. 4, pp. 919-957, Oct.1979.

[28] W. Delius, K. E. Hagbarth, A. Hongell, and B. G. Wallin, "General characteristics of sympathetic activity in human muscle nerves," *Acta Physiol Scand.*, vol. 84, no. 1, pp. 65-81, Jan.1972.

[29] J. Pan and W. J. Tompkins, "A real-time QRS detection algorithm," *IEEE Trans. Biomed. Eng*, vol. 32, no. 3, pp. 230-236, Mar.1985.

[30] R. J. Brychta, S. Tuntrakool, M. Appalsamy, N. R. Keller, C. Finney, D. Robertson, R. Shiavi, and A. Diedrich, "Spike detection in mouse renal sympathetic nerve activity using the stationary wavelet transform with automated noise level estimation," *IEEE Trans Biomed Eng*, 2006.

[31] A. Szucs, "Applications of the spike density function in analysis of neuronal firing patterns," *J Neurosci Meth*, vol. 81, no. 1-2 1998.

[32] I. Daubechies, *Ten Lectures on Wavlets*. Montpelier, Vermont: Capital City Press, 1992.

[33] C. Torrence and G. Compo, "A practical guide to wavelet analysis," *B Am Meteorol Soc B Am Meteorol Soc*, vol. 79, no. 1, pp. 61-78, 1998.

[34] K. Steiglitz and L. McBride, "A technique for identification of linear systems," *IEEE T Automat Contr*, vol. AC10, no. 4, pp. 461-464, 1965.

[35] R. G. Shiavi, *Introduction to Applied Statistical Signal Analysis*, 2nd ed. San Diego: Academic Press, 1999.

[36] Welch P.D., "The use of fast fourier transform for the estimation of Power Spectra: A method based on time averaging over short modified periodograms," *IEEE Trans. Audio Electroacoust.*, vol. AU-15, no. June, pp. 70-73, 1967.

[37] V. A. Convertino, D. A. Ludwig, and W. H. Cooke, "Stroke volume and sympathetic responses to lower-body negative pressure reveal new insight into circulatory shock in humans," *Auton. Neurosci.*, vol. 111, no. 2, pp. 127-134, Apr.2004.

[38] J. P. Saul, R. F. Rea, D. L. Eckberg, R. D. Berger, and R. J. Cohen, "Heart rate and muscle sympathetic nerve variability during reflex changes of autonomic activity," *Am. J Physiol*, vol. 258, no. 3 Pt 2, p. H713-H721, Mar.1990.

[39] R. G. Victor and W. N. Leimbach, Jr., "Effects of lower body negative pressure on sympathetic discharge to leg muscles in humans," *J Appl. Physiol*, vol. 63, no. 6, pp. 2558-2562, Dec.1987.

[40] W. H. Cooke, J. B. Hoag, A. A. Crossman, T. A. Kuusela, K. U. Tahvanainen, and D. L. Eckberg, "Human responses to upright tilt: a window on central autonomic integration," *J Physiol*, vol. 517 (Pt 2), pp. 617-628, June1999.

[41] D. S. Kimmerly and J. K. Shoemaker, "Hypovolemia and MSNA discharge patterns: assessing and interpreting sympathetic responses," *Am. J. Physiol Heart Circ. Physiol*, vol. 284, no. 4, p. H1198-H1204, Apr.2003.

[42] M. Pagani and A. Malliani, "Interpreting oscillations of muscle sympathetic nerve activity and heart rate variability," *J Hypertens.*, vol. 18, no. 12, pp. 1709-1719, Dec.2000.

[43] Task Force, "Heart rate variability: standards of measurement, physiological interpretation and clinical use. Task Force of the European Society of Cardiology and the North American Society of Pacing and Electrophysiology [see comments]," *Circulation*, vol. 93, no. 5, pp. 1043-1065, Mar.1996.

[44] D. L. Eckberg and P. Sleight, *Human baroreflexes in health and disease* Oxford Clarendon Press, 1992.

[45] H. R. Kirchheim, "Systemic arterial baroreceptor reflexes," *Physiol Rev*, vol. 56, no. 1, pp. 100-177, Jan.1976.

[46] J. B. Madwed, P. Albrecht, R. G. Mark, and R. J. Cohen, "Low-frequency oscillations in arterial pressure and heart rate: a simple computer model," *Am. J Physiol*, vol. 256, no. 6 Pt 2, p. H1573-H1579, June1989.

[47] J. P. Saul, R. D. Berger, P. Albrecht, S. P. Stein, M. H. Chen, and R. J. Cohen, "Transfer function analysis of the circulation: unique insights into cardiovascular regulation," *Am. J Physiol*, vol. 261, no. 4 Pt 2, p. H1231-H1245, Oct.1991.

[48] W. H. Cooke, J. F. Cox, A. M. Diedrich, J. A. Taylor, L. A. Beightol, J. E. Ames, J. B. Hoag, H. Seidel, and D. L. Eckberg, "Controlled breathing protocols probe human autonomic cardiovascular rhythms," *Am. J Physiol*, vol. 274, no. 2 Pt 2, p. H709-H718, Feb.1998.

[49] D. L. Eckberg, "Physiological basis for human autonomic rhythms," *Ann. Med.*, vol. 32, no. 5, pp. 341-349, July2000.

[50] G. Baselli, S. Cerutti, F. Badilini, L. Biancardi, A. Porta, M. Pagani, F. Lombardi, O. Rimoldi, R. Furlan, and A. Malliani, "Model for the assessment of heart period and arterial pressure variability interactions and of respiration influences," *Med. Biol. Eng Comput.*, vol. 32, no. 2, pp. 143-152, Mar.1994.

[51] T. Kawada, T. Sato, M. Inagaki, T. Shishido, T. Tatewaki, Y. Yanagiya, C. Zheng, M. Sugimachi, and K. Sunagawa, "Closed-loop identification of carotid sinus baroreflex transfer characteristics using electrical stimulation," *Jpn. J. Physiol*, vol. 50, no. 3, pp. 371-380, June2000.

[52] N. Charkoudian, M. J. Joyner, C. P. Johnson, J. H. Eisenach, N. M. Dietz, and B. G. Wallin, "Balance between cardiac output and sympathetic nerve activity in resting humans: role in arterial pressure regulation," *J Physiol*, vol. 568, no. Pt 1, pp. 315-321, Oct.2005.

CHAPTER VI

WAVELET SPECTRAL COMPONENTS OF VASOVAGAL SYNCOPE WITH AND WITHOUT ASYSTOLE DURING ORTHOSTATIC STRESS IN HEALHTY SUBJECTS

Abstract

Orthostatic stress can cause syncope with poorly understood etiology. In rare cases, the syncope can end in a life threatening asystole. We tested the hypothesis that different autonomic control mechanisms are responsible for the two outcomes. We retrospectively studied 40 healthy subjects without a history of syncope during orthostatic stress. All subjects experienced syncope and in 18 cases the vasovagal syncope ended with asystole > 3sec. We analyzed R-R intervals (RRI) and continuous systolic blood pressure (SBP) before syncope. A modified continuous wavelet transform capable of handling non-stationary data was used to analyze the low and high frequency oscillations (LF 0.04-0.15, HF 0.15-0.4 Hz). We identified three general patterns of syncope amongst the pooled data. Statistical comparisons were made between subjects with the most prevalent pattern, rapid onset vasovagal syncope, who experienced syncope alone and syncope with asystole. The asystole group had a higher rate of R-R prolongation which occurred over a shorter final phase of syncope. HF_{RRI} increased in both groups during the syncopal phase; however LF_{RRI} increased only in the asystole group. LF_{SBP} decreased in the group with syncope alone, but was slightly elevated in the asystole group. During the final phase of syncope, both groups showed vagal cardiac activation reflected in an increase in HF_{RRI}. In the group with syncope alone, a decrease in LF_{SBP} indicated additional peripheral sympathetic withdrawal. In contrast, sympathetic withdrawal was not present in the asystole group. In conclusion, different autonomic control mechanisms are responsible for the different outcome of syncope with and without asystole.

Introduction

Syncope is a common clinical condition [1]. It is broadly defined as a transient loss of consciousness brought about by rapid, global cerebral hypoperfusion which usually leads to falling [2]. However, the many causes of syncope are difficult to characterize and classify [3]. Most standard syncopal classifications have identified neurally mediated, or vasovagal, syncope as a distinct category of syncope [1-3]. Vasovagal syncope is generally characterized by vagally

mediated bradycardia coupled with arterial dilation and resultant hypotension in response to a number of stimuli, including orthostatic stress [2;4;5]. It can be recurrent and happen as part of a clinical syndrome that disrupts quality of life [1], but can also occur in otherwise healthy individuals in response to orthostatic stress [6-9] or infusion of vasoactive agents [10]. Although rare, vasovagal events in both patients and healthy individuals can terminate in a life threatening stoppage of the heart known as asystole [1].

Analysis of the dynamic of blood pressure and heart rate preceding vasovagal events during diagnostic and research-based orthostatic tests, such as head up tilt and lower body negative pressure, has identified several common patterns that can be used to sub-categorize the reaction [11]. While these classifications are admittedly arbitrary, they have proved useful in the clinical diagnosis and treatment of syncope [2]. To date, most vasovagal classifications have been concerned with categorizing patients with recurrent syncope. But since the “false positive” tilt response in normal subjects are also common [12], vasovagal patterns in normal subjects also deserve attention and may provide a less obstructed view of the mechanism of vasovagal syncope, independent of any underlying pathophysiology.

Profiles of the heart rate variability (HRV) and blood pressure variability (BPV) during the vasovagal reaction could help clarify and extend the definition of each sub-class of vasovagal syncope, which until now have relied on central tendencies in heart rate and blood pressure. HRV and BPV are established analysis techniques which can be used to estimate vagal [13;14] and sympathetic [15;16] activity when more direct measures are unavailable. In the past, the application of standard HRV and BPV methods, such as the Fourier transform or autoregressive (AR) modeling, to data collected during syncope have been limited because the transient, non-stationary nature of the vasovagal reaction violates the mathematical assumptions of these techniques. Recently, however, more appropriate alternative HRV and BPV analysis methods, such as complex demodulation [17] and the wavelet transform [18], have revealed similar, consistent patterns in HRV and BPV during the “classic” vasovagal reaction. These methods could also be used to study other sub-categories of the vasovagal response, including those that terminate in asystole.

While asystole has been mentioned as a potential outcome of vasovagal syncope and has even been used to sub-classify the vasovagal reaction [11], researchers have chosen to focus on the cardiac electromechanical origins of asystole [19;20] and have largely ignored the

contribution of the peripheral blood pressure and autonomic nervous system during orthostatic stress to this condition. Methods used to describe the HRV and BPV response during asystole could provide insight into its mechanism, which is important for the diagnosis and management of syncope in patients and could be useful in the development of drugs and pacemakers.

In this study, we will retrospectively analyze a population of healthy subjects who have experienced vasovagal syncope and vasovagal syncope with asystole using a modified wavelet transform technique. We hypothesize that different subclasses of the vasovagal response can be described by different HRV and BPV patterns and that separate autonomic control mechanisms are responsible for syncope with and without asystole.

Methods

Subjects and Clinical Conditions

We retrospectively studied 39 healthy subjects who experienced syncope during orthostatic stress. All subjects underwent extensive physical examination and did not have any signs of cardiovascular disease or history of syncope prior to the study. Data were collected during a baseline period, during which the subjects remained still and silent in a supine position, and during a tilt table test with or without additional lower body negative pressure suction. The orthostatic intervention was halted immediately after loss of consciousness. In 17 subjects (age 33.5 ± 3.5, 8 female) the syncope ended in asystole, while in the other 22 (age 30.9 ± 2, 15 female) it did not. The studies were conducted at three institutions and all methods were approved by the respective institutional review boards.

The application of orthostatic stress to subjects was observed to produce transient changes in the heart, blood pressure, and their variability sequences. We hypothesize that these changes are due to natural, physiologic accommodation to the new orthostatic load. In either case, we were interested only in the changes in heart rate and blood pressure prior to syncope independent of the transient affects caused by increased orthostatic stress on these variables. Therefore, only subjects that fainted at least 240 seconds after the application or modification of the orthostatic stress were analyzed. This meant that data from 7 subjects were not included in the averages or statistical comparisons in the period prior to syncope or asystole.

Instrumentation and Software

The electrocardiogram (ECG) of lead II was recorded with a Gould ECG/Biotach amplifier (Gould Electronics, Cleveland, OH, USA). The continuous finger blood pressure (BP) waveform was measured by photoplethysmographic-based volume clamp method [21] with a finger cuff on the middle finger of the non-dominant hand (Finapres, Ohmeda, Englewood, CO, USA) and verified using brachial BP obtained by automated auscultometric device (Dinamap blood pressure monitor, model 1846SX, Critikon, Tampa, FL) on the contralateral arm. The hand with the Finapres sensor was fixed at heart level. Data were acquired at 500 Hz, 14 bit resolution using the Windaq data acquisition system (DA-720, DATAQ Instruments, Akron OH). and analyzed offline with custom software written in the PV Wave (Visual Numerics Inc., Houston, TX) and MATLAB (Mathworks; Natick, MA) environments. QRS detection was performed using a modified Pan-Tompkins algorithm [22]. Systolic and diastolic values in the continuous blood pressure recordings were automatically identified as the maxima and minima for each cardiac cycle. All detections were visually verified.

Syncope Detection

The onset of RR-Interval (RRI) prolongation and systolic blood pressure (SBP) decrease were determined using semi-automated, custom written software. The RRI and SBP variability series were formed by linearly interpolating the detected values onto regular intervals of 200 msec (5 Hz). A median filter with a length of 150 data points (30 sec) was applied to each sequence to identify the median trend independent of the very low (VLF; 0.004-0.04), low (LF; 0.04 – 0.15 Hz), and high frequency (HF; 0.15 – 0.40 Hz) components defined by the Autonomic Task Force [23]. The nearest time prior to syncope at which the sign of the first difference of the median trend changed (from negative to positive for onset of RRI increase or positive to negative for onset of SBP decrease) was automatically identified. The times of onset were visually inspected and manually corrected if necessary. All of the subjects were then placed into several groups based on the time of onset of RRI increase and SBP decrease.

Mathematical Analysis

The traditional methods of obtaining time-varying spectral information, such as the short time Fourier Transform (STFT) and moving autoregressive (AR) models, typically divide the signal into an arbitrary number of consecutive or overlapping segments of equal length and

compute spectral estimates over the entire frequency bandwidth for each of these segments. The time and frequency resolution of the analysis is governed by the length of the segments. Using longer segments yields higher frequency resolution and more accurate information about broad (low frequency) trends in the signal. However, traditional analysis methods assume that the frequency content remains constant, or stationary, over the entire length of each segment [24]. Longer segments are more likely to contain intrasegmental changes in frequency content, making the assumption of stationarity invalid and leading to inaccurate spectro-temporal information.

Wavelet analysis offers a more flexible solution to the problem of time-frequency analysis. Rather than analyzing the entire bandwidth of a signal using a fixed time window, the continuous wavelet transform (CWT) uses broad, dilated wavelets to analyze long-term trends and short, compact wavelets to detect high frequency oscillations. In this way, the CWT is able to use an adjustable time window to analyze different frequency bands. Previous use of the wavelet transform to analyze nonstationary heart rate and blood pressure data is well documented [18;25-30]. A brief introduction to the subject of wavelets is presented in Appendix A, but a more complete mathematical description is given elsewhere [31].

A Hilbert-modified CWT algorithm was formulated in order to estimate instantaneous spectral power of heart rate and blood pressure variability, similar to the Hilbert-modified discrete wavelet transform used previously [28;32;33]. In this method, the CWT coefficients of the equidistantly sampled (5 Hz) RRI and SBP series were computed using the *Meyer* wavelet [34] at scales of 8, 16, 32, and 64 which have corresponding center frequencies of 0.43, 0.22, 0.11, and 0.05 Hz. The CWT coefficients (d_s) of each scale (s) contain information about a different frequency bandwidth, but in order to convert the CWT coefficients to spectral power, the instantaneous amplitude of the filtered signals must be computed using the analytic signal from the Hilbert transform (See Appendix D for more detail) [32]. The output is then squared and scales are summed to provide the approximate frequency bands prescribed by the Autonomic Task Force [35], The wavelet scales and resampling frequency (5 HZ) were chosen to produce approximate LF ($d_{32} + d_{64}$) and HF ($d_8 + d_{16}$) power bands. The *Meyer* wavelet was chosen over similar wavelets, such as *DB4* and *Symlet 8*, because its output was observed to be most similar to the output of the Fourier Transform when used on stationary signals.

Data Analysis

We analyzed the R-R interval series (RRI) and systolic blood pressure (SBP) series during a 5 minute baseline period and 5 minutes prior to syncope. The end of the syncope period was established as the cardiac cycle just prior to asystole or loss of consciousness (in the case of syncope alone). The Hilbert modified CWT described above was used to examine the dynamics of low frequency (LF; 0.04-0.15 Hz) and high frequency (HF; 0.15-0.40 Hz) oscillations during both the baseline and syncopal periods. Average values for RRI, SBP, LF_{RRI}, HF_{RRI}, LF_{SBP}, and HF_{SBP} over the last minute of the pre-syncopal phase were compared to averages over the final syncopal phase associated with RRI prolongation and blood pressure decrease. Both the slope of the RRI prolongation and the duration of the final phase were also calculated and compared.

Statistics

The non-parametric Mann-Whitney test for unpaired data was used to test for significant differences between groups and the non-paramteric Wilcoxon signed ranks test for matched-pairs was used to test for significant differences between time periods within the same group. A probability value of 0.05 was defined as the significance threshold. Unless otherwise noted, all data are reported as means ± SEM.

Results

Baseline Comparisons

The baseline information for the subjects who experienced syncope (Syncope) and syncope with asystole (Asystole) is displayed in Table 1. There were no significant differences in the ages of the two groups. The mean RR- interval (RRI) tended to be higher in the asystole group, but the difference was not significant. Both the low frequency and high frequency oscillations in RRI (LF_{RRI} and HF_{RRI}) and the low frequency oscillations in systolic blood pressure (LF_{SBP}) tended to be higher in the asystole group, but the differences were also not significant. The asystole group did have significantly lower HF_{SBP} power than the syncope alone group during resting baseline conditions.

Table 1. Baseline values for subjects who developed syncope with and without asystole.

	Syncope (N=22)	Asystole (N=17)	p
R-R Interval (msec)	**913.5 ± 24.2**	**1001.6 ± 47.5**	**0.20**
Systolic Pressure (mmHg)	**123.6 ± 3.1**	**118.1 ± 4.5**	**0.39**
Diastolic Pressure (mmHg)	**66.0 ± 2.6**	**64.4 ± 2.4**	**0.68**
LF_{RRI} ($msec^2$)	**865.4 ± 129.0**	**1292.4 ± 202.9**	**0.09**
HF_{RRI} ($msec^2$)	**675.7 ± 118.4**	**930.0 ± 261.1**	**0.64**
LF_{SBP} ($mmHg^2$)	**5.4 ± 0.9**	**9.1 ± 2.5**	**0.30**
HF_{SBP} ($mmHg^2$)	**1.9 ± 0.3**	**1.1 ± 0.2**	**0.006**

Values are expressed as the mean ± SE.

Syncope Groupings

Three general patterns of syncope from this group of subjects were empirically identified in the pooled data from observations of the time of onset of RRI prolongation and BP decrease. Representative RRI and SBP series from each pattern are depicted in Figure 1. Quantitative classifiers for the three groups can be found in Figure 2.

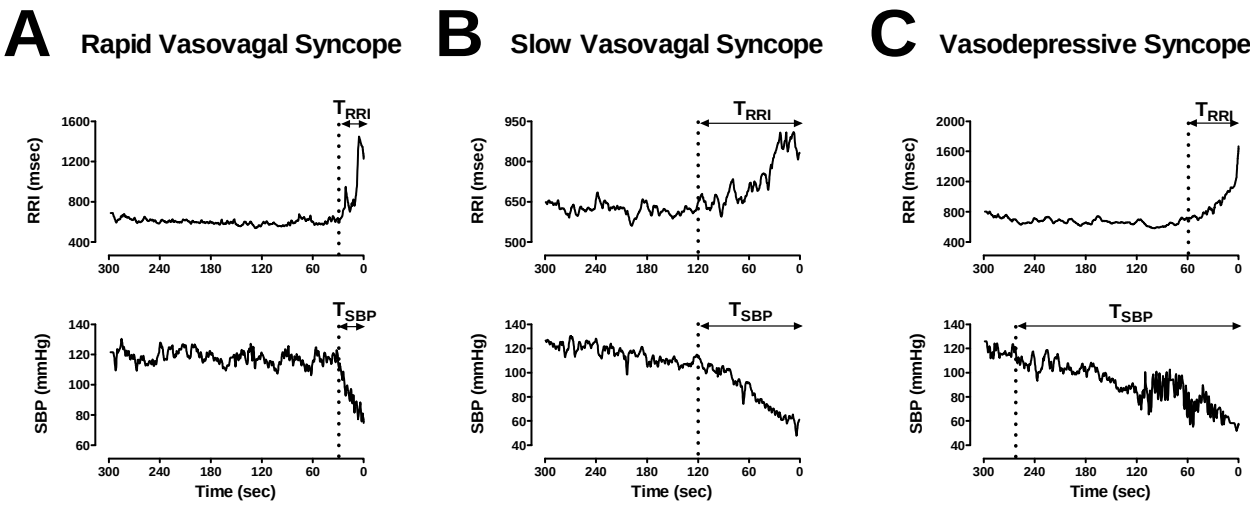

Figure 1. Three types of syncope. **(A)** Rapid vasovagal syncope occurs when the time of RRI prolongation (T_{RRI}) is roughly the same as the time of SBP decline (T_{SBP}) and the syncopal period is short (<60 sec). **(B)** Slow vasovagal syncope occurs when T_{RRI} is roughly equal to T_{SBP} and the syncopal period is longer (>60 sec). **(C)** During vasodepressive syncope the SBP drops before RRI prolongation.

The pooled syncope alone and syncope with asystole data were each first divided into two subpopulations based on the difference between the length of time of RRI prolongation (T_{RRI}) and the length of time of SBP decrease (T_{SBP}) which were both semi-automatically defined as described above. When the onset of RRI prolongation and SBP decrease occurred in roughly the same period (i.e. $T_{SBP} - T_{RRI} < 17$ sec), the reaction was classified as a combined, or vasovagal, response (Fig 2). When the onset of SBP decrease substantially preceded the onset of RRI prolongation ($T_{SBP} - T_{RRI} > 60$ sec), the reaction was classified as vasodepressive (Fig. 2). The vasovagal reaction was more prevalent than vasodepressive reaction in both the syncope alone (14 vs 6 subjects, respectively) and syncope with asystole (9 vs 3 subjects, respectively) groups. Interestingly, the difference between the time of onset of SBP decline and RRI prolongation (T_{SBP} - T_{RRI}) was significantly less in the group which experienced vasovagal syncope plus asystole than in the group which experienced vasovagal syncope alone. Additionally, in the majority of cases (6 of 9), the time of onset RRI prolongation occurred prior to the time of onset of SBP decrease ($T_{SBP} - T_{RRI}<0$) in the group with vasovagal syncope plus asystole, whereas in the group with vasovagal syncope alone, this scenario occurred in only 3 of 14 cases (Fig 2).

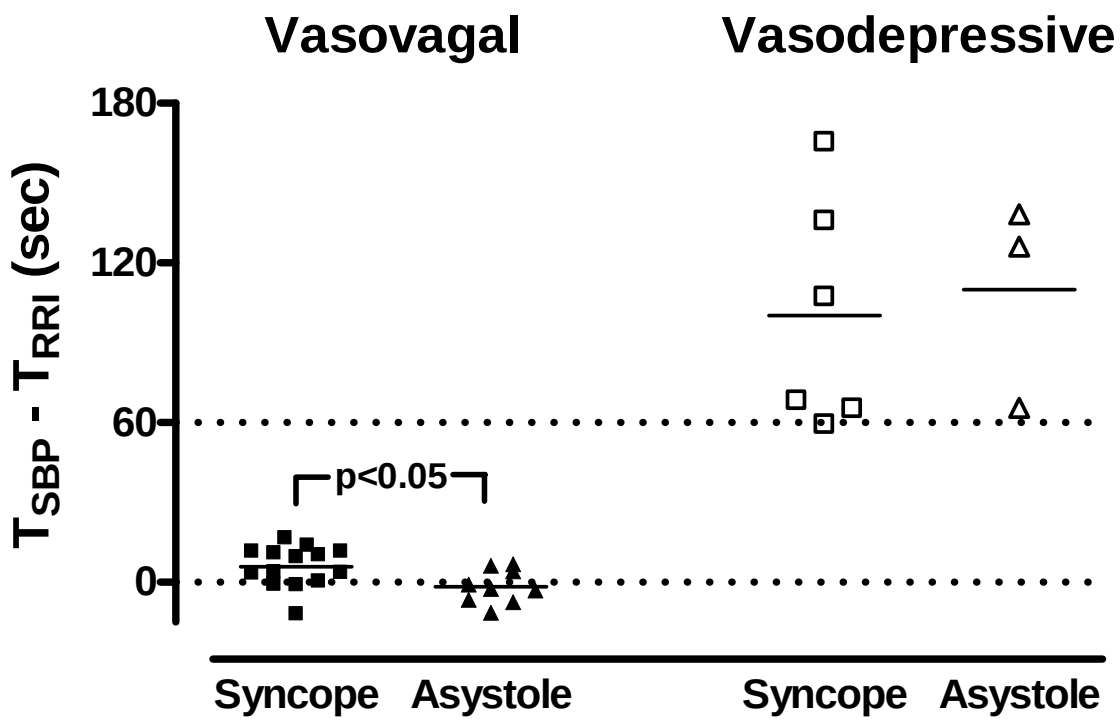

Figure 2. The difference between the duration of RRI prolongation (T_{RRI}) and SBP drop (T_{SBP}) during vasovagal syncope and vasovagal asystole (left) and vasodepressive syncope and vasodepressive asystole (right). $T_{SBP} - T_{RRI}$ is the difference in the onset of SBP decline and RRI prolongation. Dashed lines are placed at $T_{SBP} - T_{RRI} = 0$ and $T_{SBP} - T_{RRI} = 60$.

The group of subjects identified as having a vasovagal syncopal reaction was further divide based on the length of their syncopal phase. Individuals with a vasovagal reaction whose syncopal phase duration was greater than 60 seconds were said to have slow vasovagal syncope, while those with a syncopal phase less than 60 seconds experienced rapid vasovagal syncope. Slow vasovagal syncope was less prevalent and was identified in only 3 of the 14 subjects who experienced vasovagal syncope alone and in no subjects who experienced vasovagal syncope with asystole. The duration of the syncopal phase was also significantly shorter in the group with rapid vasovagal syncope ending in asystole than in the group with rapid vasovagal syncope alone (Fig. 3).

In the following sections, statistical comparisons will be made between the groups who experienced rapid vasovagal syncope alone and rapid vasovagal syncope with asystole. Since the vasodepressive groups (i.e. vasodepressive syncope alone and vasodepressive syncope with asystole) contain only a small number of subjects, no statistical comparisons can be made at this time, but average data will be presented. Since the slow vasovagal syncope group contains a

small number of individuals and has no equivalent asystole group, statistical comparisons can not be made and group averages will not be presented.

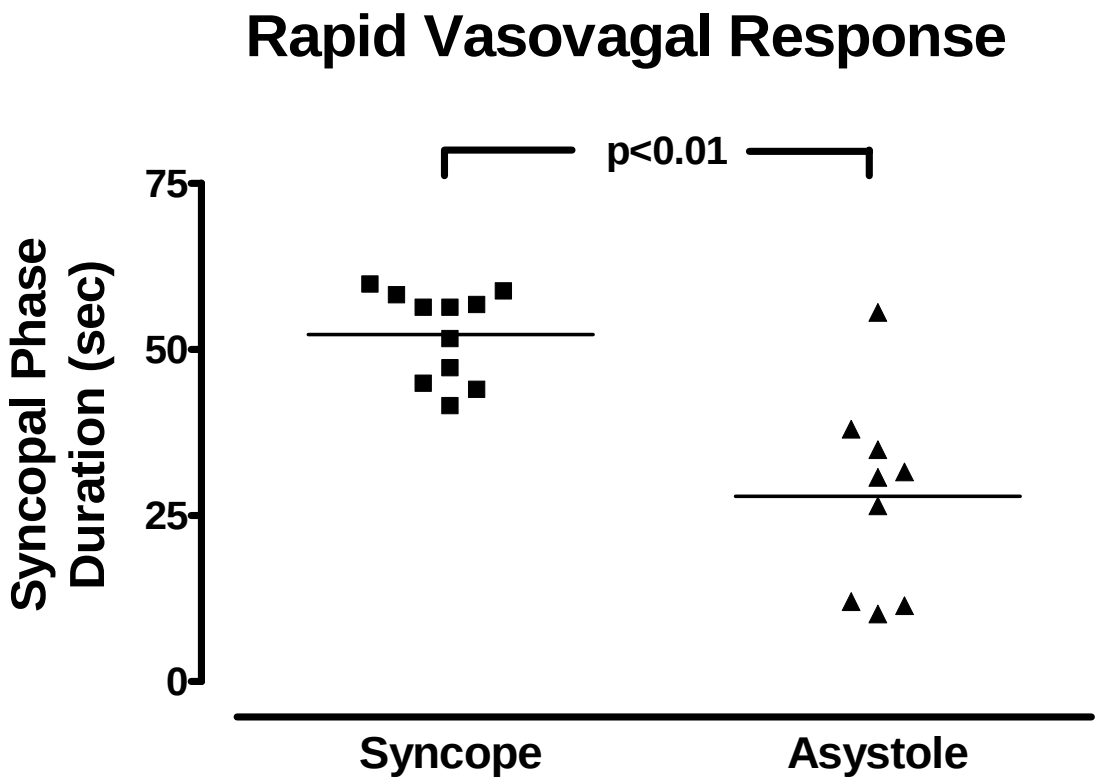

Figure 3. Duration of the pre-syncopal phase for rapid vasovagal syncope alone (Syncope; left), and rapid vasovagal syncope with asystole (right).

Time Dependent Spectral Analysis During Syncope

The average wavelet-derived LF and HF spectral series for the RRI and SBP time series for rapid vasovagal syncope alone and with asystole are shown in Fig 4A and 4B, respectively. Noticeable differences exist in the time courses of the two groups. The LF_{RRI} increases substantially in the last 30 seconds prior to asystole, but a similar increase is not evident in the LF_{RRI} of the syncope alone group. The syncope alone group shows a decrease in the LF_{SBP} in the final 60 seconds prior to syncope which is not demonstrated in the asystole group. Both groups appear to have elevated HF_{RRI} and HF_{SBP} prior to syncope.

Similar discrepancies can be seen in the wavelet-derived LF and HF components of the RRI and SBP series of the groups with vasodepressive syncope alone and vasodepressive syncope with asystole (Fig 5A and 5B, respectively). The LF_{RRI} again demonstrates an increase

over the last 30 seconds of the syncopal phase in the vasodepressive asystole group, a change which is not mirrored in the depressive syncope group. Both groups appear to have a drop in LF_{SBP} by the end of the syncopal phase, but this drop occurs much earlier in the vasodepressive asystole group, whose LF_{SBP} begins high and then drops approximately 200 seconds prior to asystole, even before the average SBP begins to fall. It must also be noted that the variability (SEM, dotted lines) in all of the parameters for both groups, but particularly for those of the vasodepressive syncope with asystole, is very high due to the small number of subjects involved in the averages.

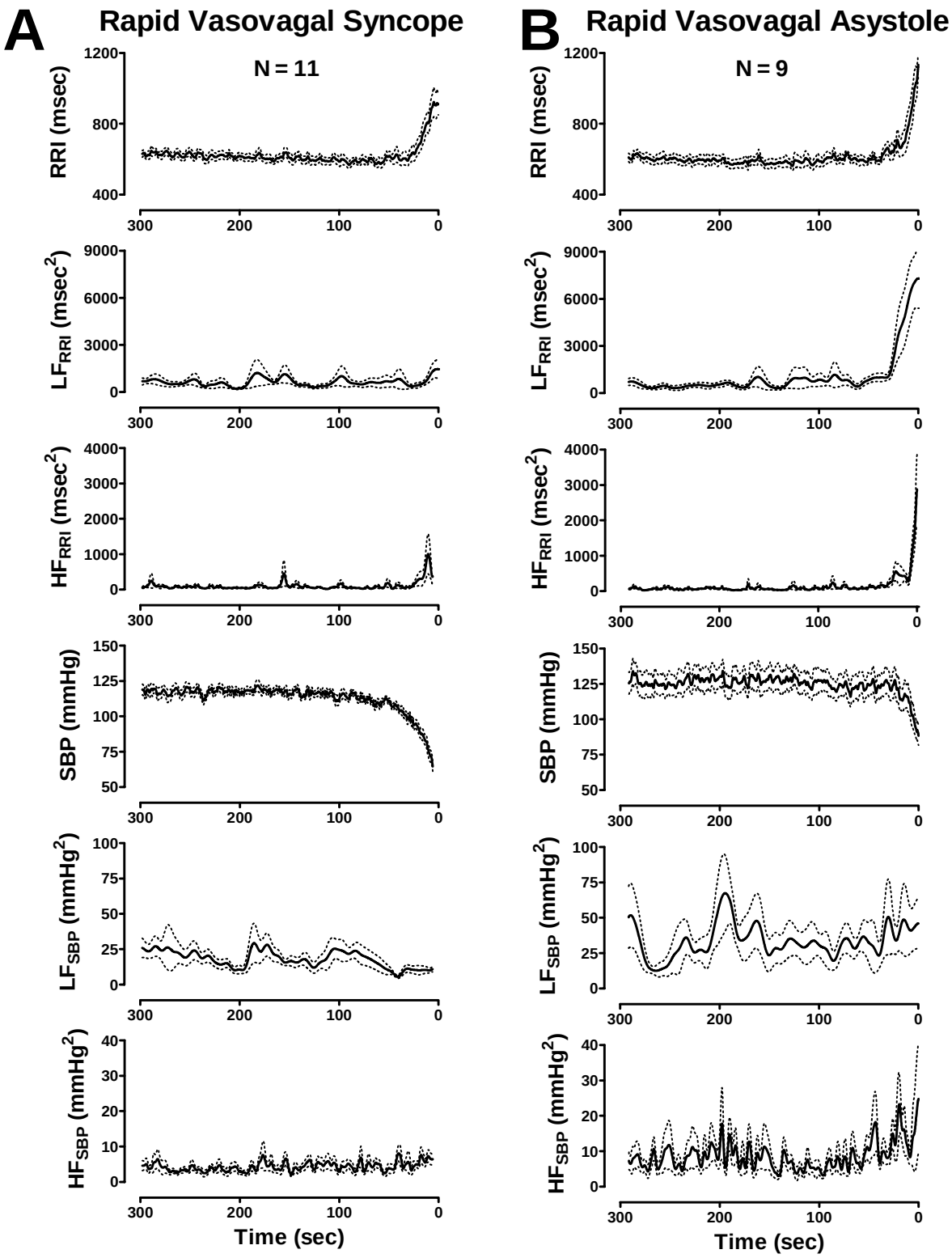

Figure 4. The mean RRI, SBP, and their time-varying wavelet low frequency (LF) and high frequency (HF) components for rapid vasovagal syncope **(A)** and rapid vasovagal syncope with asystole **(B)**. Solid line is the mean and dotted lines are the SEM.

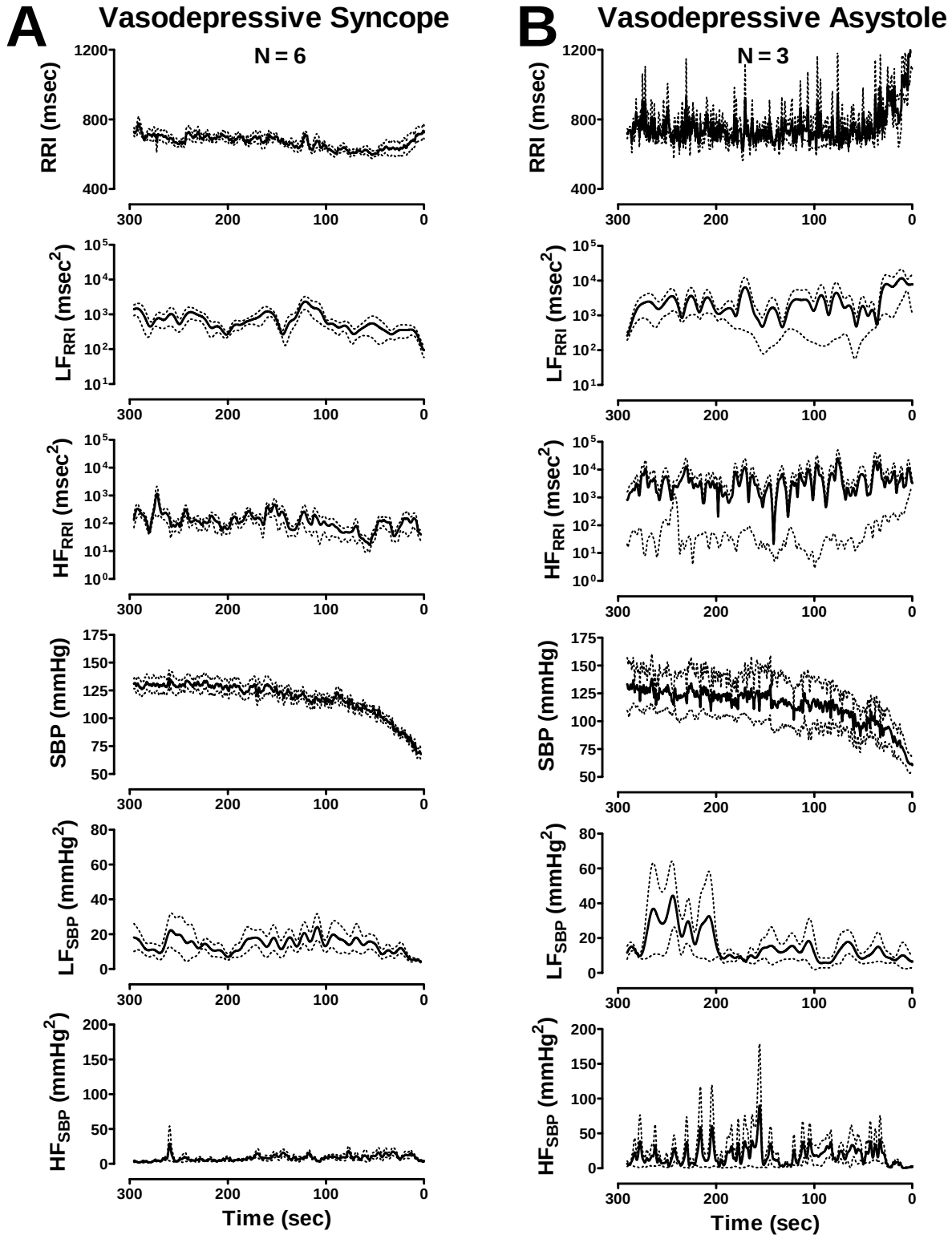

Figure 5. The mean RRI, SBP, and their time-varying wavelet low frequency (LF) and high frequency (HF) components for vasodepressive syncope **(A)** and vasodepressive syncope with asystole **(B)**. Solid lines are the means and dotted line are the SEM.

Comparison of Changes in HRV and BPV Before and During Syncope

Statistical tests were used to determine if the changes in both time domain and spectral parameters for the two groups of rapid vasovagal syncope (i.e. with and without asystole) were significant. The RRI prolongation rate, calculated as the slope of the RRI over the syncopal phase, was found to be higher in the rapid vasovagal group with asystole than in the group with syncope alone (20.1±3.5 vs 7.0±0.9 msec/sec, $p<0.01$; Fig. 5A). The LF_{RRI} was shown to increase significantly in the final phase of syncope in the vasovagal asystole group (838.6±215.8 to 4922±1354 $msec^2$, $p<0.01$), while only a slight increase occurred in the rapid vasovagal syncope alone group (525.7±200.6 to 678.3±215.5 $msec^2$, $p>0.05$; Fig. 5B). The HF_{RRI} was found to increase from 112.6±27.0 to 674.6±79.2 ms^2 ($p<0.01$) in the vasovagal asystole group and from 52.1±18.2 to 285.2±123.1 ms^2, $p<0.02$ in the rapid vasovagal syncope alone group (Fig 5D). But while the syncope alone group demonstrated a significant drop in LF_{SBP} during the final stage (20.7±4 to 9.7±1.6 $mmHg^2$, $p<0.01$), LF_{SBP} was slightly elevated in the asystole group (34.9±9.9 to 45.4±17.1 $mmHg^2$, $p>0.05$; Fig 5B)

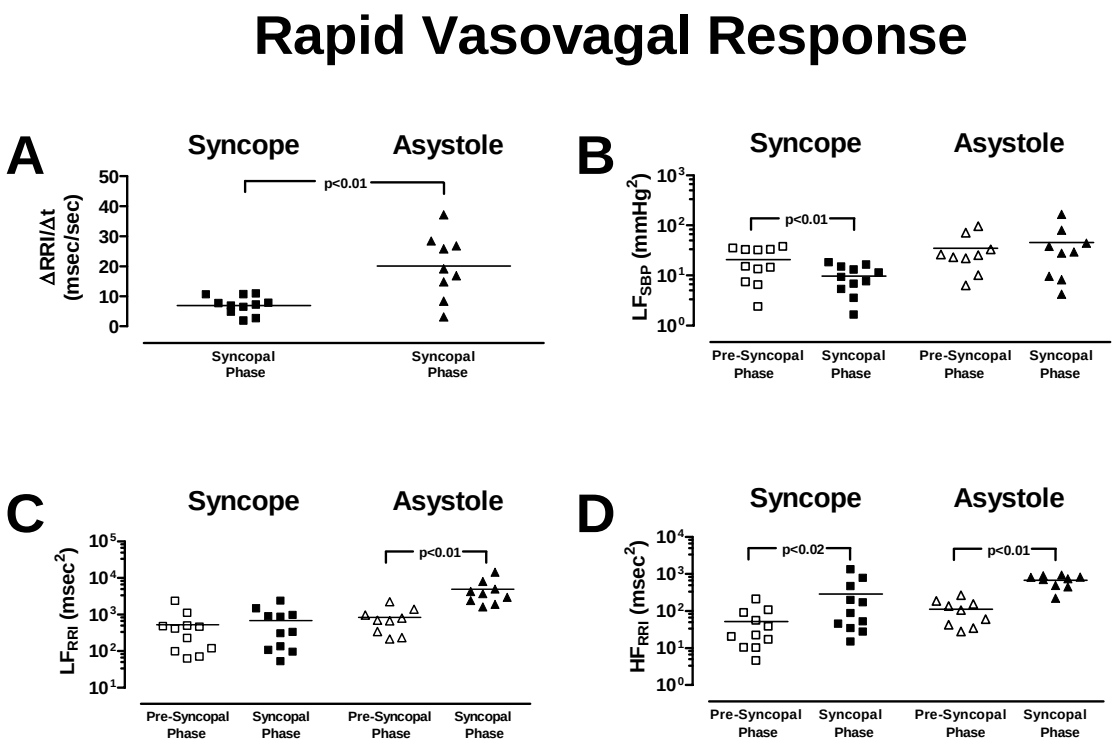

Figure 6. Difference between rapid vasovagal syncope (syncope) and rapid vasovagal syncope with asystole (asystole). The slope of the RRI increase in these two groups during the syncopal phase is compared in **(A)**. Changes in wavelet LF_{SBP} **(B)** LF_{RRI} **(C)** and HF_{RRI} **(D)** between the period of SBP decrease (syncopal phase) and 1-minute before (pre-syncopal phase) are also presented.

The same comparisons were made for the syncopal phases of the vasodepressive syncope groups with and without asystole. While tendencies are visible in the two groups, statistical comparisons did not reveal any significant differences due to the low number of subjects in each group. In both groups, the LF_{SBP} tended to decrease during the syncopal phase, Five of the six vasodepressive syncope alone subjects and all of the vasodepressive asystole subjects demonstrated reduced LF_{SBP} during vasovagal syncope (Fig. 7B). The LF_{RRI} of the vasodepressive asystole group tended to increase, as each subjects showed a greater than 2-fold increase during the syncopal phase, while the vasodepressive syncope alone group did not demonstrate this tendency, 4 of the 6 subjects showed a decreased LF_{RRI} during syncope (Fig. 7C). The other parameters (HF_{RRI} and RRI prolongation rate) demonstrated variability amongst both groups.

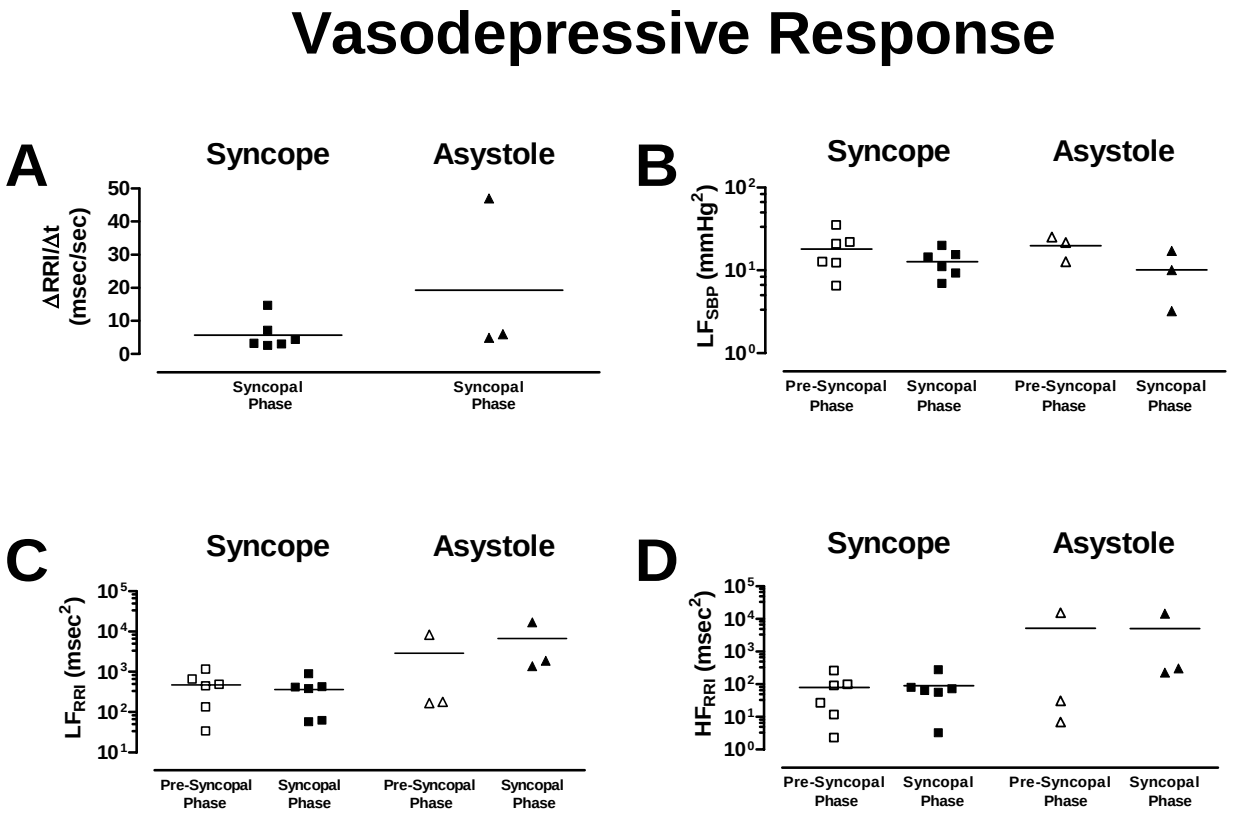

Figure 7. Changes in vasodepressive syncope (syncope) and vasodepressive syncope with asystole (asystole) during the syncopal phase. The slope of the RRI increase in these two groups during the syncopal phase is compared in **(A)**. Changes in wavelet LF_{SBP} **(B)** LF_{RRI} **(C)** and HF_{RRI} **(D)** between the period of SBP decrease (syncopal phase) and 1-minute before (pre-syncopal phase) are also presented.

Discussion

This is the first report to compare the autonomic changes that occur during syncope to those that occur during syncope with asystole in healthy subjects. We have identified three distinct syncopal groups, rapid vasovagal syncope (syncopal phase < 60 sec), slow vasovagal syncope (syncopal phase > 60 sec), and vasodepressive syncope (blood pressure drops well before heart rate). These grouping were based on the length of time of the syncopal phase and the difference between the times of onset of blood pressure decrease and R-R interval (RRI) increase. We have found that healthy subjects who develop asystole (> 3sec) during rapid vasovagal syncope undergo different changes in heart rate and blood pressure variability than those who experience rapid vasovagal syncope alone. Primarily, subjects who do not experience asystole during rapid vasovagal syncope demonstrate time varying spectral patterns that are consistent with sympathetic withdrawal, patterns which are not present in the corresponding asystole group. This suggests that sympathetic withdrawal is a protective mechanism which occurs in the late stages of syncope. The absence or failure of this mechanism during vagally induced bradycardia can lead to a near critical state of asystole which subsists until the removal of the orthostatic stress.

Syncope Groupings

The difference between the times of onset of the decline of systolic blood pressure and the rise in RRI was used to initially separate the groups into subjects who experienced a vasovagal response from those with a vasodepressive type response. The pattern described here as vasodepressive syncope was most similar to the *dysautonomic vasovagal pattern* described in the syncope literature [11]. The vasodepressive pattern identified here differs from the described dysautonomic pattern in that the fall in blood pressure did not always occur immediately after the application of orthostatic stress. However, a slow decline in the blood pressure does initiate the syncopal reaction and a noticeable rise in RRI was found to occur near the end of syncope.

The difference between the length of the SBP decrease and the length of the RRI rise was significantly lower in the group which experienced vasovagal syncope with asystole than in the group that experienced vasovagal syncope alone. Additionally, in the majority of the vasovagal asystole subjects the heart rate dropped before the blood pressure drop, which was not the case for the vasovagal syncope without asystole. This is mostly consistent with the modified VASIS

syncopal classification *Type 2B – cardioinhibitory with asystole*, which describes the heart rate fall as coinciding with or preceding the fall in blood pressure [11].

The final phase of syncope was defined as the period between the start of RRI prolongation and the loss of consciousness. Using this feature as a second criterion, we were able to identify two populations of vasovagal syncope. Rapid vasovagal syncope occurred in less than 60 seconds and was characterized by a rapid decline in SBP and heart rate, and was most similar to the *classic vasovagal syncope* described previously [11]. This syncopal period was significantly shorter in the studied individuals who developed vasovagal syncope with asystole. This suggests that asystole is not simply the result of failure to promptly eliminate orthostatic stress during a vasovagal response but may be caused by a separate mechanism than syncope alone.

Comparison of Changes in HRV and BPV Before and During Syncope

The HF_{RRI} significantly increased in the final phase of syncope in subjects with rapid vasovagal syncope with and without asystole, indicating that the bradycardia was induced by vagal cardiac activation, as previously reported in syncope patients [4;36]. Over the same period, the LF_{RRI} seen in the group with rapid vasovagal syncope with asystole increases while in the group with rapid vasovagal syncope alone LF_{RRI} does not change from presyncope. These same tendencies in LF_{RRI} are apparent in the groups with vasodepressive syncope with and without asystole, all subjects with asystole demonstrated increased LF_{RRI} and no consistent change was apparent in subjects who did not have asystole. An increase in LF_{RRI} is suggestive of sympathetic cardiac activation, but it has also been linked to an increase in parasympathetic activity as well [37].

Several previous studies involving patients with recurrent syncope have demonstrated that a dramatic withdrawal of muscle sympathetic activity is responsible for the peripheral vasodilatation during late stage vasovagal syncope [4;36]. Similarly, we found that the low frequency component of systolic blood pressure (LF_{SBP}), which has been linked to peripheral sympathetic innervations [38;39], dropped significantly during the final stages of syncope in the group with rapid vasovagal syncope alone. This pattern was consistent with the findings of similar analyses performed with wavelets [18] and complex demodulation [17] on syncope data and a similar tendency was also evident in the groups with vasodepressive syncope alone and

vasodepressive syncope with asystole. In contrast, the LF_{SBP} was slightly elevated in the group that developed vasovagal syncope with asystole, suggesting an absence of peripheral sympathetic withdrawal.

The differences in HRV and BPV parameters observed in the two rapid vasovagal groups may be indicative of a separate autonomic mechanism for rapid vasovagal syncope alone and rapid vasovagal syncope with asystole.

Limitations

This study was performed retrospectively with records compiled from several institutions because the occurrence of vasovagal syncope, in general, and vasovagal syncope with asystole, specifically, in healthy humans during orthostatic stress is extremely rare. While the nature of the orthostatic stress was similar in each case, the protocols may have differed slightly from subject to subject. We have attempted to address this issue by comparing individuals who had undergone a minimum of five minutes of constant orthostatic stress prior to the syncopal event.

We also recognize that more direct measures of autonomic activity, such as recordings of the sympathetic nerve activity, would lend more power to our conclusions. However, this information was not available in these rare recordings necessitating the use of indirect autonomic assessment through heart rate and blood pressure variability.

Conclusions

Using a Hilbert-modified continuous wavelet transform, we were able to analyze nonstationary HRV and BPV data from healthy subjects during vasovagal syncope with and without asystole. The analysis demonstrated that the asystole group demonstrated significantly different spectral patterns, particularly in the low frequency oscillations of the RR interval and systolic blood pressure series. These findings suggested that the sympathetic withdrawal typically observed during vasovagal syncope was absent in subjects with asystole. In conclusion, different autonomic control mechanisms are responsible for vasovagal syncope with and without asystole.

References

[1] R. Mosqueda-Garcia, R. Furlan, J. Tank, and R. Fernandez-Violante, "The elusive pathophysiology of neurally mediated syncope," *Circulation*, vol. 102, no. 23, pp. 2898-2906, Dec.2000.

[2] M. Brignole, P. Alboni, D. G. Benditt, L. Bergfeldt, J. J. Blanc, P. E. Bloch Thomsen, J. G. Van Dijk, A. Fitzpatrick, S. Hohnloser, J. Janousek, W. Kapoor, R. A. Kenny, P. Kulakowski, G. Masotti, A. Moya, A. Raviele, R. Sutton, G. Theodorakis, A. Ungar, and W. Wieling, "Guidelines on management (diagnosis and treatment) of syncope--update 2004," *Europace.*, vol. 6, no. 6, pp. 467-537, Nov.2004.

[3] R. D. Thijs, W. Wieling, H. Kaufmann, and D. G. van, "Defining and classifying syncope," *Clin Auton Res*, vol. 14 Suppl 1, pp. 4-8, Oct.2004.

[4] R. Mosqueda-Garcia, R. Furlan, R. Fernandez-Violante, T. Desai, M. Snell, Z. Jarai, V. Ananthram, R. M. Robertson, and D. Robertson, "Sympathetic and baroreceptor reflex function in neurally mediated syncope evoked by tilt," *J Clin Invest*, vol. 99, no. 11, pp. 2736-2744, June1997.

[5] S. Ogoh, S. Volianitis, P. B. Raven, and N. H. Secher, "Carotid baroreflex function ceases during vasovagal syncope," *Clin Auton Res*, vol. 14, no. 1, pp. 30-33, Feb.2004.

[6] A. Fitzpatrick, G. Theodorakis, P. Vardas, R. A. Kenny, C. M. Travill, A. Ingram, and R. Sutton, "The incidence of malignant vasovagal syndrome in patients with recurrent syncope," *Eur. Heart J*, vol. 12, no. 3, pp. 389-394, Mar.1991.

[7] R. H. Murray, L. J. Thompson, J. A. Bowers, and C. D. Albright, "Hemodynamic effects of graded hypovolemia and vasodepressor syncope induced by lower body negative pressure," *Am Heart J*, vol. 76, no. 6, pp. 799-811, Dec.1968.

[8] K. Sander-Jensen, N. H. Secher, A. Astrup, N. J. Christensen, J. Giese, T. W. Schwartz, J. Warberg, and P. Bie, "Hypotension induced by passive head-up tilt: endocrine and circulatory mechanisms," *Am J Physiol*, vol. 251, no. 4 Pt 2, p. R742-R748, Oct.1986.

[9] J. S. Sanders and D. W. Ferguson, "Profound sympathoinhibition complicating hypovolemia in humans," *Ann. Intern. Med.*, vol. 111, no. 5, pp. 439-441, Sept.1989.

[10] D. Robertson, G. A. Johnson, R. M. Robertson, A. S. Nies, D. G. Shand, and J. A. Oates, "Comparative assessment of stimuli that release neuronal and adrenomedullary catecholamines in man," *Circulation*, vol. 59, no. 4, pp. 637-643, Apr.1979.

[11] M. Brignole, C. Menozzi, R. A. Del, S. Costa, G. Gaggioli, N. Bottoni, P. Bartoli, and R. Sutton, "New classification of haemodynamics of vasovagal syncope: beyond the VASIS

classification. Analysis of the pre-syncopal phase of the tilt test without and with nitroglycerin challenge. Vasovagal Syncope International Study," *Europace.*, vol. 2, no. 1, pp. 66-76, Jan.2000.

[12] R. B. Hickler, R. G. Hoskins, and J. T. Hamlin, III, "The clinical evaluation of faulty orthostatic mechanisms," *Med Clin North Am*, vol. 44, pp. 1237-1250, Sept.1960.

[13] S. Akselrod, D. Gordon, F. A. Ubel, D. C. Shannon, A. C. Berger, and R. J. Cohen, "Power spectrum analysis of heart rate fluctuation: a quantitative probe of beat-to-beat cardiovascular control," *Science*, vol. 213, no. 4504, pp. 220-222, July1981.

[14] Task Force, "Heart rate variability: standards of measurement, physiological interpretation and clinical use. Task Force of the European Society of Cardiology and the North American Society of Pacing and Electrophysiology [see comments]," *Circulation*, vol. 93, no. 5, pp. 1043-1065, Mar.1996.

[15] R. Furlan, A. Porta, F. Costa, J. Tank, L. Baker, R. Schiavi, D. Robertson, A. Malliani, and R. Mosqueda-Garcia, "Oscillatory patterns in sympathetic neural discharge and cardiovascular variables during orthostatic stimulus," *Circulation*, vol. 101, no. 8, pp. 886-892, Feb.2000.

[16] M. Pagani, N. Montano, A. Porta, A. Malliani, F. M. Abboud, C. Birkett, and V. K. Somers, "Relationship between spectral components of cardiovascular variabilities and direct measures of muscle sympathetic nerve activity in humans," *Circulation*, vol. 95, no. 6, pp. 1441-1448, Mar.1997.

[17] A. Kamiya, J. Hayano, T. Kawada, D. Michikami, K. Yamamoto, H. Ariumi, S. Shimizu, K. Uemura, T. Miyamoto, T. Aiba, K. Sunagawa, and M. Sugimachi, "Low-frequency oscillation of sympathetic nerve activity decreases during development of tilt-induced syncope preceding sympathetic withdrawal and bradycardia," *Am J Physiol Heart Circ Physiol*, vol. 289, no. 4, p. H1758-H1769, Oct.2005.

[18] M. Suzuki, S. Hori, I. Nakamura, S. Nagata, Y. Tomita, and N. Aikawa, "Role of vagal control in vasovagal syncope," *Pacing Clin Electrophysiol.*, vol. 26, no. 2 Pt 1, pp. 571-578, Feb.2003.

[19] R. Sutton, M. Brignole, C. Menozzi, A. Raviele, P. Alboni, P. Giani, and A. Moya, "Dual-chamber pacing in the treatment of neurally mediated tilt-positive cardioinhibitory syncope : pacemaker versus no therapy: a multicenter randomized study. The Vasovagal Syncope International Study (VASIS) Investigators," *Circulation*, vol. 102, no. 3, pp. 294-299, July2000.

[20] J. S. Sra, M. R. Jazayeri, B. Avitall, A. Dhala, S. Deshpande, Z. Blanck, and M. Akhtar, "Comparison of cardiac pacing with drug therapy in the treatment of neurocardiogenic

(vasovagal) syncope with bradycardia or asystole," *N Engl J Med*, vol. 328, no. 15, pp. 1085-1090, Apr.1993.

[21] J. Penaz, "Photoelectric measurement of blood pressure, volume and flow in the finger," *Digest of the 10th international conference on medical and biological engineering - Dresden.*, p. 104, 1973.

[22] J. Pan and W. J. Tompkins, "A real-time QRS detection algorithm," *IEEE Trans. Biomed. Eng*, vol. 32, no. 3, pp. 230-236, Mar.1985.

[23] Task Force, "Heart rate variability: standards of measurement, physiological interpretation and clinical use. Task Force of the European Society of Cardiology and the North American Society of Pacing and Electrophysiology [see comments]," *Circulation*, vol. 93, no. 5, pp. 1043-1065, Mar.1996.

[24] R. G. Shiavi, *Introduction to Applied Statistical Signal Analysis*, 2nd ed. San Diego: Academic Press, 1999.

[25] M. Akay, G. Landesberg, W. Welkowitz, Y. M. Akay, and D. Sapoznikov, "Carotid-cardiac interaction: heart rate variability during the unblocking of the carotid artery," *Adv Exp Med Biol*, vol. 346, pp. 365-372, 1993.

[26] J. A. Crowe, N. M. Gibson, M. S. Woolfson, and M. G. Somekh, "Wavelet transform as a potential tool for ECG analysis and compression," *J Biomed Eng*, vol. 14, no. 3, pp. 268-272, 1992.

[27] V. Pichot, J. M. Gaspoz, S. Molliex, A. Antoniadis, T. Busso, F. Roche, F. Costes, L. Quintin, J. R. Lacour, and J. C. Barthelemy, "Wavelet transform to quantify heart rate variability and to assess its instantaneous changes," *J. Appl. Physiol*, vol. 86, no. 3, pp. 1081-1091, Mar.1999.

[28] K. Tanaka and A. R. Hargens, "Wavelet packet transform for R-R interval variability," *Med. Eng Phys.*, vol. 26, no. 4, pp. 313-319, May2004.

[29] E. Toledo, O. Gurevitz, H. Hod, M. Eldar, and S. Akselrod, "Wavelet analysis of instantaneous heart rate: a study of autonomic control during thrombolysis," *Am. J. Physiol Regul. Integr. Comp Physiol*, vol. 284, no. 4, p. R1079-R1091, Apr.2003.

[30] U. Wiklund, M. Akay, and U. Niklasson, "Short-term analysis of heart-rate variability by adapted wavelet transforms," *IEEE Eng Med Biol Mag*, vol. 16, no. 5, pp. 113-8, 138, 1997.

[31] A. Cohen and J. Kovacevic, "Wavelets: The mathematical background," *P Ieee*, vol. 84, no. 4, pp. 514-522, 1996.

[32] S. Olhede and A. Walden, "The Hilbert spectrum via wavelet projections.," *P ROY SOC LOND A MAT P ROY SOC LOND A MAT*, vol. 460, pp. 955-975, 2004.

[33] H. Olkkonen, P. Pesola, J. Olkkonen, and H. Zhou, "Hilbert transform assisted complex wavelet transform for neuroelectric signal analysis," *J Neurosci Methods*, vol. 151, no. 2, pp. 106-113, 2006.

[34] I. Daubechies, *Ten Lectures on Wavlets*. Montpelier, Vermont: Capital City Press, 1992.

[35] Task Force, "Heart rate variability: standards of measurement, physiological interpretation and clinical use. Task Force of the European Society of Cardiology and the North American Society of Pacing and Electrophysiology [see comments]," *Circulation*, vol. 93, no. 5, pp. 1043-1065, Mar.1996.

[36] C. A. Morillo, D. L. Eckberg, K. A. Ellenbogen, L. A. Beightol, J. B. Hoag, K. U. Tahvanainen, T. A. Kuusela, and A. M. Diedrich, "Vagal and sympathetic mechanisms in patients with orthostatic vasovagal syncope," *Circulation*, vol. 96, no. 8, pp. 2509-2513, Oct.1997.

[37] Task Force, "Heart rate variability: standards of measurement, physiological interpretation and clinical use. Task Force of the European Society of Cardiology and the North American Society of Pacing and Electrophysiology," *Circulation*, vol. 93, no. 5, pp. 1043-1065, Mar.1996.

[38] A. Diedrich, J. Jordan, J. Tank, J. R. Shannon, R. Robertson, F. C. Luft, D. Robertson, and I. Biaggioni, "The sympathetic nervous system in hypertension: assessment by blood pressure variability and ganglionic blockade," *J. Hypertens.*, vol. 21, no. 9, pp. 1677-1686, Sept.2003.

[39] R. Zhang, K. Iwasaki, J. H. Zuckerman, K. Behbehani, C. G. Crandall, and B. D. Levine, "Mechanism of blood pressure and R-R variability: insights from ganglion blockade in humans," *J. Physiol*, vol. 543, no. Pt 1, pp. 337-348, Aug.2002.

CHAPTER VII

CONCLUSIONS AND FUTURE DIRECTIONS

Summary

This thesis presents several new methodologies that can be used to advance the study and assessment of the autonomic nervous system. Direct assessment of sympathetic function is through microneurography is typically used by researchers to investigate autonomic origins of diseases and the effects of pharmacological agents on the sympathetic nervous system [1]. But, in the signals achieved through microneurography, quantification has always been an issue of debate. In response to this problem, we have devised, tested, and validated improved quantification strategies for the muscle sympathetic nerve activity in humans and the renal sympathetic nerve activity in mice. We have shown that wavelet-based spike detection methods are capable of providing accurate spike detection under a wide variety of signal qualities and states of sympathetic activation in humans and mice.

Although direct analysis of the sympathetic nerve signal is useful as a research based approach to sympathetic assessment, we recognize that this method is not always practical, particularly in clinical situations. As a result, in Chapter V, we provided a link between the detected spike rate series and the continuous blood pressure waveform. The low frequency oscillations in the sympathetic spike rate were found to have a strong linear, temporal correlation to the low frequency oscillations in the systolic blood pressure. Consequently, the power of these low frequency blood pressure oscillations could be used to indirectly estimate the power of the low frequency oscillations, or bursts, in the sympathetic spike rate. Since the continuous blood pressure waveform requires less technical skill to measure, it is more convenient clinically to derive the indirect estimates of sympathetic function from this signal than to measure sympathetic nerve activity directly.

In Chapter VI, a form of time varying spectral analysis capable of dealing with non-stationary heart rate and blood pressure data was developed using a modified wavelet transform. This method was able to exploit the relationship determined in Chapter V to indirectly estimate changes to the state of the sympathetic activity during episodes of syncope, a common symptom of many dysautonomias. Using this method of indirect analysis, potential mechanisms for

syncope alone and syncope ending in asystole, a rare stoppage of the heart, were able to be postulated.

Conclusions

In conclusion, several advancements have been made in the field of autonomic assessment as a result of the work performed in this thesis. The following generalizations can be drawn from the information presented:

1. It is possible to accurately quantify the sympathetic nerve activity through automated spike detection given that the signal to noise ratio is greater than 3 for human muscle sympathetic nerve activity or greater than 2 for murine renal sympathetic nerve activity.
2. The stationary wavelet transform is more appropriate than the discrete wavelet transform for the detection of transient spikes in high levels of noise. This conclusion is a direct result of the lack of translation invariance found in the discrete wavelet transform.
3. The most robust spike detection algorithm for human muscle sympathetic nerve activity is one which takes advantage of the synchronous, bursting properties of the sympathetic neurons and the Gaussinity of its noise. A two-stage, kurtosis de-noising algorithm, such as that proposed in Chapter III, accounts for both properties.
4. Automated, wavelet based spike detection can be translated to the mouse renal sympathetic nerve activity. However, a different detection strategy than that used in the human sympathetic activity is required to account for the different discharge patterns found in the mouse. A detector based on the stationary wavelet transform and a single level noise estimation threshold is the most robust against changes in spike rate and signal to noise ratio.
5. Automated action potential detection is important in renal sympathetic nerve activity to demonstrate the differences between normal and transgenic mouse populations.
6. As was long suspected, a definite temporal link exists between the fluctuations in blood pressure, muscle sympathetic nerve activity, and respiration in humans. This relationship was brought to light using the spike detection method described in Chapter III, and could not be found formerly when integrated parameters were used [2]. Consequently, the low frequency oscillations in the blood pressure provide a good indirect measure of the state of sympathetic activity.

7. Indirect estimates of autonomic function can be used to highlight differences in two autonomic outcomes. When used on normal subjects who experienced vasovagal syncope alone and vasovagal syncope with asystole, these indirect parameters were able to determine a potential mechanism for asystole.

Future Directions

The primary motivation for this work was to further develop both direct and indirect methods of autonomic assessment for the study and potential diagnosis of autonomic disorders. Along these lines, we hope that the sympathetic spike detection procedures developed here can be applied to the analysis of human autonomic disorders and additional transgenic mouse populations. In humans, the spike detection technique described in Chapter III was able to clarify a relationship to blood pressure which was not evident when similar analysis was done using the burst area parameter [2]. Therefore, sympathetic quantification through spike detection may also reveal differences in various autonomic disorders that may have not been evident using the burst rate or burst area rate.

As mentioned in Chapter II, single unit sympathetic activity has identified differences between normal and pathological populations in humans that were not apparent in the sympathetic burst parameters [3-6]. However, single unit recordings are extremely difficult to achieve and maintain [1]. Therefore, implementing a method to automatically sort the detected spikes into classes derived from individual neurons may serve as an alternative to traditional single-unit recordings. Spike sorting may also be useful in the analysis of mouse sympathetic activity where, to our knowledge, single unit activity has not yet been analyzed.

Although the model presented in Chapter V accounted for the majority of the fluctuations in human blood pressure, a small percentage of the variability was still unaccounted for. Some recent evidence suggests that cardiac output could play a role in both blood pressure fluctuations [2] and sympathetic activity [7]. The addition of cardiac output may improve this model. Also, the relationship between sympathetic activity and blood pressure oscillations may not be strictly linear [8] and, consequently, non-linear mathematical descriptors should also be explored.

In Chapter VI, the indirect estimates of autonomic function using wavelet derived time-varying spectral analysis were able to demonstrate differences between rapid vasovagal syncope alone and rapid vasovagal syncope with asystole. Similarly, qualitative differences were

observed in the subjects who experienced vasodepressive syncope with and without asystole, but since the number of subjects in each group was small, statistical differences could not be realized. Therefore, more data must be collected and analyzed from normal subjects that experience such events. We would also like to determine if the same patterns of time varying spectral patterns exist in patients who experience recurrent syncope.

The long term goals for this project include real-time implementations of much of the work described in this thesis. On-line detection of spikes in murine and human sympathetic nerve activity would provide the investigator with quantitative feedback of the spike rate during various interventions, which could be useful for adjusts in protocol or instrumentation. Real-time analysis of the spectral components of continuous blood pressure and heart rate could be used to alert researchers or clinicians of an impending syncopal episode. This information may also be useful in the design of pacemakers that are sensitive to changes in both heart rate and blood pressure.

References

[1] B. G. Wallin, "Sympathetic Microneurography," in *Primer on the Autonomic Nervous System*, 2 ed. D. Robertson, Ed. Oxford, UK: Elsevier, 2004, pp. 224-227.

[2] C. W. Myers, M. A. Cohen, D. L. Eckberg, and J. A. Taylor, "A model for the genesis of arterial pressure Mayer waves from heart rate and sympathetic activity," *Auton. Neurosci.*, vol. 91, no. 1-2, pp. 62-75, Aug.2001.

[3] M. Elam and V. Macefield, "Multiple firing of single muscle vasoconstrictor neurons during cardiac dysrhythmias in human heart failure," *J Appl. Physiol*, vol. 91, no. 2, pp. 717-724, Aug.2001.

[4] V. G. Macefield, B. Rundqvist, Y. B. Sverrisdottir, B. G. Wallin, and M. Elam, "Firing properties of single muscle vasoconstrictor neurons in the sympathoexcitation associated with congestive heart failure," *Circulation*, vol. 100, no. 16, pp. 1708-1713, Oct.1999.

[5] V. G. Macefield and B. G. Wallin, "Firing properties of single vasoconstrictor neurones in human subjects with high levels of muscle sympathetic activity," *J Physiol (Lond)*, vol. 516 (Pt 1), pp. 293-301, Apr.1999.

[6] D. A. Mary and J. B. Stoker, "The activity of single vasoconstrictor nerve units in hypertension," *Acta Physiol Scand.*, vol. 177, no. 3, pp. 367-376, Mar.2003.

[7] N. Charkoudian, M. J. Joyner, C. P. Johnson, J. H. Eisenach, N. M. Dietz, and B. G. Wallin, "Balance between cardiac output and sympathetic nerve activity in resting humans: role in arterial pressure regulation," *J Physiol*, vol. 568, no. Pt 1, pp. 315-321, Oct.2005.

[8] J. Tank, A. Diedrich, E. Szczech, F. C. Luft, and J. Jordan, "Baroreflex Regulation of Heart Rate and Sympathetic Vasomotor Tone in Women and Men," *Hypertension*, vol. 25, no. 6, pp. 1159-1164, May2005.

APPENDIX A.

WAVELET PROCESSING

The Continuous Wavelet Transform

To evaluate a signal, *f*, using the continuous wavelet transform (CWT), one would first define a suitable mother wavelet or wavelet function, ψ, such as the Meyer wavelet shown in Figure 1. The mother wavelet can then be scaled and translated according to Eq. 1.

$$\psi_{s,\tau}(t) = \frac{1}{\sqrt{s}}\psi\left(\frac{t-\tau}{s}\right) \quad \textbf{(1)}$$

In Eq. 1, $\psi_{s,\tau}$ is a scaled, translated version of the mother wavelet, ψ, where *s* is the *wavelet scale* and τ is the *time-shift*. In the following discussion, all wavelet functions are assumed to be real, although the properties can be extended to complex wavelet functions as well. The signal *f* could then be described in terms of the real wavelet basis using Eq. 2.

$$d^{CWT}(s,\tau) = \int f(t)\psi_{s,\tau}(t)dt = \langle f, \psi_{s,\tau} \rangle \quad \textbf{(2)}$$

In this case, $\langle \cdots \rangle$ denotes an inner product of 2 vectors. For computational purposes, the scale parameter is generally modified dyadically, i.e. $s = 2^j$ where *j* is an integer representing the *wavelet level*, and the signal is sampled at regular intervals, resulting in regular, discrete values of the time shift, $\tau = Tn$ where *T* is a user defined sampling period.

$$d_j^{CWT}(n) = \langle f(t), \psi_{2^j}(t - Tn) \rangle \quad \textbf{(3)}$$

In Eq. 3, d_j^{CWT} is the output of the convolution at wavelet level *j*, or scale 2^j. The computation described in Eq. 3 can be interpreted from two distinct points of view. The first interpretation is that of a time domain convolution, where the values contained in d_j^{CWT} represent a measure of similarity between a wavelet of scale *s* and the signal at time *Tn*. According to this view, a higher scale would indicate a more dilated form of the wavelet and the coefficients at these higher scales would indicate the presence of long term trends in the signal. The transformation in Eq. 3 can also be seen as a band-pass filtering of *f*, where the scale, *s*, dictates the center frequency and bandwidth of the filter and d_j^{CWT} is the filtered signal. A dyadic increase in the scale would then limit the bandwidth overlap of successive filters by dividing

both the bandwidth and center frequency of the filter roughly in half for each increase in *j* (Figure 1).

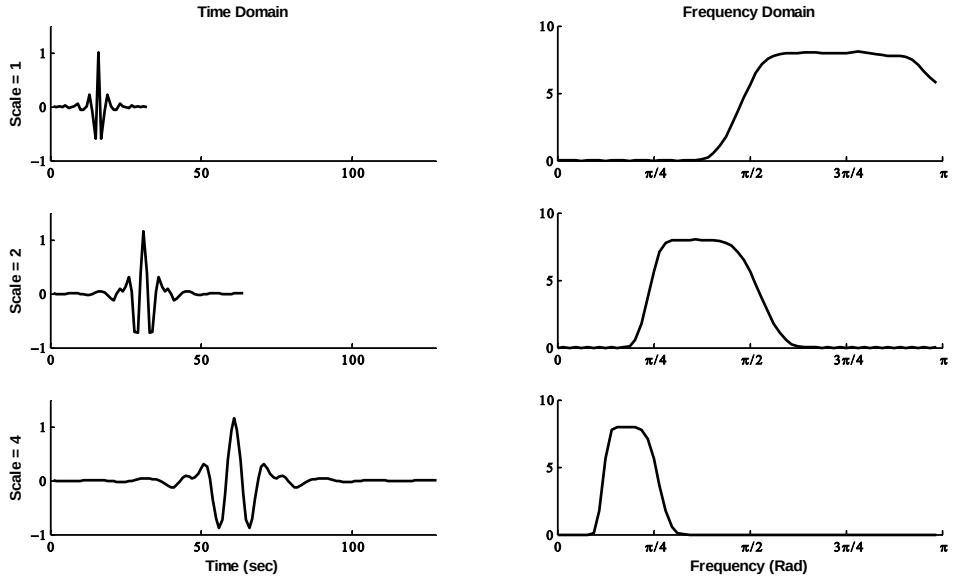

Figure 1. An example of the dyadic progression of scale and its affect on center frequency and bandwidth. The Meyer wavelet is used in this example.

The Discrete Wavelet Transform

To completely represent *f* in terms of CWT coefficients, i.e. d_j^{CWT}, an infinite number of dyadic scale steps would have to be taken, each step representing a smaller bandwidth centered on a lower frequency. An alternative approach to this operation was formulated by Mallat [1] who suggested an operator complementary to ψ called the scaling function, ϕ. If d_j^{CWT} is computed for all $j<J$, the scaling function can be used to compute all of the remaining information, i.e. the sum of d_j^{CWT} over all $j>J$. The scaling function is also scalable, as shown in Eq. 4

$$\phi_{s,\tau}(t) = \frac{1}{\sqrt{s}}\phi\left(\frac{t-\tau}{s}\right) \qquad \textbf{(4)}$$

where $\phi_{s,\tau}$ is the scaled, translated scaling function. The scaling function is applied to the signal, *f*, in a similar manner to that of the wavelet function (i.e. as in Eq. 2), as seen in Eq. 5.

$$a^{CWT}(s,\tau) = \int f(t)\frac{1}{\sqrt{s}}\phi\left(\frac{t-\tau}{s}\right)dt = \left\langle f, \phi_{s,\tau} \right\rangle \quad \textbf{(5)}$$

We have chosen to represent this transformation in a more compact form for our purposes. This can be seen in Eq. 6

$$a_j^{CWT}(n) = \left\langle f(t), \phi_{2^j}(t - Tn) \right\rangle \quad \textbf{(6)}$$

where a_j^{CWT} is the output of the scaling function convolution at wavelet level *j*.

Like the wavelet function, the scaling function can also be viewed as a filter whose bandwidth and center frequency are dictated by the scale. The bandwidth of the scaling function filter at scale *s* consists of all frequencies below that of the wavelet function at the same scale. Therefore, the coefficients found in a_j^{CWT} represent a low-pass filtered version of *f*. Figure contains the temporal and frequency information for the scaling functions that complement the Meyer wavelet functions found in Figure 2.

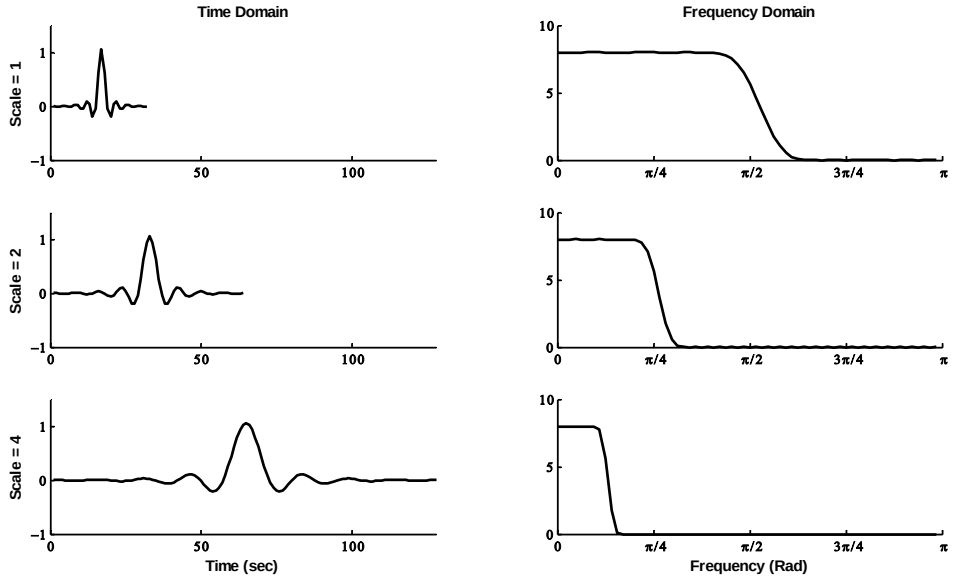

Figure 2. Time and frequency information for the Meyer scaling functions for scales 1, 2, and 4.

The temporal information found in both the a_j^{CWT} and d_j^{CWT} coefficients exhibit the same redundancy as the scaling information of the CWT. If the scale of the wavelet transform is increased dyadically, a signal of length *N* can be non-redundantly represented by $N/2^j$ dyadically sampled coefficients at scale 2^j. Therefore, the outputs of the scaling and wavelet function

operations can be simplified by letting $T = 2^j$, indicating a uniform down-sampling to eliminate redundancy. This is shown in Eq. 7 and 8.

$$a_j^{DWT}(n) = \left\langle f(t), \phi_{2^j}\left(t - 2^{-j} n\right)\right\rangle \quad \textbf{(7)}$$

$$d_j^{DWT}(n) = \left\langle f(t), \psi_{2^j}\left(t - 2^{-j} n\right)\right\rangle \quad \textbf{(8)}$$

Here, the a_j^{DWT} contain the low frequency output at level *j* and are termed the approximation coefficients of the discrete wavelet transform (DWT) because they can be used to construct a course approximation of *f*(*t*). The d_j^{DWT} contain the high frequency information at level *j* and thus are termed the detail coefficients of the DWT.

Mallat [1] noticed that the a_j^{DWT} DWT coefficients contain all of the information found in both the a_{j+1}^{DWT} and the d_{j+1}^{DWT} coefficients and purposed an efficient algorithm to compute the information found in the DWT. He defined 2 sets of mirror filters, h_0 , $\tilde{h}_0$ and g_0 , $\tilde{g}_0$ such that:

$$h_0(-m) = \int_{-\infty}^{\infty} \phi_{1,m}(t)\phi_{0,0}(t)dt \quad \textbf{(10)}$$

$$g_0(-m) = \int_{-\infty}^{\infty} \phi_{1,m}(t)\psi_{0,0}(t)dt \quad \textbf{(11)}$$

$$\tilde{h}_0(m) = h_0(-m) \quad \textbf{(12)}$$

$$\tilde{g}_0(m) = g_0(-m) \quad \textbf{(13)}$$

We will refer to h_0 as the low-pass decomposition filter, $\tilde{h}_0$ as the low-pass reconstruction filter, g_0 as the high-pass decomposition filter, and $\tilde{g}_0$ as the high-pass reconstruction filter. Using the decomposition filters, we can compute the next set of approximation and detail coefficients with the relationships described in Eq. 13 and 14.

$$a_{j+1}^{DWT}(k) = \sum_n h_0(n-2k)a_j^{DWT}(k). \quad \textbf{(13)}$$

$$d_{j+1}^{DWT}(k) = \sum_n g_0(n-2k)a_j^{DWT}(k) \quad \textbf{(14)}$$

In Eq. 13 the a_{j+1}^{DWT} coefficients are computed by convolving the a_j^{DWT} with the low-pass decomposition filter, h_0, and then down-sampling the result by two. Likewise, the d_{j+1}^{DWT} detail

coefficients are computed by filtering the a_j^{DWT} approximation coefficients with the high-pass decomposition filter and down-sampling by two. This procedure, known as a pyramidal cascade, can be iteratively continued until the desired level of decomposition ($j=J$) is obtained. During each successive iteration, the DWT splits the bandwidth of the remaining signal, storing a portion of the signal's fine detail in the detail coefficients corresponding to that level and leaving a set of approximation coefficients capable of constructing a coarser version of the original signal. Figure 3 demonstrates the bandwidth decomposition of a signal sampled at 10,000 Hz over five levels of the DWT. At each step, the red area represents the bandwidth of the approximation coefficients and the grey area represents the bandwidth of the detail coefficients.

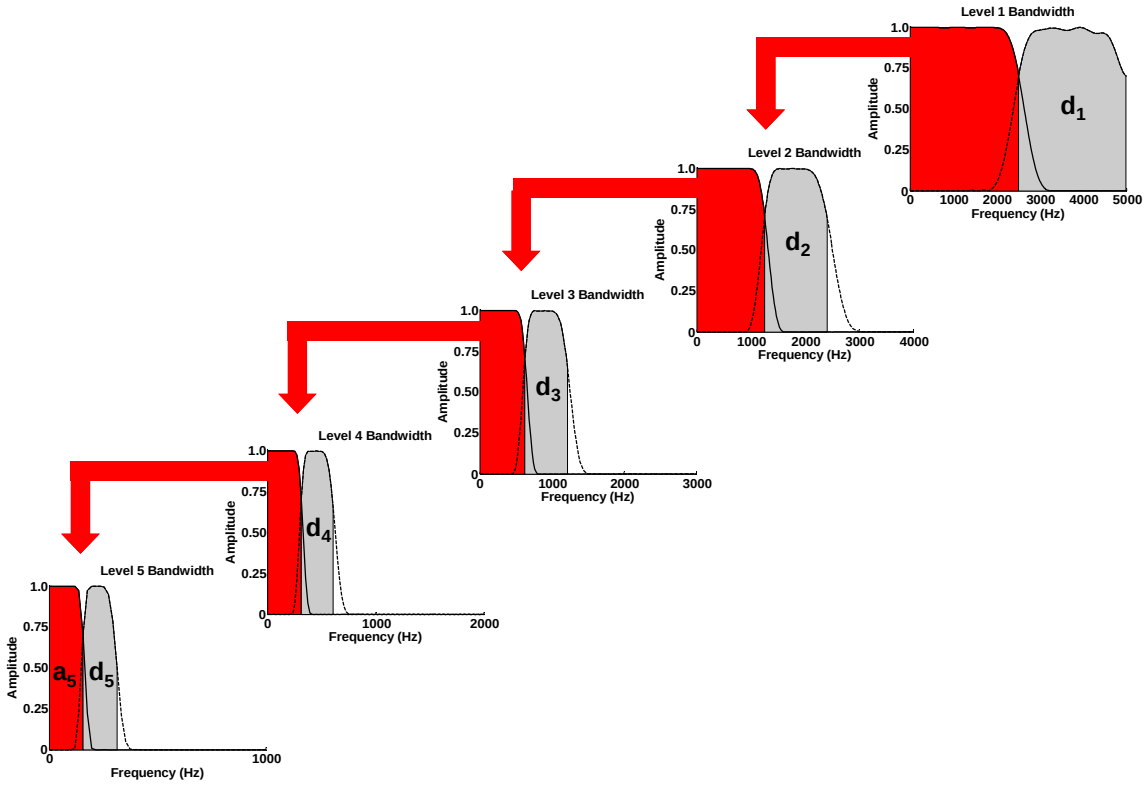

Figure 3. Approximate bandwidth of each wavelet level during DWT decomposition of a signal sampled at 10,000 Hz. At each step of the decomposition, the high-pass decomposition filter (--) creates a set of detail coefficients (d_j) whose bandwidth is indicated by grey shading. The low-pass decomposition filter (-) creates a set of approximation coefficients whose bandwidth is denoted by the red shading. The bandwidth of the approximation coefficients is then decomposed further during the next level of processing until level 5 is reached.

The pyramidal filtering scheme of the DWT represents a significant improvement in the computational efficiency of the wavelet transform. The DWT decomposition involves only 1 set of quadrature mirror filters which are computed prior to initializing the decomposition. These

filters also act on successively smaller sets of coefficients at each level of processing. In the case of the CWT, the entire length of the signal is filtered using a wavelet function specifically computed for each decomposition level. The efficiency of the DWT extends to its inverse process, which reconstructs the signal from the stored approximation and detail coefficients. During reconstruction, the a_j coefficients can be reconstructed by placing a zero between each consecutive value of both the detail and approximation coefficients of level $j+1$ (i.e. up-sampling by two), convolving the up-sampled results with the respective reconstruction filter, and summing, as shown in Eq. 15.

$$a_j^{DWT}(k) = \sum_n h_0(k-2n) a_{j+1}^{DWT}(n) + \sum_n g_0(k-2n) d_{j+1}^{DWT}(n) \quad \textbf{(15)}$$

This process can be continued iteratively until the signal, f, is fully reconstructed. Both the decomposition and the reconstruction procedures are outlined in Figure 4.

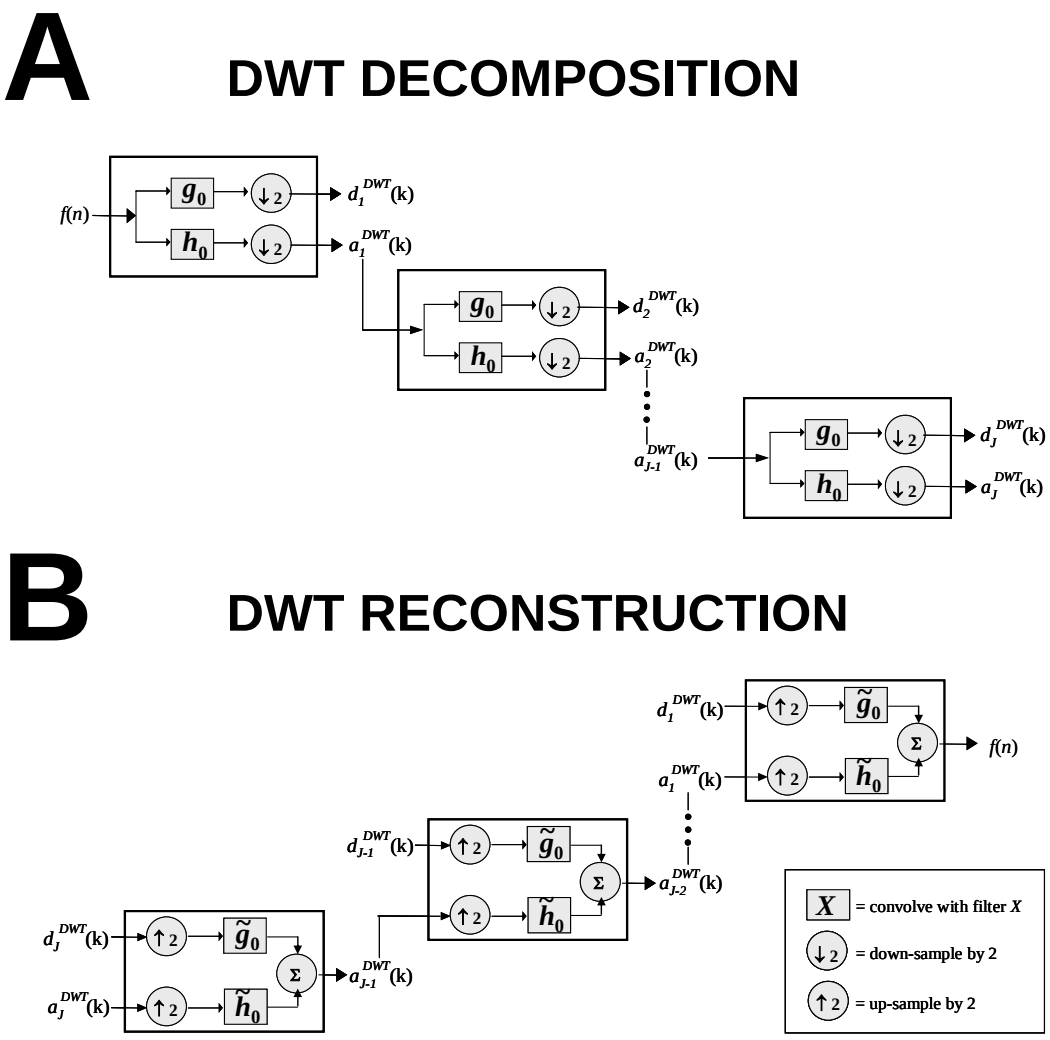

Figure 4. Block diagram of the Mallat algorithm for discrete wavelet transformation (DWT) **(A)** and reconstruction **(B)** (Mallat, 1989). The approximation coefficients at level j (a_j^{DWT}) are separately convolved with 2 complementary filters, a high pass filter (g_0) and a low pass filter (h_0). The filtered signals are subsequently decimated by a factor of 2 to eliminate redundant samples. This procedure yields the next level of low frequency approximation coefficients (a_{j+1}^{DWT}) and high frequency detail coefficients (d_{j+1}^{DWT}). This decomposition process can be repeated using the (a_{j+1}^{DWT}) coefficients as the input, resulting in another level of approximation and detail coefficients. The original input signal can then be reconstructed by reversing the process, known as inverse discrete wavelet transformation (IDWT).

The Stationary Wavelet Transform

In contrast to the DWT, the stationary wavelet transform (SWT) up-samples the decomposition filters by inserting zeros between every other filter coefficient and, consequently, avoids problems caused by the decimation step used in the DWT (Mallat, 1991) (Figure a). Therefore, the SWT uses a set of *level dependent decomposition filters,* h_j and g_j, which are the

h_0 and g_0 filters with 2^{j-1}-1 zeros between each discrete filter coefficient. The SWT approximation and detail coefficients can then be computed using Eq. 16 and 17.

$$a_{j+1}^{SWT}(k) = \sum_n h_j(n-k) a_j^{SWT}(k) \quad \textbf{(16)}$$

$$d_{j+1}^{SWT}(k) = \sum_n g_j(n-k) a_j^{SWT}(k) \quad \textbf{(17)}$$

During the SWT reconstruction, the level *j* detail and approximation coefficients are filtered with the appropriate *level dependent reconstruction filter* (i.e. $\tilde{g}_j$ and $\tilde{h}_j$, respectively) and summed to produce the a_{j-1}^{SWT} coefficients. The reconstruction filters are then down-sampled for the next level of processing. This is described in Eq. 18.

$$a_j^{SWT}(k) = \sum_n h_j(k-n) a_{j+1}^{SWT}(n) + \sum_n g_j(k-n) d_{j+1}^{SWT}(n) \quad \textbf{(18)}$$

Both the SWT decomposition and reconstruction are depicted below in Figure 5.

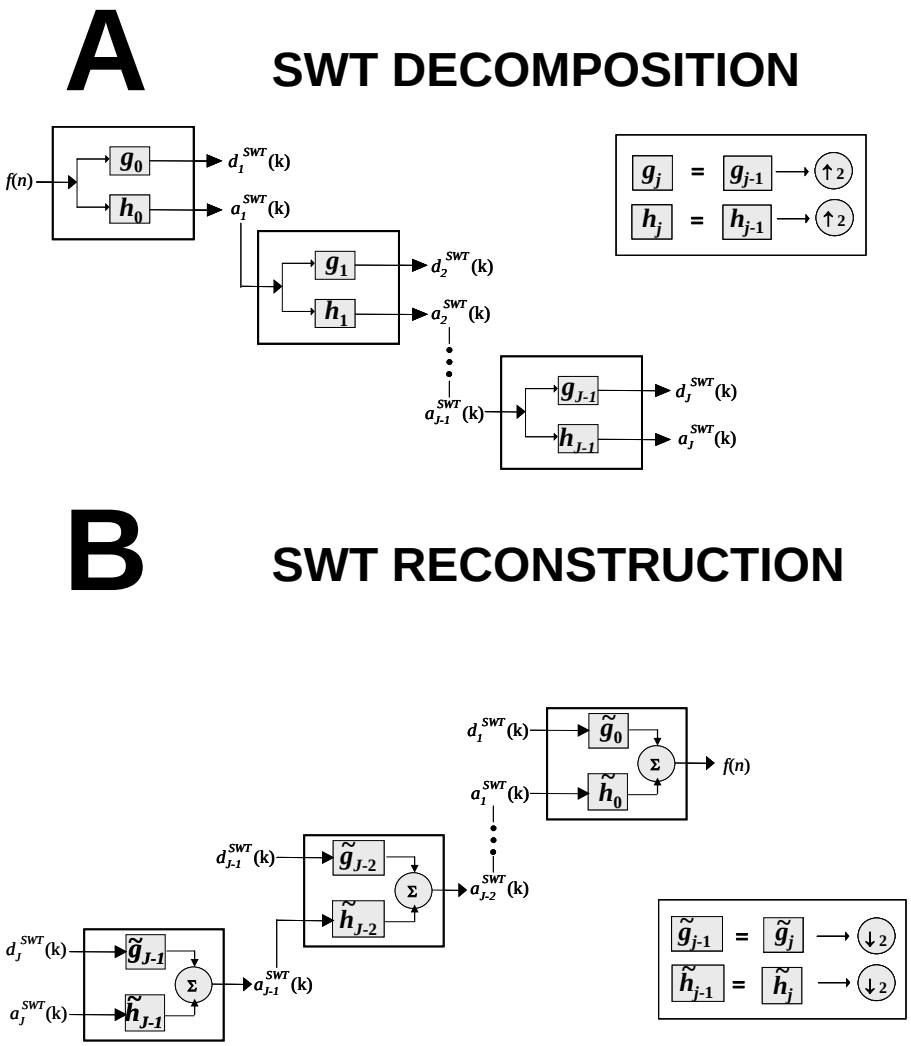

Figure 5. The SWT algorithm. **(A)** SWT Decomposition. At each wavelet level all coefficients are retained and the filters, g_j and h_j, are up-sampled for the next level of processing. **(B)** SWT Reconstruction (ISWT). At each wavelet level, the detail and approximation coefficients are filtered with appropriate reconstruction filter and summed. The filters are then down-sampled for the next level of processing.

Inserting zeros between the filter coefficients allows the SWT to analyze every possible shift of the signal while the effective sample rate at each wavelet level remains unchanged. This process is depicted in for one level of processing. In the frequency domain, up-sampling acts to halve the corner frequency of both the low-pass and high-pass decomposition filters, resulting in the same bandwidth decomposition as is found in the DWT. The result is a redundant, or over-complete, set of detail and approximation coefficients [2]. Note that the SWT detail coefficients are identical to the coefficients computed using the CWT, but they are computed using a different process.

Wavelet De-noising

The basic assumption of the de-noising algorithm proposed by Donoho [3] is that the recorded signal, *f*, is composed of a signal of interest, *s*, and a noise term, *w*, such that:

$$f(t) = s(t) + \sigma_W w(t) \quad \textbf{(19)}$$

where *w* consists of identically distributed Gaussian white noise with a mean of zero and unit variance and σ_W is the standard deviation of the noise of the recorded signal. Donoho [3] suggests that once the recorded signal, *f*, is converted to a wavelet representation the energy of the desired signal, *s*, will be concentrated into a small number of wavelet levels, whereas the energy of the white noise term will be evenly spread throughout all of the wavelet levels. Consequently, the magnitude of the *s* detail coefficients in these levels will be relatively large compared to those associated with the noise term, *w* [4]. Therefore, if a simple thresholding algorithm is applied to the detail coefficients at each decomposition level, the resultant detail coefficients can be recombined with the highest level ($j=J$) approximation coefficients to recover *s*. Donoho has demonstrated a number of efficient algorithms to determine appropriate values for this threshold, many of which are explained in [3] and [5]. One of the more common threshold computations is described below in Eq. 20.

$$T_W = \sigma_W \sqrt{2\log_e(N)} \quad \textbf{(20)}$$

In the equation listed above, T_W represents the threshold for the detail coefficients and *N* represents the number of samples contained in the entire signal. Under the standard assumption that *w* is a stationary white noise process, the noise level, σ_W, is equal for all levels of detail coefficients. Therefore, σ_W can be estimated from an arbitrary level of detail coefficients and the corresponding threshold can be applied to all levels of detail coefficients. In this document, this is referred to *single level noise estimation threshold*. In Eq. 21, the standard deviation of the noise is estimated using the median absolute deviation from zero (MAD) of the level 1 detail coefficients divided by the 75th percentile of the standard normal distribution, 0.6745. This method of estimating the standard deviation is typically used in wavelet de-noising because it less sensitive to outliers than the traditional calculation of the sample standard deviation (Hampel, 1986). In Eq. 21, $\bar{d}_1$ is the sample mean of the level 1 detail coefficients.

$$\sigma_W = \frac{median\left(\left|d_1 - \bar{d}_1\right|\right)}{0.6745} \quad \textbf{(21)}$$

In the case of correlated or colored noise, such as 1/*f* noise, the standard deviation of the noise is level dependent [6;7]. This type of noise requires a standard *level dependent noise estimation threshold*, T_j^S, which uses a level dependent noise level estimate, σ_j (Eq. 22 and 23) [6]. The superscript S in T_j^S is used to differentiate this standard colored-noise threshold from a modified colored-noise threshold, T_j^M, used elsewhere in the text (See Chapter III).

$$\sigma_j = \frac{median\left(\left|d_j - \bar{d}_j\right|\right)}{0.6745} \quad \textbf{(22)}$$

$$T_j^S = \sigma_j \sqrt{2\log_e(N)} \quad \textbf{(23)}$$

In Eq. 22, d_j is a general set of detail coefficients for level *j*. The threshold can then be implemented using a hard-threshold criterion (Eq. 24), i.e.

$$d'_j = \begin{cases} d_j & if\ \left|d_j\right| > T_j^S \\ 0 & if\ \left|d_j\right| \le T_j^S \end{cases} \quad \textbf{(24)}$$

or by using soft-thresholding (Eq. 25)

$$d'_j = \begin{cases} sign\left(d_j\right)\left(\left|d_j\right| - T_j^S\right) & if\ \left|d_j\right| > T_j^S \\ 0 & if\ \left|d_j\right| \le T_j^S \end{cases} \quad \textbf{(25)}$$

Where d'_j are the thresholded detail coefficients at level *j*.

Following the thresholding of the detail coefficients, *s* can be estimated by performing the typical wavelet reconstruction using the a_J approximation coefficients and the modified detail coefficients. Although the de-noising procedure was originally suggested for DWT detail coefficients [3], the algorithm has been shown to work using SWT coefficients as well [6;8]. More detailed descriptions of these algorithms is given in several texts, including [4;9].

References

[1] S. G. Mallat, "A Theory for Multiresolution Signal Decomposition - the Wavelet Representation," *Ieee T Pattern Anal*, vol. 11, no. 7, pp. 674-693, 1989.

[2] M. Lang, H. Guo, J. Odegard, C. Burrus, and R. Wells, "Noise reduction using an undecimated discrete wavelet transform," *IEEE SIGNAL PROC LET*, vol. 3, no. 1, pp. 10-12, 1996.

[3] D. L. Donoho, "De-Noising by Soft-Thresholding," *Ieee T Inform Theory*, vol. 41, no. 3, pp. 613-624, 1995.

[4] C. S. Burrus, R. A. Gopinath, and H. Guo, *Introduction to Wavelets and Wavelet Transforms, a primer*. Upper Saddle River, New Jersey: Prentice Hall, 1998.

[5] M. Misiti, Y. Misiti, G. Oppenheim, and J. M. Poggi, *Wavelet Toolbox User's Guide, for use with Matlab*. Natick, MA: The MathWorks, inc, 1996.

[6] I. Johnstone and B. Silverman, "Wavelet threshold estimators for data with correlated noise," *J of the Royal Statistical Society*, vol. 59, no. 2, pp. 319-351, 1997.

[7] G. Wornell, "Wavelet-Based Representations for the 1/f Family of Fractal Processes," *P Ieee*, vol. 81, no. 10, pp. 1428-1450, 1993.

[8] B. Silverman, "Wavelets in statistics: beyond the standard assumptions," *PHILOS T ROY SOC A*, vol. 357, no. 1760\, pp. 2459-2473, 1999.

[9] S. Mallat, *A Wavelet Tour of Signal Processing*, 2 ed Academic Press, 1999.

APPENDIX B

COMPARISON OF DISCRETE AND STATIONARY WAVELET TRANSFORM SPIKE DETECTION METHODS FOR HUMAN SYMAPTHETIC NERVE ACTIVITY

Motivation

In Chapter III we were able to demonstrate that a spike detection method which used the stationary wavelet transform (SWT) coupled with a two-stage kurtosis de-noising method outperformed an unsupervised amplitude discriminator and similar SWT-based methods on simulated human muscle sympathetic nerve activity (MSNA) signals with varying burst rates and signal to noise ratios (SNR). However, the spike detection method presented by Diedrich, *et al.* for the human MSNA incorporated the discrete wavelet transform (DWT) rather than the SWT [1]. Although we were able to demonstrate the drawbacks of DWT-based action potential detection in the mouse sympathetic nerve activity in Chapter IV, we did not directly compare the DWT and SWT in human sympathetic spike detection. Therefore, we have elected to include this comparison in this Appendix.

Methods

Simulations

To assess the performance of the of various discrete and stationary wavelet transform based human sympathetic spike detection methods, we again used the same simulated signals created for similar detection evaluation in Chapter III. Briefly, simulated signals were constructed with templates extracted from human MSNA recordings with sufficiently high signal to noise ratio in 8 healthy subjects during periods of sympathetic activation (head-up tilt). A short segment of noise was extracted from each recording during Phase IV of the Valsalva maneuver and modeled with a 50 order autoregressive (AR) model created using the Burg method [2]. The model was then applied to a sequence of Gaussian random numbers 60 seconds in length to create the simulated noise.

The templates were then randomly inserted into neural noise in burst fashion. The burst position, burst duration, and spike placement within each burst were all randomly assigned according to separate Poisson random variables. The average burst duration and spike rate within

each burst were fixed at 0.8 seconds and 60 spikes/sec, respectively. Each simulation was assigned either a low (5 burst/min), moderate (25 bursts/min), or high (50 bursts/min) mean burst rate. The signal to noise ratio (SNR) of the simulations was altered from 6 (high signal quality) to 1 (poor signal quality). The SNR was defined as the ratio between the absolute peak amplitude of the action potential and the standard deviation of the noise, as defined elsewhere [1;3].

Detection Methods

The performance of five wavelet-based detection methods was evaluated. The five methods included: (1) SWT decomposition with a standard colored noise threshold (SWTS), (2) SWT decomposition with a modified colored noise threshold (SWTM), (3) DWT decomposition with a standard threshold (DWTS), (4) DWT decomposition with a modified wavelet threshold, and (5) SWT decomposition with a two-stage kurtosis de-noising method (SWTK). Details of the SWT and DWT decomposition are presented in Appendix A. The standard, T_j^S, and modified, T_j^M, colored noise thresholds are displayed in Eq 1 and 2, respectively.

$$T_j^S = \sigma_j \sqrt{2\log_e(N)} \quad \textbf{(1)}$$

$$T_j^M = 0.8\sigma_j \sqrt{2\log_e(N)} \quad \textbf{(2)}$$

The standard colored noise threshold was suggested by Johnstone [4] and the 0.8 modification shown in Eq. 2 was presented by Diedrich, *et al.* [1]. In both Eq. 1 and 2, σ_j represents the robust, level-dependent estimate of the noise standard deviation shown in Eq. 3 [4].

$$\sigma_j = median\left(\left|d_j - \bar{d}_j\right|\right) / 0.6745 \quad \textbf{(3)}$$

Details of the kurtosis de-noising method were presented in Chapter III. Although a separate unsupervised amplitude discriminator was also evaluated, the results were omitted from the graphical display to avoid confusion. Details of the amplitude discriminator and its results are displayed in Chapter III.

Detection Performance

The performance of each method was quantified using the percent of correctly detected action potentials (PCD, Eq. 4) and the percent of false alarms (PFA, Eq. 5).

$$PCD = \frac{N_{CD}}{N_{AP}} \times 100 \quad \textbf{(4)}$$

$$PFA = \frac{N_{FA}}{N_{CD}} \times 100 \quad \textbf{(5)}$$

N_{CD} is the number of correctly detected APs, N_{AP} is the number of APs inserted into the simulation, and N_{FA} is the number of false alarms.

Results

The detection performance of each of the five methods is displayed in Figure 1.

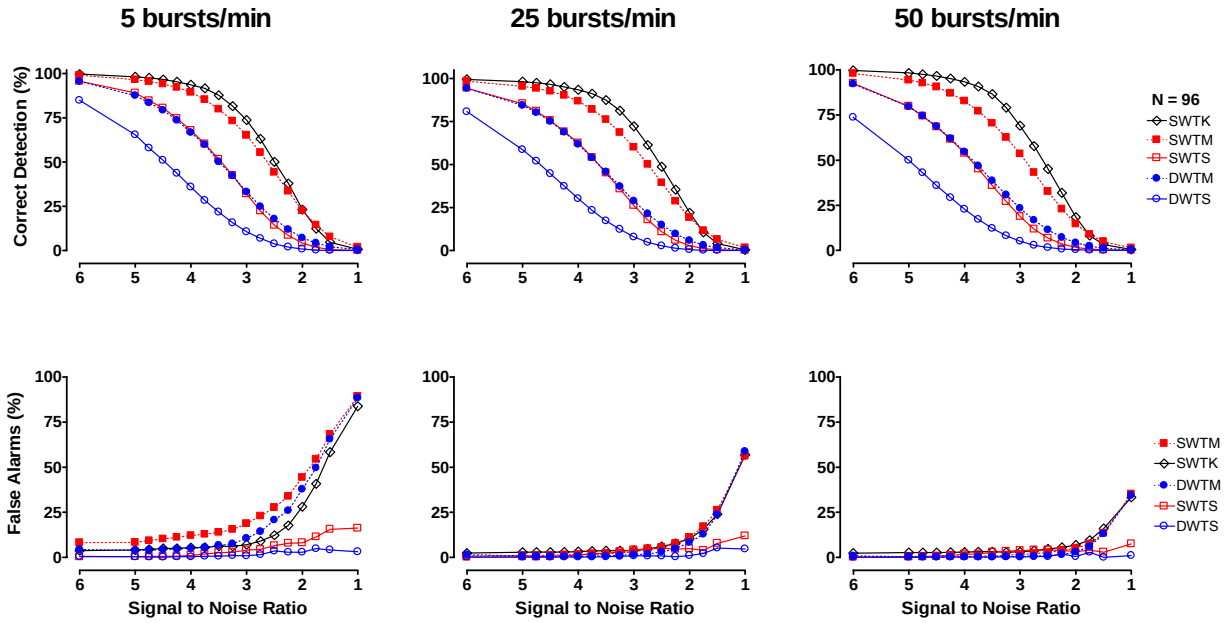

Figure 1. Mean results for simulations with varied noise levels and mean burst rates. The simulations tested the performance of SWT decomposition with standard (SWTS) and modified (SWTM) colored noise thresholds, DWT decomposition with standard (DWTS) and modified (DWTM) colored noise thresholds, and SWT decomposition with 2-stage kurtosis threshold (SWTK). Each point on each curve represents the mean result of 96 simulations.

While the DWT-based detection methods misidentified a lower percentage of false alarms (PFA) than their SWT-based counter parts, they also correctly detected substantially lower percentages of the simulated action potentials in all burst rate and SNR scenarios. Both the standard colored noise thresholds (SWTC and DWTC) have a low PFA during all of the simulations, but their percent of correctly detected spikes (PCD) also remains low under all conditions. The modification to the standard threshold in both the SWT and DWT (SWTM and

DWTM), suggested by Diedrich *et al.*, results in a higher PCD than their standard threshold counterparts (SWTC and DWTC, respectively) and the PFA remains low (<10%) for SNR>2 during moderate (25 bursts/min) and high (50 bursts/min) burst rates. The two-stage kurtosis de-noising (SWTK) demonstrates the highest PCD for SNR>2 during all burst rates and its PFA is similar to that of the modified SWT and DWT thresholds (SWTM and DWTM) at burst rates of 25 and 50 bursts/min and lower during the 5 burst/min simulations.

Discussion

We have demonstrated that action potential detection methods based on the stationary wavelet transform, in general, have better detection performance than those based on the discrete wavelet transform. SWT methods appear to correctly detect a much higher percent of simulated action potentials but detect a similar or only slightly higher percentage of false alarms than DWT methods with the same threshold rule. The higher percentage of false dismissals (undetected action potentials) in the DWT-based methods may be attributed to the transform's lack of translation invariance. The fact that the DWT decimates the number of wavelet coefficients during each level of processing combined with the fact that each action potential is represented in small number of wavelet coefficients means that chance of eliminating "spike-related" coefficients increases dramatically at higher wavelet levels. In Chapter IV, the shift-variability of the DWT was demonstrated to be detrimental to the detection sympathetic action potentials in the mouse, which characteristically have a longer duration, and thus more detectable high amplitude points, than human action potentials (see Chapter II).

Overall, SWT decomposition with a two-stage kurtosis de-nosing procedure was found to have the most robust detection performance during variable burst rates and signal to noise ratios. In conclusion, SWT-based spike detection can be useful in the quantification of sympathetic nerve activity and may play a future clinical role in the analysis of autonomic function.

References

[1] A. Diedrich, W. Charoensuk, R. J. Brychta, A. C. Ertl, and R. Shiavi, "Analysis of raw microneurographic recordings based on wavelet de-noising technique and classification algorithm: wavelet analysis in microneurography," *IEEE Trans. Biomed. Eng*, vol. 50, no. 1, pp. 41-50, Jan.2003.

[2] R. G. Shiavi, *Introduction to Applied Statistical Signal Analysis*, 2nd ed. San Diego: Academic Press, 1999.

[3] Z. Nenadic and J. W. Burdick, "Spike detection using the continuous wavelet transform," *IEEE Trans. Biomed. Eng*, vol. 52, no. 1, pp. 74-87, Jan.2005.

[4] I. Johnstone and B. Silverman, "Wavelet threshold estimators for data with correlated noise," *J of the Royal Statistical Society*, vol. 59, no. 2, pp. 319-351, 1997.

APPENDIX C

APPLICATION OF WAVELET BASED SPIKE DETECTION IN TRANSGENIC MURINE MODELS OF DYSAUTONOMIAS

Motivation

In Chapter IV we were able to demonstrate that stationary wavelet transform (SWT) based spike detectors were more robust than common unsupervised amplitude discriminators and DWT-based methods in simulated murine renal sympathetic nerve activity (RSNA) signals with varying spike rates and signal to noise ratios (SNR). Our purpose in developing such a method was its eventual implementation in the analysis of transgenic mouse models of human autonomic disorders. In the following Appendix, we will discuss the outcome of such application to the study of norepinephrine transporter (NET) deficient [1] and regulator G-protein signal 2 (RGS2) deficient mice [2;3].

Background

NET-Deficient Mice

Norepinephrine (NE) is the neurotransmitter primarily released from the post-ganglionic sympathetic neuron at the neuro-effector junction [4]. The norepinephrine transporter (NET) is responsible for reuptake of free NE following sympathetic discharge [1]. NET impairment has been implicated in human disorders such as essential hypertension and orthostatic intolerance [5]. Human studies involving blockade of NET using drugs such as reboxetine [5;6] and desipramine [7] have demonstrated a paradoxical tachycardia and elevated blood pressure with a drop in the baseline sympathetic nerve activity. Previous studies with the NET knockout mice have shown similarly high heart rate and blood pressure values, but sympathetic nerve activity was not analyzed [1].

RGS2-Deficient Mice

G-protein coupled receptors play an important role in normal cellular function and have been demonstrated to regulate sympathetic activity [8] and vascular tone [9]. The regulator of G-

protein signaling 2 (RGS2) helps to regulate G-protein-effctor interactions in cells throughout the body [3]. RGS2 deficient mice have demonstrated elevated resting blood pressure, an exaggerated depressor response to alpha-1 blockade, and increased NE excretion rate [10], all suggesting that these animals may have reduced sympathetic nerve activity.

Methods

NET-Deficient Mice

The NET knockout mice strain (NET -/-) was provided by Dr. Marc Caron of Duke University with NET gene disruption via insertion of EGFP cDNA coupled to the PGK-neomycin-resistance gene in exon 2 of the native gene. NET -/- mice derived from an interbred 129Sv/J x C57BL/6J strain were backcrossed 10X onto the C57BL/6J strain. KO mice were bred and maintained with a 12:12h light-dark cycle and fed standard mouse chow with tap water available ad libitum.

Identical surgical and experimental protocols were administered to 13 NET -/- mice (9.5±0.2 month; 30.1±0.3g) and 14 healthy C57BL/6J strain wild type mice (NET +/+) (8.8±0.3 month; 28.3±0.2g), which were used as a control group. All protocols were approved by the Vanderbilt University Institutional Animal Care and Use Committee.

RGS2-Deficient Mice

Seven adult male RGS2 deficient (RGS2 -/-) mice weighing 27±1 g and 8 male wild-type (RGS2 +/+) mice weighing 30±1 g. All animals were obtained from Washington University School of Medicine, Department of Cell Biology and Physiology, St. Louis, Missouri, USA. The animals were allowed free access to standard chow (0.25% sodium, SNIFF Spezialitäten GmbH, Soest, Germany) and drinking water. The protocol was approved by the local council on animal care in accordance with the guidelines of the American Physiological Society.

Sympathetic Nerve Recordings

Anesthesia Mice were anesthetized with 1.5% Isofluran (in 100% Oxygen) through a nose cone. Body temperature was maintained at 36-37° C with an isothermal pad (Braintree Scientific, Inc., Braintree, MA).

Nerve Recordings The left kidney was exposed through a left flank incision and with blunt dissection retroperitonaeally. A branch of the renal nerve running parallel to the renal artery was isolated carefully. A bipolar stainless steel wire electrode pair (wire 0.003 inches bare diameter and 0.0045 inches coated diameter, part number 316SS3T, MedWire Corp, NY, electrode distance 1-1.5 mm) were hooked onto the nerve. After achieving optimal signal quality, the electrodes were secured with silicone adhesive gel (QuickSeal, World Precision Instruments, Sarasota, FL). A high-pass filter (300 Hz) was applied to the nerve signal to reduce the significant low-frequency noise caused by the 60 Hz AC power and its harmonics as well as breathing artifacts. This filter setting was also recommended in previous publications [11;12]. The output was then amplified (gain 10,000) by an isolated differential amplifier (ISO-80, World Precision Instruments, Sarasota, FL).

Data Acquisition The signals were recorded using a WINDAQ data acquisition system (DI410, DATAQ, Acron, OH) with 14 Bit resolution at 10000 Hz sample frequency. The data were processed off-line using customized software written in the Matlab environment (The MathWorks, Inc., Natick, MA).

Sympathetic Nerve Analysis

A spike detection algorithm using stationary wavelet transform (SWT) decomposition with the Symlet 7 wavelet and a single level noise estimation threshold on the level 4 and 5 detail coefficients was used to quantify the sympathetic nerve activity. Further details of this spike detection algorithm are presented in Chapter IV. Spike detection was applied to five minute periods of baseline RSNA from both transgenic mouse species and the mean spike rate results were compared to those obtained from their respective wild type counterparts using a non-parametric Mann-Whitney U-Test for unpaired data.

Results

NET-Deficient Mice

The SWT spike detection method was used to analyze five minutes of baseline RSNA in wild type (NET +/+) and norepinephrine transporter deficient (NET -/-) mice. The mean baseline

spike rate for the NET +/+ group (60.1 ± 10.0 spikes/s) was found to be significantly higher than that of the NET -/- group (21.3 ± 4.9 spikes/s; $p<0.01$) as shown in Figure 1.

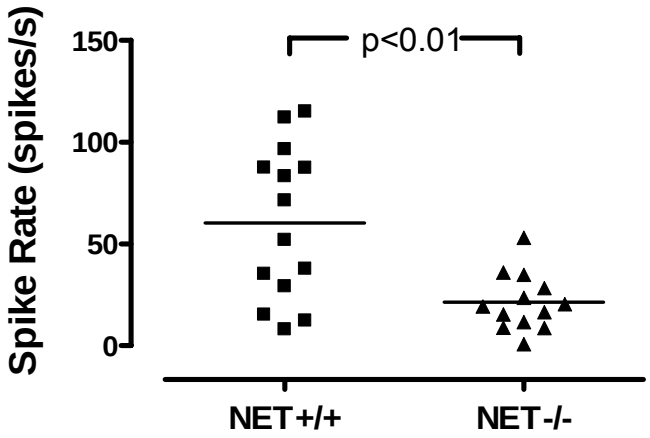

Figure 1. Baseline spike rates in 14 wild type (NET +/+) and 13 norepinephrine transporter deficient (NET-/-) mice computed using the SWT spike detection method.

RGS2-Deficient Mice

Figure 2 demonstrates that the mean baseline spike rates in the wild type (RGS2 +/+; 25.5 ± 5.1 spikes/s) mice were found to be significantly higher than those found in the knockout mice (RGS2 -/-; 17.4 ± 4.0 spikes/s; $p<0.01$). These results were reported with permission from [3].

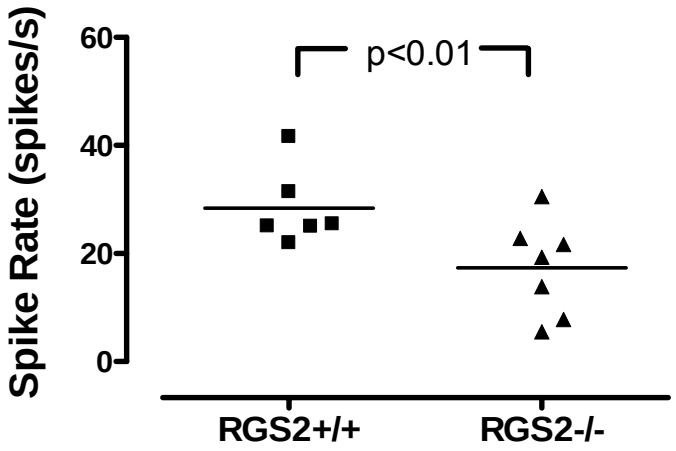

Figure 2. Baseline spike rates in 8 wild type (RGS2 +/+) and 7 RGS2 deficient (RGS2 -/-) mice computed using the SWT spike detection method. Graphic borrowed with permission from [3].

Discussion

We have demonstrated that the SWT-based spike detection method optimized in Chapter IV is capable of analyzing data from various strains of transgenic mice. The baseline spike rates for the NET +/+ and RGS2 +/+ wild type animals differed substantially different, but this may be the result of different mouse strains being used in the control group.

The genes modified in both transgenic mouse strains were found to play a role in the regulation of sympathetic function and could be important in explaining the mechanism of various disorders of the autonomic nervous system. This information may be useful in the design of pharmacological agents used to target these specific transporters and regulators in the hopes of controlling the affects of these dysautonomias. In conclusion, SWT-based spike detection can be useful in the quantification of murine sympathetic nerve activity and may play a future clinical role in the assessment of autonomic function.

References

[1] N. R. Keller, A. Diedrich, M. Appalsamy, S. Tuntrakool, S. Lonce, C. Finney, M. G. Caron, and D. Robertson, "Norepinephrine transporter-deficient mice exhibit excessive tachycardia and elevated blood pressure with wakefulness and activity," *Circulation*, vol. 110, no. 10, pp. 1191-1196, Sept.2004.

[2] M. Obst, V. Gross, A. Diedrich, Brychta RJ, K. J. Blumer, K. Heusser, J. Jordan, F. C. Luft, and J. Tank, "Sympathteic nerve traffic and circulating norepinephrine levels in RGS2-deficient mice," 2006.

[3] M. Obst, J. Tank, R. Plehm, K. J. Blumer, A. Diedrich, J. Jordan, F. C. Luft, and V. Gross, "NO-dependent blood pressure regulation in RGS2-deficient mice," *Am. J Physiol Regul. Integr. Comp Physiol*, vol. 290, no. 4, p. R1012-R1019, Apr.2006.

[4] R. M. Berne and M. N. Levy, *Physiology*. St. Louis, MO: Mosby, 1998.

[5] C. Schroeder, J. Tank, M. Boschmann, A. Diedrich, A. M. Sharma, I. Biaggioni, F. C. Luft, and J. Jordan, "Selective norepinephrine reuptake inhibition as a human model of orthostatic intolerance," *Circulation*, vol. 105, no. 3, pp. 347-353, Jan.2002.

[6] J. Tank, C. Schroeder, A. Diedrich, E. Szczech, S. Haertter, A. M. Sharma, F. C. Luft, and J. Jordan, "Selective impairment in sympathetic vasomotor control with norepinephrine transporter inhibition," *Circulation*, vol. 107, no. 23, pp. 2949-2954, June2003.

[7] M. D. Esler, G. Wallin, P. K. Dorward, G. Eisenhofer, R. Westerman, I. Meredith, G. Lambert, H. S. Cox, and G. Jennings, "Effects of desipramine on sympathetic nerve firing and norepinephrine spillover to plasma in humans," *Am J Physiol*, vol. 260, no. 4 Pt 2, p. R817-R823, Apr.1991.

[8] E. S. Vizi, "Role of high-affinity receptors and membrane transporters in nonsynaptic communication and drug action in the central nervous system," *Pharmacol. Rev*, vol. 52, no. 1, pp. 63-89, Mar.2000.

[9] K. M. Tang, G. R. Wang, P. Lu, R. H. Karas, M. Aronovitz, S. P. Heximer, K. M. Kaltenbronn, K. J. Blumer, D. P. Siderovski, Y. Zhu, and M. E. Mendelsohn, "Regulator of G-protein signaling-2 mediates vascular smooth muscle relaxation and blood pressure," *Nat Med*, vol. 9, no. 12, pp. 1506-1512, Dec.2003.

[10] V. Gross, J. Tank, M. Obst, R. Plehm, K. J. Blumer, A. Diedrich, J. Jordan, and F. C. Luft, "Autonomic nervous system and blood pressure regulation in RGS2-deficient mice," *Am J Physiol Regul. Integr. Comp Physiol*, vol. 288, no. 5, p. R1134-R1142, May2005.

[11] X. Ma, F. M. Abboud, and M. W. Chapleau, "A novel effect of angiotensin on renal sympathetic nerve activity in mice," *J Hypertens.*, vol. 19, no. 3 Pt 2, pp. 609-618, Mar.2001.

[12] X. Ma, M. W. Chapleau, C. A. Whiteis, F. M. Abboud, and K. Bielefeldt, "Angiotensin selectively activates a subpopulation of postganglionic sympathetic neurons in mice," *Circ. Res*, vol. 88, no. 8, pp. 787-793, Apr.2001.

APPENDIX D

A HILBERT-MODIFIED CONTINUOUS WAVELET TRANSFORM FOR INSTANTANEOUS SPECTRAL ANALYSIS OF HEART RATE AND BLOOD PRESSURE

Motivation

Several authors have successfully demonstrated the utility of the continuous and discrete wavelet transform in time-varying spectral analysis of heart-rate variability during dynamic cardiovascular stimulation [1-4]. Crowe et al (1992) was the first to apply wavelet analysis to heart rate variability [5]. Since this initial work, several authors have simply used the discrete wavelet transform (DWT) or the squared magnitude of its coefficient outputs to display the changes in the heart rate variability using a multiresolution approach [1;6;7]. However, the output of any form of real wavelet transform; e.g. DWT, CWT, or SWT; is simply a filtered version of the input and will oscillate significantly. Therefore, power computed in this manner will not be comparable to power computed using more traditional methods, i.e. with Fourier Transform based methods (Fig. 1). To account for this phenomenon, Toledo, et al (2003) suggests using a median filter with a length of 3 seconds to reduce the fluctuations in the output of the CWT (Toledo et al., 2003). This line of processing has two essential problems: (1) the median filter may distort the power information and (2) by averaging over 3 seconds, some time resolution is lost.

Another method of eliminating the fluctuations in the wavelet coefficients is to find the instantaneous amplitude of the wavelet coefficient oscillations using a Hilbert Transform [8]. This method was applied to the DWT and the wavelet packet transform of the heart rate variability with some success [3] and could be useful for analysis in the analysis of the CWT spectral power for heart rate and blood pressure variability.

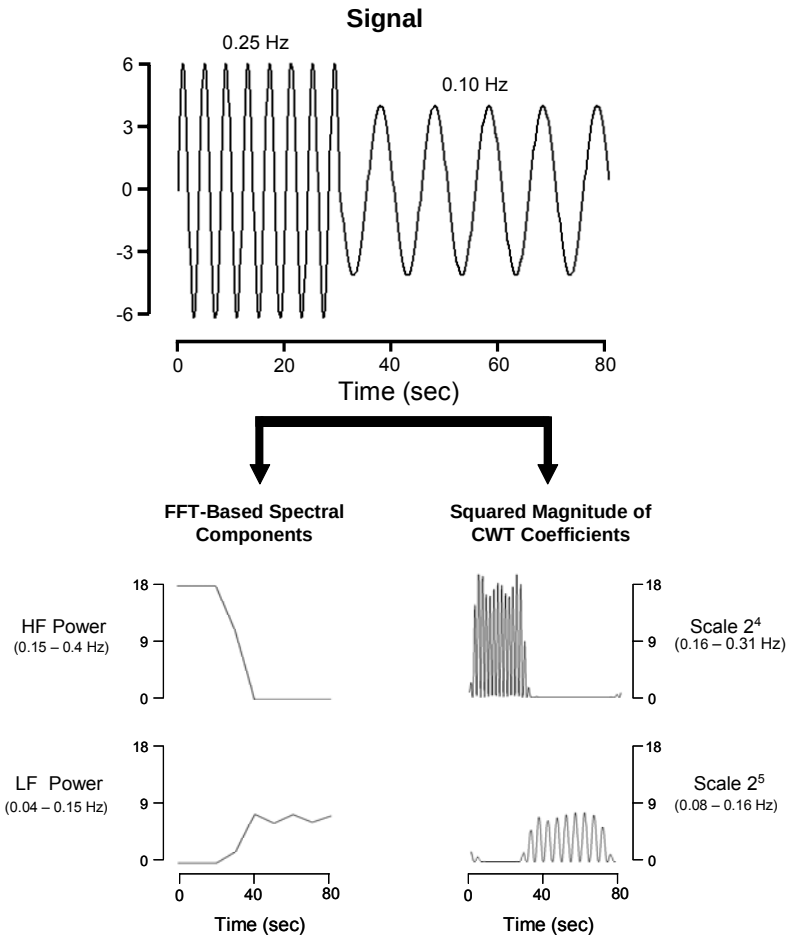

Figure 1. Wavelet decomposition versus Fourier spectral analysis. The input to each method is the simulated signal at the top. The signal contains a 0.25 Hz sinusoid from 0-30 seconds and a 0.10 Hz sinusoid from 30-80 seconds. The wavelet decomposition simply produces filtered versions of this input signal. The coefficients at each wavelet scale have an oscillatory nature. The FFT-based power calculation does not oscillate in the same manner. Note also that the wavelet components appear to resolve the change from 0.25 Hz to 0.1 Hz more rapidly in both bands.

Methods

Details of the continuous wavelet transform can be found in Appendix A. An analytic signal z_s, can be created from a set of real-valued wavelet coefficients at scale s, d_s, using Eq. 1.

$$z_s(n) = d_s(n) + iH\{d_s(n)\} \tag{1}$$

In Eq. 1, $i = \sqrt{-1}$ and $H\{\ldots\}$ denotes the Hilbert transform. The instantaneous amplitude of d_s can then be computed by calculating the magnitude of the analytic signal [9] (Eq. 2). Note, A_s is the instantaneous amplitude of d_s.

$$A_s(n) = |z_s(n)| = \sqrt{d_s^2(n) + [H\{d_s(n)\}]^2} \quad (2)$$

The instantaneous amplitude can then be converted to units of power by squaring A_s. For a more detailed description, refer to [9].

Results

In Fig. 2 below, we present a general method for a Hilbert modified continuous wavelet transform algorithm. The computing the instantaneous amplitude of each continuous wavelet coefficient scale eliminates the oscillations and the result can be used to compute the time-varying spectral power of the signal within specific frequency bands.

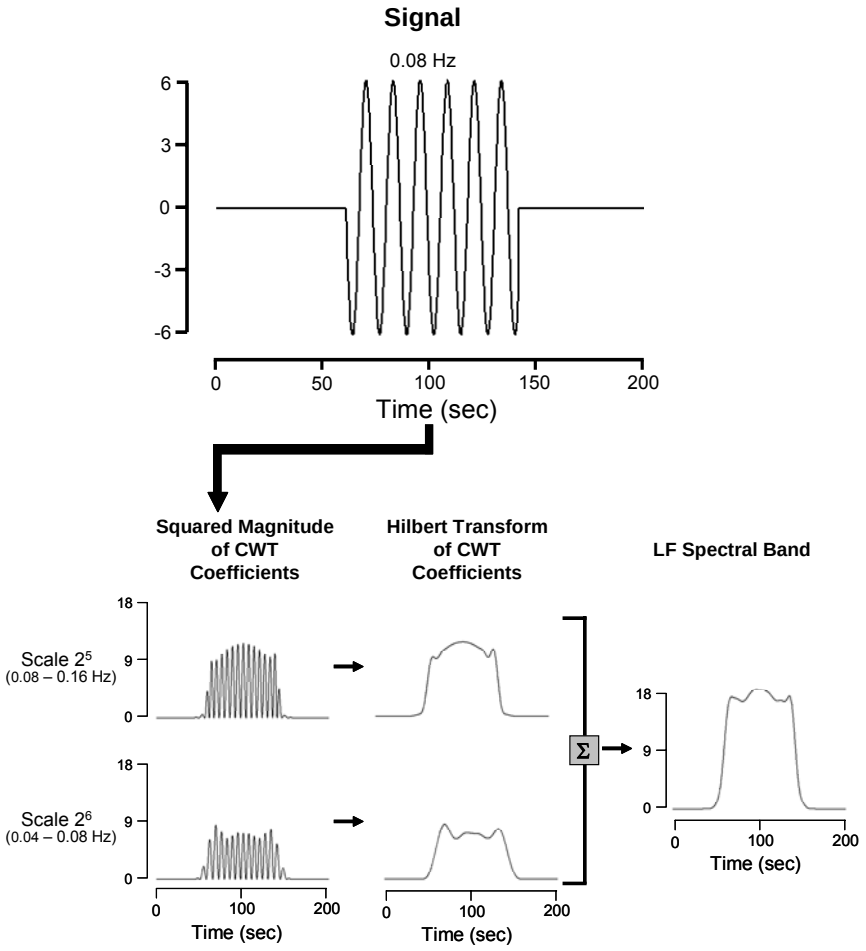

Figure 2. Hilbert-modified continuous wavelet transform (HMCWT). First, the CWT of a the signal is computed (left column). Next, the absolute value of the analytic signal of the Hilbert transform is used to display the instantaneous amplitude of the CWT (center column). These values are then squared and scaled to units of power. Finally, the appropriate scales are summed to form the approximate time-varying spectral band (right column).

Discussion

We have shown the general method for instantaneous, time varying spectral estimates using the Hilbert-modified continuous wavelet transform. This method was optimized for use in heart rate and blood pressure variability analysis and used to analyze the time course of the very low frequency (VLF), low frequency (LF), and high frequency (HF) components of a non-stationary data set in Chapter VI. This is a potentially useful technique which offers more flexibility than traditional Fourier-based time varying spectral estimates of fixed window length.

References

[1] V. Pichot, J. M. Gaspoz, S. Molliex, A. Antoniadis, T. Busso, F. Roche, F. Costes, L. Quintin, J. R. Lacour, and J. C. Barthelemy, "Wavelet transform to quantify heart rate variability and to assess its instantaneous changes," *J. Appl. Physiol*, vol. 86, no. 3, pp. 1081-1091, Mar.1999.

[2] V. Pichot, S. Buffiere, J. M. Gaspoz, F. Costes, S. Molliex, D. Duverney, F. Roche, and J. C. Barthelemy, "Wavelet transform of heart rate variability to assess autonomic nervous system activity does not predict arousal from general anesthesia," *Can. J. Anaesth.*, vol. 48, no. 9, pp. 859-863, Oct.2001.

[3] K. Tanaka and A. R. Hargens, "Wavelet packet transform for R-R interval variability," *Med. Eng Phys.*, vol. 26, no. 4, pp. 313-319, May2004.

[4] E. Toledo, O. Gurevitz, H. Hod, M. Eldar, and S. Akselrod, "Wavelet analysis of instantaneous heart rate: a study of autonomic control during thrombolysis," *Am. J. Physiol Regul. Integr. Comp Physiol*, vol. 284, no. 4, p. R1079-R1091, Apr.2003.

[5] J. A. Crowe, N. M. Gibson, M. S. Woolfson, and M. G. Somekh, "Wavelet transform as a potential tool for ECG analysis and compression," *J Biomed Eng*, vol. 14, no. 3, pp. 268-272, 1992.

[6] M. Akay, G. Landesberg, W. Welkowitz, Y. M. Akay, and D. Sapoznikov, "Carotid-cardiac interaction: heart rate variability during the unblocking of the carotid artery," *Adv Exp Med Biol*, vol. 346, pp. 365-372, 1993.

[7] U. Wiklund, M. Akay, and U. Niklasson, "Short-term analysis of heart-rate variability by adapted wavelet transforms," *IEEE Eng Med Biol Mag*, vol. 16, no. 5, pp. 113-8, 138, 1997.

[8] S. Olhede and A. Walden, "The Hilbert spectrum via wavelet projections.," *P ROY SOC LOND A MAT P ROY SOC LOND A MAT*, vol. 460, pp. 955-975, 2004.

[9] B. Boashash, "Estimating and interpreting the instantaneous frequency of a signal. I. Fundamentals," *P Ieee*, vol. 80, no. 4, pp. 520-538, 1992.